Master's thesis

NTNU
Norwegian University of Science and Technology
Faculty of Natural Sciences
Department of Physics

Herman Lileng Ottesen

Optical Conductivity of Dirac Fermions in Antiferromagnetic Semimetals

Master's thesis in Applied Physics and Mathematics
Supervisor: Alireza Qaiumzadeh
June 2021

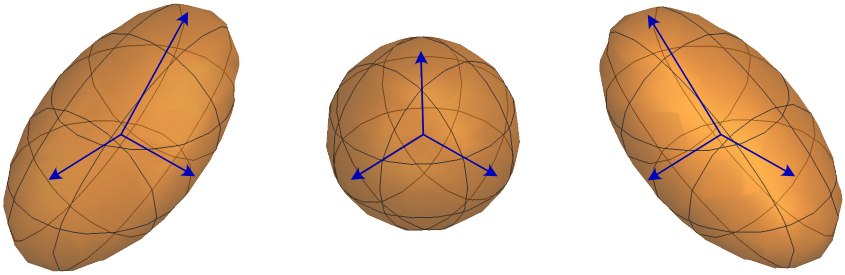

NTNU
Norwegian University of
Science and Technology

Herman Lileng Ottesen

Optical Conductivity of Dirac Fermions in Antiferromagnetic Semimetals

Master's thesis in Applied Physics and Mathematics
Supervisor: Alireza Qaiumzadeh
June 2021

Norwegian University of Science and Technology
Faculty of Natural Sciences
Department of Physics

NTNU
Norwegian University of
Science and Technology

Abstrakt (Norsk)

Del I av masteroppgaven introduserer de grunnleggende konseptene i kvantemekanikk gjennom tetthetsoperatoren, slik at statistikken til en ideell gass av kvantepartikler i kapittel 1 kan bli utledet basert på prinsippet om maksimal entropi. Matematikken som så følger dersom interaksjoner mellom kvantepartiklene blir betraktet tvinger frem realiseringen av Matsubara metoden i kapittel 2, der tid blir behandlet som en imaginær variabel og beregningene av fysiske observabler benytter seg av Matsubara Green funksjoner. I kapittel 3 blir likevektsensemblet deretter utsatt for en ytre perturbasjon, og observablene til det perturberte ensemblet beregnet i kuboformalismen fra lineær responsteori. Den resulterende kuboformelen for konduktivitet er uttrykt ved hjelp av Matsubara strømtetthetsautokorrelasjonsfunksjonen, hvis beregning krever et kjent uttrykk for hamiltonmatrisen til likevektsensemblet.

Del II utleder modellen for tettbundede elektroner i kapittel 4 for å eksemplifisere beregningen av en hamiltonmatrise og de medfølgende energibåndene for ulike krystalliske materialer, der det todimensjonale materialet grafén er særlig betraktet. Den effektive hamiltonmatrisen til grafén inntar samme form som den relativistiske Weyl hamiltonianen, og er knyttet til topologiske egenskaper ved hilbertrommet av blochfunksjoner i kapittel 3, der berryologiske størrelser for et generelt kvantesystem med to energinivåer er beregnet. I kapittel 4 er så hamiltonmatrisene til Weyl og Dirac halvmetaller introdusert som lineæriseringer omkring degenererte punkter i energibåndstrukturer med henholdsvis to og fire energibånd, hvilket resulterer i tredimensjonale generaliseringer av hamiltonmatrisen til grafén.

Til slutt, i Del III av masteroppgaven er kuboformalismen brukt til å beregne konduktivitetstensoren for en generell energibåndstruktur med to energibånd i kapittel 7, og for en generell Kramers degenerert energibåndstruktur med fire energibånd i kapittel 8. De resulterende formlene for konduktivitet benyttes henholdsvis til å beregne analytiske uttrykk for konduktivitetstensoren til en Rashba ferromagnet og til det antiferromagnetiske Dirac halvmetallet CuMnAs antatt lav uorden i krystallstrukturen ved det absolutte nullpunkt. Det endelige uttrykket for konduktivitetstensoren til den ortorombiske fasen til CuMnAs forutser en anormal Hall effekt som til forskjell fra tidligere betraktede topologiske materialer ikke kan knyttes til en endelig Berry kurvatur, men som heller oppstår som følge av geometriske egenskaper ved anisotropien til materialets fermioverflate. Den symmetriske Hall effekten antas å være målbar gjennom magneto-optiske effekter i regimet til lineær responsteori, der perturbasjonen fra det ytre elektriske feltet ikke er sterk nok til å bryte symmetrien som beskytter de firfoldig degenererte diracpunktene. Denne symmetriske Hall effekten antas å være observerbar gjennom ulike magneto-optiske effekter, der ytterligere utforskning kreves.

Abstract

In Part I, a fundamental understanding of quantum mechanics is introduced in terms of the density operator, and the statistics of an ideal quantum gas derived based on the maximum entropy principle in chapter 1. Introducing interactions between the particles the demanding mathematics provokes the realization of the Matsubara method of chapter 2, where time is treated as an imaginary variable and the calculations of observables are framed in terms of Matsubara Green functions. Finally, in chapter 3 the equilibrium ensemble is introduced to an external perturbation, and the observables of the perturbed ensemble calculated in the Kubo formalism of linear response theory. The resulting Kubo formula for conductivity is framed in terms of the Matsubara current density autocorrelation function, whose calculation involves knowledge of the Hamiltonian kernel of the equilibrium ensemble.

In Part II, the tightbinding model is derived in chapter 4 to exemplify a calculation and analyzation of the Hamiltonian kernel and corresponding energy band structures of different crystalline materials, with the two dimensional material graphene as the prime example. The effective Hamiltonian kernel of graphene locally take shape of the relativistic Weyl Hamiltonian, and is connected to topological properties of the Hilbert space of Bloch functions derived in chapter 3, in which the berryological quantities of a general two-level quantum system are calculated. In chapter 4, the Hamiltonian kernels of Weyl and Dirac semimetals are introduced as linearizations around degenerate points in the energy band structures comprising two and four bands respectively, resulting in three dimensional generalized versions of the Hamiltonian kernel of graphene.

Finally, in Part III the Kubo formalism is used to calculate the conductivity tensor for a general two-band system in chapter 7 and for a general Kramers degenerate four-band system in chapter 8. The resulting conductivity formulae are then used respectively to rederive the conductivty tensor of a Rashba ferromagnet, and to predict the conductivity tensor of the antiferromagnetic Dirac semimetal CuMnAs assuming low disorder in the zero temperature limit. The resulting analytical expression of the conductivity tensor of the orthorhombic phase of CuMnAs predicts an anomalous Hall effect which unlike previously investigated topological materials cannot be attributed to the Berry curvature of the system, which is zero due to the imposed Kramers degeneracy, but instead originates in the anisotropy of the Fermi surface. The emergence of a Hall effect is assumed to be detectable through magneto-optical effects under the confinement of linear response theory, where the perturbation of the imposed electric current is assumed weak enough to not break the symmetry protection of the fourfold degenerate Dirac points. The symmetric anomalous Hall effect is assumed to be detectable through various magneto-optical effects, where more research is needed.

Introduction

In recent years there have been several theoretical discoveries and experimental verifications of novel states of solid matter involving physical phases protected by topology rather than symmetry. Of particular interest are the *topological semimetals*, for which band crossings in the energy band structure are protected by topological invariants of the continuously connected Hilbert spaces of Bloch state vectors. The number of classes of topological semimetals has recently been expanded to include various types of band crossings [1, 2] protected by different topology and symmetry constraints. The simplest of the topological semimetals are the *Dirac and Weyl semimetals*, which contain low-energy excitations described by the same mathematical principles as theoretical Weyl and Dirac fermions of relativistic quantum theory [3, 4]. Due to the particular energy band structure of topological semimetals, these materials display exotic electronic properties not found in other solid state systems [5, 6].

The main mathematical tool for theoretically investigating the electrical transport properties in solid state systems is a calculation of the conductivity tensor [7, 8], for which many optical properties can be probed experimentally [9, 10]. Continuing on the recent progress in the field of topological semimetals, the main objective of the master thesis is to calculate the conductivity tensor for an effective model for a general Dirac semimetal. The resulting conductivity formulae will then be used to predict the conductivity tensor of the orthorhombic phase of the antiferromagnetic Dirac semimetal CuMnAs [11].

In order to solidify the theoretical background of the conductivity calculations, the thesis takes the form of a literature study split into three main parts further divided into chapters. The first part considers the fields of quantum statistics and linear response theory from which the Kubo formula for conductivity arises, while the second part investigates energy band structures under the tightbinding approach and the theory of berryological quantities from which the emergence of topological semimetals is explained. The two parts are independent and internally comprehensive, with common themes among chapters presented in the appendices. The culmination of these investigations is the particular calculations of conductivity formulae for topological materials, presented in the third and final part of the thesis. It should be noted that many of the themes involved are included to obtain a more complete picture of the physical theories, and will not necessarily contribute directly to the final calculations.

Finally, the finalized master thesis would not have been possible without the continued support and comments from my amiable supervisor, Alireza Qaiumzadeh. I am grateful for our weekly conversations throughout the past year, and I will greatly miss our partnership.

Contents

Part I

Quantum Statistics and The Kubo Formalism

Chapter 1

Introduction to Quantum Statistical Mechanics

The intention of the following introductory chapter to the first part of the thesis is to establish the nomenclature and envisage the fundamentals of the quantum theory of statistical mechanics. Besides introducing a basic understanding of quantum mechanics in terms of Hilbert spaces and the density operator, a main objective is to derive the statistics of the principal statistical ensembles in a quantum mechanical setting based on the principle of maximum entropy.

Of particular importance is also the introduction of the Fock space and the accompanying creation and annihilation operators, used in order to establish the statistics of the grand canonical ensemble. The following introduction of the thermal average is imperative for the Matsubara method of chapter 2 and the Kubo formalism of chapter 3. The creation and annihilation operators also provides the second quantization of quantum mechanical operators, which allows for the definition of Green functions in chapter 2 and used for the derivation of the tightbinding Hamiltonian in chapter 4 of Part II.

Accompanying the chapter is appendix A, in which important results from standard quantum mechanics such as the Schrödinger equation is derived. Furthermore, the fundamentals of quantum mechanics lays the rigorous foundation of the position representation, discussed in appendix B, from which the Bloch theorem is inferred. The chapter is inspired by the lecture notes from Linder [12] and Andersen [13], and the Feynman Lectures on Physics [14].

1.1 Hilbert Spaces of Quantum States

In order derive the statistical properties of quantum systems, the basic mathematical concepts surrounding quantum states should be introduced. The main results of the section is the introduction of creation and annihilation operators of the Fock space and the representation of operators in second quantization.

1.1.1 Quantum States and the Ensemble Average

In quantum mechanics, the state of a system is described by a state vector $|\psi\rangle$ being an element of a complete inner product space $\mathscr{H}$ known as a *Hilbert space*. Consider then any bounded linear map $\phi : \mathscr{H} \to \mathbb{C}$ from the Hilbert space $\mathscr{H}$ to the field of complex numbers. The space of all such maps, or *functionals*, is known as the *dual space* of the Hilbert space $\mathscr{H}$. By Riesz representation theorem [15], the Hilbert space and its dual are isometrically anti-isomorphic, in that each functional ϕ of dual space corresponds to an inner product with the *dual vector* $\langle\phi|$ by acting on state vectors as $\phi : |\psi\rangle \to \langle\phi|\psi\rangle$. For convenience, the dual vector $\langle\psi|$ corresponding to the state vector $|\psi\rangle$ is chosen such that their inner product is normalized to unity, that is $\langle\psi|\psi\rangle = 1$.

Let $|i\rangle$ be an orthonormal complete basis set of states spanning the entire Hilbert space $\mathscr{H}$, such that any general quantum state described by $|\psi\rangle$ can be written as a series expansion $|\psi\rangle = \sum_i c_i |i\rangle$. Using the orthonormality of the basis states $\langle i|j\rangle = \delta_{ij}$, the expansion coefficients are readily expressed as $c_i = \langle i|\psi\rangle$, and so $|\psi\rangle = \sum_i |i\rangle \langle i|\psi\rangle$. In consequence, any orthonormal complete set of states must satisfy the *completeness relation*

$$\sum_i |i\rangle \langle i| = \hat{I}. \tag{1.1}$$

Using the completeness relation, the dual state vector can likewise be expressed $\langle\psi| = \sum_i \langle\psi|i\rangle \langle i|$, and so by the anti-linearity of the Hilbert space inner product, its expansion coefficients are given by $\langle\psi|i\rangle = c_i^*$. From the definition of the dual vector, this restricts the expansion coefficients to satisfy $\sum_i |c_i|^2 = 1$.

In this framework, physically measurable observables O correspond to hermitian operators $\hat{O}$ on the Hilbert space $\mathscr{H}$. Consider then the eigenvalue equation of such an operator, written $\hat{O}|n\rangle = O_n |n\rangle$ with O_n being the eigenvalue corresponding to the eigenstate $|n\rangle$. The eigenvalues correspond to all possible numerical values upon measuring the observable O. If for the state $|\psi\rangle$ the observable is measured to $O = O_n$, the state vector $|\psi\rangle$ is said to *collapse* to the eigenstate $|n\rangle$; a measurement on the state $|\psi\rangle$ alters the state, retaining only the eigenstate corresponding to the single eigenvalue measured.

Because the operator $\hat{O}$ is hermitian with the adjoint operator (C4) satisfying $\hat{O}^\dagger = \hat{O}$, the eigenstates can be chosen mutually orthogonal spanning the entire Hilbert space $\mathscr{H}$. In consequence the eigenstates of hermitian operators satisfy the completeness relation (1.1), such that any inner product

$$\langle \hat{O} \rangle_\psi = \langle \psi | \, \hat{O} \, | \psi \rangle = \sum_n |\langle n | \psi \rangle|^2 O_n, \tag{1.2}$$

where the final equality comes from the orthogonality of the eigenstates $|n\rangle$. According to the *Born rule*, the absolute square of the expansion coefficients $|\langle n|\psi\rangle|^2$ gives the probability of measuring the eigenvalue O_n in the state $|n\rangle$. The expression $\langle \hat{O} \rangle_\psi$ is then physically interpreted as the average value of the observable O corresponding to the operator $\hat{O}$ in the state $|\psi\rangle$.

Notice from its expression (1.2) that finding the average value of an observable requires a multiple of measurements. However, because a single measurement will collapse the state vector, it is not possible to measure the average value of an observable through measuring a single system. Experimentally, measuring the average value of an observable thus relies on the ability to prepare a multiple of systems in the same state $|\psi\rangle$. Theoretically, such a multitude of systems described by the same quantum state $|\psi\rangle$ is known as a *quantum ensemble*. As such, the state vector $|\psi\rangle$ really represents an entire ensemble of systems, with each member of the ensemble being described by the same state. The average is therefore known as the *ensemble average* of the observable in question.

1.1.2 Product States and the Fock Space

Until now, it has been assumed that the quantum states under consideration are elements from the same Hilbert space $\mathscr{H}$. Consider instead several Hilbert spaces $\mathscr{H}_i$, with corresponding *single-states* denoted by $|\psi_i\rangle$. In order to describe quantum systems of several parts the notion of a *product space* is introduced, being a tensor product between Hilbert spaces on the form $\mathscr{H}_1 \otimes \mathscr{H}_2 \otimes \cdots \otimes \mathscr{H}_N$. A state vector from the product space will then be a linear combination of *product states*, which takes the general form $|\psi_1\rangle \otimes |\psi_2\rangle \otimes \cdots \otimes |\psi_N\rangle \equiv |\psi_1 \psi_2 \cdots \psi_N\rangle$.

In particular, if all the single-states $|\psi_i\rangle$ are elements of the same Hilbert space $\mathscr{H}$, the product space is denoted by $\mathscr{H}^N \equiv \bigotimes_{i=1}^N \mathscr{H}$. The states comprising the product state are then indistinguishable, in the sense that they are all governed by the same observables. The square of any product state must then be invariant under an interchange of two state vectors, and performing the interchange twice should bring back the original product state. These criteria are satisfied by *symmetrized* and *antisymmetrized* product states,

$$|\psi^N\} = \frac{1}{\sqrt{N!}} \sum_p \zeta^P \, |\psi_{p_1} \psi_{p_2} \cdots \psi_{p_N}\rangle \equiv |\psi_1 \psi_2 \cdots \psi_N\} \tag{1.3}$$

being elements of the symmetrized and antisymmetrized product spaces $\mathscr{H}_\zeta^N$ respectively, both being subspaces of the full product space, with the sign factor $\zeta = \pm 1$ corresponding to symmetrization and antisymmetrization. In the expression, the label p runs through all permutations of N objects and the factor ζ^P corresponds to the parity of the number of interchanges in the permutation.

The sign factor ζ depends on the nature of the original single-state vectors $|\psi_i\rangle$. For $\zeta = \pm 1$, the single-states comprising the product state are said to be

bosonic and *fermionic*, respectively. For the fermionic case $\zeta = -1$ in particular, the antisymmetrized state (1.3) leaves zero if two of the single-states $|\psi_i\rangle$ are equal, as each term of the sum then will be added to its negative counterpart. This characteristic of fermionic states is known as the *Pauli principle*.

Let the set $|\alpha\rangle$ be a complete orthonormal set of single-state vectors spanning the original Hilbert space $\mathscr{H}$, with W being the dimensionality of the space. An orthonormal basis of the product space $\mathscr{H}_\zeta^N$ can then be introduced as

$$|\{n_\alpha\}\rangle = |n_1 \cdots n_\alpha \cdots n_W\rangle = \frac{|\{1\} \cdots \{\alpha\} \cdots \{W\}\}}{\sqrt{n_1! \cdots n_W!}} \tag{1.4}$$

where the *occupation numbers* n_α denotes the number of times the state $|\alpha\rangle$ is represented in the product state $|\{n_\alpha\}\rangle$. From their construction the occupation numbers satisfies the constraint $\sum_\alpha n_\alpha = N$, where N is referred to as the *total occupation number* of the states. For bosons, the occupation numbers can take on any non-negative integer value up to N, whereas for fermions the only allowed values are $n_\alpha = 0$ and $n_\alpha = 1$ being a consequence of the Pauli principle.

The symmetrized or antisymmetrized Hilbert product spaces $\mathscr{H}_\zeta^N$ are thus characterized by the total occupation number N, giving the number of single-states comprising each product state, and the sign factor $\zeta = \pm 1$, determining the bosonic or fermionic nature of the single-states. Introduce then the symmetrized or antisymmetrized *Fock spaces*, in which the quantum states can take on any total occupation number. In terms of the symmetrized or antisymmetrized Hilbert spaces $\mathscr{H}_\zeta^N$, the Fock space is defined as the direct sum

$$\mathscr{F}_\zeta(\mathscr{H}) = \bigoplus_{N=0}^{\infty} \mathscr{H}_\zeta^N. \tag{1.5}$$

Here, the Hilbert space for $N = 0$ corresponds to the complex numbers spanned by the single vacuum state $|0\rangle$. The state vectors of Fock space are then given by $|\psi\rangle = \bigoplus_{N=0}^{\infty} c_N |\psi^N\}$, where c_N are complex expansion coefficients.

The Fock space $\mathscr{F}_\zeta(\mathscr{H})$ makes it possible to coherently define operators acting between product spaces of different total occupation number N. In particular, the *creation and annihilation operators* $\hat{b}_\alpha^\dagger$ and $\hat{b}_\alpha$ corresponding to the single-state $|\alpha\rangle$ act on the occupation number states (1.4) as

$$\begin{aligned} \hat{b}_\alpha^\dagger \, |n_1 \cdots n_\alpha \cdots n_W\rangle &= \zeta^{\sum_{\delta<\alpha} n_\delta} \sqrt{n_\alpha + 1} \, |n_1 \cdots (n_\alpha + 1) \cdots n_W\rangle \\ \hat{b}_\alpha \, |n_1 \cdots n_\alpha \cdots n_W\rangle &= \zeta^{\sum_{\delta<\alpha} n_\delta} \sqrt{n_\alpha} \, |n_1 \cdots (n_\alpha - 1) \cdots n_W\rangle \end{aligned} \tag{1.6}$$

where the annihilation operator satisfies $\hat{b}_\alpha |0\rangle = 0$. The prefactor $\zeta^{\sum_{\delta<\alpha} n_\delta}$ is known as the *Jordan-Wigner string*. In the bosonic case the Jordan-Wigner string is unity and does not depend on the ordering of the occupation numbers. In the fermionic case however, the Jordan-Wigner string will depend on the predetermined ordering of the occupation numbers; if there is an odd number of occupied fermionic states before the state α, an additional negative sign appears. Recall also that in the fermionic case the occupation numbers can only be zero

or unity. Therefore, if $n_\alpha = 1$ in the fermionic case, acting on the state with the creation operator $\hat{b}^\dagger_\alpha$ will leave zero.

The combined action of several creation and annihilation operators (1.6) can be simplified using commutation and anticommutation relations. Using the definition of the occupation number basis states (1.4), the creation and annihilation operators satisfies the three relations

$$\begin{aligned} [\hat{b}_\alpha, \hat{b}^\dagger_\beta]_\zeta \equiv \hat{b}_\alpha \hat{b}^\dagger_\beta - \zeta \hat{b}^\dagger_\beta \hat{b}_\alpha = \delta_{\alpha\beta} \\ [\hat{b}_\alpha, \hat{b}_\beta]_\zeta = [\hat{b}^\dagger_\alpha, \hat{b}^\dagger_\beta]_\zeta = 0 \end{aligned} \tag{1.7}$$

Here, the notation $[\cdot,\cdot]_\zeta$ represents the commutator for $\zeta = 1$ and the anticommutator for $\zeta = -1$. The bosonic or fermionic nature of a system can thus be modelled by enforcing commutation relations for the bosonic operators or anticommutation relations for the fermionic operators describing the system.

Introduce then the *occupation number operators* $\hat{n}_\alpha = \hat{b}^\dagger_\alpha \hat{b}_\alpha$. By the definition of the creation and annihilation operators (1.6), the occupation number operators acts on the occupation number states (1.4) as

$$\hat{n}_\alpha \left| n_1 \cdots n_\alpha \cdots n_W \right\rangle = n_\alpha \left| n_1 \cdots n_\alpha \cdots n_W \right\rangle . \tag{1.8}$$

The occupation number states are thus eigenstates to the occupation number operators $\hat{n}_\alpha$, with the occupation numbers n_α being the corresponding eigenvalues. Defining the *number operator* $\hat{N} = \bigoplus_{\alpha=1}^{W} \hat{n}_\alpha$, the total occupation number of a product state can then be revealed by the eigenvalue equation $\hat{N} \left| [n_\alpha] \right\rangle = N \left| [n_\alpha] \right\rangle$, with the total occupation number defined by $N = \sum_\alpha n_\alpha$.

1.1.3 Second Quantization

Let $\hat{o}$ be any operator acting on the Hilbert space $\mathscr{H}$, and let the operator $\hat{o}_i$ act on a general product state of $\mathscr{H}^N$ as $\hat{o}_i \left| \psi_1 \cdots \psi_N \right\rangle = \left| \psi_1 \right\rangle \otimes \cdots \otimes \hat{o} \left| \psi_i \right\rangle \otimes \cdots \otimes \left| \psi_N \right\rangle$. A corresponding operator $\hat{O}$ acting on the symmetrized or antisymmetrized basis states (1.4) can then be defined by $\hat{O} = \bigoplus_{i=1}^{N} \hat{o}_i$. Such an operator is known as a *single-state operator*, acting on the single-states of the system separately.

In particular, if the operator is on the form $\hat{o} = \left| \alpha \right\rangle \left\langle \beta \right|$, the corresponding single-state operator acting on Fock space becomes $\hat{O} = \hat{b}^\dagger_\alpha \hat{b}_\beta$. Using the completeness relation (1.1) of the orthonormal set $\left| \alpha \right\rangle$, any operator on the Hilbert space $\mathscr{H}$ can in general be written as $\hat{o} = \sum_{\alpha\beta} o_{\alpha\beta} \left| \alpha \right\rangle \left\langle \beta \right|$, where the matrix elements $o_{\alpha\beta} = \left\langle \alpha \right| \hat{o} \left| \beta \right\rangle$. In consequence, any single-state operator $\hat{O}$ acting on Fock space corresponding to the operator $\hat{o}$ can in general be written

$$\hat{O} = \sum_{\alpha\beta} o_{\alpha\beta} \hat{b}^\dagger_\alpha \hat{b}_\beta \tag{1.9}$$

This is the *second quantized form* of the single-state operator $\hat{O}$. In particular, if the states $\left| \alpha \right\rangle$ are taken to be the eigenstates of the operator $\hat{o}$, then $o_{\alpha\beta} = o_\alpha \delta_{\alpha\beta}$, and the sum reduces to a single sum over the single-states $\left| \alpha \right\rangle$.

1.2 Mixed Quantum States

The main purpose of this section is to introduce the concepts of mixed quantum states, which enables incorporation of classical uncertainty in quantum systems. Together with the concept of the Fock space of section 1.1, the resulting density operator formalism forms the basis of quantum statistical mechanics. In particular, the introduction of the Von Neumann entropy allows for a quantum mechanical calculation of the density operators of the principal ensembles known from classical statistical mechanics, being the theme of section 1.3.

1.2.1 Pure State Projection Operators

Quantum states fully described by state vectors $|\psi\rangle$ are known as *pure states*. According to the Born rule, measurements on such quantum systems are inherently probabilistic, as the state vector can only provide the probability that a specific measurement will occur. In consequence, even though the state vector describes all knowable properties of a system, measurements on the system are not fully deterministic. This property is known as *quantum uncertainty*.

The quantum system described by the state vector $|\psi\rangle$ may instead be described by the corresponding *projection operator*, defined by $\hat{P}_\psi \equiv |\psi\rangle\langle\psi|$ and acting on state vectors $|\phi\rangle$ as $\hat{P}_\psi|\phi\rangle = \langle\psi|\phi\rangle|\psi\rangle$; the projection operator $\hat{P}_\psi$ projects out the component of $|\phi\rangle$ parallel to the state $|\psi\rangle$. In consequence the projection operator is idempotent, with $\hat{P}_\psi^2 = \hat{P}_\psi$, from which it follows that its only eigenvalues are zero and unity. The zero eigenvalue corresponds to any state vector orthogonal to $|\psi\rangle$, whereas unity corresponds to the vector $|\psi\rangle$ itself.

Consider then a finite dimensional Hilbert space and introduce the *trace* over an operator with respect to some complete basis set $|i\rangle$, given by

$$\mathrm{Tr}\{\hat{O}\} = \sum_i \langle i|\hat{O}|i\rangle . \tag{1.10}$$

The trace is evidently a linear operation, and using the completeness relation (1.1) its value is independent on the basis used. Choosing the operator eigenstates as the basis set, the trace over a hermitian operator will be the sum of its eigenvalues. Furthermore, inserting the completeness relation twice, the trace also inherits the cyclic property $\mathrm{Tr}\{ABC\} = \mathrm{Tr}\{CAB\} = \mathrm{Tr}\{BCA\}$.

Reverting to the expression for the average (1.2) of the observable O, the probability of measuring the eigenvalue O_n can be expressed in terms of the projection operator as $|\langle n|\psi\rangle|^2 = \langle n|\hat{P}_\psi|n\rangle$. In consequence, the trace of the projection operator is unity, $\mathrm{Tr}\,\hat{P}_\psi = 1$, reflecting that the trace of an operator equals the sum of its eigenvalues. With this, ensemble averages can be expressed

$$\langle\hat{O}\rangle_\psi = \mathrm{Tr}\{|\psi\rangle\langle\psi|\hat{O}\} = \mathrm{Tr}\{\hat{P}_\psi\hat{O}\}. \tag{1.11}$$

Because only the expectation value is physically observable, any property of the quantum state described by the state vector $|\psi\rangle$ can then equally be written in terms of the corresponding projection operator $\hat{P}_\psi$.

1.2.2 The Density Operator

In reality, the state vector describing a quantum system may not be fully known, due to a classical lack of knowledge of the system. Systems involving both classical and quantum uncertainty can be described by a classical statistical distribution over quantum state vectors, where a statistical weight w_p is associated with the system being in the pure state described by $|\psi_p\rangle$. The total system is then said to be in a *mixed quantum state*. Using the ensemble average of pure quantum states (1.11), averages in mixed quantum states can be expressed

$$\langle \hat{O} \rangle = \sum_p w_p \langle \psi_p | \hat{O} | \psi_p \rangle = \sum_p w_p \, \mathrm{Tr}\Big\{ |\psi_p\rangle \langle \psi_p | \hat{O} \Big\} \equiv \mathrm{Tr}\{\hat{\rho}\hat{O}\}, \tag{1.12}$$

where the linearity of the trace was used. The expression defines the *density operator*, being the weighted sum of the pure state projection operators:

$$\hat{\rho} = \sum_p w_p |\psi_p\rangle \langle \psi_p| \,. \tag{1.13}$$

Effectively, the density operator takes over the role as a projection operator for mixed quantum states; any property of a mixed quantum state is described by the corresponding density operator. From the unit trace of projection operators,

$$\mathrm{Tr}\{\hat{\rho}\} = \sum_p w_p = 1, \tag{1.14}$$

where the mixing weights are all positive and sum to unity by their definition.

The pure states $|\psi_p\rangle$ comprising the density operator (1.13) are in general not orthogonal. Due to the hermiticity of the projection operators however, the density operator is itself hermitian, meaning its eigenvectors can be chosen to comprise a complete orthonormal set. Denoting the eigenvalue equation of the density operator by $\hat{\rho} |\rho_n\rangle = \rho_n |\rho_n\rangle$, the density operator can thus be written on a form known as its *eigenvalue decomposition*

$$\hat{\rho} = \sum_{n=1}^{W} |\rho_n\rangle \, \rho_n \, \langle \rho_n| \,. \tag{1.15}$$

The number W is the number of eigenstates of the density operator, and equals the dimensionality of the Hilbert space spanned by the original pure states $|\psi_p\rangle$ of the definition of the density operator (1.13). Notice that W does not in general correspond to the number of original pure states $|\psi_p\rangle$.

Recall that projection operators are idempotent, in that the square of the operator equals the operator itself. For the square of the density operator however, by using the eigenvalue decomposition (1.15) and recalling the orthonormal eigenstates, the trace over the square of the density operator

$$\mathrm{Tr}\big\{\hat{\rho}^2\big\} = \sum_{n=1}^{W} \rho_n^2 \leq \Big(\sum_{n=1}^{W} \rho_n \Big)^2 = \mathrm{Tr}\{\hat{\rho}\}^2. \tag{1.16}$$

Due to the unit trace of the density operator (1.14), then $\mathrm{Tr}\{\hat{\rho}^2\} \leq 1$. Equality occurs if all the eigenvalues are zero except one. Hence, if the trace of the square of the density operator is unity, the eigenvalue decomposition consists of only one term, and the state described is a pure state with the density operator being the corresponding projection operator. The square of the density operator thus separates mathematically whether the state described is a pure or a mixed state.

In order to calculate traces in practice, the density operator is expanded in a complete basis $|i\rangle$, giving the *density matrix* elements $\rho_{ij} = \langle i|\,\hat{\rho}\,|j\rangle$. Likewise, the operator $\hat{O}$ has the corresponding matrix elements $O_{ij} = \langle i|\,\hat{O}\,|j\rangle$. Using the completeness relation (1.1), the ensemble average (1.12) is then written

$$\langle \hat{O} \rangle = \sum_i \sum_j \rho_{ij} O_{ji} = \mathrm{tr}\{\rho O\},$$

Hence, ensemble averages can be calculated as the trace of the product between the density and operator matrices, independent on their representation.

Assume now the operator $\hat{O}$ commutes with the density operator $\hat{\rho}$. The eigenfunctions of the density operator $|\rho_n\rangle$ can then be chosen to be simultaneous eigenfunctions with the operator $\hat{O}$, satisfying $\hat{O}\,|\rho_n\rangle = O_n\,|\rho_n\rangle$. Choosing then these states as the basis states for the operator and density matrices, then $O_{nm} = O_n \delta_{nm}$ and $\rho_{nm} = \rho_n \delta_{nm}$, and the ensemble average becomes

$$\langle \hat{O} \rangle = \mathrm{Tr}\{\rho O\} = \sum_n \rho_n O_n \tag{1.17}$$

In this case then, the eigenvalues ρ_n of the density matrix corresponds to the probability of measuring the eigenvalue $O = O_n$ of the operator $\hat{O}$.

Even if the statistical weights w_p of the density operator are fixed in time, the corresponding pure quantum states $|\psi_p\rangle$ will in general be time dependent. In appendix A, it is found that the time evolution of pure states is governed by the Schrödinger equation (A2), with the generator of time translations being the Hamiltonian operator $\hat{H}$. By performing the time derivation of its definition, the time evolution of the density operator (1.13) then becomes governed by the *Von Neumann equation*, being the density operator equation of state given by

$$\frac{\partial \hat{\rho}}{\partial t} = -\frac{i}{\hbar}[\hat{H}, \hat{\rho}]. \tag{1.18}$$

This is the quantum analogue to the Liouville equation from classical statistical mechanics. The Von Neumann equation describes the time evolution of mixed quantum states, being the mixed state equivalent to the Schrödinger equation. In the Heisenberg picture, the corresponding density operator $\hat{\rho}_H$ is by the Heisenberg equation of motion (A7) then seen to be time independent. This effect originates in the time independence of the pure quantum states in the Heisenberg picture, which by definition translates to the density operator (1.13).

1.2.3 Variability and Von Neumann Entropy

From the eigenvalue decomposition of the density operator (1.15), it is possible to derive an unambiguous measure of the *mixedness* of a mixed state, describing how distant the mixed state is to being a pure state. In the following, the mixedness will be characterized by the *variability* of the set of eigenvalues ρ_n of the density operator, viewing these as describing a statistical distribution of the density operator eigenstates. For a general distribution, the variability quantifies the degree of diversity among the distributed elements. The derivation of the measure of variability, and indeed the following connection between variability and entropy, is inspired by Carcassi, Aidala and Barbour [16].

If the eigenvalues of the density operator are more similar, and hence further from unity, the diversity of the mixed state will increase. The variability should be maximum if all the eigenvalues are equal, describing a uniform distribution over the eigenstates. In that case, the density operator is said to describe a *completely mixed state*. Denoting by $S[\hat{\rho}]$ the variability of the eigenstate distribution of a general density operator, and by $S[W]$ the variability of a uniform distribution of W eigenstates, the variability should satisfy:

A *Continuity*: The variability of the mixed state $S = S[\hat{\rho}]$ should depend only on the eigenvalues ρ_n, and the dependence is continuous; an infinitesimal change in the eigenvalues leads to an infinitesimal change in the variability.

B *Monotonicity for uniform distributions*: For a fixed dimensionality W of the eigenspace, the variability $S[\hat{\rho}]$ of the mixed state is maximal if the distribution of the eigenstates is uniform with equal eigenvalues $\rho_n = 1/W$. The variability of completely mixed states $S[W]$ should be monotonically increasing with the number of eigenvalues W.

C *Linearity under subset merging*: If a subset of the eigenstates are merged to a single pure state, the total variability of the set should decrease with the variability of the subset weighted by the summed subset eigenvalues. In this context, merging a subset signifies comparing the system with a similar system where the subset is exchanged for a single state.

These three properties uniquely characterises the measure of variability $S[\hat{\rho}]$.

Consider a completely mixed state whose eigenspace has dimensionality W, and merge a subset of W_1 eigenstates. According to properties B and C, the variability will decrease by $S[W_1] \cdot W_1/W$. Hence, dividing all eigenstates into $W_2 = W/W_1$ subsets of equal cardinality W_1, the variability will decrease by $S[W_1]$. The resulting variability will then be $S[W_2]$, as each subset has merged into a single eigenstate with eigenvalue $1/W_2$. This leaves the constraint

$$S[W] = S[W_1] + S[W_2] \qquad \text{for} \qquad W = W_1 W_2,$$

giving the general expression $S[W] = k \ln W$. Here, due to the monotonicity of the variability as proposed by property B, the constant k must be positive. The constant thus changes the base of the logarithm, and can be arbitrarily chosen.

To arrive at an expression of the variability of an arbitrary distribution, consider again a uniform distribution $S[W]$ and distribute the equiprobal eigenstates into a number of subsets, with subset n containing W_n states. Merging each subset, the eigenvalue of each resulting eigenstate becomes $\rho_n = W_n/W$, and the variability decreases by a value $S[W_n] \cdot W_n/W$. Inserting the formula $S[W] = k \ln W$, the variability of the resulting mixed state

$$S[\hat{\rho}] = k \ln W - \sum_n \frac{W_n}{W} k \ln W_n = k \sum_n \frac{W_n}{W} \ln\left(\frac{W}{W_n}\right),$$

where it was used that the sum $\sum_n W_n = W$. Notice here that the eigenvalues $\rho_n = W_n/W$ are rational. However, this argument can be made for arbitrary numbers W and W_n, and because the variability is assumed continuous due to property A, the expression is extrapolated to all real numbers.

Hence, the only measure of the variability of mixed states which is continuous, monotonic and linear under subset merging is the *Shannon entropy* [16]

$$S[\hat{\rho}] = -k \sum_{n=1}^{W} \rho_n \ln \rho_n. \tag{1.19}$$

For a pure state there is only one eigenvalue of the density operator equal to unity, leaving a Shannon entropy of zero. If more eigenstates are included, the unit is distributed across more eigenvalues, and the Shannon entropy increases. In this way, the Shannon entropy gives a measure of the mixedness of a state.

The Shannon Entropy is known from information theory, where it serves as a measure of the average level of information obtained when measuring an outcome of a distribution. In that case, the constant k is chosen such that the logarithm becomes $\log_2$, suitable when information content is given in bits.

The form of the expression for Shannon entropy (1.19) is equivalent to the Gibbs entropy of classical statistical mechanics, where the constant $k = k_B$ is the Boltzmann constant, giving the entropy the dimensions of energy per temperature. Notice also that inserting $\rho_n = 1/W$ for a completely mixed state, the expression $S[W] = k_B \ln W$ is regained. This is the Boltzmann entropy of classical statistical mechanics, where W is interpreted as the number of microstates corresponding to a given macrostate. As such, the Boltzmann entropy is a measure of the variability of microstates within a given macrostate.

Both the Shannon entropy and the Gibbs entropy are classical expressions, describing phenomena regarding classical statistical distributions. A mixed quantum state however also incorporates quantum uncertainty. The quantum nature is made explicit by writing the expression for Shannon entropy (1.19) as

$$S[\hat{\rho}] = -k_B \operatorname{Tr}\{\hat{\rho} \ln \hat{\rho}\}. \tag{1.20}$$

This measure is known as the *Von Neumann entropy* of the mixed quantum state, being the quantum ensemble average of the operator $\ln \hat{\rho}$. The trace can be calculated as the sum over the eigenvalues of the operator $\hat{\rho} \ln \hat{\rho}$, which become $\rho_n \ln \rho_n$, giving back the original expression for Shannon entropy (1.19).

1.3 Statistics of the Principal Ensembles

A mixed quantum state is said to be in *equilibrium* if its density operator (1.13) is time independent. From the Von Neumann equation (1.18) the density operator then commutes with the Hamiltonian, satisfying $[\hat{\rho}, \hat{H}] = 0$. In general, density operators for systems in equilibrium thus acquires a dependence $\hat{\rho} = \hat{\rho}(\hat{H})$.

Because the density operator and the system Hamiltonian commutes, the eigenstates of the density operator $|\rho_n\rangle$ can for a system in equilibrium be chosen so as to satisfy the eigenvalue equation of the Hamiltonian, defined through the relations $\hat{H}\,|\rho_n\rangle = E_n\,|\rho_n\rangle$ and $\hat{\rho}\,|\rho_n\rangle = \rho_n\,|\rho_n\rangle$. The eigenvalue decomposition of the density operator (1.15) with diagonal density matrix elements $\rho_{nm} = \rho_n\delta_{nm}$ then defines the *energy representation* of the density operator. Notice that the eigenspace dimensionality W of the density operator now corresponds also to the number of energy eigenvalues E_n, including degeneracies.

According to the *principle of maximum entropy* a mixed state will in equilibrium, if left unmeasured, gain a statistical distribution such that the Von Neumann entropy (1.20) is maximized. The exact form of the diagonal matrix elements ρ_n will otherwise depend on the characteristics of the ensemble under consideration. In the following of this section, the shape of the density operator $\hat{\rho}$ is derived for the three principal statistical ensembles known from thermodynamics: the *microcanonical*, the *canonical* and the *grand canonical* ensembles. For simplicity, the Von Neumann entropy will be considered dimensionless.

1.3.1 The Microcanonical and Canonical Ensembles

A microcanonical ensemble is a fully isolated ensemble, in that it cannot interact with its surroundings. Hence, the total energy of the ensemble is restricted to take only one eigenvalue of the Hamiltonian operator, denoted by E. Notice however that this eigenvalue can be multiply degenerate, and the dimensionality W of the eigenspace now corresponds to the energy degeneracy. The only constraint on the density matrix in this case is the condition of unit trace (1.14). By the principle of maximum entropy, the density matrix for the microcanonical ensemble will then be the matrix maximizing the Von Neumann entropy (1.20) under the condition of unit trace (1.14). From section 1.2, it is already known that the entropy then becomes maximized by a uniform distribution.

However, the density matrix can also be derived from the Von Neumann entropy itself, using Lagrange multipliers. In order to find an expression for the density matrix in this case, introduce the Lagrange functional

$$\mathcal{L}[\rho, \alpha] = -\sum_n \rho_n \ln \rho_n - \alpha(\sum_n \rho_n - 1),$$

where α is a Lagrange multiplier. The density matrix of the microcanonical ensemble will correspond to an extremal point of this Lagrangian functional. Derivation with respect to the diagonal element ρ_m gives $\ln \rho_m = -1 - \alpha$, such that the diagonal elements take the form $\rho_n = e^{-(1+\alpha)}$, independent on the

index n. The condition of unit trace (1.14) now gives $e^{-(1+\alpha)}W = 1$, leaving the diagonal matrix elements of the density operator in the microcanonical ensemble

$$\rho_n = \frac{1}{W}. \tag{1.21}$$

As foretold, a mixed state of the microcanonical ensemble is a uniform distribution over the W degenerate eigenfunctions of the Hamiltonian. In general, the energy E and its degeneracy W will depend on the system and its Hamiltonian. The density operator of the microcanonical ensemble thus becomes

$$\hat{\rho}_{mic} = \frac{1}{W}\sum_{n=1}^{W} |\rho_n\rangle \langle\rho_n| = \frac{1}{W}\hat{I}_W, \tag{1.22}$$

where $\hat{I}_W$ is the identity operator on the eigenspace of the density operator, following from the completeness relation (1.1) of the eigenstates. Thus in general, the density operator of a completely mixed state takes the shape of an identity operator, weighted by the inverse of the dimensionality of its eigenspace.

Reinserting the matrix elements into the Von Neumann entropy (1.20) again gives the celebrated formula for the Boltzmann entropy

$$S = \ln W \tag{1.23}$$

If the energy characterizing the ensemble is non-degenerate, the dimensionality of the eigenspace is $W = 1$ and the density matrix describes a pure state. In that case, the Von Neumann entropy of the system is zero.

Assume now the system is able to exchange energy with its surroundings, but is otherwise isolated. The ensembles of such systems are known as *canonical ensembles*. In this case, the system can take on any energy eigenvalue of the Hamiltonian operator. Measuring the energy of members of the ensemble will then yield some energy eigenvalue E_n, and the average energy of the ensemble is calculated as the ensemble average over the Hamiltonian, denoted $\langle\hat{H}\rangle \equiv U$.

The density matrix is then found by extremizing the Von Neumann entropy (1.20) under the condition of unit trace (1.14) and satisfying $\mathrm{Tr}\{\hat{\rho}\hat{H}\} = U$. The corresponding Lagrangian functional then takes the form

$$\mathcal{L}[\rho, \alpha, \beta] = -\sum_n \rho_n \ln \rho_n - \alpha(\sum_n \rho_n - 1) - \beta(\sum_n \rho_n E_n - U)$$

where α and β are Lagrange multipliers. Derivation with respect to ρ_m now leaves the equation $\ln \rho_m = -\beta E_m - \alpha - 1$. Combined with the condition of unit trace (1.14), the factor $Z_C \equiv e^{-(\alpha+1)}$ takes the form

$$Z_C = \sum_n e^{-\beta E_n} = \mathrm{Tr}\Big\{e^{-\beta\hat{H}}\Big\} \tag{1.24}$$

This is known as the *partition function* of the canonical ensemble. Written in terms of the canonical partition function, the eigenstates of the density operator becomes distributed according to the *Maxwell-Boltzmann distribution*

$$\rho_n = \frac{1}{Z_C} e^{-\beta E_n}$$

Recalling that E_n are the eigenvalues of the Hamiltonian $\hat{H}$, the density operator for the canonical ensemble is rewritten on the basis independent form

$$\hat{\rho}_C = \frac{1}{Z_C} e^{-\beta \hat{H}} \tag{1.25}$$

By arguments from statistical thermodynamics, the Lagrange multiplier β can be related to the *temperature* T of the ensemble as $\beta = 1/k_B T$, where k_B again is the Boltzmann constant, converting between temperature and energy.

The density operator of the canonical ensemble (1.25) can then be reinserted into the expression for Von Neumann entropy (1.20) to give the relation

$$S[\hat{\rho}_C] = \beta \operatorname{Tr}\{\hat{\rho}_C \hat{H}\} + \operatorname{Tr}\{\hat{\rho}_C \ln Z_C\} = \beta U - \beta F, \tag{1.26}$$

where the *free energy* is defined $F = -\ln Z_C/\beta$. Hence, the *internal energy* of the system can be expressed $U = F + TS$, as known from thermodynamics.

1.3.2 The Grand Canonical Ensemble

The statistics of the grand canonical ensemble are derived explicitly in Fock space (1.5), as described by section 1.1. Let now the orthonormal set $|\alpha\rangle$ spanning the Hilbert space $\mathscr{H}$ be the eigenstates of a Hamiltonian operator $\hat{\mathfrak{h}}$ with corresponding eigenvalues ε_α. For simplicity, consider a system whose Hamiltonian $\hat{H}$ acting on Fock space is a single-state operator (1.9),

$$\hat{H} = \sum_\alpha \varepsilon_\alpha \hat{n}_\alpha \tag{1.27}$$

The Hamiltonian then commutes with the number operator $\hat{N}$, with the occupation number states (1.4) also being eigenfunctions of the Hamiltonian, with eigenvalues given by the sum $\sum_\alpha n_\alpha \varepsilon_\alpha \equiv E_{\{n_\alpha\}}$. Thus, the eigenvalues of the Hamiltonian $\hat{H}$ are the summed single-state energies of the eigenstate $|\{n_\alpha\}\rangle$. The density operator $\hat{\rho}$ of the grand canonical ensemble then commutes both with the Hamiltonian $\hat{H}$ and the number operator $\hat{N}$, such that the occupation number states also satisfies the eigenvalue equation $\hat{\rho}\,|\{n_\alpha\}\rangle = \rho_{\{n_\alpha\}}\,|\{n_\alpha\}\rangle$.

Systems of the grand canonical ensemble will then have an average energy U, and an average total occupation number $\langle N\rangle$. The density operator is again found by extremizing the Von Neumann entropy (1.20) under the condition of unit trace (1.14), average energy $\operatorname{Tr}\{\hat{\rho}\hat{H}\} = \langle E\rangle$ and average total occupation number $\operatorname{Tr}\{\hat{\rho}\hat{N}\} = \langle N\rangle$. The corresponding Lagrangian functional then becomes

$$\begin{aligned}\mathcal{L}[\rho,\alpha,\beta,\gamma] = &-\sum_{\{n_\alpha\}} \rho_{\{n_\alpha\}} \ln \rho_{\{n_\alpha\}} - \alpha\Big(\sum_{\{n_\alpha\}} \rho_{\{n_\alpha\}} - 1\Big) \\ &- \beta\Big(\sum_{\{n_\alpha\}} \rho_{\{n_\alpha\}} E_{\{n_\alpha\}} - \langle E\rangle\Big) - \gamma\Big(\sum_{\{n_\alpha\}} \rho_{\{n_\alpha\}} N - \langle N\rangle\Big)\end{aligned}$$

where α, β and γ are Lagrange multipliers. The extremum of the functional is found for $\ln \rho_{\{n_\alpha\}} = -\alpha - 1 - \beta E_{\{n_\alpha\}} - \gamma N$. Denoting $Z \equiv e^{-(1+\alpha)}$, and recasting the multiplier $\gamma \equiv \beta\mu$ corresponding to the average number of particles, the condition of unit trace (1.14) then gives the *grand canonical partition function*

$$Z = \sum_{\{n_\alpha\}} e^{-\beta(E_{\{n_\alpha\}} - \mu N)} = \mathrm{Tr}\Big\{ e^{-\beta(\hat{H} - \mu\hat{N})} \Big\}. \tag{1.28}$$

Here, the sum is over all configurations of occupation numbers n_α, for all total occupation numbers N given by $\sum_\alpha n_\alpha = N$. From statistical thermodynamics, the Lagrange multiplier μ is interpreted as a *chemical potential* of the grand canonical ensemble, whereas β again is interpreted as an inverse temperature. In terms of the grand canonical partition function (1.28), the matrix elements

$$\rho_{\{n_\alpha\}} = \frac{1}{Z} e^{-\beta(E_{\{n_\alpha\}} - \mu N)} = \frac{1}{Z} e^{-\beta \sum_\alpha n_\alpha(\varepsilon_\alpha - \mu)},$$

leaving the basis independent density operator of the grand canonical ensemble

$$\hat{\rho} = \frac{1}{Z} e^{-\beta(\hat{H} - \mu\hat{N})}. \tag{1.29}$$

Recall here that the Hamiltonian (1.27) and the number operator commutes.

For the grand canonical partition function (1.28), it is advantageous to split the original sum over occupation number configurations n_α into a sum over the total occupation number N and a sum over configurations satisfying the condition $\sum_\alpha n_\alpha = N$. Introducing the *fugacity* of the grand canonical ensemble $z = e^{\beta\mu}$, the grand canonical partition function can then be expressed

$$Z = \sum_{N=0}^{\infty} \sum_{|N|} z^N e^{-\beta E_{\{n_\alpha\}}} = \sum_{N=0}^{\infty} z^N Z_N, \tag{1.30}$$

where the notation $|N|$ signifies all configurations $\{n_\alpha\}$ with the same total occupation number N. The partition funciton Z_N corresponds to a canonical ensemble (1.24) described by the Hamiltonian $\hat{H}$ whose states reside in the symmetrized or antisymmetrized product space $\mathscr{H}_\zeta^N$, and can be expressed

$$Z_N = \mathrm{Tr}\{e^{-\beta\hat{H}}\} = \sum_{|N|} e^{-\beta \sum_\alpha n_\alpha \varepsilon_\alpha}, \tag{1.31}$$

where the energy eigenvalues $E_{\{n_\alpha\}} = \sum_\alpha n_\alpha \varepsilon_\alpha$ has been inserted.

Using the latter expression for the grand canonical partition function (1.30), the grand canonical ensemble average of an observable $\hat{O}$ can be written

$$\langle \hat{O} \rangle = \frac{1}{Z} \mathrm{Tr}\Big\{ \hat{O} e^{-\beta(\hat{H} - \mu\hat{N})} \Big\} = \frac{\sum_{N=0}^{\infty} z^N Z_N \langle \hat{O} \rangle_N}{\sum_{N=0}^{\infty} z^N Z_N}. \tag{1.32}$$

For the canonical and grand canonical ensembles, the ensemble average is known as the *thermal average* of the operator. Here, the canonical thermal average corresponding to the canonical partition function Z_N is denoted by $\langle \hat{O} \rangle_N$.

1.4 Ideal Quantum Gases

A *quantum gas* is a system of indistinguishable bosonic or fermionic quantum particles. For quantum gases in the grand canonical approach, the states $|\alpha\rangle$ of the previous section corresponds to single-particle fermionic or bosonic energy eigenstates, the occupation numbers n_α denotes how many particles occupy each single-particle state, and the total occupation number N gives the total number of particles in the system. In general however, the particles will interact among each other, adding other contributions to the Hamiltonian $\hat{H}$ than the sum of single-particle terms (1.27). Due to these interaction terms, the Hamiltonian describing a quantum gas will not in general commute with the number operator $\hat{N}$. In this section however, it will be assumed that the particles constitute a non-interacting *ideal quantum gas*, such that the system is readily described by the derived grand canonical density operator (1.29). The theory of interacting quantum gases will be partially covered in chapter 2.

Reverting to its derived expression, the grand canonical partition function (1.30) for an ideal quantum gas can be rewritten on the form

$$Z = \sum_{N=0}^{\infty} \sum_{|N|} \prod_{\alpha=1}^{W} \left(ze^{-\beta\varepsilon_\alpha}\right)^{n_\alpha} = \prod_{\alpha=1}^{W} \sum_{n_\alpha} \left(ze^{-\beta\varepsilon_\alpha}\right)^{n_\alpha}.$$

Here, the double sum has been combined to independent sums over all possible values of the occupation numbers n_α. Recall then that in the bosonic case, the occupation numbers can take on any non-negative integer, whereas for fermions the occupation numbers can only be zero or unity. The fermionic sum is then trivial, leaving $(1 + ze^{-\beta\varepsilon_\alpha})$ for each α in the product. For bosons, the sum takes the form of a geometrical series. Hence, using the sign factor $\zeta = \pm 1$ for distinguishing the fermionic and bosonic grand canonical partition functions,

$$Z_\zeta = \prod_{\alpha=1}^{W} \left[1 - \zeta ze^{-\beta\varepsilon_\alpha}\right]^{-\zeta}. \tag{1.33}$$

This is simply a reformulation of the general expression for the grand canonical partition function (1.28) for non-interacting systems.

From the original expression of the partition function (1.28), the thermal average of the occupation number n_α can be calculated as

$$n_\zeta(\varepsilon_\alpha) \equiv \langle n_\alpha \rangle = -\frac{\partial \ln Z_\zeta}{\partial(\beta\varepsilon_\alpha)} = \frac{1}{e^{\beta(\varepsilon_\alpha - \mu)} - \zeta}, \tag{1.34}$$

where the derivative is readily calculated for the grand partition function of an ideal quantum gas (1.33). This expression gives the mean of the statistical distribution over occupation numbers for ideal quantum gases. The bosonic case $\zeta = 1$ gives the *Bose-Einstein distribution*, and the fermionic case $\zeta = -1$ gives the *Fermi-Dirac distribution*. Notice the temperature dependence of this expression through the Lagrange multiplier $\beta = 1/k_B T$; at temperature T, the average number of particles with the single-particle energy ε_α is given by $n_\zeta(\varepsilon_\alpha)$.

Chapter 2

Green Functions of the Matsubara Method

Chapter 1 derived the statistics of ideal quantum gases in the grand canonical approach. In reality, each quantum particle of the ensemble will in general exert a mutually interactive force on the other particles, and the ideally non-interacting ensemble cannot reproduce the experimental results of many physical systems. Often however, the interactive part of the Hamiltonian describing the system will be dominated by the single-particle terms from the non-interactive case, and the calculation of the physical properties of the ensemble can be approximated using perturbation theory.

For interactive systems the computation of the thermal averages of observables becomes more involved, because the eigenstates and the corresponding eigenvalues of the interactive Hamiltonian in general are unknown. The computational difficulty is somewhat mitigated by introducing Green functions, with quantum states and operators represented in the Heisenberg picture. In this regard, the Matsubara method of treating time as an imaginary variable turns out mathematically convenient for the computation of Green functions at finite temperatures. Therefore, the chapter starts out introducing dynamical quantum pictures in imaginary time, before treating the quantum statistics of interactive ensembles. The corresponding real time dynamical pictures are introduced in appendix A, on which the first section of the current chapter is dependent. The chapter is based on the book by Mahan [8].

Green functions is an integral part of solid state physics, and a majority of formulae for physical properties can be reduced to the calculation of Green functions based on perturbation theory. A particular example is the calculation of optical conductivity, which is the objective of chapter 3.

2.1 The Matsubara Method

In appendix A, the time evolution of quantum mechanical states is modelled in different dynamical quantum pictures. The formalism introduced the evolution operator of quantum states (A4), taking the form of a unitary exponential operator with the exponent being imaginary and dependent on time t. Furthermore, in the calculation of thermal averages of chapter 1, the canonical (1.25) and grand canonical (1.29) density operators take the form of exponential operators with a real exponent dependent on the statistical parameter β.

To mathematically mitigate the inconvenience of having separately real and imaginary exponents, there are two conceivable formalisms: the statistical parameter $\beta = 1/k_B T$ can be considered an *imaginary time*, or the exponent $it/\hbar$ can be considered a *real temperature*. The latter formalism is known as the *Matsubara method*, where time t is considered an imaginary quantity, and time evolution is modelled using the then real time variable $\tau = it$.

The Matsubara method is mostly used for systems described by time independent Hamiltonians $\hat{H}$. In terms of the real time variable τ, the time evolution operator of the Schrödinger picture (A4) then takes on the form

$$\hat{U}(\tau, \tau') = e^{-\hat{H}(\tau - \tau')/\hbar}. \tag{2.1}$$

Introducing imaginary time thus makes the time evolution operator non-unitary.

Introduce then the *imaginary time Heisenberg picture*, in which operators are connected to time-independent operators of the Schrödinger picture through

$$\hat{O}(\tau) = e^{\hat{H}\tau/\hbar}\hat{O}e^{-\hat{H}\tau/\hbar} \qquad \hat{O}^\dagger(\tau) = e^{\hat{H}\tau/\hbar}\hat{O}^\dagger e^{-\hat{H}\tau/\hbar}, \tag{2.2}$$

analogous to operators in the real time Heisenberg picture (A6). In the imaginary time Heisenberg picture however, because the evolution operator (2.1) is non-unitary, the adjoint operator $[\hat{O}(\tau)]^\dagger \neq \hat{O}^\dagger(\tau)$. Thus, the two operators $\hat{O}(\tau)$ and $\hat{O}^\dagger(\tau)$ are not adjoint operators and need separate definitions.

In the following only systems at equilibrium will be considered, leaving all observables with no explicit time dependence; whether operators are given in the Schrödinger or imaginary time Heisenberg pictures is asserted by the time argument τ. Taking the derivative of the definition of the imaginary time Heisenberg operators (2.2), the *imaginary time Heisenberg equation* thus becomes

$$\frac{\mathrm{d}\hat{O}(\tau)}{\mathrm{d}\tau} = \frac{1}{\hbar}[\hat{H}, \hat{O}(\tau)], \tag{2.3}$$

being analogous to the real time Heisenberg equation (A7).

Likewise for a system whose Hamiltonian takes the form $\hat{H} = \hat{H}_0 + \hat{V}$, introduce the *imaginary time Dirac picture*, analogous to the real time Dirac picture described in appendix A. Operators in the imaginary time Dirac picture are denoted $\hat{O}_I(\tau)$, where the subscript I separates between the imaginary time Dirac and Heisenberg pictures. As for the definition of operators in the real time Dirac picture (A8), operators of the imaginary time Dirac picture are connected to their imaginary time Heisenberg and Schrödinger equivalents as

$$\hat{O}_I(\tau) = \hat{U}_I^{-1}(\tau, 0)\hat{O}(\tau)\hat{U}_I(\tau, 0) = e^{\tau\hat{H}_0/\hbar}\hat{O}e^{-\tau\hat{H}_0/\hbar}, \tag{2.4}$$

where the modified imaginary time evolution operator, analogous to its real time Dirac picture counterpart (A16), can be written as the Dyson series

$$\hat{U}_I(\tau, \tau') = e^{\hat{H}_0\tau/\hbar}e^{-\hat{H}(\tau-\tau')/\hbar}e^{-\hat{H}_0\tau'/\hbar} = \hat{\mathrm{T}}\{e^{-\frac{1}{\hbar}\int_{\tau'}^{\tau}\mathrm{d}\sigma\hat{V}_I(\sigma)}\}. \tag{2.5}$$

Here, the imaginary time ordering operator $\hat{\mathrm{T}}$ arranges imaginary time valued operators according to descending imaginary time arguments, being defined analogous to the real time ordering operator (A15).

Reconsider a canonical or grand canonical ensemble governed by the Hamiltonian $\hat{H}$, as described in section 1.4, and notice that setting $\tau = \hbar\beta$ and $\tau' = 0$ in the expression for the imaginary time evolution operator (2.1) leaves

$$\hat{\rho} \equiv \hat{U}(\hbar\beta, 0) = e^{-\beta\hat{H}}. \tag{2.6}$$

This is nothing but the unnormalized density operator of the canonical ensemble (1.25), demonstrating the mathematical convenience of modelling time as an imaginary variable. In terms of the unnormalized density operator, the canonical partition function (1.28) is defined $Z = \mathrm{Tr}\{\hat{\rho}\}$. Alternately, by implicitly exchanging the Hamiltonian $\hat{H}$ by $\hat{H} - \mu\hat{N}$ where $\hat{N}$ is the total occupation number operator, while also redefining the trace to additionally run over all configurations of occupation numbers, the density operator $\hat{\rho}$ and its corresponding partition function Z describes the statistics of a grand canonical ensemble.

In the derivation of the statistics of ideal quantum gases (1.33), the quantum particles of the ensemble were assumed non-interactive, described by a Hamiltonian of only single-particle terms (1.9). In order to incorporate interactions between the particles comprising the ensemble, introduce the interaction term $\hat{V}$ to the unperturbed single-particle Hamiltonian, now denoted $\hat{H}_0$. The statistics of the non-interactive ensemble described by $\hat{H}_0$ are then fully known, whereas the statistics of the interactive ensemble described by the total Hamiltonian $\hat{H} = \hat{H}_0 + \hat{V}$ can be calculated using perturbation theory.

In equilibrium, the interaction term and hence the total Hamiltonian of the ensemble $\hat{H} = \hat{H}_0 + \hat{V}$ will be time independent. Due to the shape of the Hamiltonian, calculations are conveniently performed in the imaginary time Dirac picture. In terms of the modified imaginary time evolution operator (2.5), the unnormalized density operator (2.6) of the interacting system can be expressed

$$\hat{\rho}_I \equiv \hat{U}_I(\hbar\beta, 0) = e^{\beta\hat{H}_0}e^{-\beta\hat{H}} = \hat{\mathrm{T}}\{e^{-\frac{1}{\hbar}\int_0^{\hbar\beta}\mathrm{d}\sigma\hat{V}_I(\sigma)}\}.$$

Reverting to the Schrödinger picture, the unnormalized density operator of the interactive grand canonical ensemble is then readily given by

$$\hat{\rho} = e^{-\beta\hat{H}} = e^{-\beta\hat{H}_0}\hat{\mathrm{T}}\{e^{-\frac{1}{\hbar}\int_0^{\hbar\beta}\mathrm{d}\sigma\hat{V}_I(\sigma)}\}. \tag{2.7}$$

Denoting the average over the non-interactive ensemble by $\langle\hat{O}\rangle_0 = \mathrm{Tr}\{\hat{\rho}_0\hat{O}\}/Z_0$, where the unnormalized non-interactive density operator and partition function

are denoted by $\hat{\rho}_0 = e^{-\beta \hat{H}_0}$ and $Z_0 = \mathrm{Tr}\{\hat{\rho}_0\}$ respectively, the corresponding interactive grand canonical partition function can be expressed as the average

$$Z = \mathrm{Tr}\{\hat{\rho}\} = Z_0 \Big\langle \hat{\mathrm{T}}\{e^{-\frac{1}{\hbar}\int_0^{\hbar\beta} \mathrm{d}\sigma \hat{V}_I(\sigma)}\} \Big\rangle_0. \tag{2.8}$$

Hence, the calculation of the partition function for the interactive system has been reduced to the calculation of a thermal average over the corresponding non-interactive system, where the statistics of the ensemble are known.

Consider then a time ordered product of operators $\hat{\mathrm{T}}\{\hat{O}_1(\tau_1)\cdots\hat{O}_n(\tau_n)\}$, where the operators are evaluated in the imaginary time Heisenberg picture (2.2). Assuming the Hamiltonian describing the time evolution of the operators is on the form $\hat{H} = \hat{H}_0 + \hat{V}$, the thermal average over the time ordered product can be calculated using the density operator (2.7) as

$$\big\langle \hat{\mathrm{T}}\{\hat{O}_1(\tau_1)\cdots\hat{O}_n(\tau_n)\}\big\rangle = \frac{\mathrm{Tr}\Big\{e^{-\beta\hat{H}_0}\hat{\mathrm{T}}\{e^{-\frac{1}{\hbar}\int_0^{\hbar\beta}\mathrm{d}\sigma\hat{V}_I(\sigma)}\hat{O}_1(\tau_1)\cdots\hat{O}_n(\tau_n)\}\Big\}}{\mathrm{Tr}\Big\{e^{-\beta\hat{H}_0}\hat{\mathrm{T}}\{e^{-\frac{1}{\hbar}\int_0^{\hbar\beta}\mathrm{d}\sigma\hat{V}_I(\sigma)}\}\Big\}}.$$

However, due to the form of the Hamiltonian, it would be beneficial to express the operators in the imaginary time Dirac picture where the time evolution of the operators $\hat{O}_{iI}(\tau)$ is governed by the Hamiltonian $\hat{H}_0$ whose properties are known. Using the connection between imaginary time Heisenberg and Dirac operators (2.4) in reverse, the operators $\hat{O}(\tau) = \hat{U}_I^{-1}(\tau,0)\hat{O}_I(\tau)\hat{U}_I(\tau,0)$ where $\hat{U}_I(\tau,\tau')$ is the imaginary time modified evolution operator (2.5). The thermal average over the time ordered product of operators in the Heisenberg picture can be written in terms of the corresponding operators in the Dirac picture, as

$$\big\langle \hat{\mathrm{T}}\{\hat{O}_1(\tau_1)\cdots\hat{O}_n(\tau_n)\}\big\rangle = \frac{\Big\langle \hat{\mathrm{T}}\{e^{-\frac{1}{\hbar}\int_0^{\hbar\beta}\mathrm{d}\sigma\hat{V}_I(\sigma)}\hat{O}_{1I}(\tau_1)\cdots\hat{O}_{nI}(\tau_n)\}\Big\rangle_0}{\Big\langle \hat{\mathrm{T}}e^{-\frac{1}{\hbar}\int_0^{\hbar\beta}\mathrm{d}\sigma\hat{V}_I(\sigma)}\Big\rangle_0}, \tag{2.9}$$

where all the evolution operators cancel under the time ordering due to their group properties. In this way, the thermal average over an interacting ensemble of a time ordered product of operators whose time evolution is non-trivial has been reduced to the calculation of a thermal average over the corresponding non-interactive ensemble where the time evolution of the operators is known. Expanding the exponential operators, the resulting averages can be arranged in *Feynman diagrams*, and calculated diagrammatically. The expression found is the basis of perturbation theory in many-body physics.

In the final calculations of the thesis the interactions between the quantum particles will be assumed negligible, such that the Hamiltonian operator assumes the form of a single-particle operator (1.9). Here and in the following, the discussions on the internal interactions of a system is included for completeness, and the theory surrounding Feynman diagrams will for brevity not be considered.

2.2 Introduction to Matsubara Green Functions

Through the process of second quantization (1.9), any quantum operator can be written as a product between creation and annihilation operators $\hat{b}^\dagger_\alpha$ and $\hat{b}_\alpha$. In particular, for the Matsubara method the creation and annihilation operators $\hat{b}^\dagger_\alpha(\tau)$ and $\hat{b}_\alpha(\tau)$ are considered in the imaginary time Heisenberg picture (2.2), motivating the definition of the $2n$-point *Matsubara Green function*

$$\mathcal{G}^{(n)}(\{\tau_i\alpha_i;\sigma_i\beta_i\}) = \frac{(-1)^n}{\hbar^n}\big\langle \hat{\mathrm{T}}\{\hat{b}_{\alpha_1}(\tau_1)\cdots\hat{b}_{\alpha_n}(\tau_n)\hat{b}^\dagger_{\beta_1}(\sigma_1)\cdots\hat{b}^\dagger_{\beta_n}(\sigma_n)\}\big\rangle \quad (2.10)$$

where $\hat{\mathrm{T}}$ is the imaginary time ordering operator (A15). In general, the average is taken with respect to the specific quantum ensemble at hand. The Matsubara method is however convenient mostly for systems at nonzero temperatures described by the density operator of the ensemble (2.6). Here, the indices β_i must not be confused with the statistical parameter $\beta = 1/k_BT$.

The purpose of the section at hand is to give a brief introduction to the general properties of the Matsubara Green functions (2.10) using the density operator (2.6) corresponding to a general Hamiltonian operator $\hat{H}$. At the end of the section the Matsubara Green functions are connected to their real time counterparts through analytical continuation. For simplicity, all properties are derived and written in terms of the two-point Matsubara Green function.

2.2.1 The Equation of Motion for Green Functions

Many of the general properties of the Matsubara Green functions (2.10) are most readily derived and exemplified using the *two-point Matsubara Green function*, being the lowest order Matsubara Green function written on the form

$$\begin{aligned}\mathcal{G}_{\alpha\beta}(\tau-\sigma) \equiv \mathcal{G}^{(1)}(\tau,\alpha;\sigma,\beta) &= -\frac{1}{\hbar}\big\langle \hat{\mathrm{T}}\{\hat{b}_\alpha(\tau)\hat{b}^\dagger_\beta(\sigma)\}\big\rangle \\ &= -\frac{1}{\hbar}\Theta(\tau-\sigma)\big\langle \hat{b}_\alpha(\tau)\hat{b}^\dagger_\beta(\sigma)\big\rangle - \zeta\frac{1}{\hbar}\Theta(\sigma-\tau)\big\langle \hat{b}^\dagger_\beta(\sigma)\hat{b}_\alpha(\tau)\big\rangle,\end{aligned} \quad (2.11)$$

where $\Theta(t)$ is the Heaviside function originating from time ordering and $\zeta = \pm 1$ corresponds to fermionic and bosonic operators, respectively. The ensemble is assumed at equilibrium, such that the Hamiltonian $\hat{H}$ becomes time independent. The two-point Matsubara Green function is then dependent only on time differences, as shown by the argument $(\tau - \sigma)$. Because the Green function is homogeneous in time, it is customary to set the second time argument $\sigma = 0$, leaving the Green function denoted $\mathcal{G}_{\alpha\beta}(\tau) \equiv -\big\langle \hat{\mathrm{T}}\{\hat{b}_\alpha(\tau)\hat{b}^\dagger_\beta(0)\}\big\rangle/\hbar$.

Consider the derivative of the two-point Green function (2.11), taken with respect to the parameter τ. Because the system is considered at equilibrium, the density operator is time independent and the derivative can be moved inside the average. From its definition, the derivative of the time ordered product

$$\frac{\partial}{\partial\tau}\hat{\mathrm{T}}\{\hat{b}_\alpha(\tau)\hat{b}^\dagger_\beta(0)\} = -\delta(\tau)\big[\hat{b}_\alpha(\tau)\hat{b}^\dagger_\beta(0) - \zeta\hat{b}^\dagger_\beta(0)\hat{b}_\alpha(\tau)\big] - \Theta(\tau)\frac{\partial\hat{b}_\alpha(\tau)}{\partial\tau}\hat{b}^\dagger_\beta(0) - \zeta\Theta(-\tau)\hat{b}^\dagger_\beta(0)\frac{\partial\hat{b}_\alpha(\tau)}{\partial\tau}.$$

The delta-function originates in the discontinuity present at $\tau = 0$ due to time ordering. Its presence enforces the real time parameter to take the value $\tau = 0$ in the first term, which leaves the commutator or anticommutator of the creation and annihilation operators (1.7). Using also the imaginary time Heisenberg equation (2.3) for the annihilation operator $\hat{b}_\alpha(\tau)$ in the second term, the equation of motion for the two-point Matsubara Green function becomes

$$\hbar\frac{\partial}{\partial\tau}\mathcal{G}_{\alpha\beta}(\tau) = -\delta(\tau)\delta_{\alpha\beta} - \frac{1}{\hbar}\big\langle\hat{\mathrm{T}}\{[\hat{H},\hat{b}_\alpha(\tau)]\hat{b}^\dagger_\beta(0)\}\big\rangle. \tag{2.12}$$

The appearance of the delta-function in the derivative leads to a discontinuity of the function at $\tau = 0$. From the derivation of the equation of motion the discontinuity is caused by the commutation or anticommutation relation of the creation and annihilation operators, and will hence be present in general.

2.2.2 Periodicity and Matsubara Frequencies

Due to the discontinuity as portrayed by the equation of motion (2.12), the two-point Matsubara Green function (2.11) is ill defined at the origin. The discontinuity is expressed clearly by writing the function as

$$\mathcal{G}_{\alpha\beta}(\tau) = \begin{cases} -\big\langle\hat{b}_\alpha(\tau)\hat{b}^\dagger_\beta(0)\big\rangle/\hbar & \text{if} \quad \tau > 0 \\ -\zeta\big\langle\hat{b}^\dagger_\beta(0)\hat{b}_\alpha(\tau)\big\rangle/\hbar & \text{if} \quad \tau < 0 \end{cases}, \tag{2.13}$$

where the Heaviside functions of the original expression has been inserted.

Consider the two-point Matsubara Green function (2.13) for the time interval $-\hbar\beta < \tau < 0$, being given by $\mathcal{G}_{\alpha\beta}(\tau) = -\zeta\langle\hat{b}^\dagger_\beta(0)\hat{b}_\alpha(\tau)\rangle/\hbar$. Here, the average is taken using the unnormalized density operator (2.6). Inserting the imaginary time Heisenberg representation of the operators (2.2), the trace

$$\begin{aligned}\mathrm{Tr}\{\hat{\rho}\hat{b}^\dagger_\beta(0)\hat{b}_\alpha(\tau)\} &= \mathrm{Tr}\{e^{-\beta\hat{H}}\hat{b}^\dagger_\beta e^{\hat{H}\tau/\hbar}\hat{b}_\alpha e^{-\hat{H}\tau/\hbar}\} = \mathrm{Tr}\{e^{\hat{H}\tau/\hbar}\hat{b}_\alpha e^{-\hat{H}\tau/\hbar}e^{-\beta\hat{H}}\hat{b}^\dagger_\beta\} \\ &= \mathrm{Tr}\{e^{-\beta\hat{H}}e^{\hat{H}(\tau+\hbar\beta)/\hbar}\hat{b}_\alpha e^{-\hat{H}(\tau+\hbar\beta)/\hbar}\hat{b}^\dagger_\beta\} = \mathrm{Tr}\{\hat{\rho}\hat{b}_\alpha(\tau+\hbar\beta)\hat{b}^\dagger_\beta(0)\},\end{aligned}$$

where the cyclic property of the trace was used. Notice here that the time argument $\tau + \hbar\beta > 0$. Thus, the two-point Matsubara Green function satisfies

$$\mathcal{G}_{\alpha\beta}(\tau+\hbar\beta) = \zeta\mathcal{G}_{\alpha\beta}(\tau) \tag{2.14}$$

for $-\hbar\beta < \tau < 0$, effectively giving a connection between the two parts of the two-point Matsubara Green function at each side of the discontinuity.

Recalling the statistical sign $\zeta = \pm 1$, the relation (2.14) between the two parts of the two-point Matsubara Green function (2.13) means the bosonic and the fermionic versions of the function is periodic and antiperiodic with the statistical parameter $\hbar\beta$, respectively. This suggests that the discontinuity at the origin is transferred periodically with $\hbar\beta$; indeed, the argument leading to the periodic relation can readily be made for the time interval $\tau \in (\hbar\beta, 2\hbar\beta)$ as well.

Furthermore, because $\zeta^2 = 1$, the two-point Matsubara Green function can be continued periodically as $\mathcal{G}_{\alpha\beta}(\tau + 2n\hbar\beta) = \mathcal{G}_{\alpha\beta}(\tau)$, for any integer n. Due to this periodicity, the Green function can be decomposed into a Fouriér series

$$\mathcal{G}_{\alpha\beta}(\tau) = \frac{1}{\beta} \sum_{n=-\infty}^{\infty} \tilde{\mathcal{G}}_{\alpha\beta}(n) e^{-\frac{in\pi}{\hbar\beta}\tau}.$$

In order for the Fouriér transform to be well defined the time argument is here conventionally restricted to the interval $\tau \in (-\hbar\beta, \hbar\beta)$, on which the two-point Matsubara Green function $\mathcal{G}_{\alpha\beta}(\tau)$ is completely defined. The Fouriér coefficients $\tilde{\mathcal{G}}_{\alpha\beta}(n)$ can then be calculated as the integral

$$\tilde{\mathcal{G}}_{\alpha\beta}(n) = \frac{1}{2}\Big(1 + \zeta e^{in\pi}\Big) \int_0^{\hbar\beta} \mathrm{d}\tau \mathcal{G}_{\alpha\beta}(\tau) e^{\frac{in\pi}{\hbar\beta}\tau}.$$

Here, the integration over the interval $\tau \in (-\hbar\beta, 0)$ has been converted to run over $\tau \in (0, \hbar\beta)$ using the periodic relation (2.14) of the function $\mathcal{G}_{\alpha\beta}(\tau)$.

Due to the prefactor before the integral, the two-point Matsubara Green function Fouriér coefficients $\tilde{\mathcal{G}}_{\alpha\beta}(n)$ vanishes whenever the integer n is even for $\zeta = -1$ and odd for $\zeta = 1$, motivating the definition of the *Matsubara frequencies*

$$\text{Bosonic}: \quad \omega_n = \frac{2n\pi}{\hbar\beta} \qquad\qquad \text{Fermionic}: \quad \nu_n = \frac{(2n+1)\pi}{\hbar\beta}. \tag{2.15}$$

In the following, a general Matsubara frequency will be denoted by μ_n, being either fermionic or bosonic depending on the Matsubara Green function at hand. Notice that the Matsubara frequencies μ_n can be both positive and negative, with n being any integer. The bosonic Matsubara frequencies also include zero, while all fermionic Matsubara frequencies are nonzero.

In terms of the Matsubara frequencies (2.15), the Fouriér transform of the Matsubara Green functions and its inverse can be written on the form

$$\mathcal{G}_{\alpha\beta}(\tau) = \frac{1}{\hbar\beta} \sum_{\mu_n} \tilde{\mathcal{G}}_{\alpha\beta}(i\mu_n) e^{-i\mu_n\tau} \qquad\qquad \tilde{\mathcal{G}}_{\alpha\beta}(i\mu_n) = \int_0^{\hbar\beta} \mathrm{d}\tau \mathcal{G}_{\alpha\beta}(\tau) e^{i\mu_n\tau}. \tag{2.16}$$

Here, when the temperature approaches zero with $\beta \to \infty$, the spacing between the discrete Matsubara frequencies (2.15) goes to zero and the sum over Matsubara frequencies turns into an integration over the frequency domain.

2.2.3 The Spectral Weight and Analytical Continuation

In viewing the Matsubara method of introducing imaginary time as a mathematical tool for simplifying calculations at nonzero temperatures, a scheme should be devised for translating the two-level Matsubara Green function (2.11) to a real time equivalent. In this regard, introduce the real time two-point *retarded* and *advanced Green functions*, respectively defined by

$$G^{r,a}_{\alpha\beta}(t,s) = \mp\frac{i}{\hbar}\Theta\big(\pm(t-s)\big)\big\langle[\hat{b}_\alpha(t),\hat{b}^\dagger_\beta(s)]_\zeta\big\rangle \equiv \mp i\Theta\big(\pm(t-s)\big)C_{\alpha\beta}(t,s), \quad (2.17)$$

where the upper and lower signs corresponds to the retarded and advanced Green functions $G^r_{\alpha\beta}(t)$ and $G^a_{\alpha\beta}(t)$, respectively. Due to the Heaviside functions, the retarded and advanced Green functions are zero for $t > s$ and $t < s$ respectively, reflecting their naming. The expression also defines the *spectral weight* $C_{\alpha\beta}(t,s) \equiv \big\langle \hat{b}_\alpha(t)\hat{b}^\dagger_\beta(s) - \zeta\hat{b}^\dagger_\beta(s)\hat{b}_\alpha(t)\big\rangle/\hbar$, averaging over the commutator or anticommutator with $\zeta = \pm 1$ being the statistical sign. The operators $\hat{b}^\dagger_\alpha(t)$ and $\hat{b}_\alpha(t)$ are evaluated in the real time Heisenberg picture (A6).

Analogous to the Matsubara Green functions, for systems in equilibrium the Green functions becomes homogeneous in time, with $G^{r,a}_{\alpha\beta}(t,s) = G^{r,a}_{\alpha\beta}(t-s)$. Due to the homogeneous time argument, it is convenient to introduce Fouriér transforms for the advanced and retarded two-point Green functions, given by

$$\tilde{G}^{r,a}_{\alpha\beta}(\omega) = \int_{-\infty}^{\infty} \mathrm{d}t\; G^{r,a}_{\alpha\beta}(t)e^{i\omega t} \qquad G^{r,a}_{\alpha\beta}(t) = \int_{-\infty}^{\infty}\frac{\mathrm{d}\omega}{2\pi}\;\tilde{G}^{r,a}_{\alpha\beta}(\omega)e^{-i\omega t}, \quad (2.18)$$

Inserting the expressions for the Green functions (2.17), the Fouriér transforms satisfies $\tilde{G}^r_{\alpha\beta}(\omega) = (\tilde{G}^a_{\alpha\beta}(\omega))^*$. Thus, a computation of the retarded Green function $\tilde{G}^r_{\alpha\beta}(\omega)$ will automatically yield the advanced Green function $\tilde{G}^a_{\alpha\beta}(\omega)$.

Seeing that the retarded and advanced Green functions (2.17) consist of a product of functions, their Fouriér transforms (2.18) can be calculated as a convolution on the frequency domain between the Fouriér transforms $\tilde{\Theta}(\omega)$ and $\tilde{C}_{\alpha\beta}(\omega)$. However, the Fouriér transform of the Heaviside function is not well defined: direct calculation leaves an oscillating term at the upper or lower infinite limit, respectively. The inconvenience can be mitigated by extending the frequency to the complex plane and adding a complex part $\pm i\eta$ with $\eta > 0$. The limit at infinity will then leave zero, and the Fouriér integral readily becomes

$$\mp\int_{-\infty}^{\infty}\mathrm{d}t\; e^{i(\omega\pm i\eta)t}i\Theta(\pm t) = -i\int_0^{\pm\infty}\mathrm{d}t\; e^{i(\omega\pm i\eta)t} = \frac{1}{\omega\pm i\eta}$$

The explicit expression for the convolution over the real frequency axis then gives a complex valued function, defining the *spectral representation*

$$\tilde{G}_{\alpha\beta}(z) = \int_{-\infty}^{\infty}\frac{\mathrm{d}\omega_1}{2\pi}\frac{\tilde{C}_{\alpha\beta}(\omega_1)}{z-\omega_1} \quad (2.19)$$

with the retarded and advanced Green functions given by the limits

$$\tilde{G}^{r,a}_{\alpha\beta}(\omega) = \lim_{\eta\to 0} \tilde{G}_{\alpha\beta}(\omega \pm i\eta) \tag{2.20}$$

From the expression for the convolution (2.19), the Fouriér transform of the retarded Green function is seen to be analytic in the upper half of the complex plane with poles infinitesimally below the real axis. For times $t < 0$, the inverse Fouriér transform (2.18) can then be calculated as a contour integral around the upper half of the complex plane, leaving zero due to the analyticity, effectively giving rise to the Heaviside function of the original definition (2.17).

Extending both the time t and the parameter of the Matsubara method τ to the complex plane, the complex time parameters become related by the relations $\operatorname{Re} t = \operatorname{Im}\tau$ and $\operatorname{Im} t = -\operatorname{Re}\tau$. Reconsider then the Fouriér coefficients $\tilde{G}_{\alpha\beta}(i\mu_n)$ of the two-point Matsubara Green function (2.16) and assume the Matsubara frequency (2.15) is positive, denoted $\mu_n > 0$. In that case, due to the exponential in the Fouriér transform, the value of the integrand approaches zero as the imaginary part $\operatorname{Im}\tau = \operatorname{Re} t$ approaches infinity. Hence, the integral

$$\begin{aligned}\tilde{\mathcal{G}}_{\alpha\beta}(i\mu_n) &= \int_0^{\hbar\beta} \mathrm{d}\tau \mathcal{G}_{\alpha\beta}(\tau) e^{i\mu_n\tau} = -\frac{1}{\hbar}\int_0^{\hbar\beta} \mathrm{d}\tau \big\langle \hat{b}_\alpha(\tau)\hat{b}^\dagger_\beta(0)\big\rangle e^{i\mu_n\tau} \\ &= -\frac{i}{\hbar}\int_0^{\infty} \mathrm{d}t \big\langle \hat{b}_\alpha(t)\hat{b}^\dagger_\beta(0)\big\rangle e^{i\mu_n(it)} + \frac{i}{\hbar}\int_0^{\infty} \mathrm{d}t \big\langle \hat{b}_\alpha(t-i\hbar\beta)\hat{b}^\dagger_\beta(0)\big\rangle e^{i\mu_n(it+\hbar\beta)}\end{aligned}$$

In the last integral, the exponential factor $e^{i\hbar\beta\mu_n} = \zeta$. Furthermore, using the cyclic property of the trace, the final average can readily be verified to equal $\big\langle \hat{b}^\dagger_\beta(0)\hat{b}_\alpha(t)\big\rangle$. Inserting these results, the integral is seen to equal

$$\int_0^{\hbar\beta} \big\langle \hat{b}_\alpha(\tau)\hat{b}^\dagger_\beta(0)\big\rangle e^{i\mu_n\tau} = i\int_{-\infty}^{\infty} \mathrm{d}t \big\langle [\hat{b}_\alpha(t), \hat{b}^\dagger_\beta(0)]_\zeta \big\rangle \Theta(t) e^{i(i\mu_n)t}$$

where also a Heaviside function was inserted to obtain the negative infinity limit. Hence, the two-point Matsubara Green function allows a spectral representation

$$\tilde{\mathcal{G}}_{\alpha\beta}(i\mu_n) = \int_{-\infty}^{\infty} \frac{\mathrm{d}\omega_1}{2\pi} \frac{\tilde{C}_{\alpha\beta}(\omega_1)}{i\mu_n - \omega_1} = \tilde{G}_{\alpha\beta}(i\mu_n). \tag{2.21}$$

The derivation relies on a positive Matsubara frequency $\mu_n > 0$, such that $i\mu_n$ lies in the upper half of the complex plane.

Recalling that the retarded Green function (2.17) is analytical in this region, it is possible to connect the retarded Green function with the two-point Matsubara Green function through the analytical continuation

$$\tilde{G}^{r}_{\alpha\beta}(\omega) = \lim_{i\mu_n\to\omega+i\eta} \tilde{\mathcal{G}}_{\alpha\beta}(i\mu_n). \tag{2.22}$$

Hence, the retarded Green function can be calculated as an analytical continuation of the Matsubara Green function. Likewise, for $\mu_n < 0$ the analytical continuation $i\mu_n \to \omega - i\eta$ yields the advanced Green function.

2.3 Non-Interactive Matsubara Green Functions

In the grand canonical approach to ideal quantum gases of section 1.3, a gas of mutually non-interacting quantum particles was described by a Hamiltonian $\hat{\mathfrak{h}}$ whose eigenstates were assumed to be known with corresponding eigenvalues denoted by ε_α. Letting then the states $|\alpha\rangle$ denote the eigenstates of the Hamiltonian, the matrix elements takes the form $\mathcal{H}_{\alpha\beta} = \varepsilon_\alpha \delta_{\alpha\beta}$. For simplicity, the energy contribution from the chemical potential μ can also be inserted as part of the Hamiltonian, and the non-interactive ensemble becomes described by

$$\hat{H}_0 = \sum_\alpha (\varepsilon_\alpha - \mu) \hat{b}_\alpha^\dagger \hat{b}_\alpha \equiv \sum_\alpha \xi_\alpha \hat{n}_\alpha, \tag{2.23}$$

where the matrix element $\xi_\alpha \equiv \varepsilon_\alpha - \mu$. The operator $\hat{n}_\alpha = \hat{b}_\alpha^\dagger \hat{b}_\alpha$ is a number operator counting the number of particles occupying the single-particle eigenstate $|\alpha\rangle$. The operator $\hat{N} = \sum_\alpha \hat{n}_\alpha$ counts the total number of particles of the ensemble, with the chemical potential μ fixing the average number of particles at equilibrium. In this notation, the unnormalized grand canonical density operator (2.6) can be written on the form $\hat{\rho}_0 = e^{-\beta \hat{H}_0}$.

In the following, the Matsubara Green functions (2.10) are calculated for the non-interactive Hamiltonian (2.23) in particular, and then for single-particle Hamiltonians (2.40) in general. The two cases are separated by marking the different non-interactive quantities or averages with a zero label, as for $\hat{H}_0$.

2.3.1 Wick Decomposition

From the shape of the non-interactive Hamiltonian (2.23), the general commutation or anticommutation relations of the creation and annihilation operators (1.7) gives directly the commutators with the Hamiltonian as

$$\hat{H}_0 \hat{b}_\alpha^\dagger = \xi_\alpha \hat{b}_\alpha^\dagger + \hat{b}_\alpha^\dagger \hat{H}_0 \qquad\qquad \hat{H}_0 \hat{b}_\alpha = -\xi_\alpha \hat{b}_\alpha + \hat{b}_\alpha \hat{H}_0. \tag{2.24}$$

Inserted into the operator definition of the imaginary time Heisenberg picture (2.2), these commutation relations in turn gives the direct time dependence

$$\hat{b}_\alpha^\dagger(\tau) = e^{\xi_\alpha \tau/\hbar} \hat{b}_\alpha^\dagger \qquad\qquad \hat{b}_\alpha(\tau) = e^{-\xi_\alpha \tau/\hbar} \hat{b}_\alpha. \tag{2.25}$$

Notice that the time evolution is identical for fermionic and bosonic operators, which is a consequence of the single-particle form of the Hamiltonian (2.23).

For the non-interactive system, averages are calculated using the density operator $\hat{\rho}_0$. The commutation relations between the non-interactive Hamiltonian and the creation and annihilation operators (2.24) then gives the relations

$$\hat{b}_\alpha^\dagger \hat{\rho}_0 = e^{\beta \xi_\alpha} \hat{\rho}_0 \hat{b}_\alpha^\dagger \qquad\qquad \hat{b}_\alpha \hat{\rho}_0 = e^{-\beta \xi_\alpha} \hat{\rho}_0 \hat{b}_\alpha \tag{2.26}$$

Denote by operators $\hat{\mathfrak{b}}_{\alpha_i}$ either a creation operator $\hat{b}_\alpha^\dagger$ or an annihilation operator $\hat{b}_\alpha$ and by s_i a sign factor where $s_i = +1$ corresponds to $\hat{\mathfrak{b}}_{\alpha_i}$ being a creation

operator and $s_i = -1$ corresponds to $\hat{\mathfrak{b}}_{\alpha_i}$ being an annihilation operator. The relation found can then be written as $\hat{\mathfrak{b}}_{\alpha_i}\hat{\rho}_0 = e^{s_i\beta\xi_{\alpha_i}}\hat{\rho}_0\hat{\mathfrak{b}}_{\alpha_i}$.

Consider a product of two such operators, written $\hat{\mathfrak{b}}_{\alpha_1}\hat{\mathfrak{b}}_{\alpha_2}$. Inserting the commutator for bosonic and anticommutator for fermionic operators, the trace

$$\mathrm{Tr}\{\hat{\rho}_0\hat{\mathfrak{b}}_{\alpha_1}\hat{\mathfrak{b}}_{\alpha_2}\} = [\hat{\mathfrak{b}}_{\alpha_1}, \hat{\mathfrak{b}}_{\alpha_2}]_\zeta \,\mathrm{Tr}\{\hat{\rho}_0\} + \zeta e^{s_1\beta\xi_{\alpha_1}} \,\mathrm{Tr}\{\hat{\rho}_0\hat{\mathfrak{b}}_{\alpha_1}\hat{\mathfrak{b}}_{\alpha_2}\}.$$

To obtain the final term, the cyclic property of the trace together with the relation with the density operator (2.26) was used. Furthermore, the commutation relations of the creation and annihilation operators (1.7) gives that the commutator or anticommutator is proportional to the unit operator, and so can be written symbolically outside of the trace. Rearranging the terms, and dividing by the trace over the density operator, the equation is rewritten as

$$\left\langle \hat{\mathfrak{b}}_{\alpha_1}\hat{\mathfrak{b}}_{\alpha_2}\right\rangle_0 = \frac{[\hat{\mathfrak{b}}_{\alpha_1}, \hat{\mathfrak{b}}_{\alpha_2}]_\zeta}{1 - \zeta e^{s_1\beta\xi_{\alpha_1}}} = \frac{[\hat{\mathfrak{b}}_{\alpha_2}, \hat{\mathfrak{b}}_{\alpha_1}]_\zeta}{e^{s_1\beta\xi_{\alpha_1}} - \zeta} \tag{2.27}$$

where the last equality is found by multiplying in the factor $-\zeta$. From the commutation relations of the creation and annihilation operators (1.7), the only unique non-zero average is found by choosing $\hat{\mathfrak{b}}_{\alpha_1} = \hat{b}^\dagger_\alpha$ and $\hat{\mathfrak{b}}_{\alpha_2} = \hat{b}_\beta$, leaving

$$\left\langle \hat{b}^\dagger_\alpha \hat{b}_\beta\right\rangle_0 = \frac{\delta_{\alpha\beta}}{e^{\beta\xi_\alpha} - \zeta} = n_\zeta(\xi_\alpha)\delta_{\alpha\beta} \tag{2.28}$$

The distribution function $n_\zeta(\xi_\alpha)$ gives the Bose-Einstein distribution for $\zeta = 1$ and the Fermi-Dirac distribution for $\zeta = -1$, corresponding to bosonic and fermionic statistics respectively. The result is equivalent to the calculation of section 1.4, where the distribution function (1.34) was found as a derivative of the grand canonical partition function of the ideal quantum gas.

Consider then a string of operators on the general form $\hat{\mathfrak{b}}_{\alpha_1}\cdots\hat{\mathfrak{b}}_{\alpha_m}$. Commuting or anticommuting the first operator $\hat{\mathfrak{b}}_{\alpha_1}$ with the second operator $\hat{\mathfrak{b}}_{\alpha_2}$ here leaves a string of the remaining operators with the commutator and a string of all operators but where the operators $\hat{\mathfrak{b}}_{\alpha_1}$ and $\hat{\mathfrak{b}}_{\alpha_2}$ are interchanged. In this second string, the operator $\hat{\mathfrak{b}}_{\alpha_1}$ can similarly be commuted with the third operator $\hat{\mathfrak{b}}_{\alpha_3}$, and continuing the process finally leaves the equality

$$\begin{aligned}\hat{\mathfrak{b}}_{\alpha_1}\cdots\hat{\mathfrak{b}}_{\alpha_m} = {}& [\hat{\mathfrak{b}}_{\alpha_1}, \hat{\mathfrak{b}}_{\alpha_2}]\hat{\mathfrak{b}}_{\alpha_3}\hat{\mathfrak{b}}_{\alpha_4}\cdots\hat{\mathfrak{b}}_{\alpha_m} + \zeta[\hat{\mathfrak{b}}_{\alpha_1}, \hat{\mathfrak{b}}_{\alpha_3}]\hat{\mathfrak{b}}_{\alpha_2}\hat{\mathfrak{b}}_{\alpha_4}\cdots\hat{\mathfrak{b}}_{\alpha_m} + \cdots \\ & + \zeta^{m-2}[\hat{\mathfrak{b}}_{\alpha_1}, \hat{\mathfrak{b}}_{\alpha_m}]\hat{\mathfrak{b}}_{\alpha_2}\cdots\hat{\mathfrak{b}}_{\alpha_{(m-1)}} + \zeta^{m-1}\hat{\mathfrak{b}}_{\alpha_2}\cdots\hat{\mathfrak{b}}_{\alpha_m}\hat{\mathfrak{b}}_{\alpha_1}\end{aligned}$$

Recall that the commutators are proportional to the unit operator, and so can be placed outside of the string of operators. Multiply now by the density operator $\hat{\rho}_0$ and take the trace on both sides of the equality. Using the cyclic property of the trace and the relation with the density operator (2.26), the original string of operators is recovered. Rearranging terms, the equality is rewritten as

$$\begin{aligned}\mathrm{Tr}\{\hat{\rho}_0\hat{\mathfrak{b}}_{\alpha_1}\cdots\hat{\mathfrak{b}}_{\alpha_m}\} &= \frac{[\hat{\mathfrak{b}}_{\alpha_1},\hat{\mathfrak{b}}_{\alpha_2}]_\zeta}{1-\zeta^{m-1}e^{s_1\beta\xi_\alpha}}\,\mathrm{Tr}\{\hat{\rho}_0\hat{\mathfrak{b}}_{\alpha_3}\hat{\mathfrak{b}}_{\alpha_4}\cdots\hat{\mathfrak{b}}_{\alpha_m}\}\\ &+\zeta\frac{[\hat{\mathfrak{b}}_{\alpha_1},\hat{\mathfrak{b}}_{\alpha_3}]_\zeta}{1-\zeta^{m-1}e^{s_1\beta\xi_\alpha}}\,\mathrm{Tr}\{\hat{\rho}_0\hat{\mathfrak{b}}_{\alpha_2}\hat{\mathfrak{b}}_{\alpha_4}\cdots\hat{\mathfrak{b}}_{\alpha_m}\}+\cdots\\ &+\zeta^{m-2}\frac{[\hat{\mathfrak{b}}_{\alpha_1},\hat{\mathfrak{b}}_{\alpha_m}]_\zeta}{1-\zeta^{m-1}e^{s_1\beta\xi_\alpha}}\,\mathrm{Tr}\{\hat{\rho}_0\hat{\mathfrak{b}}_{\alpha_2}\hat{\mathfrak{b}}_{\alpha_3}\cdots\hat{\mathfrak{b}}_{\alpha_{(m-1)}}\}\end{aligned}$$

Dividing here by the trace over the density operator gives the non-interactive thermal averages over the strings of operators, and the equality is rewritten

$$\big\langle\hat{\mathfrak{b}}_{\alpha_1}\cdots\hat{\mathfrak{b}}_{\alpha_m}\big\rangle_0=\sum_{i=2}^{m}\frac{\zeta^{i-2}[\hat{\mathfrak{b}}_{\alpha_1},\hat{\mathfrak{b}}_{\alpha_i}]_\zeta}{1-\zeta^{m-1}e^{s_1\beta\xi_\alpha}}\big\langle\hat{\mathfrak{b}}_{\alpha_2}\cdots\hat{\mathfrak{b}}_{\alpha_{(i-1)}}\hat{\mathfrak{b}}_{\alpha_{(i+1)}}\cdots\hat{\mathfrak{b}}_{\alpha_m}\big\rangle_0 \qquad (2.29)$$

Notice that the factor ζ^{i-2} gives the parity of the number of anticommutations in the fermionic case where $\zeta=-1$, while being unity in the bosonic case.

The obtained formula (2.29) can be reiterated for all strings of operators in the sum. If m is an odd number the average over a single creation or annihilation operator will then remain for each term. Due to the relation with the density operator (2.26), using the cyclic property of the trace, the thermal averages

$$\mathrm{Tr}\{\hat{\rho}_0\hat{b}_\alpha^\dagger\}=\mathrm{Tr}\{\hat{\rho}_0\hat{b}_\alpha\}=0. \qquad (2.30)$$

In consequence, the thermal average over a string of operators (2.29) is nonzero only if the number of operators is an even number. For $m=2n$, the prefactor to each trace on the right hand side equals the average over the two operators within the commutator (2.28). Reiteration of the formula then leaves

$$\big\langle\hat{\mathfrak{b}}_{\alpha_1}\cdots\hat{\mathfrak{b}}_{\alpha_{2n}}\big\rangle_0=\sum_p\zeta^P\big\langle\hat{\mathfrak{b}}_{\alpha_{p_1}}\hat{\mathfrak{b}}_{\alpha_{p_2}}\big\rangle_0\cdots\big\langle\hat{\mathfrak{b}}_{\alpha_{p_{2n-1}}}\hat{\mathfrak{b}}_{\alpha_{p_{2n}}}\big\rangle_0. \qquad (2.31)$$

Here the label p runs over all permutations of the operators, with ζ^P being the parity of the permutation in the fermionic case and unity in the bosonic case. The resulting calculation procedure is known as *Wick decomposition*, and holds whenever the Hamiltonian takes the form of a single-particle operator (2.40).

Recall then the formula for the thermal average over the string of two operators (2.27), which can be nonzero only for the product of one creation and one annihilation operator. If then the numbers of creation and annihilation operators in the string $\hat{\mathfrak{b}}_{\alpha_1}\cdots\hat{\mathfrak{b}}_{\alpha_{2n}}$ are different, all terms in the sum of permutations constituting their average (2.31) will then contain at least one average over two operators which leaves zero. Hence, only strings of an equal number n of creation and annihilation operators can leave a nonzero average.

Reconsider the definition of the $2n$-point Matsubara Green functions (2.10). Due to the explicit time dependence of the creation and annihilation operators in the non-interactive case (2.25), the calculation of the thermal average over the

time-ordered product (A15) reduces to calculating the average over all permutations of products between the creation and annihilation operators. Because time ordering is a linear operation for operator strings of equal length, the Wick decomposition (2.31) then transfers to the Matsubara Green functions, leaving

$$\begin{aligned}\mathcal{G}^{0(n)}(\{\tau_i\alpha_i;\sigma_i\beta_i\}) &= \frac{(-1)^n}{\hbar^n}\big\langle \hat{\mathrm{T}}\{\hat{b}_{\alpha_1}(\tau_1)\cdots\hat{b}_{\alpha_n}(\tau_n)\hat{b}^\dagger_{\beta_1}(\sigma_1)\cdots\hat{b}^\dagger_{\beta_n}(\sigma_n)\}\big\rangle_0 \\ &= \sum_p \zeta^P \mathcal{G}^0_{\alpha_{p_1}\beta_{p_2}}(\tau_{p_1},\sigma_{p_2})\cdots\mathcal{G}^0_{\alpha_{p_{2n-1}}\beta_{p_{2n}}}(\tau_{p_{2n-1}},\sigma_{p_{2n}})\end{aligned} \tag{2.32}$$

Thus, the $2n$-point Matsubara Green functions corresponding to the Hamiltonian of the non-interactive ensemble (2.23) can be calculated as the sum over all possible permutations of two-point Matsubara Green functions (2.11). This property, which originates in the Wick decomposition of a string of creation and annihilation operators, serves as the underlying motivation for the exact shape of the written definition of the $2n$-point Matsubara Green functions. In conclusion, for non-interactive systems it is sufficient to calculate only the two-point Green function, from which all other Green functions follows.

2.3.2 The Non-Interactive Two-Point Green Function

Recall the equation of motion for the two-point Matsubara Green function (2.12). Inserting the commutation relation with the non-interacting Hamiltonian (2.24) the product $\hat{\mathrm{T}}\{[\hat{H}_0,\hat{b}_\alpha(\tau)]\hat{b}^\dagger_\beta(0)\} = \xi_\alpha\hat{\mathrm{T}}\{\hat{b}_\alpha(\tau)\hat{b}^\dagger_\beta(0)\}$, leaving

$$\Big(-\hbar\frac{\partial}{\partial\tau}-\xi_\alpha\Big)\mathcal{G}_{\alpha\beta}(\tau) = \delta(\tau)\delta_{\alpha\beta}. \tag{2.33}$$

Hence, the two-point Matsubara Green function $\mathcal{G}_{\alpha\beta}(\tau)$ is the solution to an inhomogeneous differential equation, where the right hand side of the equation is proportional to the delta function $\delta(\tau)$. In mathematical literature, the derived equation of motion is the original definition for Green functions. In this way, the two-point Green functions (2.11) corresponding to the single-particle Hamiltonian (2.40) are Green functions with respect to the mathematical definition as well as the definition from quantum many-body theory (2.10).

Due to the direct time dependence (2.25) of the creation and annihilation operators in the non-interactive ensemble, an expression for the two-point Matsubara Green function (2.11) can be calculated directly from its definition. With the Heaviside function satisfying $\Theta(-\tau) = 1-\Theta(\tau)$, and using the resulting commutation relation between the creation and annihilation operators (1.7), then

$$\mathcal{G}^0_{\alpha\beta}(\tau) = -\frac{1}{\hbar}\big\langle\hat{\mathrm{T}}\{\hat{b}_\alpha(\tau)\hat{b}^\dagger_\beta(0)\}\big\rangle_0 = -e^{-\xi_\alpha\tau/\hbar}\big[\Theta(\tau)\delta_{\alpha\beta}+\zeta\big\langle\hat{b}^\dagger_\beta\hat{b}_\alpha\big\rangle_0\big].$$

The expression found is readily confirmed to be the solution to the equation of motion (2.33). The remaining average (2.28) is zero unless $\alpha=\beta$ for which the

occupation number distribution function $\langle \hat{b}_\alpha^\dagger \hat{b}_\alpha \rangle_0 = n_\zeta(\xi_\alpha)$ denotes the Bose-Einstein distribution for $\zeta = 1$ and the Fermi-Dirac distribution for $\zeta = -1$. The two-point Matsubara Green function in the non-interactive case is thus readily decomposed as $\mathcal{G}_{\alpha\beta}(\tau) \equiv \delta_{\alpha\beta}\mathcal{G}_\alpha(\tau)$, defining the *Matsubara propagator*

$$\mathcal{G}_\alpha^0(\tau) = -e^{-\xi_\alpha \tau/\hbar}\big[\Theta(\tau) + \zeta n_\zeta(\xi_\alpha)\big], \tag{2.34}$$

The Matsubara propagator describes the propagation of a single particle through the non-interactive ensemble, created by the operator $\hat{b}_\alpha^\dagger$ and annihilated by the operator $\hat{b}_\alpha$ at the later time τ. Notice the anticipated discontinuity (2.13) at $\tau = 0$, effectuated by the Heaviside function $\Theta(\tau)$.

The Matsubara propagator (2.34) allows for a direct calculation of the corresponding Fouriér coefficients (2.16), which becomes

$$\tilde{\mathcal{G}}_\alpha^0(i\mu_n) = \frac{1}{i\mu_n\hbar - \xi_\alpha}, \tag{2.35}$$

giving the Matsubara propagator in the frequency domain where μ_n is either a bosonic or a fermionic Matsubara frequency (2.15). The result can also be found directly by taking the Fouriér transform of the equation of motion (2.33).

2.3.3 Matsubara Frequency Summation Rules

From the Fouriér transform (2.16) of the two-point Matsubara Green function $\mathcal{G}_{\alpha\beta}(\tau)$, general Matsubara frequency summation rules can be devised. In particular, due to the discontinuity at $\tau = 0$, the summation of $\tilde{\mathcal{G}}_{\alpha\beta}(i\mu_n)$ over all Matsubara frequencies μ_n is divergent. The sum can be regularized by taking the limit $\tau = \pm\eta$, where $\eta > 0$ is an infinitesimal. From the expression of the two-point Matsubara Green function (2.13), the sum is seen to converge to different values depending on the sign of the infinitesimal. Conventionally the negative sign is chosen, giving the regularized sum

$$\frac{1}{\beta}\sum_{\mu_n} \tilde{\mathcal{G}}_{\alpha\beta}(i\mu_n) = -\zeta\big\langle \hat{b}_\beta^\dagger \hat{b}_\alpha \big\rangle. \tag{2.36}$$

If instead the positive sign is chosen, the result of the summation likewise becomes $\langle \hat{b}_\alpha \hat{b}_\beta^\dagger \rangle$; the two regularizations differ by $\delta_{\alpha\beta}$, and hence give the same result only for $\alpha \neq \beta$. The summation rule holds in general, and will explicitly depend on the density operator and in turn the Hamiltonian of the system.

In particular, consider the general summation rule (2.36) for the non-interactive case. From the expression of the Matsubara propagator of the frequency domain (2.35), the general summation rule translates to the formula

$$\frac{1}{\beta}\sum_{i\mu_n} \frac{1}{i\hbar\mu_n - \xi_\alpha} = -\zeta n_\zeta(\xi_\alpha). \tag{2.37}$$

In consequence, the Matsubara frequencies (2.15) constitute the complex poles of the occupation number distribution function (1.34). Again it should be noted that the summation rule holds only under the chosen regularization scheme.

From the obtained summation rule (2.37), other summation rules readily follow. Consider in particular the partial fraction decomposition

$$\frac{1}{(i\hbar\mu_n-\xi_\alpha)(i\hbar\mu_n-\xi_\beta)}=\frac{1}{\xi_\alpha-\xi_\beta}\Big(\frac{1}{i\hbar\mu_n-\xi_\alpha}-\frac{1}{i\hbar\mu_n-\xi_\beta}\Big).$$

Summing over the Matsubara frequencies here gives the summation rule

$$\frac{1}{\beta}\sum_{\mu_n}\frac{1}{(i\hbar\mu_n-\xi_\alpha)(i\hbar\mu_n-\xi_\beta)}=-\zeta\frac{n_\zeta(\xi_\alpha)-n_\zeta(\xi_\beta)}{\xi_\alpha-\xi_\beta}, \tag{2.38}$$

where sum converges independent on the regularization scheme used; using the other regularization scheme for the original summation rule (2.37) the same result is obtained. Inserting the limit $\xi_\beta\to\xi_\alpha$ then gives the relation

$$\frac{1}{\beta}\sum_{\mu_n}\frac{1}{(i\hbar\mu_n-\xi_\alpha)^2}=-\zeta\frac{\partial n_\zeta(\xi_\alpha)}{\partial\xi_\alpha}=\beta n_\zeta(\xi_\alpha)\big[\eta+n_\zeta(\xi_\alpha)\big]. \tag{2.39}$$

where the derivative of the distribution function follows from its definition (1.34). Other frequency summation rules can likewise be calculated for the particular choice of regularization. For non-interactive systems, the Matsubara frequency summation rules are often used in calculations of observable averages, which regularly can be written in terms of Green functions.

2.4 The Matrix of Matsubara Green Functions

In the previous subsection, an explicit expression was calculated for the two-point Matsubara Green function (2.11) using the Hamiltonian of a non-interactive ensemble (2.23). In this case, the resulting functions (2.34) were seen to be diagonal, satisfying $\mathcal{G}^0_{\alpha\beta}(\tau)=\delta_{\alpha\beta}\mathcal{G}^0_\alpha(\tau)$. The result is due to the diagonal form of the Hamiltonian, which also dictates the dependence of the Fouriér coefficients (2.35) on the single-particle energy eigenvalue ξ_α.

Consider instead a general quantum ensemble of non-interacting particles, where the Hamiltonian operator independent on the chosen basis can be expressed in second quantized form as a single-particle operator (1.9), written

$$\hat{H}=\sum_{\alpha\beta}\mathcal{H}_{\alpha\beta}\hat{b}^\dagger_\alpha\hat{b}_\beta. \tag{2.40}$$

Here, the creation and annihilation operators $\hat{b}^\dagger_\alpha$ and $\hat{b}_\alpha$ create and annihilate a particle in the single-particle state $|\alpha\rangle$, respectively. The matrix elements are given by $\mathcal{H}_{\alpha\beta}=\langle\alpha|\,\hat{\mathfrak{h}}\,|\beta\rangle$, where $\hat{\mathfrak{h}}$ denotes the Hamiltonian operator describing the dynamics of a single particle of the ensemble. In general, the eigenstates of the Hamiltonian $\hat{\mathfrak{h}}$ and the corresponding eigenvalues may not be known.

Recall then the equation of motion (2.12) for the two-point Matsubara Green function. Using the commutation or anticommutation relations of the creation and annihilation operators (1.7), the commutator is readily calculated

$$[\hat{H}, \hat{b}_\alpha] = -\sum_\gamma \mathcal{H}_{\alpha\gamma}\hat{b}_\gamma \tag{2.41}$$

Because the Hamiltonian operator commutes with itself, the commutation relation is transferred to the imaginary time Heisenberg operator $\hat{b}_\alpha(\tau)$. In consequence, using the linearity of the thermal average, the time ordered product

$$\big\langle \hat{\mathrm{T}}\{[\hat{H}, \hat{b}_\alpha(\tau)]\hat{b}^\dagger_\beta(0)\}\big\rangle = -\sum_\gamma \mathcal{H}_{\alpha\gamma}\big\langle \hat{\mathrm{T}}\hat{b}_\gamma(\tau)\hat{b}^\dagger_\beta(0)\big\rangle.$$

In consequence, the equation of motion for the two-point Matsubara Green function for a general single-particle Hamiltonian operator (2.40) becomes

$$\hbar\frac{\partial}{\partial\tau}\mathcal{G}_{\alpha\beta}(\tau) = -\delta(\tau)\delta_{\alpha\beta} - \sum_\gamma \mathcal{H}_{\alpha\gamma}\mathcal{G}_{\gamma\beta}(\tau). \tag{2.42}$$

Hence, the non-diagonal form of the Hamiltonian results in a set of coupled differential equations for the two-point Matsubara Green functions.

For systems where the Hamiltonian $\hat{\mathfrak{h}}$ has a finite number W of energy eigenvalues, the matrix elements $\mathcal{H}_{\alpha\beta}$ make up the *Hamiltonian matrix* $\mathcal{H}$, being a square matrix of size $(W \times W)$. Introduce then the *matrix of Green functions* $\mathcal{G}(\tau)$ whose matrix elements are the two-point Matsubara Green functions $\mathcal{G}_{\alpha\beta}(\tau)$. With this notation, the equations of motion for the two-point Matsubara Green functions (2.42) can be written in the form of the matrix equation

$$\Big(-\hbar\frac{\partial}{\partial\tau} - \mathcal{H}\Big)\mathcal{G}(\tau) = \delta(\tau)\mathcal{I}. \tag{2.43}$$

where now $\mathcal{I}$ denotes the $(W \times W)$ unit matrix. If here the Hamiltonian matrix is diagonal, the equation of motion for the Green matrix (2.43) decouple into W independent equations, and the equation of motion for the two-point Matsubara Green functions in the non-interactive case (2.33) is retrieved. Thus, the Green functions corresponding to the non-interactive Hamiltonian (2.23) and the more general single-particle Hamiltonian (2.40) are related by the unitary transform that diagonalizes the Hamiltonian matrix $\mathcal{H}$. As a consequence of this, the Wick decomposition scheme for the non-interactive Matsubara Green functions (2.31) holds in general for systems governed by any single-particle Hamiltonian.

By the direct use of the Fouriér transform (2.16), the differential equation of motion (2.43) for the matrix of Green functions can be translated to an algebraic equation in the frequency domain, written as the matrix equation

$$\big(i\hbar\mu_n - \mathcal{H}\big)\tilde{\mathcal{G}}(i\mu_n) = \mathcal{I}. \tag{2.44}$$

Hence, the matrix of Green functions of the frequency domain $\tilde{\mathcal{G}}(i\mu_n)$ can be calculated as the inverse of the matrix $(i\hbar\mu_n - \mathcal{H})$, allowing for a simple calculation of the two-point Matsubara Green functions (2.11) for systems described by a Hamiltonian matrix of finite dimensionality.

Chapter 3

Conductivity Formulas in the Kubo Formalism

The statistics of non-interactive ensembles was derived in chapter 1, and then expanded upon by adding interactions in chapter 2. In this final chapter of Part I, an additional external perturbation is imposed on the ensemble and the following response of the system derived. For a diminutive perturbation the response can be calculated using linear response theory, for which the quantum mechanical framework is known as the Kubo formalism. The main result of the chapter is the derivation of a Kubo formula for the conductivity of a material.

The conductivity of a material is quantified by the conductivity tensor, whose elements describe the current response in one direction from the externally applied current in another direction. The conductivity tensor is the main observable for describing electronic transport properties, and can be experimentally probed to investigate the electronic or magnetic structure of different materials.

In order to properly define the current response in a semiclassical setting, the chapter initiates with a description of the quantum mechanical current density operator. The matrix elements of the current density operator are then calculated for systems with both continuous and discrete translation invariance, following from the discussion in appendix B on the Bloch theorem.

The Kubo formulae are derived in accordance with the original derivation by Kubo [17], accompanied by the textbook by Mahan [8] and the classical article by Rammer and Smith [7].

3.1 Quantum Mechanical Current Density

The following section introduces the concept of *current density* in a quantum mechanical framework, and calculates the matrix elements of the current density operator for a general crystalline system, investigated in appendix B. The section is highly dependent on the theory surrounding Blochs theorem (B16) and on the second quantization scheme (1.9) considered in chapter 1.

3.1.1 Current Density Operators

Classically, the *electric current density* $\boldsymbol{j}_\iota(\boldsymbol{r},t)$ of a single particle ι with charge Q is related to its velocity vector through $\boldsymbol{j}_\iota(\boldsymbol{r},t) = Q\boldsymbol{v}_\iota\delta(\boldsymbol{r}_\iota-\boldsymbol{r})$, where $\boldsymbol{r}_\iota$ is the position vector and $\boldsymbol{v}_\iota$ the velocity vector of the particle. Quantum mechanically, the position vector $\boldsymbol{r}_\iota$ is exchanged for the position vector operator denoted by $\hat{\boldsymbol{r}}_\iota$ and considered in the Heisenberg picture (A6). From the Heisenberg equation of motion (A7), as the position operator carries no explicit time dependence by definition, the *velocity operator* is introduced as

$$\hat{\boldsymbol{v}}_\iota = \frac{1}{i\hbar}\big[\hat{\boldsymbol{r}}_\iota, \hat{\mathfrak{h}}\big]. \tag{3.1}$$

where $\hat{\mathfrak{h}}$ is the Hamiltonian operator describing the single particle. Notice then that the current density is a product of two functions. In order to obtain hermiticity, its quantum analogue is defined as a symmetrization of the corresponding quantized operators, which can be written as the anticommutator

$$\hat{\boldsymbol{j}}_\iota(\boldsymbol{r}) = \frac{1}{2}\big(Q\hat{\boldsymbol{v}}_\iota\delta(\hat{\boldsymbol{r}}_\iota-\boldsymbol{r}) + Q\delta(\hat{\boldsymbol{r}}_\iota-\boldsymbol{r})\hat{\boldsymbol{v}}_\iota\big) = \frac{Q}{2}\{\hat{\boldsymbol{v}}_\iota, \delta(\hat{\boldsymbol{r}}_\iota-\boldsymbol{r})\} \tag{3.2}$$

Here, $\boldsymbol{r}$ is an ordinary position vector while $\hat{\boldsymbol{r}}_\iota$ is the position operator of the particle and must not be confused with an ordinary unit vector. It is then viable to also define the spatial Fouriér transform of the current density operator

$$\hat{\boldsymbol{j}}_\iota(\boldsymbol{q}) = \int \mathrm{d}^3r\, \hat{\boldsymbol{j}}(\boldsymbol{r})e^{-i\boldsymbol{q}\cdot\boldsymbol{r}} = \frac{Q}{2}\{\hat{\boldsymbol{v}}_\iota, e^{-i\boldsymbol{q}\cdot\hat{\boldsymbol{r}}_\iota}\} \tag{3.3}$$

where the final expression is written in terms of an exponential operator. In particular, for the uniform limit $\boldsymbol{q} = 0$ the Fouriér transform of the current density operator becomes directly given by the velocity operator as $\hat{\boldsymbol{j}} = Q\hat{\boldsymbol{v}}$.

The total current density $\boldsymbol{J}(\boldsymbol{r},t)$ of the system is the accumulation of all individual single-particle current densities (3.2), with the corresponding operator

$$\hat{\boldsymbol{J}}(\boldsymbol{r}) = \sum_\iota \hat{\boldsymbol{j}}_\iota(\boldsymbol{r}), \tag{3.4}$$

where the symbol ι is the particle index. Alternately, through the second quantization scheme (1.9), the total current density operator can be written in terms of the creation and annihilation operators (1.6) of the particles, expanded in terms of the matrix elements of the single-particle current density operator (3.2).

Consider in particular a system which is continuously translation invariant, such that the Hamiltonian operator $\hat{\mathfrak{h}}(\hat{\boldsymbol{p}})$ can be written in terms of the momentum operator $\hat{\boldsymbol{p}}$ introduced in appendix B. In this case, the eigenstates of the Hamiltonian operator will coincide with the eigenstates $|\boldsymbol{p}\rangle$ of the momentum operator (B6), with the energy eigenvalue equation given by $\hat{\mathfrak{h}}(\hat{\boldsymbol{p}})\,|\boldsymbol{p}\rangle = \varepsilon_{\boldsymbol{p}}\,|\boldsymbol{p}\rangle$. Furthermore, using the canonical commutation relation (B4) between the position and momentum operators, the velocity operator (3.1) corresponding to the Hamiltonian operator $\hat{\mathfrak{h}}(\hat{\boldsymbol{p}})$ is readily expressed on the form

$$\hat{\boldsymbol{v}} = \frac{1}{i\hbar}\big[\hat{\boldsymbol{r}}, \hat{\mathfrak{h}}(\hat{\boldsymbol{p}})\big] = \nabla_{\hat{\boldsymbol{p}}}\hat{\mathfrak{h}}(\hat{\boldsymbol{p}}), \tag{3.5}$$

where the particle index has been neglected for convenience of notation. Hence, the matrix elements of the velocity operator in the momentum representation

$$\langle \boldsymbol{p}_1|\,\hat{\boldsymbol{v}}\,|\boldsymbol{p}_2\rangle = \delta(\boldsymbol{p}_2 - \boldsymbol{p}_1)\nabla_{\boldsymbol{p}_2}\varepsilon_{\boldsymbol{p}_2}. \tag{3.6}$$

Likewise, using the completeness relation of the position operator eigenbasis (B1) and the explicit form of the wavefunction (B6) corresponding to the momentum eigenstate $|\boldsymbol{p}\rangle$, the matrix elements of the exponential operator

$$\langle \boldsymbol{p}_1|\,e^{-i\boldsymbol{q}\cdot\hat{\boldsymbol{r}}}\,|\boldsymbol{p}_2\rangle = \int \frac{\mathrm{d}^d r}{(2\pi\hbar)^d}\; e^{-i\boldsymbol{p}_1\cdot\boldsymbol{r}/\hbar}e^{-i\boldsymbol{q}\cdot\boldsymbol{r}}e^{i\boldsymbol{p}_2\cdot\boldsymbol{r}/\hbar} = \delta(\boldsymbol{p}_2 - \boldsymbol{p}_1 - \hbar\boldsymbol{q}) \tag{3.7}$$

In conclusion, the matrix elements of the Fouriér transformed current density operator (3.3) in the momentum representation can be calculated

$$\begin{aligned}\langle \boldsymbol{p}_1|\,\hat{\boldsymbol{\jmath}}(\boldsymbol{q})\,|\boldsymbol{p}_2\rangle &= \frac{Q}{2}\int \mathrm{d}^d p_3 \Big[\langle \boldsymbol{p}_1|\,\hat{\boldsymbol{v}}\,|\boldsymbol{p}_3\rangle\langle \boldsymbol{p}_3|\,e^{-i\boldsymbol{q}\cdot\hat{\boldsymbol{r}}}\,|\boldsymbol{p}_2\rangle + \langle \boldsymbol{p}_1|\,e^{-i\boldsymbol{q}\cdot\hat{\boldsymbol{r}}}\,|\boldsymbol{p}_3\rangle\langle \boldsymbol{p}_3|\,\hat{\boldsymbol{v}}\,|\boldsymbol{p}_2\rangle\Big] \\ &= \frac{Q}{2}\int \mathrm{d}^d p_3 \Big[\nabla_{\boldsymbol{p}_3}\varepsilon_{\boldsymbol{p}_3}\delta(\boldsymbol{p}_3 - \boldsymbol{p}_1)\delta(\boldsymbol{p}_2 - \boldsymbol{p}_3 - \hbar\boldsymbol{q}) + \delta(\boldsymbol{p}_3 - \boldsymbol{p}_1 - \hbar\boldsymbol{q})\nabla_{\boldsymbol{p}_2}\varepsilon_{\boldsymbol{p}_2}\delta(\boldsymbol{p}_2 - \boldsymbol{p}_3)\Big].\end{aligned}$$

Using the delta functions from the velocity operator matrix elements (3.6) to perform the integral, the momentum representation matrix elements of the current density operator (3.2) corresponding to a Hamiltonian operator $\hat{\mathfrak{h}}(\hat{\boldsymbol{p}})$ of a system invariant continuously on spatial translation becomes

$$\langle \boldsymbol{p}_1|\,\hat{\boldsymbol{\jmath}}(\boldsymbol{q})\,|\boldsymbol{p}_2\rangle = \frac{Q}{2}\Big[\nabla_{\boldsymbol{p}}\varepsilon_{\boldsymbol{p}}\Big|_{\boldsymbol{p}=\boldsymbol{p}_1} + \nabla_{\boldsymbol{p}}\varepsilon_{\boldsymbol{p}}\Big|_{\boldsymbol{p}=\boldsymbol{p}_1+\hbar\boldsymbol{q}}\Big]\delta(\boldsymbol{p}_2 - \boldsymbol{p}_1 - \hbar\boldsymbol{q}) \tag{3.8}$$

In the uniform limit where $\boldsymbol{q} = 0$, the momentum eigenstates (B6) are thus also eigenstates of the current density operator, with $\hat{\boldsymbol{\jmath}}\,|\boldsymbol{p}\rangle = Q\hat{\boldsymbol{v}}\,|\boldsymbol{p}\rangle = Q\nabla_{\boldsymbol{p}}\varepsilon_{\boldsymbol{p}}\,|\boldsymbol{p}\rangle$.

For free non-relativistic particles in particular, the Hamiltonian operator takes the known form $\hat{\mathfrak{h}}(\hat{\boldsymbol{p}}) = \hat{\boldsymbol{p}}^2/2m$ with the corresponding energy eigenvalues $\varepsilon_{\boldsymbol{p}} = \boldsymbol{p}^2/2m$. The velocity operator (3.5) then takes the intuitive form $\hat{\boldsymbol{v}} = \hat{\boldsymbol{p}}/m$, similar to the basic definition of momentum in classical physics.

3.1.2 Current Density in the Bloch Basis

In general, the Hamiltonian operator $\hat{\mathfrak{h}}$ describing the dynamics of a single particle will not only be dependent on the momentum operator $\hat{\boldsymbol{p}}$, but also contain other dependencies from external influences. Consider then a Hamiltonian operator dependent on both the momentum and the position operators, denoted $\hat{\mathfrak{h}}(\hat{\boldsymbol{r}}, \hat{\boldsymbol{p}})$. Because the position operator commutes with itself, the velocity operator (3.1) will then take the same form (3.5) as for a Hamiltonian $\hat{\mathfrak{h}}(\hat{\boldsymbol{p}})$ invariant under continuous spatial translation. However, because the Hamiltonian $\hat{\mathfrak{h}}(\hat{\boldsymbol{p}}, \hat{\boldsymbol{r}})$ does not commute with the momentum operator, the eigenstates of the momentum operator will no longer be simultaneous eigenstates of the Hamiltonian operator. The matrix elements of the current density operator (3.8) should then be expanded in the Hamiltonian eigenbasis, and not the momentum eigenbasis.

Consider in particular a general crystalline system as described in appendix B, where the Hamiltonian operator $\hat{\mathfrak{h}}(\hat{\boldsymbol{r}}, \hat{\boldsymbol{p}})$ describes a single electron residing in a lattice periodic potential. The matrix elements of the current density operator (3.2) is then readily calculated in the Bloch basis, where the basis elements $|\psi_{\boldsymbol{k}}\rangle$ are the Bloch eigenstates of the Hamiltonian (B14) corresponding to the real space wavefunctions $\psi_{\boldsymbol{k}}(\boldsymbol{r}) = \langle \boldsymbol{r}|\psi_{\boldsymbol{k}}\rangle$ satisfying the Bloch theorem (B16); here, the energy band index is suppressed for ease of notation. The reciprocal vector $\boldsymbol{k}$ of the Brillouin zone is the crystal momentum of the particular electronic state, originating in the discrete translation invariance of the system.

Assuming the Bloch functions $|\psi_{\boldsymbol{k}}\rangle$ are properly orthogonalized (B21) over the crystal lattice, then using the second lattice orthogonality relation (B13), the matrix elements of the exponential operator are readily calculated

$$\langle \psi_{\boldsymbol{k}_1}| \, e^{-i\hat{\boldsymbol{r}}\cdot\boldsymbol{q}} \, |\psi_{\boldsymbol{k}_2}\rangle = \int \mathrm{d}^d\boldsymbol{r} \psi^*_{\boldsymbol{k}_1}(\boldsymbol{r})\psi_{\boldsymbol{k}_2}(\boldsymbol{r})e^{-i\boldsymbol{r}\cdot\boldsymbol{q}} = \delta(\boldsymbol{k}_2 - \boldsymbol{k}_1 - \boldsymbol{q}). \tag{3.9}$$

In a similar manner, the matrix elements of the velocity operator (3.1) become diagonal, satisfying $\langle \psi_{\boldsymbol{k}_1}| \, \hat{\boldsymbol{v}} \, |\psi_{\boldsymbol{k}_2}\rangle = \langle \psi_{\boldsymbol{k}_2}| \, \hat{\boldsymbol{v}} \, |\psi_{\boldsymbol{k}_2}\rangle \, \delta(\boldsymbol{k}_2 - \boldsymbol{k}_1)$. In order to calculate the remaining diagonal elements, recall that the Bloch states $|\psi_{\boldsymbol{k}}\rangle$ are related to lattice periodic states $|u_{\boldsymbol{k}}\rangle$ through the transform $|\psi_{\boldsymbol{k}}\rangle = e^{i\boldsymbol{k}\cdot\hat{\boldsymbol{r}}} \, |u_{\boldsymbol{k}}\rangle$, where the exponential operator is a map between their respective Hilbert spaces for a particular value of $\boldsymbol{k}$. Then, denoting by $\hat{\mathfrak{h}}(\boldsymbol{k}) = e^{i\boldsymbol{k}\cdot\hat{\boldsymbol{r}}}\hat{\mathfrak{h}}e^{-i\boldsymbol{k}\cdot\hat{\boldsymbol{r}}}$ the Hamiltonian operator for the lattice periodic states, the matrix element

$$\langle \psi_{\boldsymbol{k}}| \, [\hat{\boldsymbol{r}}, \hat{\mathfrak{h}}] \, |\psi_{\boldsymbol{k}}\rangle = \langle u_{\boldsymbol{k}}| \, [\hat{\boldsymbol{r}}, \hat{\mathfrak{h}}(\boldsymbol{k})] \, |u_{\boldsymbol{k}}\rangle = \langle u_{\boldsymbol{k}}| \, i\nabla_{\boldsymbol{k}}\hat{\mathfrak{h}}(\boldsymbol{k}) \, |u_{\boldsymbol{k}}\rangle \, .$$

The final matrix element can be calculated by a derivation of the eigenvalue equation $\hat{\mathfrak{h}}(\boldsymbol{k}) \, |u_{\boldsymbol{k}}\rangle = \varepsilon_{\boldsymbol{k}} \, |u_{\boldsymbol{k}}\rangle$ followed by left multiplication with $\langle u_{\boldsymbol{k}}|$, leaving

$$\langle \psi_{\boldsymbol{k}_1}| \, \hat{\boldsymbol{v}} \, |\psi_{\boldsymbol{k}_2}\rangle = \frac{1}{\hbar}\nabla_{\boldsymbol{k}_2}\varepsilon_{\boldsymbol{k}_2}\delta(\boldsymbol{k}_2 - \boldsymbol{k}_1). \tag{3.10}$$

Recall here that $\varepsilon_{\boldsymbol{k}}$ is also the eigenvalue corresponding to the Bloch state $|\psi_{\boldsymbol{k}}\rangle$. The quantity $\nabla_{\boldsymbol{k}}\varepsilon_{\boldsymbol{k}}/\hbar = \langle \psi_{\boldsymbol{k}}| \, \hat{\boldsymbol{v}} \, |\psi_{\boldsymbol{k}}\rangle$ is physically interpreted as the *effective velocity* of the single-particle electron state described by the Bloch state $|\psi_{\boldsymbol{k}}\rangle$.

The Bloch functions $|\psi_{\boldsymbol{k}}\rangle$ constitute a complete orthonormal set over the Brillouin zone, and so obey a continuous completeness relation (1.1) with respect to the crystal momentum $\boldsymbol{k}$. The Bloch basis matrix elements of the Fouriér transform of the current density operator (3.3) can then calculated from the elements of the exponential operator (3.9) and the velocity operator (3.10) as

$$\langle\psi_{\boldsymbol{k}_1}|\,\hat{\boldsymbol{\jmath}}(\boldsymbol{q})\,|\psi_{\boldsymbol{k}_2}\rangle = -\frac{e}{2\hbar}\Big[\nabla_{\boldsymbol{k}}\varepsilon_{\boldsymbol{k}}\big|_{\boldsymbol{k}=\boldsymbol{k}_1} + \nabla_{\boldsymbol{k}}\varepsilon_{\boldsymbol{k}}\big|_{\boldsymbol{k}=\boldsymbol{k}_1+\boldsymbol{q}}\Big]\delta(\boldsymbol{k}_2-\boldsymbol{k}_1-\boldsymbol{q}) \tag{3.11}$$

analogous to the momentum representation (3.8) with $Q=-e$ being the electron charge. The visual similarity between the matrix elements originates in the assumed translation invariance. For the crystal Hamiltonian (B14) however the translation invariance is discrete, and the crystal momentum $\hbar\boldsymbol{k}$ is only defined within the Brillouin zone of the reciprocal crystal lattice.

In conclusion, for an ensemble of non-interacting electrons residing in a crystal lattice, the second quantization (1.9) of the spatial Fouriér transform of the total current density operator (3.4) is written in the Bloch basis as

$$\hat{\boldsymbol{J}}(\boldsymbol{q}) = -\sum_{\boldsymbol{k}}\frac{e}{2\hbar}\left[\nabla_{\boldsymbol{k}_1}\varepsilon_{\boldsymbol{k}_1}\Big|_{\boldsymbol{k}_1=\boldsymbol{k}} + \nabla_{\boldsymbol{k}_1}\varepsilon_{\boldsymbol{k}_1}\Big|_{\boldsymbol{k}_1=\boldsymbol{k}+\boldsymbol{q}}\right]\hat{c}^\dagger_{\boldsymbol{k}}\hat{c}_{\boldsymbol{k}+\boldsymbol{q}} \equiv \sum_{\boldsymbol{k}}\boldsymbol{\mathcal{J}}(\boldsymbol{k},\boldsymbol{q})\hat{c}^\dagger_{\boldsymbol{k}}\hat{c}_{\boldsymbol{k}+\boldsymbol{q}} \tag{3.12}$$

where the sum is written implicitly over the reciprocal vectors $\boldsymbol{k}$ of the Brillouin zone. The operators $\hat{c}^\dagger_{\boldsymbol{k}}$ and $\hat{c}_{\boldsymbol{k}}$ are the creation and annihilation operators (1.6) of an electron occupying the Bloch state $|\psi_{\boldsymbol{k}}\rangle$. The resulting expression also introduces the quantities $\boldsymbol{\mathcal{J}}(\boldsymbol{k},\boldsymbol{q})$, being the matrix elements of the current density operator (3.11) disregarding the delta function.

Recall from appendix A that the Bloch functions besides the crystal momentum $\boldsymbol{k}$ are labelled by a discrete band index n. Consider then a finite number of energy bands, and let the Bloch eigenstates $|\psi_{n\boldsymbol{k}}\rangle$ be written as linear combinations of another complete and orthonormalized set of Bloch states $|\chi_{\boldsymbol{k}\alpha}\rangle$, where α denotes some finite set of discrete quantum numbers such as the electron spin. The calculation of the matrix elements (3.12) can then be performed with respect to the basis $|\chi_{\boldsymbol{k}\alpha}\rangle$. These states are however not the Bloch eigenstates of the single-particle Hamiltonian $\hat{\mathfrak{h}}$, and the energy eigenvalues $\varepsilon_{\boldsymbol{k}}$ are exchanged for the Hamiltonian matrix elements $\mathcal{H}_{\alpha\beta}(\boldsymbol{k}) = \langle\chi_{\boldsymbol{k}\alpha}|\,\hat{\mathfrak{h}}\,|\chi_{\boldsymbol{k}\beta}\rangle$. Expressed in the basis $|\chi_{\boldsymbol{k}\alpha}\rangle$, the total current density operator then becomes

$$\hat{\boldsymbol{J}}(\boldsymbol{q}) = \sum_{\boldsymbol{k}\alpha\beta}\boldsymbol{\mathcal{J}}_{\alpha\beta}(\boldsymbol{k},\boldsymbol{q})\hat{c}^\dagger_{\boldsymbol{k}\alpha}\hat{c}_{(\boldsymbol{k}+\boldsymbol{q})\beta} \tag{3.13}$$

where now $\hat{c}^\dagger_{\boldsymbol{k}\alpha}$ and $\hat{c}_{\boldsymbol{k}\alpha}$ are the creation and annihilation operators (1.6) of the state $|\chi_{\boldsymbol{k}\alpha}\rangle$, and the elements of the *current density matrices* are defined

$$\boldsymbol{\mathcal{J}}_{\alpha\beta}(\boldsymbol{k},\boldsymbol{q}) = -\frac{e}{2\hbar}\Big[\nabla_{\boldsymbol{k}_1}\mathcal{H}_{\alpha\beta}(\boldsymbol{k}_1)\big|_{\boldsymbol{k}_1=\boldsymbol{k}} + \nabla_{\boldsymbol{k}_1}\mathcal{H}_{\alpha\beta}(\boldsymbol{k}_1)\big|_{\boldsymbol{k}_1=\boldsymbol{k}+\boldsymbol{q}}\Big]. \tag{3.14}$$

If the current density is uniform in space with $\boldsymbol{q}=0$, the current density matrices can be written in terms of the Hamiltonian matrix as $\boldsymbol{\mathcal{J}}(\boldsymbol{k}) = -e\nabla_{\boldsymbol{k}}\mathcal{H}(\boldsymbol{k})/\hbar$.

3.1.3 Current Density from Electromagnetic Coupling

Due to the electric charge $Q = -e$, electrons couple to the electromagnetic field, as explained relativistically in subappendix D.4. Consider in particular the Coulomb gauge, where the electric field is connected to the electromagnetic vector potential $\boldsymbol{A}(\boldsymbol{r},t)$ through the relation $\boldsymbol{E}(\boldsymbol{r},t) = -\partial_t \boldsymbol{A}(\boldsymbol{r},t)$. From the minimal coupling principle (D19), the coupling between the electron and the electromagnetic field is classically effectuated by the exchange $\boldsymbol{p} \to \boldsymbol{p} + e\boldsymbol{A}$, where $\boldsymbol{p}$ denotes the kinetic momentum of the electron. In a semiclassical approach, the momentum corresponds to the momentum operator $\hat{\boldsymbol{p}}$ while the electromagnetic vector potential $\boldsymbol{A}(\hat{\boldsymbol{r}},t)$ can be considered a semiclassical field.

Consider then the single-electron crystal Hamiltonian (B14), hereby denoted $\hat{\mathfrak{h}}(\hat{\boldsymbol{p}})$ disregarding the electromagnetic influence, which couples to the electromagnetic field in the Coulomb gauge through the factor $\hat{\boldsymbol{p}}^2/2m$ as

$$\hat{\mathfrak{h}}\big(\hat{\boldsymbol{p}} + e\boldsymbol{A}(\hat{\boldsymbol{r}},t)\big) = \hat{\mathfrak{h}}(\hat{\boldsymbol{p}}) + \frac{e}{2m}\Big(\hat{\boldsymbol{p}}\boldsymbol{A}(\hat{\boldsymbol{r}},t) + \boldsymbol{A}(\hat{\boldsymbol{r}},t)\hat{\boldsymbol{p}}\Big) + \frac{e^2}{2m}\boldsymbol{A}^2(\hat{\boldsymbol{r}},t) \tag{3.15}$$

Here, the latter quadratic factor represents the energy content of the electromagnetic field itself, whereas the central terms describe the coupling between the electrons and the electromagnetic field for the specific system. The Hamiltonian operator $\hat{\mathfrak{h}}\big(\hat{\boldsymbol{p}} + e\boldsymbol{A}(\hat{\boldsymbol{r}},t)\big)$ describing the electromagnetic coupling can then be inserted into the expression for the velocity operator (3.1), which gives

$$\hat{\boldsymbol{v}} = \frac{1}{i\hbar}[\hat{\boldsymbol{r}}, \hat{\mathfrak{h}}(\hat{\boldsymbol{p}})] + \frac{e}{m}\boldsymbol{A}(\hat{\boldsymbol{r}},t) \equiv \hat{\boldsymbol{v}}_P + \hat{\boldsymbol{v}}_D \tag{3.16}$$

where the canonical commutation relation (B4) was used. Hence, under the influence of a perturbing electromagnetic field the velocity operator gains a *diamagnetic* term $\hat{\boldsymbol{v}}_D$, in addition to the *paramagnetic* term $\hat{\boldsymbol{v}}_P = \hat{\boldsymbol{p}}/m$ equal to the velocity operator (3.1) without the coupling. These terms in turn correspond to a paramagnetic and a diamagnetic part of the current density operator (3.2), which after reinstating the particle index ι can be written

$$\hat{\boldsymbol{\jmath}}_\iota(\boldsymbol{r}) = -\frac{e}{2m}\{\hat{\boldsymbol{p}}_\iota, \delta(\hat{\boldsymbol{r}}_\iota - \boldsymbol{r})\} - \frac{e^2}{2m}\boldsymbol{A}(\hat{\boldsymbol{r}}_\iota,t)\delta(\hat{\boldsymbol{r}}_\iota - \boldsymbol{r}) \equiv \hat{\boldsymbol{\jmath}}^P(\boldsymbol{r}) + \hat{\boldsymbol{\jmath}}^D(\boldsymbol{r}) \tag{3.17}$$

where it was used that the vector potential $\boldsymbol{A}(\hat{\boldsymbol{r}}_\iota,t)$ commutes with the position operator $\hat{\boldsymbol{r}}_\iota$. Hence, the application of an electromagnetic field may drive an electric current with the corresponding diamagnetic current density $\hat{\boldsymbol{\jmath}}^D(\boldsymbol{r})$.

The semiclassical electromagnetic vector potential can be written

$$\boldsymbol{A}(\hat{\boldsymbol{r}}_\iota,t) = \int \mathrm{d}^d r \boldsymbol{A}(\boldsymbol{r},t)\delta(\hat{\boldsymbol{r}}_\iota - \boldsymbol{r}).$$

From the expression of the Hamiltonian under the minimal coupling principle (3.15) and the corresponding current density operator (3.17), the Hamiltonian can then be written on the form $\hat{\mathfrak{h}}\big(\hat{\boldsymbol{p}}_\iota + e\boldsymbol{A}(\hat{\boldsymbol{r}}_\iota,t)\big) = \hat{\mathfrak{h}}(\hat{\boldsymbol{p}}_\iota) + \hat{\mathrm{V}}_\iota(t)$, with

$$\hat{\mathrm{V}}_\iota(t) = -\int \mathrm{d}^d r\, \hat{\boldsymbol{j}}_\iota(\boldsymbol{r}) \cdot \boldsymbol{A}(\boldsymbol{r}, t). \tag{3.18}$$

Here, the electromagnetic vector potential $\boldsymbol{A}(\boldsymbol{r}, t)$ is considered a classical field.

Consider then an entire ensemble of electrons residing in a crystal lattice, described by the total Hamiltonian $\hat{H}$ at equilibrium. Assuming the electrons are non-interacting, the Hamiltonian takes the form of a sum over single-electron terms $\hat{\mathfrak{h}}_\iota$, where each term takes the form of the single-electron crystal Hamiltonian (B14). An external electromagnetic field will then couple independently to each of the individual electrons through the derived single-electron potential term (3.18). The total perturbation term $\hat{\mathrm{V}}(t)$ originating in the minimal coupling principle for the entire non-interacting ensemble thus becomes

$$\hat{\mathrm{V}}(t) = \sum_\iota \hat{\mathrm{V}}_\iota(t) = -\int \mathrm{d}^d r \hat{\boldsymbol{J}}(\boldsymbol{r}) \cdot \boldsymbol{A}(\boldsymbol{r}, t). \tag{3.19}$$

where $\hat{\boldsymbol{J}}(\boldsymbol{r})$ is the total current density operator (3.12), being a sum over single-electron current densities (3.2). It should here be noted that both the single-particle and total current density operators implicitly carries a time argument t, which has been neglected in the discussion for ease of notation. The time dependence originates both from the Heisenberg representation (A6) of the operators, as well as a possible explicit time dependence from the electromagnetic vector potential for the diamagnetic term.

Finally, it should be emphasized that the minimal coupling principle for the semiclassical theory states that the electromagnetic vector potential $\boldsymbol{A}(\hat{\boldsymbol{r}}, t)$ couples to the momentum operator $\hat{\boldsymbol{p}}$ of the electron, and not the momentum operator eigenvalues $\boldsymbol{p}$. However, for the case where the Hamiltonian operator is dependent solely on the momentum operator, there is a direct correspondence between the dependence of the Hamiltonian operator $\hat{\mathfrak{h}}$ on the momentum operator $\hat{\boldsymbol{p}}$, and the dependence of the corresponding energy eigenvalues $\varepsilon_{\boldsymbol{p}}$ on the momentum eigenvalue $\boldsymbol{p}$. In this case, the paramagnetic and diamagnetic terms of the current density operator (3.17) can be deduced from the explicit momentum dependence of the energy eigenvalues $\varepsilon_{\boldsymbol{p}}$.

For a crystalline system however, the continuous translation invariance is reduced to a discrete translation invariance, and the energy bands $\varepsilon_{\boldsymbol{k}}$ become continuously dependent on the crystal momentum $\boldsymbol{k}$ instead of the kinetic momentum $\boldsymbol{p}$. The underlying crystal potential here modulates the electronic wavefunction, and the direct correspondence of momentum dependence between the Hamiltonian operator $\hat{\mathfrak{h}}$ and its energy eigenvalues $\varepsilon_{\boldsymbol{k}}$ is no longer guaranteed. In general however, the electrons can be assumed described by the single-electron crystal Hamiltonian (B14), where the dependence on the momentum operator lies entirely within the non-relativistic kinetic term $\hat{\boldsymbol{p}}^2/2m$. In conclusion, the form of the energy bands $\varepsilon_{\boldsymbol{k}}$ for a crystalline system will not reveal the form of the current density operator (3.2), but it can be assumed to contain a paramagnetic and a diamagnetic term (3.17) corresponding to a square dependence of the Hamiltonian operator on the momentum operator.

3.2 The Kubo Formula for Conductivity

The current section introduces the concept of conductivity, which quantifies the ability of a material to lead an electric current. The section initializes with the computation of observables for perturbed ensembles in linear response theory, which is specialized to yield a Kubo formula for the conductivity tensor. A main result of the section is the introduction of the current density autocorrelation function, which can be calculated using the Matsubara method of chapter 2.

3.2.1 Linear Response Theory

Recall the statistics of the principal ensembles derived in section 1.2 under the condition of equilibrium, for which the density operator (1.13) describing the ensemble carries no time dependence. From the Von Neumann equation (1.18), the density operator $\hat{\rho}$ then gains a dependence $\hat{\rho} = \hat{\rho}(\hat{H})$, where $\hat{H}$ is the Hamiltonian operator of the system, possibly including internal interactions.

Let then an external, time-dependent perturbation couple to an observable D of the system, removing the ensemble from equilibrium. Assuming the perturbation can be modelled by a classical field strength $F(t)$, the total Hamiltonian of the perturbed system in general takes the form $\hat{\mathrm{H}}(t) = \hat{H} - \hat{D}F(t)$, where the negative sign is introduced for later convenience. The density operator describing the perturbed ensemble will then also gain a time dependence governed by the Von Neumann equation (1.18), hereby denoted $\hat{\varrho}(t)$.

Due to the form of the perturbed Hamiltonian $\hat{\mathrm{H}}(t)$, it is pertinent to consider the time evolution of the system in the Dirac picture as described in appendix A, letting the time evolution of operators be governed by the unperturbed Hamiltonian $\hat{H}$. Denoting by $\hat{\mathrm{V}}_I(t) = -\hat{D}_I(t)F(t)$ the perturbation and by $\hat{\varrho}_I(t)$ the perturbed density operator in the Dirac picture (A8), the Von Neumann equation describing the time evolution of the density operator becomes

$$\frac{\mathrm{d}\hat{\varrho}_I}{\mathrm{d}t} = \frac{i}{\hbar}\Big[\hat{H}, \hat{\varrho}_I\Big] + \left(\frac{\partial\hat{\varrho}}{\partial t}\right)_I = -\frac{i}{\hbar}\Big[\hat{\mathrm{V}}_I(t), \hat{\varrho}_I\Big]. \tag{3.20}$$

Here, the partial derivative in the middle expression is given by the Von Neumann equation in the Schrödinger picture (1.18) with the total Hamiltonian $\hat{\mathrm{H}}(t) = \hat{H} + \hat{\mathrm{V}}(t)$, thus leaving only the commutator with $\hat{\mathrm{V}}_I(t)$. The solution to this equation depends on the boundary conditions of the perturbation.

Assume the ensemble is initially isolated and perturb the system adiabatically from $t \to -\infty$, giving the boundary condition $F(t \to -\infty) = 0$ for the coupling field. The ensemble is then initially described by the unperturbed density matrix $\hat{\rho}$ satisfying $[\hat{H}, \hat{\rho}] = 0$, corresponding to the unperturbed equilibrium. Integrating the Von Neumann equation for the density operator (3.20) with the boundary condition, the system equation of state then becomes

$$\hat{\varrho}_I(t) = \hat{\rho} - \frac{i}{\hbar}\int_{-\infty}^{t} \mathrm{d}s\Big[\hat{\mathrm{V}}_I(s), \hat{\varrho}_I(s)\Big]. \tag{3.21}$$

This gives an integral equation for the density operator $\hat{\rho}_I(t)$, which can be iterated to achieve an arbitrarily high degree of accuracy. The perturbed density operator can thus be expressed $\hat{\varrho}(t) = \hat{\rho} + \delta\hat{\varrho}(t)$, where $\delta\hat{\varrho}(t)$ is a *response term* describing the reaction of the unperturbed system described by $\hat{\rho}$ to the external perturbation $\hat{\mathrm{V}}(t)$. Notice that the unperturbed density operator $\hat{\rho}$ is the same in both the Dirac and Schrödinger pictures (A8), as it commutes with the unperturbed Hamiltonian $\hat{H}$ due to the condition of equilibrium.

In *linear response theory*, the integral equation (3.21) for $\hat{\varrho}(t)$ is only iterated to linear order by exchanging $\hat{\varrho}(t)$ for the time independent initial density operator $\hat{\rho}$ in the integral. Hence, in linear response theory the response term

$$\delta\hat{\varrho}_I(t) = \frac{i}{\hbar}\int_{-\infty}^{t} \mathrm{d}s \Big[\hat{D}_I(s), \hat{\rho}\Big] F(s) \tag{3.22}$$

in the Dirac picture, where the particular perturbation $\hat{\mathrm{V}}_I(t) = -\hat{D}_I(t)F(t)$ has been reinserted. The expression is only dependent on the time independent unperturbed Hamiltonian $\hat{H}$ of the ensemble at equilibrium, which appears both in the expression of the equilibrium density operator $\hat{\rho} = \hat{\rho}(\hat{H})$ and in the time evolution of the operators in the Dirac picture (A8).

The response of the ensemble to the perturbation is observed through the change δO of a physical observable O, whose ensemble average under the perturbation is time dependent and can be calculated $\langle\hat{O}\rangle_t = \mathrm{Tr}\{\hat{O}\hat{\varrho}(t)\}$. From the expression of the perturbed density operator (3.21), this expectation value can be written $\langle\hat{O}\rangle_t = \langle\hat{O}\rangle + \langle\delta\hat{O}\rangle_t$, where now $\langle\hat{O}\rangle$ denotes the ensemble average with respect to the unperturbed ensemble; the ensemble average in the perturbed and unperturbed ensembles are separated using the subscript t. Recalling that ensemble averages are independent on the dynamical picture used, the response of the observable O can be calculated

$$\langle\delta\hat{O}\rangle_t = \mathrm{Tr}\{\hat{O}_I(t)\delta\hat{\varrho}_I(t)\} = \frac{i}{\hbar}\int_{-\infty}^{t} \mathrm{d}s\, \mathrm{Tr}\Big\{\hat{\rho}\big[\hat{O}_I(t), \hat{D}_I(s)\big]\Big\} F(s),$$

where the cyclic property of the trace has been used to move the equilibrium density operator $\hat{\rho}$ outside of the commutator. Notice here that the calculation of the average only involves the unperturbed Hamiltonian $\hat{H}$ of the ensemble at equilibrium; Dirac operators of the perturbed ensemble are identical to Heisenberg operators of the unperturbed ensemble. Hence, the calculation of the response of physical observables in the perturbed ensemble has been reduced to the calculation of an average of the corresponding ensemble in equilibrium, as

$$\langle\hat{O}\rangle_t = \langle\hat{O}\rangle + \frac{i}{\hbar}\int_{-\infty}^{t} \mathrm{d}s \Big\langle\big[\hat{O}(t), \hat{D}(s)\big]\Big\rangle F(s). \tag{3.23}$$

The resulting formula is known as a *Kubo formula*, where the operators are considered in the Heisenberg picture (A6) of the ensemble at equilibrium described by the density operator $\hat{\rho}$ and unperturbed Hamiltonian $\hat{H}$.

3.2.2 Calculation of Conductivity in the Kubo Formalism

The *electrical conductivity* of a material describe the ability of the material to conduct an electrical current upon the application of an electric field $\boldsymbol{E}(\boldsymbol{r}, t)$. For a wide class of materials the measured *current response* $\boldsymbol{J}(\boldsymbol{r}, t)$ to the electric perturbation is associated to the applied electric field through the *conductivity tensor*, defined by the linear spacetime response relation

$$J_i(\boldsymbol{r}, t) = \sum_l \int \mathrm{d}^d x \int \mathrm{d}s \; \sigma_{il}(\boldsymbol{r}, t; \boldsymbol{x}, s) E_l(\boldsymbol{x}, s). \tag{3.24}$$

The conductivity tensor element σ_{il} here describes the coupling of the current response component J_i to the electric field component E_l. The relation between the applied electric field and the current response is known as *Ohms law*.

Consider the stationary case, where the flow of current is at equilibrium and constant in time. The conductivity tensor (3.24) then becomes homogeneous in time, dependent only on time differences as $\sigma_{il}(\boldsymbol{r}, t; \boldsymbol{x}, s) = \sigma_{il}(\boldsymbol{r}, \boldsymbol{x}, t - s)$, for which the temporal Fouriér transform is introduced

$$\sigma_{il}(\boldsymbol{r}, \boldsymbol{x}, \omega) = \int \mathrm{d}t \, e^{i\omega t} \sigma_{il}(\boldsymbol{r}, \boldsymbol{x}, t) \qquad \sigma_{il}(\boldsymbol{r}, \boldsymbol{x}, t) = \int \frac{\mathrm{d}\omega}{2\pi} e^{-i\omega t} \sigma_{il}(\boldsymbol{r}, \boldsymbol{x}, \omega). \tag{3.25}$$

Inserting the Fouriér transformed quantities into the defining relation of the conductivity tensor (3.24), the relation is written in the frequency domain as

$$J_i(\boldsymbol{r}, \omega) = \sum_l \int \mathrm{d}^d x \; \sigma_{il}(\boldsymbol{r}, \boldsymbol{x}, \omega) E_l(\boldsymbol{x}, \omega), \tag{3.26}$$

where ω is interpreted as the frequency of the imposed electric field $\boldsymbol{E}(\boldsymbol{r}, t)$.

For a general system the obtained conductivity tensor $\sigma_{il}(\boldsymbol{r}, \boldsymbol{x}, \omega)$ is not homogeneous in space due to the microscopic details of the system. However, for crystalline systems in particular, the macroscopic conductivity can be regarded an average of the microscopic conductivity over several unit cells. In performing such a microscopic spatial average, the system effectively becomes translationally invariant in space, and the conductivity tensor takes on the spatial dependence $\sigma_{il}(\boldsymbol{r}, \boldsymbol{x}, \omega) = \sigma_{il}(\boldsymbol{r} - \boldsymbol{x}, \omega)$. Similarly to the temporal Fouriér transforms (3.27), it is then viable to introduce the spatial Fouriér transforms

$$\sigma_{il}(\boldsymbol{q}, \omega) = \int \mathrm{d}^d r \; e^{-i\boldsymbol{q}\cdot\boldsymbol{r}} \sigma_{il}(\boldsymbol{r}, \omega) \qquad \sigma_{il}(\boldsymbol{r}, \omega) = \int \frac{\mathrm{d}^d q}{(2\pi)^3} \; e^{i\boldsymbol{q}\cdot\boldsymbol{r}} \sigma_{il}(\boldsymbol{q}, \omega), \tag{3.27}$$

where the momentum $\boldsymbol{q}$ is interpreted as the wavevector of the electric field $\boldsymbol{E}$. Defining the spatial Fouriér transform of the current response and the electric field in a similar manner, the current response (3.26) can be expressed

$$J_i(\boldsymbol{q}, \omega) = \sum_l \sigma_{il}(\boldsymbol{q}, \omega) E_l(\boldsymbol{q}, \omega). \tag{3.28}$$

Hence, in the frequency domain Ohms law takes the form of a matrix equation.

Consider again the Coulomb gauge, where the electric field is related to the electromagnetic vector potential as $\boldsymbol{E}(\boldsymbol{r},t) = -\partial_t \boldsymbol{A}(\boldsymbol{r},t)$. The Fouriér transformations of the electric field and the electromagnetic vector potential are then related by $\boldsymbol{E}(\boldsymbol{q},\omega) = i\omega \boldsymbol{A}(\boldsymbol{q},\omega)$. Hence, the current response (3.28) can also be expressed in terms of the electromagnetic vector potential as

$$J_i(\boldsymbol{q},\omega) = -\sum_l K_{il}(\boldsymbol{q},\omega) A_l(\boldsymbol{q},\omega) \tag{3.29}$$

where the *electromagnetic response function* is defined $K_{il}(\boldsymbol{q},\omega) = -i\omega\sigma_{il}(\boldsymbol{q},\omega)$. It should here be noted that the electromagnetic response function is defined in the Coulomb gauge. For an arbitrary gauge, both the electromagnetic response function and the electromagnetic vector potential will be gauge dependent in such a way that the observable conductivity tensor is gauge independent.

Quantum mechanically, the current response $\boldsymbol{J}(\boldsymbol{r},t)$ can be calculated as the ensemble average over the total current density operator $\hat{\boldsymbol{J}}(\boldsymbol{r},t)$, which in the stationary case carries no explicit time dependence. Thus, the total current density (3.12) is analogous to the observable O in the general Kubo formula (3.23). From the coupling to the electromagnetic field (3.19) which serves as the external perturbation, the current density is also analogous to the observable D of the formula, whereas the electromagnetic vector potential $\boldsymbol{A}(\boldsymbol{r},t)$ serves as the external field $F(t)$. The Kubo formula for current response thus becomes

$$J_i(\boldsymbol{r},t) = \langle \hat{J}_i(\boldsymbol{r},t)\rangle + \frac{i}{\hbar}\int_{-\infty}^{t} \mathrm{d}s \int \mathrm{d}^d x \sum_l \Big\langle \big[\hat{J}_i(\boldsymbol{r},t), \hat{J}_l(\boldsymbol{x},s)\big]\Big\rangle A_l(\boldsymbol{x},t), \tag{3.30}$$

where the spatial integration from the perturbation term (3.19) has been moved outside of the commutator. The time dependence of the current density operators in the commutator is due to their Heisenberg representation (A6).

Recall that the single-particle current density operator (3.17) can be decomposed as $\hat{\boldsymbol{\jmath}}(\boldsymbol{r}) = \hat{\boldsymbol{\jmath}}^P(\boldsymbol{r}) + \hat{\boldsymbol{\jmath}}^D(\boldsymbol{r})$, where the paramagnetic and diamagnetic parts $\hat{\boldsymbol{\jmath}}^P(\boldsymbol{r})$ and $\hat{\boldsymbol{\jmath}}^D(\boldsymbol{r})$ are independent of and proportional to the electromagnetic vector potential $\boldsymbol{A}(\boldsymbol{r},t)$, respectively. Consider then the two terms of the Kubo formula for current response (3.30). In the first term, the average $\langle \boldsymbol{J}^P(\boldsymbol{r})\rangle$ is zero, as there is no current in the equilibrium ensemble without the application of an electric field. The average $\langle \boldsymbol{J}^D(\boldsymbol{r})\rangle$ however may take on a finite value, being the average over the current density induced by the electric field but averaged over the equilibrium ensemble. In the second term all terms proportional to $\boldsymbol{J}^D(\boldsymbol{r})$ can be neglected, seeing that the Kubo formalism is considered to linear order in the field. Introduce then the *current density autocorrelation function*, hereby referred to simply as the *autocorrelation function*, given by

$$\Pi_{il}(\boldsymbol{r},t;\boldsymbol{x},s) = -\frac{i}{\hbar}\Theta(t-s)\Big\langle \big[\hat{J}_i^P(\boldsymbol{r},t), \hat{J}_l^P(\boldsymbol{x},s)\big]\Big\rangle. \tag{3.31}$$

Like the conductivity tensor, the autocorrelation function is in the stationary case homogeneous in time due to the time independence of the Hamiltonian of

the equilibrium ensemble, and it is homogeneous in space due to the spatial averaging, thus satisfying $\Pi_{il}(\boldsymbol{r},t;\boldsymbol{x},s)=\Pi_{il}(\boldsymbol{r}-\boldsymbol{x},t-s)$. Taking the temporal (3.25) and spatial (3.27) Fouriér transforms, the current response (3.30) becomes

$$J_i(\boldsymbol{q},\omega)=\langle J_i^D(\boldsymbol{q},\omega)\rangle-\sum_l \Pi_{il}(\boldsymbol{q},\omega)A_l(\boldsymbol{q},\omega), \tag{3.32}$$

Notice here that the diamagnetic term (3.17) is dependent on the frequency ω only through its proportionality with the perturbing field $\boldsymbol{A}(\boldsymbol{q},\omega)$.

Comparing the result to the definition of the electromagnetic response function (3.29), the Kubo formula for current response (3.32) implies the function can be split into a diamagnetic part $K_{il}^D(\boldsymbol{q})$ independent on the frequency ω and a paramagnetic part $K_{il}^P(\boldsymbol{q},\omega)$ equal to the current density autocorrelation function $\Pi_{il}(\boldsymbol{q},\omega)$. Recalling that the conductivity tensor (3.28) can be expressed in terms of the electromagnetic response function as $\sigma_{il}(\boldsymbol{q},\omega)=iK_{il}(\boldsymbol{q},\omega)/\omega$, the diamagnetic term of the conductivity is seen to be divergent in the limit $\omega\to 0$. The divergence of the diamagnetic term is the main reason for an infinite conductivity in superconductive materials. Excepting the superconductive case however, the divergence is amended for through an equal but negative sign from the current density autocorrelation function; that is, disregarding superconductivity the diamagnetic term $K_{il}^D(\boldsymbol{q})=-K_{il}^P(\boldsymbol{q},0)=-\Pi_{il}(\boldsymbol{q},0)$. From this reasoning, the *Kubo formula for conductivity* can be expressed

$$\sigma_{il}(\boldsymbol{q},\omega)=\frac{i}{\omega}\Big[\Pi_{il}(\boldsymbol{q},\omega)-\Pi_{il}(\boldsymbol{q},0)\Big] \tag{3.33}$$

Hence, the calculation of the conductivity tensor has been reduced to calculating the current density autocorrelation function (3.31). In particular, for $\boldsymbol{q}=0$ the *direct current conductivity* σ_{il} can be calculated in the $\omega\to 0$ as the derivative

$$\sigma_{il}\equiv\lim_{\omega\to 0}\sigma_{il}(\omega)=\lim_{\omega\to 0}\frac{\Pi_{il}(\omega)-\Pi_{il}(0)}{i\omega}=i\frac{\partial\Pi_{il}}{\partial\omega}\bigg|_{\omega=0}, \tag{3.34}$$

where the uniform conductivity tensor is defined $\sigma_{il}(\omega)\equiv\sigma_{il}(0,\omega)$.

3.2.3 The Matsubara Autocorrelation Function

The current density autocorrelation function (3.31) is an example of a *retarded response function*, being analogous to the retarded Green function (2.17), and can readily be calculated in the framework of the Matsubara method of chapter 2. Performing the spatial Fouriér transform (3.27), introducing imaginary time and denoting the real time argument $\tau=it$, the *Matsubara autocorrelation function*

$$\pi_{il}(\boldsymbol{q},i\omega_m)=-\frac{1}{\hbar}\int_0^{\hbar\beta}\mathrm{d}\tau e^{i\omega_m\tau}\Big\langle\hat{\mathrm{T}}\hat{J}_i^P(\boldsymbol{q},\tau)\hat{J}_l^P(-\boldsymbol{q},0)\Big\rangle. \tag{3.35}$$

Here, the current operators are related to fermionic states, and so are anti-periodic (2.14) with a time translation by $\hbar\beta$. Because the Matsubara autocorrelation function is made up of the product of two such operators, it is

thus periodic with $\hbar\beta$. The frequency ω_m appearing in the expression for the Matsubara autocorrelation function is therefore a bosonic Matsubara frequency (2.15). The current density autocorrelation function (3.31) is then retrieved by the analytical continuation scheme

$$\Pi_{il}(\boldsymbol{q},\omega) = \lim_{i\omega_m \to \omega + i\eta} \pi_{il}(\boldsymbol{q}, i\omega_m), \tag{3.36}$$

which follows from the analysis and derivations of section 2.2.

Inserting the total current density operators (3.13), the Matsubara autocorrelation function (3.35) will involve the average over four fermionic creation and annihilation operators, given by $\langle \hat{\mathrm{T}} \hat{c}^\dagger_\alpha(\tau)\hat{c}_\beta(\tau)\hat{c}^\dagger_\gamma(0)\hat{c}_\delta(0)\rangle$. Assuming the Hamiltonian operator is a single-particle operator, a general average over four operators can be calculated using Wick decomposition (2.31) and written in terms of two-point Matsubara Green functions (2.11), which gives

$$\begin{aligned} &\frac{1}{\hbar^2}\big\langle \hat{\mathrm{T}}\{\hat{c}^\dagger_\alpha(\sigma_1)\hat{c}_\beta(\tau_1)\hat{c}^\dagger_\gamma(\sigma_2)\hat{c}_\delta(\tau_2)\}\big\rangle \\ &\quad = \mathcal{G}_{\beta\alpha}(\tau_1,\sigma_1)\mathcal{G}_{\delta\gamma}(\tau_2,\sigma_2) - \mathcal{G}_{\delta\alpha}(\tau_2,\sigma_1)\mathcal{G}_{\beta\gamma}(\tau_1,\sigma_2) \end{aligned} \tag{3.37}$$

Inserting here $\tau_1 = \sigma_1 = \tau$ and $\tau_2 = \sigma_2 = 0$, the first term is seen to involve the average $\langle J^P_l(-\boldsymbol{q})\rangle$, which is zero; there is no current in the equilibrium ensemble.

Consider then in particular a crystalline system where the Bloch states are labelled by the crystal momentum $\boldsymbol{k}$ in addition to a set of discrete quantum numbers α. Because the Hamiltonian matrix by its definition is diagonalized with respect to the crystal momentum, the average over the two operators

$$-\frac{1}{\hbar}\big\langle \hat{\mathrm{T}}\{\hat{c}_{\boldsymbol{k}_1\alpha}(\tau)\hat{c}^\dagger_{\boldsymbol{k}_2\beta}(\sigma)\}\big\rangle = \mathcal{G}_{\alpha\beta}(\boldsymbol{k}_2,\tau,\sigma)\delta(\boldsymbol{k}_2-\boldsymbol{k}_1) \tag{3.38}$$

where the Matsubara Green function satisfies $\mathcal{G}_{\alpha\beta}(\boldsymbol{k};\tau,\sigma) = \mathcal{G}_{\alpha\beta}(\boldsymbol{k};\tau-\sigma)$ in the stationary case. Inserting then the total current density operator (3.13) into the definition of the Matsubara autocorrelation function (3.35) then leaves

$$\begin{aligned} \pi_{il}(\boldsymbol{q},\tau) &= -\frac{1}{\hbar}\Big\langle \hat{\mathrm{T}}\hat{J}^P_i(\boldsymbol{q},\tau)\hat{J}^P_l(-\boldsymbol{q},0)\Big\rangle \\ &= -\frac{1}{\hbar}\sum_{\substack{\alpha\beta\gamma\delta \\ \boldsymbol{k}_1\boldsymbol{k}_2}} \mathcal{J}_{i,\alpha\beta}(\boldsymbol{k}_1,\boldsymbol{q})\mathcal{J}_{l,\gamma\delta}(\boldsymbol{k}_2,-\boldsymbol{q})\Big\langle \hat{\mathrm{T}}\hat{c}^\dagger_{\boldsymbol{k}_1,\alpha}(\tau)\hat{c}_{\boldsymbol{k}_1+\boldsymbol{q},\beta}(\tau)\hat{c}^\dagger_{\boldsymbol{k}_2,\gamma}(0)\hat{c}_{\boldsymbol{k}_2-\boldsymbol{q},\delta}(0)\Big\rangle. \end{aligned}$$

Using here the Wick decomposition (3.37) followed by the insertion of the average over two operators (3.38), the Matsubara autocorrelation function for a system with discrete translation invariance can thus be written

$$\begin{aligned} \pi_{il}(\boldsymbol{q},\tau) &= \hbar\sum_{\alpha\beta\gamma\delta,\boldsymbol{k}} \mathcal{J}_{i,\alpha\beta}(\boldsymbol{k},\boldsymbol{q})\mathcal{J}_{l,\gamma\delta}(\boldsymbol{k}+\boldsymbol{q},-\boldsymbol{q})\mathcal{G}_{\beta\gamma}(\boldsymbol{k}+\boldsymbol{q},\tau)\mathcal{G}_{\delta\alpha}(\boldsymbol{k},-\tau) \\ &= \hbar\int\frac{\mathrm{d}^d k}{(2\pi)^d}\,\mathrm{Tr}\{\mathcal{J}_i(\boldsymbol{k},\boldsymbol{q})\mathcal{G}(\boldsymbol{k}+\boldsymbol{q},\tau)\mathcal{J}_l(\boldsymbol{k}+\boldsymbol{q},-\boldsymbol{q})\mathcal{G}(\boldsymbol{k},-\tau)\}. \end{aligned} \tag{3.39}$$

Here, $\mathcal{G}(\boldsymbol{k},\tau)$ is the matrix of two-point Matsubara Green functions (2.44) and $\mathcal{J}_i(\boldsymbol{k},\boldsymbol{q})$ the components of the current density matrices (3.14) in the Bloch basis. Notice that the sum over the discrete quantum numbers has been restated as a trace, and the remaining integral is implicitly written over the Brillouin zone.

The Matsubara autocorrelation function (3.35) can now be brought to the frequency domain through a discrete Fouriér transform (2.16), which leaves a discrete convolution between the two Matsubara Green functions. Hence, the Matsubara autocorrelation function can be calculated

$$\pi_{il}(\boldsymbol{q},i\omega_m)=\frac{1}{\beta}\int\frac{\mathrm{d}^d k}{(2\pi)^d}\sum_{\nu_n}\mathrm{Tr}\{\mathcal{J}_i(\boldsymbol{k},\boldsymbol{q})\mathcal{G}(\boldsymbol{k}+\boldsymbol{q},i\nu_n+i\omega_m)\mathcal{J}_l(\boldsymbol{k}+\boldsymbol{q},-\boldsymbol{q})\mathcal{G}(\boldsymbol{k},i\nu_n)\} \tag{3.40}$$

Recall that the frequency $i\omega_m$ is a bosonic Matsubara frequency originating in the definition of the autocorrelation function, whereas the summation frequency $i\nu_n$ is a fermionic Matsubara frequency (2.15) corresponding to the fermionic nature of the matrix of two-point Matsubara Green functions $\mathcal{G}(\boldsymbol{k},i\nu_n)$.

For many applications the spatial dependence of the imposed electric field can be neglected. In particular, whenever the modulations of the electric field extends over several atomic distances of the underlying crystal structure, the conductivity is reasonably approximated by the uniform conductivity tensor $\sigma_{il}(\omega)\equiv\sigma_{il}(0,\omega)$, calculated from the corresponding autocorrelation function

$$\pi_{il}(i\omega_m)=\frac{1}{\beta}\int\frac{\mathrm{d}^d k}{(2\pi)^d}\sum_{\nu_n}\mathrm{Tr}\{\mathcal{J}_i(\boldsymbol{k})\mathcal{G}(\boldsymbol{k},i\nu_n+i\omega_m)\mathcal{J}_l(\boldsymbol{k})\mathcal{G}(\boldsymbol{k},i\nu_n)\}. \tag{3.41}$$

where the current density matrices (3.14) can be calculated $\mathcal{J}_i(\boldsymbol{k})=-e\partial_i\mathcal{H}(\boldsymbol{k})$.

In conclusion, the current density autocorrelation function (3.31) can be calculated as an analytical continuation of the Matsubara autocorrelation function $\pi_{il}(i\omega_m)$, which from its expression (3.35) is dependent on the current density matrices (3.13) and the Matsubara Green matrices (2.44), both of which are dependent only on the Hamiltonian kernel $\mathcal{H}(\boldsymbol{k})$ of the unperturbed system. A conventional path for providing the Hamiltonian kernel of periodic crystalline materials is given by the tightbinding model, which is derived in chapter 4.

The derived Matsubara autocorrelation function (3.41) has been derived for the current density operator matrix elements (3.14) evaluated in the Bloch basis. Hence, the integral over the crystal momentum $\boldsymbol{k}$ is implicitly written over the Brillouin zone of the reciprocal crystal lattice. For many effective models however, only a specific part of the Brillouin zone close to the Fermi surface is considered. The calculation then usually considers the *continuum limit*, where the interatomic distances within the lattice are considered small enough that the Brillouin zone effectively extends to infinity. The continuum limit is a viable simplification with respect to the microscopic averaging over the unit cells, which removes the microscopic details of the crystal lattice.

3.3 The Conductivity for a Single Energy Band

In order to exemplify a calculation using the Kubo formula for conductivity (3.33), the formula is used to derive the Drude conductivity formula for a single energy band. The considered approximations and resulting conductivity formulae are used in the final calculations of the thesis in Part III.

3.3.1 The Single Band Conductivity Formula

Consider a system whose energy spectrum consists of a single energy band denoted $\varepsilon_{\boldsymbol{k}}$. In that case, the current density elements can be calculated as $\mathcal{J}_i(\boldsymbol{k}) = -e\partial_i\varepsilon_{\boldsymbol{k}}/\hbar$, where the notation $\partial_i \equiv \partial/\partial k_i$ is adopted. Inserting this into the formula for the Matsubara autocorrelation function (3.41) then gives

$$\pi_{il}(i\omega_m) = \frac{e^2}{\beta}\int \frac{\mathrm{d}^d k}{(2\pi)^d}\frac{\partial_i\varepsilon_{\boldsymbol{k}}}{\hbar}\frac{\partial_l\varepsilon_{\boldsymbol{k}}}{\hbar}\sum_{\nu_n}\mathcal{G}(\boldsymbol{k}, i\nu_n + i\omega_m)\mathcal{G}(\boldsymbol{k}, i\nu_n), \tag{3.42}$$

Here, the Matsubara Green functions are non-interactive (2.35), such that the sum over Matsubara frequencies can be performed directly using the second Matsubara frequency summation rule (2.38), which gives

$$\frac{1}{\beta}\sum_{\nu_n}\frac{1}{(i\hbar\nu_n - \xi)(i\hbar\nu_n + i\hbar\omega_m - \xi)} = \frac{n_F(\varepsilon - i\hbar\omega_m) - n_F(\varepsilon)}{i\hbar\omega_m}. \tag{3.43}$$

where $n_F(\varepsilon)$ is the Fermi-Dirac distribution function (1.34). Performing then the analytical continuation $i\omega_m \to \omega + i\eta$ where η is an infinitesimal yields the current density autocorrelation function (3.31)

$$\Pi_{il}(\omega) = \frac{e^2}{\hbar}\frac{1}{\omega + i\eta}\int \frac{\mathrm{d}^d k}{(2\pi)^d}\frac{\partial_i\varepsilon_{\boldsymbol{k}}}{\hbar}\frac{\partial_l\varepsilon_{\boldsymbol{k}}}{\hbar}\big[n_F(\varepsilon_{\boldsymbol{k}} - \hbar\omega) - n_F(\varepsilon_{\boldsymbol{k}})\big] \tag{3.44}$$

where the infinitesimal η has been neglected for the second distribution function.

The formula for the single band current density autocorrelation function (3.44) can be simplified further by considering the limit $\mu \gg \hbar\omega$. In that case, the difference of the Fermi-Dirac distributions can be approximated by

$$\frac{1}{\hbar\omega}\big[n_F(\varepsilon - \hbar\omega) - n_F(\varepsilon)\big] \approx -\frac{\partial n_F(\varepsilon)}{\partial\varepsilon} = \frac{\partial n_F(\varepsilon)}{\partial\mu} \tag{3.45}$$

which leaves the expression for the single band autocorrelation function

$$\Pi_{il}(\omega) = \frac{e^2\omega}{\omega + i\eta}\int \frac{\mathrm{d}^d k}{(2\pi)^d}\frac{\partial_i\varepsilon_{\boldsymbol{k}}}{\hbar}\frac{\partial_l\varepsilon_{\boldsymbol{k}}}{\hbar}\frac{\partial n_F(\varepsilon_{\boldsymbol{k}})}{\partial\mu} \tag{3.46}$$

Notice here that the entire dependence on the frequency ω lies outside the integral over momentum. In consequence, the zero frequency limit can be taken,

which by virtue of the infinitesimal gives $\Pi_{il}(0) = 0$. In conclusion, the corresponding conductivity tensor (3.33) can be expressed $\sigma_{il}(\omega) = i\Pi_{il}(\omega)/\omega$, giving

$$\sigma_{il}(\omega) = \frac{e^2}{\eta - i\omega} \int \frac{\mathrm{d}^d k}{(2\pi)^d} \frac{\partial_i \varepsilon_{\boldsymbol{k}}}{\hbar} \frac{\partial_l \varepsilon_{\boldsymbol{k}}}{\hbar} \frac{\partial n_F(\varepsilon_{\boldsymbol{k}})}{\partial \mu}. \tag{3.47}$$

Here, the parameter η can be phenomenologically interpreted as a *scattering rate*, physically originating in impurities in the crystal structure which are absent in the ideally periodic lattice considered. In a more rigorous calculation, the microscopic spatial average considered in the derivation of the contuctivity tensor (3.33) constitute an *impurity average*, and the Matsubara Green functions employed should be exchanged for their impurity averaged counterparts, which in the weak scattering limit would leave a similar result. For the impurity averaged Matsubara Green functions however, the Matsubara frequency summation rules (2.37) cannot be applied directly, and the calculations will involve an analytical continuation into the complex frequency plane. Here and in the following however, the investigations will mostly involve non-zero frequencies ω, for which the impurity scattering is of less importance.

Seeing that the remaining integral over momentum (3.47) serves only as a parameter dependent constant of the particular system, the conductivity can under the current assumptions in general be expressed

$$\sigma_{il}(\omega) = \frac{\sigma_{il}^0}{1 - i\omega/\eta} \tag{3.48}$$

where $\sigma_{il}^0 \equiv \sigma_{il}(0)$ is the direct current conductivity (3.34), whose expression thus depends on the exact form of the integral over momentum.

3.3.2 Kubo Conductivity for Isotropic Energy Bands

In the particular case that the energy is independent on the direction of the crystal momentum, with $\varepsilon_{\boldsymbol{k}} = \varepsilon(k)$, the formula for the conductivity tensor (3.47) can be further simplified. Introducing spherical coordinates such that the differential $\mathrm{d}^d k = k^{d-1} \mathrm{d}k \mathrm{d}\Omega$ with Ω being the solid angle element, then

$$\frac{\partial \varepsilon(k)}{\partial k_i} = \frac{k_i}{k} \frac{\partial \varepsilon(k)}{\partial k} = (\hat{\boldsymbol{k}})_i \frac{\partial \varepsilon(k)}{\partial k},$$

where the expression $k_i/k = (\hat{\boldsymbol{k}})_i$ is independent on the magnitude of the crystal momentum. Furthermore, in the zero temperature limit the Fermi-Dirac distribution (1.34) becomes a Heaviside step function, with the derivative

$$\frac{\partial n_F(\varepsilon)}{\partial \mu} = \frac{\partial}{\partial \mu} \Theta(\mu - \varepsilon(k)) = \delta(\mu - \varepsilon(k)) = \sum_a \frac{\delta(k - k_0^a)}{\left| \frac{\partial \varepsilon}{\partial k}(k_0^a) \right|} \tag{3.49}$$

where k_0^a denote the solutions of the equation $\varepsilon(k_0^a) - \mu = 0$. Inserting these results into the single band Kubo conductivity formula (3.47) thus gives

$$\sigma_{il}(\omega) = \frac{e^2}{\hbar^2}\frac{1}{\eta - i\omega}\int \mathrm{d}k\; k^{d-1}\sum_a \left[\frac{\partial\varepsilon}{\partial k}\right]^2 \frac{\delta(k-k_0^a)}{\left|\frac{\partial\varepsilon}{\partial k}(k_0^a)\right|}\int\frac{\mathrm{d}\Omega}{(2\pi)^d}(\hat{\boldsymbol{k}})_i(\hat{\boldsymbol{k}})_l.$$

Here, the integrals over the magnitude and over the solid angle element has been separated, seeing that the factors k_i/k are the only parts of the integrand being dependent and only dependent on the direction $\hat{\boldsymbol{k}}$ of the crystal momentum. Using hyperspherical coordinates in d dimensions, the solid angle integral is readily seen to be finite only for $i = l$, for which the integral becomes the volume of the unit sphere in d-dimensions, and can be expressed

$$\int \mathrm{d}\Omega(\hat{\boldsymbol{k}})_i(\hat{\boldsymbol{k}})_l = \frac{\pi^{d/2}}{\Gamma(\frac{d}{2}+1)}\delta_{il} \tag{3.50}$$

where $\Gamma(z)$ is the gamma function. Performing then the integration over k using the delta functions, the formula finally becomes

$$\sigma_{il}(\omega) = \frac{\delta_{il}}{2^d\pi^{d/2}\Gamma(\frac{d}{2}+1)}\frac{e^2}{\hbar^2}\frac{1}{\eta - i\omega}\sum_a (k_0^a)^{d-1}\left|\frac{\partial\varepsilon}{\partial k}(k_0^a)\right|. \tag{3.51}$$

Hence, if the energy function is independent on the direction of the crystal momentum $\boldsymbol{k}$, the transverse components of the conductivity are zero.

Consider in particular the free electron case, whose isotropic energy function

$$\varepsilon_{\boldsymbol{k}} = \frac{\hbar^2\boldsymbol{k}^2}{2m}. \tag{3.52}$$

In this case, the equation $\varepsilon(k) - \mu = 0$ has only a single solution, conventionally denoted $k_0^a \equiv k_F = \sqrt{2m\mu}/\hbar$ being the momentum of the electrons residing at the now spherical Fermi surface in momentum space. Inserting these considerations into the obtained conductivity formula for isotropic bands (3.51),

$$\sigma_{il}(\omega) = \frac{\delta_{il}}{\eta - i\omega}\frac{e^2}{m}\frac{1}{(2\pi)^d}\frac{\pi^{d/2}k_F^d}{\Gamma(\frac{d}{2}+1)}.$$

Here, the latter factor is the volume of the Fermi sphere of occupied states in d dimensions. Combined with the factor $1/(2\pi)^d$, this gives the *electron density* n of the crystalline system. In conclusion, the conductivity tensor for free electrons

$$\sigma_{il}(\omega) = \frac{\delta_{il}}{\eta - i\omega}\frac{e^2 n}{m}. \tag{3.53}$$

The derived expression is the celebrated *Drude formula* for conductivity, which originally was derived describing electrons classically using Newtonian physics. The expression holds for certain well behaved crystalline systems in the low-energy limit, as will be derived in chapter 4.

Part II

Topological Band Theory

Chapter 4

The Tightbinding Model

Appendix B introduced the quantum mechanical states describing a solitary electron residing in a periodic lattice potential. For this ideal situation, the electronic wavefunction will be a Bloch function, taking the form of a plane wave modulated by a function periodic with the crystal lattice. In real materials there is instead a myriad of electrons residing on the crystal structure, ideally leaving the system charge neutral. The electrons of the crystalline system will in general mutually interact through the Coulomb interaction, affecting the electronic wavefunctions and the energy band structure of the crystalline system compared to the overtly theoretical single-electron case.

For isolated atoms the electrons arrange in orbitals at different energy levels residing at different proximity to the atomic nucleus. When atoms combine to form crystals, different electrons may likewise be more or less affixed to their nuclei. For many materials the electrons are highly localized around the atomic nuclei of the crystal, such that their mutual interactions can be neglected compared to the interactions with the underlying crystal lattice. This assumption underpins the tightbinding model, which is the theme of the current chapter.

The tightbinding model allows for a calculation of the Hamiltonian kernel for crystalline systems, revealing the energy band structure of the electrons. In particular, under the assumptions of a single valence orbital and nearest neighbour interactions the Hamiltonian becomes solely dependent on the crystal structure. From the derivation of a general tightbinding Hamiltonian, the model is exemplified by calculating the energy band structure for a square lattice and for the two dimensional carbon-based material graphene.

For graphene, the low-energy effective Hamiltonian takes on the same shape as the Weyl Hamiltonian describing relativistic fermions of quantum field theory. This makes graphene an example of a two dimensional Weyl semimetal, a class of materials whose emergence and description are investigated in chapter 6. The derived graphene Hamiltonian will also be used to exemplify calculations of berryological quantities in chapter 5.

4.1 The Tightbinding Approximation

Consider a large collection of electrons residing in a crystal lattice (B8), with the single-electron Hamiltonian (B14) of appendix B giving the energy contribution for each individual electron and describing the interaction with the underlying crystal lattice. In general, the interactions between the different electrons must additionally be taken into account, modelled by the Coulomb interaction $V(\boldsymbol{r})$. The Hamiltonian describing the crystalline system then becomes

$$\hat{H} = \sum_{\iota} \left[\frac{\hat{\boldsymbol{p}}_{\iota}^{2}}{2m} + \hat{U}(\hat{\boldsymbol{r}}_{\iota}) \right] + \sum_{\iota,\kappa} \hat{V}(\hat{\boldsymbol{r}}_{\iota} - \hat{\boldsymbol{r}}_{\kappa}), \tag{4.1}$$

where $\hat{\boldsymbol{r}}_{\iota}$ and $\hat{\boldsymbol{p}}_{\iota}$ are the position and momentum operators of electron ι, and the sums are over all the electrons of the system. The potential from the underlying crystal structure is periodic with the crystal lattice, satisfying $U(\boldsymbol{r}+\boldsymbol{R}_i) = U(\boldsymbol{r})$, with $\boldsymbol{R}_i$ being a lattice vector (B8) as explained in appendix B.

In the following, the tightbinding Hamiltonian is derived from the basic Hamiltonian (4.1) above using the second quantization scheme (1.9) with single-electron states based on the discussions of appendix B. The resulting tightbinding model is then exemplified in sections 4.2 and 4.3 by calculating the energy bands of a square lattice and of graphene, respectively.

4.1.1 Tightbinding Hamiltonian in the Wannier Basis

In the tightbinding model the electrons are assumed tightly bound to the individual atoms, interacting only weakly with the surrounding atoms and electrons through quantum tunnelling between different primitive unit cells. In this case the electron-electron interactions can be neglected, such that the remaining Hamiltonian (4.1) consists only of a sum of single-electron terms $\hat{\mathfrak{h}}_{\iota}$. In the second quantization scheme, the Hamiltonian (4.1) describing the electron ensemble thus becomes a single-particle operator (1.9), with expansion coefficients given by the matrix elements of the single-electron Hamiltonian (B14) denoted $\hat{\mathfrak{h}}$.

The eigenfunctions of the single-electron Hamiltonian $\hat{\mathfrak{h}}$ are the Bloch states (B18) denoted by $|\psi_{n\boldsymbol{k}}\rangle$, with n denoting the band index and $\boldsymbol{k}$ being the crystal momentum. Consider then the crystal lattice being a Bravais lattice, with only a single atom in each unit cell. In that case, the electronic orbitals at at the atomic nucleus located at $\boldsymbol{R}_i$ will then be the Wannier states (B23) denoted by $|w_{ni}\rangle$, related to the Bloch states through the lattice Fouriér transforms

$$|\psi_{n\boldsymbol{k}}\rangle = \sum_{i} e^{i\boldsymbol{k}\cdot\boldsymbol{R}_i} |w_{ni}\rangle \qquad |w_{ni}\rangle = V_C \int_{\mathrm{BZ}} \mathrm{d}^d k \; e^{-i\boldsymbol{k}\cdot\boldsymbol{R}_i} |\psi_{n\boldsymbol{k}}\rangle \,. \tag{4.2}$$

Here, V_C denotes the volume of the primitive unit cell of the crystal lattice and the crystal momentum is integrated over the first Brillouin zone. For the Wannier states, the quantum number n is interpreted as an orbital index, labelling the different types of electronic orbitals found at each individual lattice site.

The Wannier states (4.2) can be orthonormalized (B25) and comprise a complete set of basis states. The matrix elements of the single-electron Hamiltonian (B14) can thus be expanded in the Wannier basis as

$$-t_{ij}^{nm} \equiv \langle w_{ni}| \hat{\mathfrak{h}} |w_{mj}\rangle = \int \mathrm{d}^3 r \; w_{ni}^*(\boldsymbol{r}) \Big[-\frac{\hbar^2}{2m}\nabla^2 + U(\boldsymbol{r}) \Big] w_{mj}(\boldsymbol{r}). \tag{4.3}$$

Here, the crystal is assumed to be magnetically trivial such that any interaction between the spins of the electrons and the atomic nuclei can be neglected. The incorporation of discrete quantum numbers is investigated in the following.

Introducing then the creation and annihilation operators (1.6) for the Wannier state $|w_{ni}\rangle$ denoted by $\hat{c}_{ni}^\dagger$ and $\hat{c}_{ni}$ respectively, the second quantized form of the Hamiltonian (4.1) describing the non-interactive electron ensemble becomes

$$\hat{H} = -\sum_{i,j,n,m} t_{ij}^{nm} \hat{c}_{ni}^\dagger \hat{c}_{mj} \tag{4.4}$$

The expression gives a natural physical interpretation of the matrix element, in the following referred to as the *tunnelling rate*: the tunneling rate t_{ij}^{nm} is the amplitude corresponding to an electron quantum tunnelling from an orbital of type m at lattice site $\boldsymbol{R}_j$ to an orbital of type n at lattice site $\boldsymbol{R}_i$.

Consider in particular the lattice elements on the form $t_{ii}^{nn} \equiv \mu_{ni}$. The corresponding operator $\hat{c}_{ni}^\dagger \hat{c}_{ni}$ is a number operator, counting the number of electrons in the single-electron state $|w_{ni}\rangle$ to either 0 or 1. As such, μ_{ni} can be interpreted as the *on-site energy* for an electron in orbital n at lattice site i, which acts as a chemical potential. Separating these terms from the sum (4.4) leaves the final form of the Hamiltonian for Bravais lattices

$$\hat{H} = -\sum_{ni,mj} t_{ij}^{nm} \hat{c}_{ni}^\dagger \hat{c}_{mj} - \sum_{n,i} \mu_{ni} \hat{c}_{ni}^\dagger \hat{c}_{ni}. \tag{4.5}$$

The former sum runs implicitly over terms with $n \neq m$ and $i \neq j$ simultaneously. Other than neglecting the mutual interactions between the electrons of the crystal, the derived Hamiltonian describes the crystalline system exactly.

For many crystalline systems, the single outermost electron orbital $n = o$ will be the main contributor to interactions. Such a single-orbital approximation is incorporated into the tunnelling rate by letting $t_{ij}^{nm} \equiv t_{ij}\delta_{no}\delta_{mo}$. The sum over orbital indices in the Hamiltonian (4.5) thus leaves only the creation and annihilation operators for this single orbital, rewritten $\hat{c}_{oi}^\dagger \equiv \hat{c}_i^\dagger$ and $\hat{c}_{oi} \equiv \hat{c}_i$.

Furthermore, from the expression of the Wannier wavefunctions (B23) by virtue of the Bloch theorem (B16), the electronic Wannier orbitals $w_{ni}(\boldsymbol{r})$ are seen to decay away from their lattice site $\boldsymbol{R}_i$. In the *tightbinding approximation*, the decay is assumed fast enough such that the electrons can be considered localized around the individual atomic nuclei, leaving the Wannier functions centered at different lattice sites $\boldsymbol{R}_i$ and $\boldsymbol{R}_j$ with negligible overlaps. Seeing that the single-band tunnelling rate (4.3) is dependent only on the distance between

the lattice sites $t_{ij} \equiv t(\boldsymbol{R}_i - \boldsymbol{R}_j)$, a suitable approximation is to consider only tunnelling between nearest neighbouring lattice sites, denoted $\langle i, j \rangle$.

Within the single-band and tightbinding approximations, the derived Hamiltonian (4.5) takes the form of the *tightbinding Hamiltonian*

$$\hat{H} = -\sum_{\langle i,j \rangle} t_{ij} \hat{c}_i^\dagger \hat{c}_j - \sum_i \mu_i \hat{c}_i^\dagger \hat{c}_i, \tag{4.6}$$

where the on-site energy $t_{ii} \equiv \mu_i$. Due to the non-diagonal matrix elements t_{ij} the tightbinding Hamiltonian (4.6) is not diagonalized. Recall then that the Bloch states are defined as the eigenstates of the single-electron Hamiltonian (B14). Hence, with a Bravais crystal lattice the tightbinding Hamiltonian will be diagonalized through a change from the Wannier to the Bloch basis. This is performed by introducing the Bloch creation and annihilation operators $\hat{c}_{n\boldsymbol{k}}^\dagger$ and $\hat{c}_{n\boldsymbol{k}}$ respectively, related to the Wannier creation and annihilation operators from the relation between the Bloch and Wannier states (4.2) as

$$\begin{aligned} \hat{c}_{n\boldsymbol{k}}^\dagger &= \sum_i e^{i\boldsymbol{k}\cdot\boldsymbol{R}_i} \hat{c}_{ni}^\dagger \qquad & \hat{c}_{n\boldsymbol{k}} &= \sum_i e^{-i\boldsymbol{k}\cdot\boldsymbol{R}_i} \hat{c}_{ni} \\ \hat{c}_{ni}^\dagger &= V_C \int_{\mathrm{BZ}} \frac{\mathrm{d}^d k}{(2\pi)^d}\, e^{-i\boldsymbol{k}\cdot\boldsymbol{R}_i} \hat{c}_{n\boldsymbol{k}}^\dagger \qquad & \hat{c}_{ni} &= V_C \int_{\mathrm{BZ}} \frac{\mathrm{d}^d k}{(2\pi)^d}\, e^{i\boldsymbol{k}\cdot\boldsymbol{R}_i} \hat{c}_{n\boldsymbol{k}} \end{aligned} . \tag{4.7}$$

This change of basis will reveal the electronic band structure of the system, from which many of the physical properties of the crystal can be calculated. The exact band structure will however depend on the structure of the lattice, exemplified by the tightbinding calculations of the square lattice in section 4.2.

4.1.2 Tightbinding with a Polyatomic Primitive Unit Cell

Consider then instead a non-Bravais crystal lattice where each primitive unit cell comprise a number of W atomic nuclei, located at the relative positions $\boldsymbol{r}_\alpha$. For a Bravais lattice, where each primitive unit cell consists of only a single atomic nucleus, each electron can be described by a Wannier state (4.2) corresponding to a highly localized electronic orbital at a specific lattice point. For a polyatomic unit cell, it can similarly be postulated that each electron will reside in highly localized orbitals around a specific atomic nucleus α of the primitive unit cell. In general, there will be a number of possible electronic orbitals at each of the atomic nuclei within each primitive unit cell. For simplicity however, adopt the single-orbital approximation and consider only a single electronic orbital at each of the atomic nuclei within each primitive unit cell.

Denote by $|\phi_{i\alpha}\rangle$ the quantum state corresponding to the single electronic orbital at the atomic nucleus labelled α residing in the primitive unit cell located at $\boldsymbol{R}_i$. These states are then analogous to the Wannier states of a Bravais crystal lattice. Introduce also the *Bloch sums*, given by the transformations

$$|\chi_{\boldsymbol{k}\alpha}\rangle = \sum_i e^{i\boldsymbol{k}\cdot(\boldsymbol{R}_i+\boldsymbol{r}_\alpha)}\,|\phi_{i\alpha}\rangle \qquad |\phi_{i\alpha}\rangle = V_C \int_{\mathrm{BZ}} \mathrm{d}^d k\; e^{-i\boldsymbol{k}\cdot(\boldsymbol{R}_i+\boldsymbol{r}_\alpha)}\,|\chi_{\boldsymbol{k}\alpha}\rangle \quad (4.8)$$

analogous to the transformations between the Bloch and Wannier bases (4.2). In the position representation, the Bloch sums $\chi_{\boldsymbol{k}\alpha}(\boldsymbol{r}) = \langle \boldsymbol{r}|\chi_{\boldsymbol{k}\alpha}\rangle$ are readily seen to satisfy the Bloch theorem (B16) with $\chi_{\boldsymbol{k}\alpha}(\boldsymbol{r}-\boldsymbol{R}_i) = e^{i\boldsymbol{k}\cdot\boldsymbol{R}_i}\chi_{\boldsymbol{k}\alpha}(\boldsymbol{r})$, and are thus eigenfunctions of the discrete translation operator. In fact, seeing that the reciprocal lattice of the crystal lattice is dependent only on the underlying Bravais lattice and not on the arrangement of the atomic nuclei within the primitive unit cell, the crystal momentum $\boldsymbol{k}$ originates by the exact same discrete translation invariance as for the Bloch states $|\psi_{n\boldsymbol{k}}\rangle$. Even so, the Bloch sums may not be eigenfunctions of the single-electron Hamiltonian (B14).

By the analysis of Lödwin [18], the Bloch eigenfunctions of the single-electron Hamiltonian are postulated to be expressed in terms of Bloch sums (4.8) as

$$|\psi_{\boldsymbol{k}}\rangle = \sum_{\alpha=1}^{W} \psi_\alpha(\boldsymbol{k})\,|\chi_{\boldsymbol{k}\alpha}\rangle\,, \quad (4.9)$$

where the sum is over the different atomic nuclei α of the primitive unit cell. Consider then the eigenvalue equation of the single-electron Hamiltonian (B14), written $\hat{\mathfrak{h}}\,|\psi_{\boldsymbol{k}}\rangle = \varepsilon_{\boldsymbol{k}}\,|\psi_{\boldsymbol{k}}\rangle$. Assuming the Bloch sums are normalized to unity but not necessarily orthogonal, inserting the postulated Bloch function and left multiplying by the state $\langle\chi_{\boldsymbol{k}\beta}|$ then leaves the eigenvalue equation

$$\sum_\alpha \mathcal{H}_{\beta\alpha}(\boldsymbol{k})\psi_\alpha(\boldsymbol{k}) = \varepsilon_{\boldsymbol{k}} \sum_\alpha \mathcal{S}_{\beta\alpha}(\boldsymbol{k})\psi_\alpha(\boldsymbol{k}). \quad (4.10)$$

The equation introduces the matrix elements of the *Hamiltonian kernel* $\mathcal{H}$ and the *overlap matrix* $\mathcal{S}$, respectively defined by $\mathcal{H}_{\beta\alpha}(\boldsymbol{k}) = \langle\chi_{\beta\boldsymbol{k}}|\,\hat{\mathfrak{h}}\,|\chi_{\boldsymbol{k}\alpha}\rangle$ and $\mathcal{S}_{\beta\alpha}(\boldsymbol{k}) = \langle\chi_{\boldsymbol{k}\beta}|\chi_{\boldsymbol{k}\alpha}\rangle$. Denoting also by $\boldsymbol{\psi}(\boldsymbol{k})$ the vector whose elements are the expansion coefficients $\psi_\alpha(\boldsymbol{k})$, the eigenvalue equation for the Hamiltonian $\hat{\mathfrak{h}}$ has been rewritten to the matrix equation $\mathcal{H}(\boldsymbol{k})\boldsymbol{\psi}(\boldsymbol{k}) = \varepsilon_{\boldsymbol{k}}\mathcal{S}(\boldsymbol{k})\boldsymbol{\psi}(\boldsymbol{k})$.

In general, the electronic orbitals situated at different atomic nuclei will not be orthogonal, with nearby orbitals having some spatial overlap. In the tightbinding approximation however, the orbitals are assumed highly localized around each respective atomic nucleus, and the overlaps can be considered negligible. In that case, the different Bloch sums $|\chi_{\boldsymbol{k}\alpha}\rangle$ can be approximated as orthogonal for different α, and the expansion coefficients of the Bloch function (4.9) can be expressed $\psi_\alpha(\boldsymbol{k}) = \langle\chi_{\boldsymbol{k}\alpha}|\psi_{\boldsymbol{k}}\rangle$. The overlap matrix $\mathcal{S}_{\beta\alpha}(\boldsymbol{k}) = \langle\chi_{\boldsymbol{k}\beta}|\chi_{\boldsymbol{k}\alpha}\rangle$ is thus approximated diagonal, and the eigenvalue equation for the single-electron Hamiltonian (B14) can be expressed

$$\mathcal{H}(\boldsymbol{k})\boldsymbol{\psi}(\boldsymbol{k}) = \varepsilon_{\boldsymbol{k}}\boldsymbol{\psi}(\boldsymbol{k}). \quad (4.11)$$

Hence, under the tightbinding approximation the energy band spectrum $\varepsilon_{\boldsymbol{k}}$ will be given by the eigenvalues of the Hamiltonian kernel $\mathcal{H}(\boldsymbol{k})$, with the corresponding Bloch states being expanded in Bloch sums (4.8) with the expansion

coefficients given by the eigenvectors of the Hamiltonian kernel $\boldsymbol{\psi}(\boldsymbol{k})$. Both the eigenvalues and eigenfunctions can thus be labelled by the index α as $\varepsilon_{\boldsymbol{k}\alpha}$ and $\boldsymbol{\psi}_\alpha(\boldsymbol{k})$ respectively, which serves as a band index even under the single-orbital approximation. Hence, the introduction of localized orbitals at each of the atomic nuclei in the primitive unit cell thus corresponds to the introduction of a discrete degree of freedom, termed the *orbital degree of freedom*.

For non-Bravais lattices, a tightbinding Hamiltonian analogous to the tightbinding Hamiltonian for Bravais lattices (4.6) can be devised by expanding the single-electron Hamiltonian (B14) in the orbital basis spanned by the states $|\phi_{i\alpha}\rangle$. The resulting matrix elements $-t_{ij}^{\alpha\beta} \equiv \langle\phi_{i\alpha}|\,\hat{\mathfrak{h}}\,|\phi_{j\beta}\rangle$ are again interpreted as tunnelling rates (4.3), here describing the quantum tunnelling of an electron from the atomic nucleus localized at $\boldsymbol{R}_j + \boldsymbol{r}_\beta$ to the atomic nucleus located at $\boldsymbol{R}_i + \boldsymbol{r}_\alpha$. Recall here that the discussion at hand is within the single-orbital approximation; if several types of atomic orbitals are considered for each atomic nucleus, two more indices will be added to the tunnelling rate.

Introducing then the creation and annihilation operators $\hat{c}_{i\alpha}^\dagger$ and $\hat{c}_{i\alpha}$ corresponding to the quantum states $|\phi_{i\alpha}\rangle$, the tightbinding Hamiltonian for non-Bravais lattices within the single-orbital approximation thus takes the form

$$\hat{H} = -\sum_{i\alpha,j\beta} t_{ij}^{\alpha\beta}\hat{c}_{i\alpha}^\dagger\hat{c}_{j\beta} - \sum_{i\alpha}\mu_{i\alpha}\hat{c}_{i\alpha}^\dagger\hat{c}_{i\alpha}, \tag{4.12}$$

where as before the chemical potentials $\mu_{i\alpha} \equiv t_{ii}^{\alpha\alpha}$ have been extracted. The derived form of the Hamiltonian is identical to the general Hamiltonian (4.5) for a Bravais lattice. Here however, the index α refers to the different atomic nuclei of the primitive unit cell, and not to the different orbitals on a single atomic nucleus. Furthermore, the Hamiltonian is here expanded in the orbital basis $|\phi_{i\alpha}\rangle$, and not the Wannier basis $|w_{ni}\rangle$ as in the Bravais case.

From appendix B, the reciprocal lattice of a crystal lattice is dependent only on the underlying real space Bravais lattice, and not on the arrangement of atomic nuclei within the primitive unit cell. In consequence, the creation and annihilation operators $\hat{c}_{i\alpha}^\dagger$ and $\hat{c}_{i\alpha}$ can be written in terms of creation and annihilation operators of the Bloch sums (4.8) denoted $\hat{c}_{\boldsymbol{k}\alpha}^\dagger$ and $\hat{c}_{\boldsymbol{k}\alpha}$, as

$$\hat{c}_{i\alpha}^\dagger = V_C\int_{\mathrm{BZ}}\frac{\mathrm{d}^d k}{(2\pi)^d}e^{-i\boldsymbol{k}\cdot(\boldsymbol{R}_i+\boldsymbol{r}_\alpha)}\hat{c}_{\boldsymbol{k}\alpha}^\dagger \qquad \hat{c}_{i\alpha} = V_C\int_{\mathrm{BZ}}\frac{\mathrm{d}^d k}{(2\pi)^d}e^{i\boldsymbol{k}\cdot(\boldsymbol{R}_i+\boldsymbol{r}_\alpha)}\hat{c}_{\boldsymbol{k}\alpha} \tag{4.13}$$

In this case however, a change of basis from the orbital basis $|\phi_{i\alpha}\rangle$ to the Bloch sum basis $|\chi_{i\alpha}\rangle$ will not diagonalize the Hamiltonian, but instead reveal the Hamiltonian kernel (4.11) of the system. For W atomic nuclei in the primitive unit cell, a diagonalization corresponding to a change to the proper Bloch basis $|\psi_{\boldsymbol{k}\alpha}\rangle$ will then reveal W energy bands of the energy band spectrum.

Finally, it should be noted that the set of indices α may incorporate other quantum numbers than the specific atomic nucleus within the primitive unit cell. In chapter 6, the electron spin is taken into account, which doubles the dimensionality of the Hamiltonian kernel (4.11) compared to the spinless case.

4.2 Tightbinding Model for a Square Lattice

In the following, a general expression for the energy band structure of Bravais crystal lattices is derived, as a continuation on the calculation of the Bravais tightbinding model (4.6) in section 4.1. From this, the energy band structure of a square lattice is calculated and then expanded in the low-energy regime.

4.2.1 Tightbinding Calculation for a Bravais Lattice

For Bravais crystal lattices, the crystalline system is homogeneous at the level of atomic nuclei. Then, all lattice sites are equivalent excepting a translation, leaving the tightbinding parameters $t_{ij} \equiv t_j$ and $\mu_i \equiv \mu$ equal for all lattice sites. Introduce also the vector $\boldsymbol{\delta}_j$ running through all nearest neighbours. Two neighbouring lattice vectors can then be related by $\boldsymbol{R}_j = \boldsymbol{R}_i + \boldsymbol{\delta}_j$, and the nearest-neighbour sum of the tightbinding Hamiltonian (4.6) is split into a sum over all lattice sites $\boldsymbol{R}_i$ and a sum over the nearest neighbour vectors $\boldsymbol{\delta}_j$.

The Hamiltonian (4.6) is rewritten in the Bloch basis by inserting the Bloch transforms of the creation and annihilation operators (4.7). Using the lattice orthogonality relations (B13), the nearest-neighbour sum can then be expressed

$$\begin{aligned}
&\sum_i \sum_j t_j V_C \int_{\mathrm{BZ}} \frac{\mathrm{d}^d k_1}{(2\pi)^d} \hat{c}^\dagger_{\boldsymbol{k}_1} e^{-i\boldsymbol{k}_1 \cdot \boldsymbol{R}_i} V_C \int_{\mathrm{BZ}} \frac{\mathrm{d}^d k_2}{(2\pi)^d} \hat{c}_{\boldsymbol{k}_2} e^{i\boldsymbol{k}_2 \cdot (\boldsymbol{R}_i + \boldsymbol{\delta}_j)} \\
&= V_C^2 \int_{\mathrm{BZ}} \frac{\mathrm{d}^d k_1}{(2\pi)^d} \frac{\mathrm{d}^d k_2}{(2\pi)^d} \hat{c}^\dagger_{\boldsymbol{k}_1} \hat{c}_{\boldsymbol{k}_2} \sum_i e^{i(\boldsymbol{k}_2 - \boldsymbol{k}_1)\cdot \boldsymbol{R}_i} \sum_j t_j e^{i\boldsymbol{k}_2 \cdot \boldsymbol{\delta}_j} \equiv \sum_{\boldsymbol{k}} \phi(\boldsymbol{k}) \hat{c}^\dagger_{\boldsymbol{k}} \hat{c}_{\boldsymbol{k}}.
\end{aligned}$$

Here, the last sum is conventionally written over reciprocal vectors $\boldsymbol{k}$ within the Brillouin zone. The expression introduces the *structure factor* of the lattice,

$$\phi(\boldsymbol{k}) = \sum_j t_j e^{i\boldsymbol{k}\cdot\boldsymbol{\delta}_j}, \tag{4.14}$$

which under the current approximations is the only part of the tightbinding Hamiltonian dependent on the spatial structure of the crystalline system. Notice here that the structure factor will be a real quantity, as both $\boldsymbol{\delta}_j$ and $-\boldsymbol{\delta}_j$ will be nearest-neighbour vectors for any Bravais lattice.

Seeing that the chemical potential term (4.6) is diagonalized by default, the tightbinding Hamiltonian of a general Bravais lattice can be expressed

$$H = -\sum_{\boldsymbol{k}} \phi(\boldsymbol{k}) \hat{c}^\dagger_{\boldsymbol{k}} \hat{c}_{\boldsymbol{k}} - \mu \sum_{\boldsymbol{k}} \hat{c}^\dagger_{\boldsymbol{k}} \hat{c}_{\boldsymbol{k}} \equiv \sum_{\boldsymbol{k}} \varepsilon(\boldsymbol{k}) \hat{c}^\dagger_{\boldsymbol{k}} \hat{c}_{\boldsymbol{k}}. \tag{4.15}$$

As foretold, expressing the Hamiltonian in the Bloch basis leaves it diagonal, and reveals the energy band structure of the electrons in a Bravais crystal lattice

$$\varepsilon(\boldsymbol{k}) = -\phi(\boldsymbol{k}) - \mu. \tag{4.16}$$

The chemical potential μ acts as a constant shift in energy, and serves the same physical role as the chemical potential of the Fermi-Dirac distribution (1.34).

4.2.2 Square Lattice Energy Band Structure

Consider a d-dimensional regular square lattice with lattice spacing a, shown in figure 4.1 together with its reciprocal lattice for $d = 2$. There are $2d$ nearest neighbours to each lattice point with nearest neighbour vectors $\boldsymbol{\delta}_j \in \{\pm a\hat{\boldsymbol{x}}_l\}_{l=1}^{d}$. Due to the isotropy of the lattice, the tunnelling rate is equal for all sites: $t_j \equiv t$.

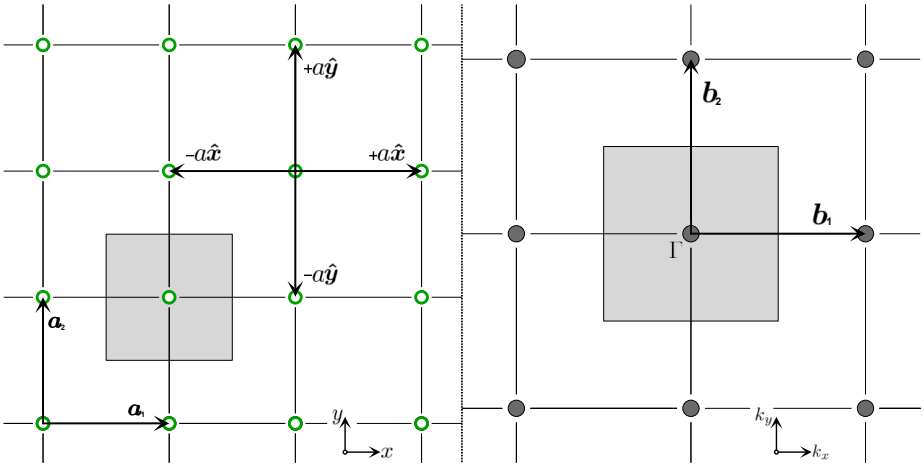

Figure 4.1: Square Bravais lattice in two dimensions. The left figure shows the real space square lattice with lattice constant a, primitive lattice vectors $\boldsymbol{a}_1$ and $\boldsymbol{a_2}$, and all nearest neighbour vectors. The right figure shows the reciprocal lattice, with primitive lattice vectors $\boldsymbol{b}_1$ and $\boldsymbol{b}_2$ of length $2\pi/a$. The shaded gray areas shows the real Wigner-Seitz cell and reciprocal Brillouin zone, respectively, the latter of which has a critical point at its center Γ.

The square lattice is a Bravais lattice with a single atomic nucleus in each primitive unit cell, as seen in the Wigner-Seitz cell of figure 4.1. Inserting the nearest neighbour vectors, the corresponding structure factor (4.14) becomes

$$\phi(\boldsymbol{k}) = \sum_{l=1}^{d} \left[te^{iak_l} + te^{-iak_l} \right] = 2t \sum_{l=1}^{d} \cos(ak_l).$$

Inserting this structure factor into the energy band for Bravais lattices (4.16) gives the expression for the single electronic energy band

$$\varepsilon(\boldsymbol{k}) = -2t \sum_{l=1}^{d} \cos(ak_l) - \mu. \tag{4.17}$$

Notice that this function is invariant under the point symmetries of the square lattice, and under translations by the reciprocal lattice vectors $\boldsymbol{b}_m = \frac{2\pi}{a}\hat{\boldsymbol{k}}_m$. The energy band for the square lattice is shown in figure 4.2 for $d = 2$. The geometrical shape is typical for that of a *conduction band*, the lowest vacant energy band at zero temperature. If more single-electron orbitals had been taken into account in the tightbinding model, both vacant and occupied energy bands above and below the conduction band would emerge in the calculations.

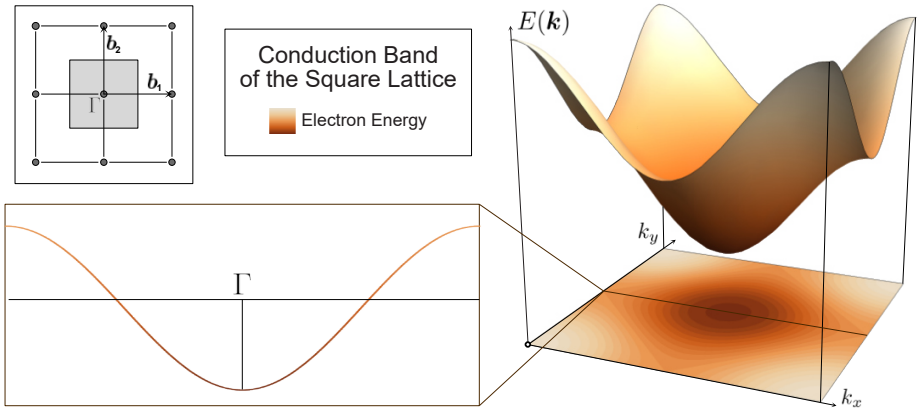

Figure 4.2: The electron energy band structure for the square Bravais lattice in two dimensions in the single-band approximation of the tightbinding model. The energy band is calculated for crystal momenta $\boldsymbol{k}$ inside the Brillouin zone, given on the upper left, and is periodic with the reciprocal lattice vectors $\boldsymbol{b}_1$ and $\boldsymbol{b}_2$. An intersection of the band at $k_y = 0$ displays the cosine form of the band on the lower left, giving rise to an effective mass.

At the ground state of the system the conduction band will be vacant. For low but non-zero temperatures however, some electrons will have the energy to occupy electronic states in the vicinity of the conduction band minimum. The minimum of the conduction band (4.17) is at the center Γ of the Brillouin zone, at the energy $\varepsilon_0 \equiv \varepsilon(\boldsymbol{k} = 0) = -2td - \mu$. Expanding the cosine-functions about this minimum leaves $\cos(ak_l) \approx 1 - a^2k_l^2/2$, such that for low energies

$$\varepsilon(\boldsymbol{k}) \approx -2t\sum_{l=1}^{d}(1 - \frac{1}{2}a^2k_l^2) - \mu = \varepsilon_0 + ta^2\boldsymbol{k}^2 \equiv \varepsilon_0 + \frac{\hbar^2\boldsymbol{k}^2}{2m^*}. \tag{4.18}$$

Here, $m^* \equiv \hbar^2/2ta^2$ is the *effective mass* of the electrons near the energy minimum; comparing the expansion above (4.18) to the free electron dispersion relation (3.52), then near the conduction band minimum the electrons behave as if they were free electrons but with a renormalized mass m^*.

The expansion condition $ka \ll 1$ translates to the wavelength of the electron being much longer than the interatomic distance. The apparent free electron behaviour at low temperatures thus allows for a simple physical interpretation: if the wavelength of the electron is much larger than the modulations of the underlying periodic crystal potential, the electrons are effectively unaffected by the crystal potential and hence can be mathematically described as free electrons, but with a renormalized mass. Notice that this effective mass m^* is inversely proportional to t; if the tunnelling rate is large, meaning tunnelling between atoms is more recurrent, the effective mass is smaller. It is also smaller for a longer lattice spacing a, being the distance the electron is transported for each tunnelling event between neighbouring atoms.

4.3 Tightbinding Model for Graphene

Carbon is the sixth element of the periodic table, with four electrons residing in the two lowest s-orbitals denoted $1s$ and $2s$, and two electrons distributed among the three $2p$-orbitals. When atoms of carbon are forced to bond in a two dimensional plane, the $2s$-orbital and two of the $2p$-orbitals hybridize to form three sp^2-orbitals, forming a two-dimensional hexagonal crystal structure known as *graphene*. Pure graphene has been known theoretically for many decades, but was not experimentally isolated until 2004 by Novoselov and Geim [19]. The electrons residing in the remaining $2p$-orbitals of the atoms interact with eachother to form π-bonds, which in combination with the hexagonal crystal structure gives graphene many exotic electronic properties.

This subsection derives a tightbinding model for diatomic primitive unit cells in general, and then applies this model to the π-bonds of graphene; the electrons of the sp^2-orbitals are too tightly bound to contribute to the conductive properties of the material. The crystal lattice in question then refers to the spatial configuration of these single $2p$-orbitals of the carbon atoms in the graphene sheet, as these electrons are the ones responsible for the electronic properties. Hereafter, there will be no further reference to the origins of the atomic orbitals.

4.3.1 Tightbinding with a Diatomic Primitive Unit Cell

Consider now a crystal with a diatomic primitive unit cell, where the two atoms are separated by some distance a. The lattice will then be a *bipartite lattice*, meaning the lattice can be separated into two sublattices A and B such that all nearest neighbours of sublattice A lies in sublattice B and vice versa. Denote by $\hat{c}_{ia}^\dagger$ and $\hat{c}_{ia}$ the creation and annihilation operators of electrons in sublattice A, and by $\hat{c}_{ib}^\dagger$ and $\hat{c}_{ib}$ the creation and annihilation operators of electrons in sublattice B, as introduced in section 4.1. The two labels a and b here constitute the orbital degree of freedom for the diatomic primitive unit cell.

Let then the denotation $\langle a, b\rangle$ signify two nearest-neighbouring atomic nuclei of the diatomic bipartite lattice, whether part of the same or different primitive unit cells. By separating the sum over the entire lattice into two sublattice sums, the non-Bravais tightbinding Hamiltonian (4.12) can then be written

$$\hat{H} = -\sum_{i,j,\langle a,b\rangle} t_j^{ab} \hat{c}_{ia}^\dagger \hat{c}_{jb} - \sum_{i,j,\langle a,b\rangle} t_j^{ba} \hat{c}_{ib}^\dagger \hat{c}_{ja} - \sum_i \mu_{ia} \hat{c}_{ia}^\dagger \hat{c}_{ia} - \sum_i \mu_{ib} \hat{c}_{ib}^\dagger \hat{c}_{ib}, \qquad (4.19)$$

where again the system is isotropic at the level of primitive unit cells, such that the tunnelling rates $t_{ij}^{ab} = t_j^{ab}$ and chemical potentials $\mu_{ia} = \mu_a$ for each of the two sublattices. Notice that for this Hamiltonian to be hermitian, satisfying $\hat{H}^\dagger = \hat{H}$, the tunnelling rates t_j^{ab} must be equal to the complex conjugate of the tunnelling rate t_j^{ba}, denoted $t_j^{ab} = (t_j^{ba})^* \equiv t_j$. If this had not been the case, there would be a higher rate of electrons tunnelling to lattice sites in one of the sublattices, and the crystal would not be stable. This is also clear from

the definition of the tunnelling rate (4.3), which in addition shows that the tunnelling rate t_j is a real parameter for the model at hand.

Introduce then the nearest-neighbouring vectors $\boldsymbol{\delta}_{aj}$ and $\boldsymbol{\delta}_{bj}$ running through nearest-neighbouring atomic nuclei for lattice points in the sublattices A and B respectively. The vector $\boldsymbol{\delta}_{aj}$ are then defined by $\boldsymbol{R}_j + \boldsymbol{r}_b = \boldsymbol{R}_i + \boldsymbol{r}_a + \boldsymbol{\delta}_{aj}$, with $\boldsymbol{r}_\alpha$ being the relative positions of the atomic nuclei within the primitive unit cell. Inserting the operators of the Bloch sum basis (4.13) and using the lattice orthogonality relations (B13), the relative coordinates $\boldsymbol{r}_a$ cancels out, and the bipartite lattice tightbinding Hamiltonian (4.19) takes the form

$$\hat{H} = -\sum_{\boldsymbol{k}} \Big[\phi_a(\boldsymbol{k}) \hat{c}^\dagger_{\boldsymbol{k}a} \hat{c}_{\boldsymbol{k}b} + \phi_b(\boldsymbol{k}) \hat{c}^\dagger_{\boldsymbol{k}b} \hat{c}_{\boldsymbol{k}a} + \mu_a \hat{c}^\dagger_{\boldsymbol{k}a} \hat{c}_{\boldsymbol{k}a} + \mu_b \hat{c}^\dagger_{\boldsymbol{k}a} \hat{b}_{\boldsymbol{k}} \Big], \tag{4.20}$$

where the structure factors (4.14) denoted by $\phi_a(\boldsymbol{k})$ and $\phi_b(\boldsymbol{k})$ runs over the nearest-neighbour vectors of their corresponding sublattices. Hermiticity of the Hamiltonian then translates to $\phi_a(\boldsymbol{k}) = \phi^*_b(\boldsymbol{k}) \equiv \phi(\boldsymbol{k})$. By the construction of the bipartite lattice, this condition is a reflection of the fact that the nearest-neighbour vectors are arranged in pairs $\boldsymbol{\delta}_{aj} = -\boldsymbol{\delta}_{bj} \equiv \boldsymbol{\delta}_j$.

Hence, the change to the Bloch sum basis (4.13) does not diagonalize the Hamiltonian (4.20). Introduce then the operator doublet $\hat{\Psi}_{\boldsymbol{k}} = (\hat{c}_{\boldsymbol{k}a}, \hat{c}_{\boldsymbol{k}b})$, such that the Hamiltonian assumes the quadratic form

$$\hat{H} = -\sum_{\boldsymbol{k}} \hat{\Psi}^\dagger_{\boldsymbol{k}} \begin{bmatrix} \mu_a & \phi(\boldsymbol{k}) \\ \phi^*(\boldsymbol{k}) & \mu_b \end{bmatrix} \hat{\Psi}_{\boldsymbol{k}} \equiv \sum_{\boldsymbol{k}} \hat{\Psi}^\dagger_{\boldsymbol{k}} \mathcal{H}(\boldsymbol{k}) \hat{\Psi}_{\boldsymbol{k}}, \tag{4.21}$$

where the matrix $\mathcal{H}(\boldsymbol{k})$ is the Hamiltonian kernel of the system. The introduction of the Hamiltonian kernel allows for a two-level description of the system. Two-level systems in general are investigated further as a part of chapter 5.

Notice that the derived Hamiltonian kernel (4.21) satisfies $\mathcal{H}^\dagger = \mathcal{H}$, thus inheriting the hermiticity of the total Hamiltonian $\hat{H}$. The Hamiltonian kernel of the diatomic primitive unit cell can thus be written in terms of the complete set of hermitian (2×2) matrices conventionally denoted $(\tau_0, \boldsymbol{\tau}) = (\tau_0, \tau_x, \tau_y, \tau_z)$, where τ_0 is the identity matrix and $\boldsymbol{\tau}$ are the Pauli matrices (C8), as

$$\mathcal{H}(\boldsymbol{k}) = -\frac{\mu_a + \mu_b}{2}\tau_0 - \mathrm{Re}\{\phi(\boldsymbol{k})\}\tau_x + \mathrm{Im}\{\phi(\boldsymbol{k})\}\tau_y - \frac{\mu_a - \mu_b}{2}\tau_z. \tag{4.22}$$

Because the Pauli matrices are also used to describe the spin degree of freedom σ for electrons as explained in appendix C, the orbital degree of freedom for the diatomic primitive unit cell is said to be a type of *pseudospin degree of freedom*, denoted $\tau = \pm 1$. In general, the appearance of a pseudospin degree of freedom can be attributed to any discrete quantum number taking on two values.

The two energy bands corresponding to the two atomic nuclei in the primitive unit cell are then calculated as the eigenvalues of the Hamiltonian kernel

$$\varepsilon_\tau(\boldsymbol{k}) = -\frac{\mu_a + \mu_b}{2} + \tau \sqrt{|\phi(\boldsymbol{k})|^2 + \Big(\frac{\mu_a - \mu_b}{2}\Big)^2}.$$

The first term of the band energies is the arithmetic average of the on-site energies of the two sublattices, and can be considered a reference energy. The reference energy is subsumed into the energy function $\varepsilon_\tau(\boldsymbol{k})$ without changing the eigenstates of the Hamiltonian. The second part is dependent on the on-site energy difference between the sublattices $\Delta \equiv \mu_a - \mu_b$ and the absolute value of the structure factor (4.14). The energy bands are then recast into the form

$$\varepsilon_\tau(\boldsymbol{k}) = \tau\varepsilon_{\boldsymbol{k}} = \tau\sqrt{|\phi(\boldsymbol{k})|^2 + \frac{\Delta^2}{4}}. \tag{4.23}$$

Hence, with a diatomic primitive unit cell the range of electronic energies is split into two bands. These are the *valence band* $\varepsilon_-(\boldsymbol{k})$ and the *conduction band* $\varepsilon_+(\boldsymbol{k})$. The valence band constitute the highest range of occupied electron energies, and the conduction band the lowest range of vacant electron energies at absolute zero temperature when the crystalline system is in its ground state.

From the energy function (4.23), the maximum of the valence band and the minimum of the conduction band are given by points $\boldsymbol{k} = \boldsymbol{K}$ in reciprocal space for which the structure factor $\phi(\boldsymbol{K}) = 0$. In consequence, if the difference between the on-site energies of the two sublattices Δ is unequal to zero, a *bandgap* between the valence band and conduction band emerges with no available electronic states. The width of this bandgap is given by $\varepsilon_+(\boldsymbol{K}) - \varepsilon_-(\boldsymbol{K}) = \Delta$. Hence, from now on the parameter Δ will simply be referred to as the bandgap.

Because the Hamiltonian kernel (4.22) is hermitian, its eigenvectors $\boldsymbol{\psi}^\pm_{\boldsymbol{k}}$ corresponding to the eigenvalues $\varepsilon_\pm(\boldsymbol{k})$ will be orthogonal by default. These eigenvectors represent two-component Bloch states, and can be chosen

$$\psi^+_{\boldsymbol{k}}(\boldsymbol{r}) = \frac{1}{D(\boldsymbol{k})}\begin{bmatrix} \frac{\Delta}{2} - \varepsilon(\boldsymbol{k}) \\ \phi^*(\boldsymbol{k}) \end{bmatrix} e^{i\boldsymbol{k}\cdot\boldsymbol{r}} \qquad \psi^-_{\boldsymbol{k}}(\boldsymbol{r}) = \frac{1}{D(\boldsymbol{k})}\begin{bmatrix} \phi(\boldsymbol{k}) \\ -\frac{\Delta}{2} + \varepsilon(\boldsymbol{k}) \end{bmatrix} e^{i\boldsymbol{k}\cdot\boldsymbol{r}}. \tag{4.24}$$

These eigenvectors are then orthonormal, with the normalization constant given by $D^2(\boldsymbol{k}) = 2\varepsilon(\boldsymbol{k})(\varepsilon(\boldsymbol{k}) - \Delta/2)$. The corresponding combined eigenvector matrix $\mathcal{M} = [\ \psi^+_{\boldsymbol{k}} \quad \psi^-_{\boldsymbol{k}}\ ]$ is both unitary and hermitian, satisfying $\mathcal{M}^{-1} = \mathcal{M}^\dagger = \mathcal{M}$. Introduce then new creation and annihilation operators through

$$\begin{bmatrix} \hat{c}_{\boldsymbol{k}+} \\ \hat{c}_{\boldsymbol{k}-} \end{bmatrix} = \mathcal{M}\hat{\Psi}_{\boldsymbol{k}} = \psi^+_{\boldsymbol{k}}\hat{c}_{\boldsymbol{k}a} + \psi^-_{\boldsymbol{k}}\hat{c}_{\boldsymbol{k}b}. \tag{4.25}$$

Using the unitary transform $\mathcal{M}$, the Hamiltonian (4.21) is readily diagonalized

$$\hat{H} = \sum_{\boldsymbol{k}} \left(\varepsilon_+(\boldsymbol{k})\hat{c}^\dagger_{\boldsymbol{k}+}\hat{c}_{\boldsymbol{k}+} + \varepsilon_-(\boldsymbol{k})\hat{c}^\dagger_{\boldsymbol{k}-}\hat{c}_{\boldsymbol{k}-} \right) \tag{4.26}$$

The operators $\hat{c}_{\boldsymbol{k}+}$ and $\hat{c}_{\boldsymbol{k}-}$ are here interpreted as the annihilation operators of the single-electron Bloch states with energy $\varepsilon_\pm(\boldsymbol{k})$, respectively.

4.3.2 The Energy Band Structure of Graphene

In the two-dimensional crystal graphene, the carbon atoms are arranged in a hexagonal lattice with two atoms in each unit cell separated by the distance a. The primitive lattice vectors of the underlying triangular Bravais lattice are

$$\boldsymbol{a}_1 = \frac{\sqrt{3}a}{2}\hat{\boldsymbol{x}} + \frac{3a}{2}\hat{\boldsymbol{y}}, \qquad \boldsymbol{a}_2 = \frac{\sqrt{3}a}{2}\hat{\boldsymbol{x}} - \frac{3a}{2}\hat{\boldsymbol{y}}.$$

From their defining relation (B11), the reciprocal lattice vectors can be chosen

$$\boldsymbol{b}_1 = \frac{2\pi}{\sqrt{3}a}\hat{\boldsymbol{k}}_x + \frac{2\pi}{3a}\hat{\boldsymbol{k}}_y, \qquad \boldsymbol{b}_2 = -\frac{2\pi}{\sqrt{3}a}\hat{\boldsymbol{k}}_x + \frac{2\pi}{3a}\hat{\boldsymbol{k}}_y,$$

spanning a triangular reciprocal lattice rotated with respect to the real space lattice. The graphene lattice with its diatomic Wigner-Seitz cell is shown in figure 4.3, along with the corresponding reciprocal lattice and Brillouin zone.

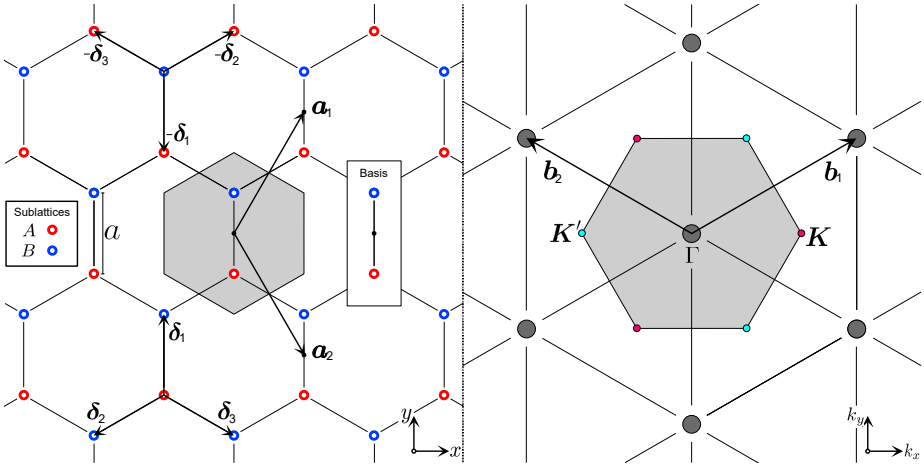

Figure 4.3: The two-dimensional hexagonal crystal lattice and the corresponding reciprocal lattice. The underlying triangular Bravais lattice is spanned by the primitive lattice vectors $\boldsymbol{a}_l$, with two atomic nuclei in each unit cell separated by the distance a. The crystal lattice is bipartite, separated into two triangular sublattices denoted by A and B. There are three nearest-neighbour vectors of the same length for each atomic nucleus, denoted by $\boldsymbol{\delta}_j$ for sublattice A. The reciprocal lattice spanned by the reciprocal vectors $\boldsymbol{b}_m$ is triangular, rotated with respect to the real space Bravais lattice. The Wigner-Seitz cell and the Brillouin Zone are shaded in gray, and the Brillouin zone center is denoted Γ. Due to the periodicity of the Brillouin zone there are only two distinct Brillouin zone corner points, denoted $\boldsymbol{K}$ and $\boldsymbol{K}'$.

The hexagonal lattice is bipartite with the nearest neighbour vectors $\boldsymbol{\delta}_1$, $\boldsymbol{\delta}_2$ and $\boldsymbol{\delta}_3$ as shown in figure 4.3. In coordinate form, these are given by

$$\boldsymbol{\delta}_1 = a\hat{\boldsymbol{y}}, \qquad \boldsymbol{\delta}_2 = -\frac{a}{2}\hat{\boldsymbol{y}} + \frac{\sqrt{3}a}{2}\hat{\boldsymbol{x}}, \qquad \boldsymbol{\delta}_3 = -\frac{a}{2}\hat{\boldsymbol{y}} - \frac{\sqrt{3}a}{2}\hat{\boldsymbol{x}}. \tag{4.27}$$

Because each sublattice is isotropic in the directions of the vectors $\boldsymbol{\delta}_j$, the tunnelling rate is independent on the nearest-neighbour index, denoted by $t_j \equiv t$.

Inserting the nearest neighbour vectors into the definition of the structure factor (4.14), the structure factor of the hexagonal lattice is readily expressed

$$\phi(\boldsymbol{k}) = te^{iak_y} + 2te^{-\frac{ia}{2}k_y}\cos\left(\frac{\sqrt{3}a}{2}k_x\right). \tag{4.28}$$

The energy band structure of graphene is then calculated by inserting the structure factor into the energy band formula for diatomic bipartite lattices (4.23)

$$\varepsilon_{\pm}(\boldsymbol{k}) = \pm\sqrt{\left[3+2\cos\left(\sqrt{3}ak_x\right)+4\cos\left(\frac{\sqrt{3}}{2}ak_x\right)\cos\left(\frac{3}{2}ak_y\right)\right]t^2 + \frac{\Delta^2}{4}}. \tag{4.29}$$

For pure suspended single-layered graphene, the bandgap $\Delta = 0$ and the graphene lattice becomes invariant under space inversion. If however the graphene sheet is deposited on some other material, the space inversion symmetry of the lattice can be broken due to interactions with the substrate, inducing a bandgap $\Delta \neq 0$. The energy bands are drawn for both of these cases in figure 4.4.

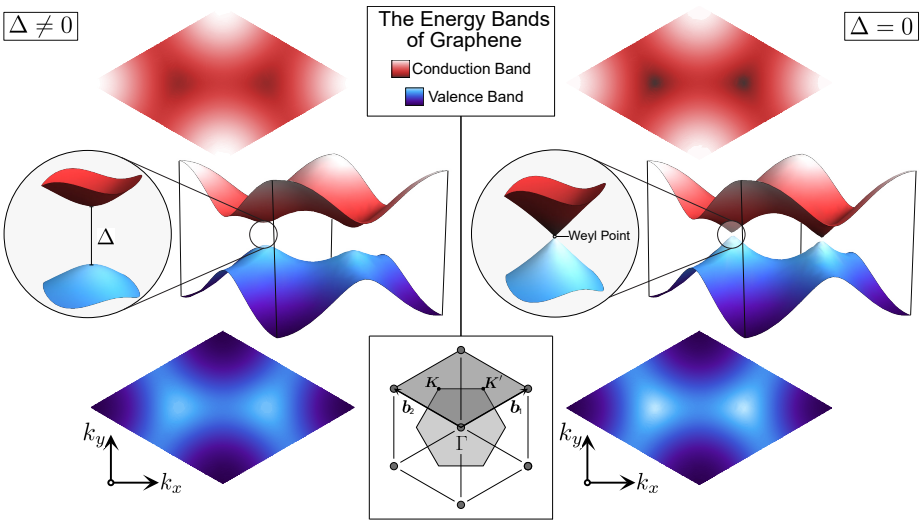

Figure 4.4: The conduction and valence bands of graphene, with a bandgap $\Delta \neq 0$ and $\Delta = 0$, respectively. The framed central figure shows a section of the reciprocal lattice of graphene, the shaded hexagon being the Brillouin zone and the parallelogram being subtended by the primitive reciprocal lattice vectors $\boldsymbol{b}_1$ and $\boldsymbol{b}_2$. The energy bands are drawn for crystal momenta $\boldsymbol{k}$ within the parallelogram unit cell, and is periodic with the reciprocal lattice. For the case $\Delta = 0$ the two bands meet at the Brillouin zone corners $\boldsymbol{K}$ and $\boldsymbol{K}'$, forming Weyl points.

Because of the diatomic primitive unit cell of graphene, the electrons of the system will at zero temperature occupy all the available states in the valence band, whereas the conduction band is completely vacant. For energies minutely higher than this crystalline ground state, the electrons will then begin occupying states near the minima of the conduction band. It is due to these conduction

band electrons that graphene obtains its exotic conduction properties. In order to investigate the behaviour of these electrons, let the conduction band be expanded about its minima, located at reciprocal vectors $\boldsymbol{k} = \boldsymbol{K}$ for which the structure factor (4.28) vanishes. The condition $\phi(\boldsymbol{K}) = 0$ here translates to

$$1 + 2e^{\frac{-3ai}{2}K_y}\cos\left(\frac{\sqrt{3}a}{2}K_x\right) = 0,$$

from which the reciprocal vectors $\boldsymbol{K}$ can be found. Separating this into a real and an imaginary part gives two equations for the two variables K_x and K_y,

$$\begin{cases} \cos\left(\frac{3a}{2}K_y\right)\cos\left(\frac{\sqrt{3}a}{2}K_x\right) = -\frac{1}{2} \\ \sin\left(\frac{3a}{2}K_y\right)\cos\left(\frac{\sqrt{3}a}{2}K_x\right) = 0 \end{cases}$$

The simplest solutions to these equations are found for $K_y = 0$, giving

$$\boldsymbol{K} = \Big(\frac{4\pi}{3\sqrt{3}a}, 0\Big), \qquad \boldsymbol{K}' = \Big(-\frac{4\pi}{3\sqrt{3}a}, 0\Big). \tag{4.30}$$

These points correspond to two of the corner points of the Brillouin zone in reciprocal space. Choosing instead $K_x = \pm 2\pi/3a$ would give the coordinates of the other four corner points. However, due to the periodicity of the Brillouin zone, the points $\boldsymbol{K}$ and $\boldsymbol{K}'$ are the only two distinct solutions; in figure 4.3, it is seen that either solution is separated from two other corner points of the Brillouin zone by reciprocal lattice vectors. That $\boldsymbol{K}$ lies at the Brillouin zone corner points follows directly from the symmetries of the graphene lattice [20].

The low-energy behaviour of the conduction electrons can now be found by expanding the structure factor around the Brillouin zone corner points, defining

$$\phi_{\boldsymbol{K}}(\boldsymbol{q}) \equiv \phi(\boldsymbol{K} + \boldsymbol{q}) \approx q_x \frac{\partial}{\partial q_x}\phi(\boldsymbol{K} + \boldsymbol{q})\Big|_{\boldsymbol{q}=0} + q_y \frac{\partial}{\partial q_y}\phi(\boldsymbol{K} + \boldsymbol{q})\Big|_{\boldsymbol{q}=0}.$$

Here the reciprocal vector $\boldsymbol{q} = (q_x, q_y)$ has its origin in the Brillouin zone corner point $\boldsymbol{K}$, whereas the usual reciprocal vector $\boldsymbol{k}$ has its origin in the Brillouin zone center Γ, seen in figure 4.3. The notation of $\boldsymbol{q}$ is introduced to differ between these origins. Inserting the found Brillouin zone corner points (4.30), then near the minima of the conduction band the structure factor behaves as

$$\phi_{\boldsymbol{K}}(\boldsymbol{q}) = \frac{3at}{2}(-q_x + iq_y) \qquad \phi_{\boldsymbol{K}'}(\boldsymbol{q}) = \frac{3at}{2}(q_x + iq_y). \tag{4.31}$$

Here, the prefactor $3at/2 \equiv v_F$ can be interpreted as the Fermi-velocity of the electrons. The corresponding behaviour of the Hamiltonian kernel (4.22) near the conduction band minima is then found by inserting these effective structure factors, and can be written in terms of the pseudospin Pauli matrices (C8) as

$$\mathcal{H}(\boldsymbol{q}) = \begin{bmatrix} -\Delta/2 & v_F(\pm q_x - iq_y) \\ v_F(\pm q_x + iq_y) & \Delta/2 \end{bmatrix} = \pm v_F q_x \tau_x + v_F q_y \tau_y - \frac{\Delta}{2}\tau_z. \quad (4.32)$$

Here, the upper sign refers to the corner point $\boldsymbol{K}$ and the lower to $\boldsymbol{K}'$, and must not be confused with the signs distinguishing the energy bands (4.23), which are seen to be equivalent for the Brillouin zone corner points and equal to

$$\varepsilon_\pm(\boldsymbol{q}) = \pm\sqrt{\frac{9a^2t^2}{4}\boldsymbol{q}^2 + \frac{\Delta^2}{4}} \equiv \pm\sqrt{v_F^2\boldsymbol{q}^2 + \frac{\Delta^2}{4}}. \quad (4.33)$$

The positive sign here describes the low-energy behaviour of electrons occupying states in the conduction band, and the negative sign the effective behaviour of the vacant electron states in the valence band which acts as positively charged quasiparticles known as *electron holes*.

The resulting low-energy band structure (4.33) is on the same form as the energy-momentum relation from special relativity, with the Fermi velocity v_F serving as an effective speed of light and the bandgap Δ as an effective rest mass energy. In particular, for pure isolated graphene the on-site energies for the two atoms in the primitive unit cell are equal, leading to a vanishing bandgap or effective rest mass energy $\Delta = 0$. In this case the valence and conduction energy bands meet at a doubly degenerate *Weyl point* at the Brillouin zone corner points, around which the energy band structure is locally given by

$$\varepsilon_\pm(\boldsymbol{q}) = \pm v_F|\boldsymbol{q}|. \quad (4.34)$$

In consequence, for pure graphene the energy band structure for conduction electrons is linear in momentum, as if the electrons were ultra-relativistic. The non-relativistic conduction electrons of graphene are therefore describable by the same mathematics as relativistic fermions in quantum field theory, making graphene an example of a two-dimensional *Weyl semimetal*.

In consequence, due to the lattice symmetries of graphene the effective Schrödinger equation for non-relativistic crystalline electrons has been recast into the same shape as the two-dimensional Weyl equation for relativistic fermions. In general for crystalline systems however, the mathematical description is not restricted to obey the symmetries of spacetime. In chapter 6, other systems of solid state physics with linear dispersion relations are investigated, while the mathematical formalisms of relativistic theory of fermions and the resulting Dirac and Weyl equations are presented in appendix D.

The reader should be aware that graphene originally was categorized as a *Dirac semimetal* [2], because the two Hamiltonian kernels (4.32) describing the system near the two Brillouin zone corner points can be combined to form a (4×4) Hamiltonian kernel analogous to the Dirac Hamiltonian (D8) of relativistic quantum theory. This categorization has since been abandoned after the discovery and taxonomy of Dirac and Weyl semimetals in three dimensional systems, being the main topics of investigation of chapter 6.

Chapter 5

The Berry Phase and Berryological Quantities

Under the early development of the theory of quantum mechanics the prevailing notion was that the phase of a quantum state is arbitrary and inherently unphysical. In 1984 however, M. V. Berry [21] argued that quantum states may attain a geometrical phase observable through interference upon a cyclic evolution with respect to a set of system parameters. The geometrical phase, named the Berry phase after its discoverer, is analogous to the anholonomy angle appearing upon a cyclic parallel transport on curved topological surfaces.

The original derivation of the Berry phase is based on the adiabatic theorem and cyclic evolution in time. The same year of the discovery, B. Simon [22] interpreted the Berry phase as the holonomy in a hermitian line bundle. This allowed for the possibility of defining a berryology for the Brillouin zone, and served as the theoretical foundation for a class of solid state systems known as topological materials; of particular interest are topological semimetals, investigated in chapter 6. In general, it is not necessary to consider time evolution in order to coherently define berryological quantities, and the following section introduces the theory of berryological quantities based on the evolution of a general parameter set. On this basis, the current chapter investigates the background and derives the expressions for the Berry phase, the Berry connection and the Berry curvature for different systems. The theory presented is indebted to the introductory textbooks by Bernevig [23] and Vanderbilt [24].

Furthermore, the chapter introduces the general description of a quantum two-level system, for which the berryological quantities are calculated in order to exemplify the theory. Finally, the berryological quantities of the Brillouin zone and of two-level systems are combined in order to calculate the berryological quantities of graphene, whose Hamiltonian is derived in chapter 4.

5.1 Introduction to Berryology

Consider a quantum mechanical system for which the Hamiltonian operator is dependent on a set of parameters $\boldsymbol{\mathcal{R}} = (\mathcal{R}_\mu)$, spanning a *parameter space*. Then, each point in parameter space gives rise to a Hamiltonian $\hat{H} = \hat{H}(\boldsymbol{\mathcal{R}})$ with a set of eigenstates $\{|n_{\boldsymbol{\mathcal{R}}}\rangle\}$ defined through the eigenvalue equation

$$\hat{H}(\boldsymbol{\mathcal{R}})\,|n_{\boldsymbol{\mathcal{R}}}\rangle = E_n(\boldsymbol{\mathcal{R}})\,|n_{\boldsymbol{\mathcal{R}}}\rangle\,. \tag{5.1}$$

For simplicity the eigenvalue spectrum $E_n(\boldsymbol{\mathcal{R}})$ is assumed non-degenerate, and the Hamiltonian, its eigenvalues and corresponding eigenstates are assumed to vary continuously with the parameter set. Furthermore, only the phases of the eigenstates are of interest, and the eigenstates are assumed normalized to unity.

For each realization of the parameter set $\boldsymbol{\mathcal{R}}$, the eigenstates $\{|n_{\boldsymbol{\mathcal{R}}}\rangle\}$ spans a complete Hilbert space. Hence, through the eigenvalue equation (5.1), the parameter space corresponds to a continuous set of related Hilbert spaces, mathematically analogous to the set of tangent spaces on a topological manifold. This analogy will in the following be referred to as the *Hilbert space manifold*.

5.1.1 Definition of the Berry Phase

Denote by $\mathcal{C}$ a curve in parameter space, choose two points $\boldsymbol{\mathcal{R}}_1$ and $\boldsymbol{\mathcal{R}}_2$ along this curve and consider a single eigenstate $|n_{\boldsymbol{\mathcal{R}}}\rangle$ evaluated at these two points. In general, the inner products of different Hilbert spaces are not compatible. However, it is possible to define a common inner product for the combined Hilbert space corresponding to the two realizations of the parameter set. In this setting, the phase difference $\Delta\gamma$ between the two states can be calculated by

$$e^{-i\Delta\gamma} = \frac{\langle n_{\boldsymbol{\mathcal{R}}_1}|n_{\boldsymbol{\mathcal{R}}_2}\rangle}{|\langle n_{\boldsymbol{\mathcal{R}}_1}|n_{\boldsymbol{\mathcal{R}}_2}\rangle|},$$

which upon taking the logarithm gives an expression for the phase difference

$$\Delta\gamma = -\operatorname{Im}\{\ln\langle n_{\boldsymbol{\mathcal{R}}_1}|n_{\boldsymbol{\mathcal{R}}_2}\rangle\}$$

This phase difference is entirely arbitrary with the choice of phases for the two states, and may also differ with the definition of the combined inner product.

Assume then the eigenstate is differentiable along the parameter space curve $\mathcal{C}$, and let the two points along the curve be separated by an infinitesimal parameter space distance $\mathrm{d}\boldsymbol{\mathcal{R}}$. Then, in the continuous limit the logarithm

$$\begin{aligned}\ln\langle n_{\boldsymbol{\mathcal{R}}}|n_{\boldsymbol{\mathcal{R}}+\mathrm{d}\boldsymbol{\mathcal{R}}}\rangle &= \ln\langle n_{\boldsymbol{\mathcal{R}}}|\left(|n_{\boldsymbol{\mathcal{R}}}\rangle + \mathrm{d}\boldsymbol{\mathcal{R}}\cdot\nabla_{\boldsymbol{\mathcal{R}}}|n_{\boldsymbol{\mathcal{R}}}\rangle + \mathcal{O}(\mathrm{d}\boldsymbol{\mathcal{R}}^2)\right)\\ &= \ln\big(1 + \mathrm{d}\boldsymbol{\mathcal{R}}\cdot\langle n_{\boldsymbol{\mathcal{R}}}|\nabla_{\boldsymbol{\mathcal{R}}}|n_{\boldsymbol{\mathcal{R}}}\rangle + \mathcal{O}(\mathrm{d}\boldsymbol{\mathcal{R}}^2)\big)\\ &= \mathrm{d}\boldsymbol{\mathcal{R}}\,\langle n_{\boldsymbol{\mathcal{R}}}|\nabla_{\boldsymbol{\mathcal{R}}}|n_{\boldsymbol{\mathcal{R}}}\rangle + \mathcal{O}(\mathrm{d}\boldsymbol{\mathcal{R}}^2).\end{aligned}$$

By derivation of the normalization condition $\langle n_{\boldsymbol{\mathcal{R}}}|n_{\boldsymbol{\mathcal{R}}}\rangle = 1$, the remaining term here is completely imaginary. Hence, in the continuous limit the infinitesimal phase change along the curve $\mathcal{C}$ can be given by the linear differential form

$$\mathrm{d}\gamma_n = \langle n_{\boldsymbol{\mathcal{R}}} |\, i\nabla_{\boldsymbol{\mathcal{R}}}\, | n_{\boldsymbol{\mathcal{R}}} \rangle \cdot \mathrm{d}\boldsymbol{\mathcal{R}} \equiv \boldsymbol{\mathcal{A}}^{(n)}(\boldsymbol{\mathcal{R}}) \cdot \mathrm{d}\boldsymbol{\mathcal{R}} \tag{5.2}$$

where $\boldsymbol{\mathcal{A}}^{(n)}(\boldsymbol{\mathcal{R}})$ is the *Berry connection* for the eigenstate $|n_{\boldsymbol{\mathcal{R}}}\rangle$ in particular. The Berry connection $\boldsymbol{\mathcal{A}}^{(n)}(\boldsymbol{\mathcal{R}})$ continuously connects the Hilbert spaces, or rather the relation between the inner products of the Hilbert spaces along the Hilbert space manifold. From its definition, it will naturally depend on both the chosen state $|n_{\boldsymbol{\mathcal{R}}}\rangle$ and on the parameter space curve $\mathcal{C}$.

Introduction of the Berry connection allows for integration of the phase difference along the curve. Letting $\boldsymbol{\mathcal{R}}_0$ and $\boldsymbol{\mathcal{R}}_T$ be the initial and final parameter sets along the parameter space curve, the total phase difference along the curve

$$\Delta\gamma_n = \int_{\boldsymbol{\mathcal{R}}_0}^{\boldsymbol{\mathcal{R}}_T} \langle n_{\boldsymbol{\mathcal{R}}} |\, i\nabla_{\boldsymbol{\mathcal{R}}}\, | n_{\boldsymbol{\mathcal{R}}} \rangle \cdot \mathrm{d}\boldsymbol{\mathcal{R}}. \tag{5.3}$$

Again, this phase difference is completely arbitrary with the choice of phases.

Let then the parameter space curve $\mathcal{C}$ form a closed contour in parameter space, such that the curve begins and ends at the same parameter space point. The phase difference along the contour is then given by the *Berry phase*

$$\gamma_n = \oint_{\mathcal{C}} \boldsymbol{\mathcal{A}}^{(n)}(\boldsymbol{\mathcal{R}}) \cdot \mathrm{d}\boldsymbol{\mathcal{R}} = \oint_{\mathcal{C}} \langle n_{\boldsymbol{\mathcal{R}}} |\, i\nabla_{\boldsymbol{\mathcal{R}}}\, | n_{\boldsymbol{\mathcal{R}}} \rangle \cdot \mathrm{d}\boldsymbol{\mathcal{R}}. \tag{5.4}$$

Clearly, if the Berry connection $\boldsymbol{\mathcal{A}}^{(n)}(\boldsymbol{\mathcal{R}})$ is a single valued function, the Berry phase γ_n will be zero. However, if the topology of the Hilbert space manifold is non-trivial, the Berry phase can take on a non-zero value.

5.1.2 Gauge Freedom and Parallel Transport

For any single quantum mechanical state the phase of the state is of no physical importance, and so the physical observables for any realization of the parameter set $\boldsymbol{\mathcal{R}}$ are unaffected by a *gauge transform* of the eigenstates, given by

$$|\tilde{n}_{\boldsymbol{\mathcal{R}}}\rangle = e^{-i\theta_n(\boldsymbol{\mathcal{R}})}\, |n_{\boldsymbol{\mathcal{R}}}\rangle\,, \tag{5.5}$$

where $\theta_n(\boldsymbol{\mathcal{R}})$ is the chosen phase change for the state $|n_{\boldsymbol{\mathcal{R}}}\rangle$. The gauge transform is said to be *local* in parameter space if the phase changes θ_n are dependent and *global* if they are independent on the parameter set $\boldsymbol{\mathcal{R}}$.

Reconsider then the curve $\mathcal{C}$ in parameter space. A gauge transform (5.5) individually changes the basis states $\{|n_{\boldsymbol{\mathcal{R}}}\rangle\}$ of each Hilbert space along this line by a phase. In consequence, the connection between these spaces must also change. Inserting the gauge transformed states into the definition of the Berry connection (5.2), the gauge transformed Berry connection becomes

$$\widetilde{\boldsymbol{\mathcal{A}}}^{(n)}(\boldsymbol{\mathcal{R}}) = \boldsymbol{\mathcal{A}}^{(n)}(\boldsymbol{\mathcal{R}}) + \nabla_{\boldsymbol{\mathcal{R}}}\theta_n(\boldsymbol{\mathcal{R}}); \tag{5.6}$$

for local gauge transforms the Berry connection is not gauge invariant.

The gauge variance of the Berry connection will naturally transfer to the Berry phase (5.4). Consider the total change of the phase shift $\theta_n(\boldsymbol{\mathcal{R}})$ upon

moving around the parameter space contour. Because the state at the beginning of the contour must be retrieved, the total change of the phase shift going around the contour once must be $\Delta\theta_n = 2\pi c$, where c is some integer. Inserting the gauge transformed Berry connection (5.6) into the definition of the Berry phase, the Berry phase will under a local gauge transform change by $\Delta\theta_n$, such that

$$\widetilde{\gamma}_n = \gamma_n + 2\pi c. \tag{5.7}$$

The Berry phase is therefore said to be gauge invariant modulo 2π. Thus, the *Berry phase factor* $e^{i\gamma_n}$ is a gauge invariant quantity, and cannot be made to vanish using a gauge transform. Although not sufficient, gauge invariance is a necessary condition for a quantity to represent a physical observable.

A particular choice for a gauge transform is one in which the linear differential form (5.2) is zero; $\mathrm{d}\gamma_n = 0$. In that case the Berry connection $\boldsymbol{\mathcal{A}}^{(n)} = 0$, and the inner product $\langle n_{\boldsymbol{\mathcal{R}}} | n_{\boldsymbol{\mathcal{R}}+\mathrm{d}\boldsymbol{\mathcal{R}}} \rangle = 1$, retaining the normalization to linear order in $\mathrm{d}\boldsymbol{\mathcal{R}}$ along the curve $\mathcal{C}$. This is equivalent to the notion of *parallel transport* on curved manifolds, in that the inner product $\langle n_{\boldsymbol{\mathcal{R}}} | \psi \rangle$ between any general state vector $|\psi\rangle$ and the eigenstate $|n_{\boldsymbol{\mathcal{R}}}\rangle$ is constant along the curve in this gauge.

Let again the curve $\mathcal{C}$ be a contour, and consider the definition of the Berry phase (5.4) in the parallel transport gauge $\boldsymbol{\mathcal{A}}^{(n)} = 0$. Clearly, if the Berry phase is non-zero such a gauge cannot be applied along the entire contour; at some point, the Berry connection must obtain a singularity, corresponding to a phase shift equal to the Berry phase. In this way, the Berry phase is analogous to an anholonomy angle which appears when parallel transporting vectors on curved manifolds. This also means the Berry phase is a result of the topology of the manifold of Hilbert spaces: if the topology is non-trivial, the Berry phase may attain a non-zero value dependent on the parameter space curve.

5.1.3 Berry Curvature and Chern Numbers

Until this point, the Berry connection has been defined only along a curve in parameter space. Consider instead a surface $\mathcal{S}$ in parameter space whose boundary is the parameter space contour $\mathcal{C} = \partial\mathcal{S}$. Assume then there exists a gauge for the Berry connection (5.6) which makes it smooth and continuous on the entire surface, such that the connection components $\mathcal{A}_\mu^{(n)}(\boldsymbol{\mathcal{R}})$ becomes differentiable with respect to the parameters $\mathcal{R}_\mu$ for every point $\boldsymbol{\mathcal{R}}$ on $\mathcal{S}$. It is then possible to define everywhere on this surface the components of a real, antisymmetric rank-2 tensor $\Omega_{\mu\nu}^{(n)}(\boldsymbol{\mathcal{R}})$ known as the *Berry curvature*, written

$$\Omega_{\mu\nu}^{(n)} = \partial_\mu \mathcal{A}_\nu^{(n)} - \partial_\nu \mathcal{A}_\mu^{(n)} = -2\,\mathrm{Im}\,\langle \partial_\mu n_{\boldsymbol{\mathcal{R}}} | \partial_\nu n_{\boldsymbol{\mathcal{R}}} \rangle \tag{5.8}$$

where the shorthand notation $\partial_\mu |u\rangle \equiv |\partial_\mu u\rangle$ is used and the partial derivative $\partial_\mu \equiv \partial/\partial\mathcal{R}_\mu$. In viewing the Berry connection as analogous to an affine connection on the Hilbert space manifold, the Berry curvature is mathematically interpreted as the corresponding analogous curvature tensor.

In calculations, it is often preferable to rewrite the expression for the Berry curvature (5.8) in terms of the Hamiltonian of the system. By derivating the

eigenvalue equation for the Hamiltonian (5.1) with respect to the parameter $\mathcal{R}_\mu$, left multiplying with some state vector $\langle m_{\boldsymbol{\mathcal{R}}}| \neq \langle n_{\boldsymbol{\mathcal{R}}}|$ and using the orthogonality condition $\langle m_{\boldsymbol{\mathcal{R}}}|n_{\boldsymbol{\mathcal{R}}}\rangle = 0$, it is readily shown that

$$\langle m_{\boldsymbol{\mathcal{R}}}|\partial_\mu n_{\boldsymbol{\mathcal{R}}}\rangle = \frac{\langle m_{\boldsymbol{\mathcal{R}}}|\left[\partial_\mu \hat{H}\right]|n_{\boldsymbol{\mathcal{R}}}\rangle}{E_n - E_m}$$

Inserting the completeness relation (1.1) of the eigenstates $|m_{\boldsymbol{\mathcal{R}}}\rangle$ in between the inner product of the original expression for the Berry curvature (5.8) then gives

$$\Omega_{\mu\nu}^{(n)} = -2\,\mathrm{Im}\sum_{m\neq n}\frac{\langle n_{\boldsymbol{\mathcal{R}}}|\left[\partial_\mu \hat{H}\right]|m_{\boldsymbol{\mathcal{R}}}\rangle\langle m_{\boldsymbol{\mathcal{R}}}|\left[\partial_\nu \hat{H}\right]|n_{\boldsymbol{\mathcal{R}}}\rangle}{(E_n - E_m)^2} \tag{5.9}$$

The term for $|m_{\boldsymbol{\mathcal{R}}}\rangle = |n_{\boldsymbol{\mathcal{R}}}\rangle$ is left out of the sum, as $\langle n_{\boldsymbol{\mathcal{R}}}|\partial_\mu n_{\boldsymbol{\mathcal{R}}}\rangle$ is completely imaginary and hence when multiplied by a similar term vanishes when taking the imaginary part. Recall also the assumption of non-degenerate eigenvalues.

By inserting the gauge transform of the Berry connection (5.6) into the definition of the Berry curvature (5.8), it is clear that the Berry curvature is inherently gauge invariant. Notice however that the choice of gauge now is restricted to a gauge for which the Berry connection is differentiable in the regions where the Berry curvature is defined. This gauge will also fix the value of the Berry phase (5.4), which by the generalized Stokes theorem now can be calculated as a surface integral in parameter space as

$$\gamma_n = \oint_{\mathcal{C}} \boldsymbol{\mathcal{A}}^{(n)}(\boldsymbol{\mathcal{R}})\cdot \mathrm{d}\boldsymbol{\mathcal{R}} = \int_{\mathcal{S}} \Omega_{\mu\nu}^{(n)}\mathrm{d}s_\mu \wedge \mathrm{d}s_\nu. \tag{5.10}$$

Here, the expression $\mathrm{d}s_\mu \wedge \mathrm{d}s_\nu$ is an infinitesimal area element on the surface $\mathcal{S}$, and the Einstein summation convention applies.

Let then the surface $\mathcal{S}$ be a closed smooth manifold in parameter space, and choose a closed contour $\mathcal{C}$ on this manifold, separating it into two regions. For either region, choose gauges such that the Berry connection is differentiable inside both regions separately. Integrating the Berry connection along these regions will then leave γ_n and $-\gamma_n + 2\pi c_n$ respectively, where the integer multiple of 2π arises due to the possibly different gauges. Combining the two integrals will then give the total integral of the Berry curvature over the manifold as

$$\oint_{\mathcal{S}} \Omega_{\mu\nu}^{(n)}\mathrm{d}s_\mu \wedge \mathrm{d}s_\nu = 2\pi c_n. \tag{5.11}$$

This is a version of the *Chern theorem*, stating that the integral of the Berry curvature over any closed manifold is an integer multiple of 2π. The integer c_n is known as the *Chern number*, and will in general depend on the manifold chosen. If the Chern number is non-zero, it is not possible to choose a gauge which is differentiable on the entire enclosed surface; at some located points or regions on the surface, the Berry connection will be singular. The proof is easily generalized to piecewise smooth manifolds by choosing several closed contours along the boundaries of the differentiable regions.

By derivating the orthonormality condition $\langle m_{\boldsymbol{\mathcal{R}}} | n_{\boldsymbol{\mathcal{R}}} \rangle = \delta_{mn}$ and using the completeness relation (1.1) of the eigenstates, it can be shown that the sum

$$\sum_n \langle \partial_\mu n_{\boldsymbol{\mathcal{R}}} | \partial_\nu n_{\boldsymbol{\mathcal{R}}} \rangle = \sum_n \langle \partial_\mu n_{\boldsymbol{\mathcal{R}}} | \partial_\nu n_{\boldsymbol{\mathcal{R}}} \rangle^* .$$

This sum over all eigenstates hence leaves no imaginary part. From the original definition of the Berry curvature (5.8), it is then clear that

$$\sum_n \Omega_{\mu\nu}^{(n)} = 0. \tag{5.12}$$

In consequence, within the gauge permitting a definition of the Berry curvature, the sum over all Berry phases (5.10) corresponding to the different eigenstates must be zero for any curve in parameter space: $\sum_n \gamma_n = 0$. Likewise, from its definition (5.11), the sum over all Chern numbers corresponding to the different eigenstates must also be zero: $\sum_n c_n = 0$.

5.2 The Berryology of the Brillouin Zone

In solid state physics, the Hamiltonian $\hat{\mathfrak{h}}$ for crystalline systems (B14) is invariant under discrete translations by lattice vectors (B8), as described in appendix B. The eigenstates of the Hamiltonian can then be chosen as Bloch states (B18) for each energy band n, denoted $|\psi_{n\boldsymbol{k}}\rangle$. Besides being energy eigenstates, these Bloch functions are eigenfunctions of the discrete translation operator, and are labelled by the crystal momentum $\boldsymbol{k}$ corresponding to their translation operator eigenvalues. For each energy band n of the crystalline system, the state vector $|\psi_{n\boldsymbol{k}}\rangle$ is continuously dependent on the components of the crystal momentum $\boldsymbol{k}$ of reciprocal space, which hence may serve as the parameter space $\boldsymbol{\mathcal{R}}$.

According to Blochs theorem (B16), for a d-dimensional reciprocal space the Brillouin zone has the topological shape of a d-torus, on which parameter space contours and surfaces are well defined. Hence, it is possible to devise a berryology of the Brillouin zone of systems in solid state physics. The berryological consideration of the Brillouin zone is the basis for defining *topological materials*, such as the Weyl semimetals investigated in chapter 6.

5.2.1 Berryological Quantities of the Brillouin Zone

Recall from appendix B that the crystal momentum $\boldsymbol{k}$ is solely a consequence of translation invariance, and hence does not appear as a parameter in the eigenvalue equation for the crystal Hamiltonian (B14). In consequence, all Bloch states $|\psi_{n\boldsymbol{k}}\rangle$ reside in the same Hilbert space, being the eigenspace of the crystal Hamiltonian $\hat{\mathfrak{h}}$. Therefore, the mathematical framework surrounding the Berry phase cannot be applied directly to the Bloch states themselves.

The berryology of the Brillouin zone is instead framed with respect to the lattice periodic states $|u_{n\boldsymbol{k}}\rangle$ whose Hamiltonian (B19), connected to the single-electron Hamiltonian as $\hat{\mathfrak{h}}(\boldsymbol{k}) = e^{i\boldsymbol{k}\cdot\hat{\boldsymbol{r}}} \hat{\mathfrak{h}} e^{-i\boldsymbol{k}\cdot\hat{\boldsymbol{r}}}$, indeed treats the crystal momen-

tum as a parameter. For each point $\boldsymbol{k}$ in the Brillouin zone, the set of eigenstates $|u_{n\boldsymbol{k}}\rangle$ corresponding to the different energy bands n spans an independent Hilbert space, as for the generic states $|n_{\boldsymbol{\mathcal{R}}}\rangle$ presented in section 5.1. The inner products (B20) of these Hilbert spaces are defined separately for each point $\boldsymbol{k}$ of the Brillouin zone, and can be mathematically connected by the Berry connection (5.2) of the Brillouin zone, which consequently is defined

$$\boldsymbol{\mathcal{A}}^{(n)}(\boldsymbol{k}) = i \langle u_{n\boldsymbol{k}} | \nabla_{\boldsymbol{k}} | u_{n\boldsymbol{k}} \rangle = i \int_{V_C} \mathrm{d}^d r \; u^*_{n\boldsymbol{k}}(\boldsymbol{r}) \nabla_{\boldsymbol{k}} u_{n\boldsymbol{k}}(\boldsymbol{r}). \tag{5.13}$$

From Blochs theorem and the periodic properties of the lattice periodic functions $u_{n\boldsymbol{k}}(\boldsymbol{r})$ in reciprocal space (B17), the Berry connection of the Brillouin zone satisfies $\boldsymbol{\mathcal{A}}^{(n)}(\boldsymbol{k} - \boldsymbol{G}_j) = \boldsymbol{\mathcal{A}}^{(n)}(\boldsymbol{k})$. Hence, the Berry connection is periodic with the Brillouin zone, consistent with its interpretation as an affine connection.

The Berry connection of the Brillouin zone (5.13) is associated with a specific energy band n. Similarly, the Berry phase associated with band n is defined

$$\gamma_n = \oint_{\mathcal{C}} \boldsymbol{\mathcal{A}}^{(n)}(\boldsymbol{k}) \cdot d\boldsymbol{k} \tag{5.14}$$

for some closed contour $\mathcal{C}$ in the Brillouin zone. Recall then that the Brillouin zone has the topological shape of a d-torus, periodic in the directions given by the reciprocal lattice vectors $\boldsymbol{b}_m$. It is then possible to construct closed contours in the direction given by $\boldsymbol{b}_m$; the Brillouin zone is not simply connected.

For most materials the crystal lattice and hence the reciprocal space will be three dimensional, with $d = 3$. In this case, the three independent components of the antisymmetric Berry curvature (5.8) for band n can be written as a pseudovector denoted by $\boldsymbol{\mathcal{B}}^{(n)}$, whose components are connected to the original definition of the Berry curvature through $\mathcal{B}^{(n)}_\lambda = \frac{1}{2}\varepsilon_{\lambda\mu\nu}\Omega^{(n)}_{\mu\nu}$, leaving

$$\begin{aligned} \boldsymbol{\mathcal{B}}^{(n)}(\boldsymbol{k}) &\equiv \nabla_{\boldsymbol{k}} \times \boldsymbol{\mathcal{A}}^{(n)}(\boldsymbol{k}) = -\operatorname{Im} \langle \nabla_{\boldsymbol{k}} u_{n\boldsymbol{k}} | \times | \nabla_{\boldsymbol{k}} u_{n\boldsymbol{k}} \rangle \\ &= -\operatorname{Im} \sum_{m \neq n} \frac{\langle u_{n\boldsymbol{k}} | \left[\nabla_{\boldsymbol{k}} \hat{\mathfrak{h}}(\boldsymbol{k}) \right] | u_{m\boldsymbol{k}} \rangle \times \langle u_{m\boldsymbol{k}} | \left[\nabla_{\boldsymbol{k}} \hat{\mathfrak{h}}(\boldsymbol{k}) \right] | u_{n\boldsymbol{k}} \rangle}{[\varepsilon_n(\boldsymbol{k}) - \varepsilon_m(\boldsymbol{k})]^2}. \end{aligned} \tag{5.15}$$

By virtue of the periodicity of the Berry connection of the Brillouin zone (5.2), the corresponding Berry curvature is periodic with the Brillouin zone, satisfying the condition $\boldsymbol{\mathcal{B}}^{(n)}(\boldsymbol{k} - \boldsymbol{G}_j) = \boldsymbol{\mathcal{B}}^{(n)}(\boldsymbol{k})$.

The Chern number (5.11) of any closed two-dimensional manifold in the three dimensional Brillouin zone is then readily defined using the Berry curvature (5.15). Notice then that any plane at any fixed value of k_z will constitute a closed torus, due to the periodicity of the Brillouin zone. Assuming energy band n is isolated, any property of the band will evolve smoothly with k_z. In consequence, because the Chern number of the closed torus is integer valued, it must take the same value for any k_z. The argument is identical also for planes in the k_x and k_y directions. Thus, any fully isolated band n of a three dimensional crystal can be characterized by a triplet of Chern numbers (c_{nx}, c_{ny}, c_{nz}).

For two-dimensional crystals with a corresponding two-dimensional reciprocal space, the Berry curvature (5.8) of each energy band n has only one component, conventionally written $\Omega_{xy}^{(n)}(\boldsymbol{k}) = \mathcal{B}_z^{(n)}(\boldsymbol{k})$. In this case the Brillouin zone has the topological shape of a regular torus, and hence constitutes a two-dimensional closed manifold itself. In consequence, even though the parameter space is two-dimensional, a Chern number (5.11) for two-dimensional crystalline systems can be defined by integrating over the entire Brillouin zone as

$$c_n = \frac{1}{2\pi} \oiint_{BZ} \mathcal{B}_z^{(n)}(\boldsymbol{k}) \mathrm{d}k_x \mathrm{d}k_y. \tag{5.16}$$

If the Chern number is non-zero, the two-dimensional crystalline system is classified as a *quantum anomalous Hall insulator*, also known as a *Chern insulator*. The Chern number will then be directly linked to the anomalous Hall conductivity of the material [24], briefly introduced in chapter 7.

5.2.2 Symmetry Restrictions on Berryological Quantities

For many crystalline systems the Hamiltonian is invariant under the operations of time reversal $\mathcal{T}$ and space inversion $\mathcal{P}$, both described in appendix B, which in turn puts restrictions on the berryological quantities of the Brillouin zone. Seeing that all derived quantities are dependent on the lattice periodic state vector, the general behaviour of the berryological quantities under space inversion and time reversal can be found by first investigating the corresponding behaviour of the lattice periodic function $u_{n\boldsymbol{k}}(\boldsymbol{r}) = \langle \boldsymbol{r} | u_{n\boldsymbol{k}} \rangle$.

Under both space inversion and time reversal, the crystal momentum $\boldsymbol{k}$ is inverted, whereas the position vector $\boldsymbol{r}$ is inverted only under space inversion. Additionally, the time reversal operator $\mathcal{T}$ involves a complex conjugation, being an antiunitary operator (C2). In conclusion, the lattice periodic function transforms under these operations as $\mathcal{P}u_{n\boldsymbol{k}}(\boldsymbol{r}) = u_{n-\boldsymbol{k}}(-\boldsymbol{r})$ and $\mathcal{T}u_{n\boldsymbol{k}}(\boldsymbol{r}) = u_{n-\boldsymbol{k}}^*(\boldsymbol{r})$.

A more rigorous derivation of the transformation properties can be found using the Bloch function, defined by $\psi_{n\boldsymbol{k}}(\boldsymbol{r}) = e^{i\boldsymbol{k}\cdot\boldsymbol{r}} u_{n\boldsymbol{k}}(\boldsymbol{r})$. Consider in particular the space inverted function $\mathcal{P}\psi_{n\boldsymbol{k}}(\boldsymbol{r})$, which transforms under a lattice translation as $T_{\boldsymbol{R}}\mathcal{P}\psi_{n\boldsymbol{k}}(\boldsymbol{r}) = \mathcal{P}T_{-\boldsymbol{R}}\psi_{n\boldsymbol{k}}(\boldsymbol{r}) = e^{i(-\boldsymbol{k})\cdot(-\boldsymbol{R})}\mathcal{P}\psi_{n\boldsymbol{k}}(\boldsymbol{r})$ by virtue of the Bloch theorem (B16). Assuming the Bloch functions corresponding to different bands can be made orthogonal (B21), the space inverted Bloch function thus becomes $\mathcal{P}\psi_{n\boldsymbol{k}}(\boldsymbol{r}) = \psi_{n-\boldsymbol{k}}(-\boldsymbol{r})$, which transfers directly to the lattice periodic function $u_{n\boldsymbol{k}}(\boldsymbol{r})$. In conclusion, the transformation property holds as long as the lattice periodic function is square integrable over the unit cell of the lattice. This condition holds in general whenever the energy bands are isolated, which is a prerequisite for defining the Berryological quantities of the Brillouin zone.

The transformation properties of the lattice periodic function under space inversion and time reversal can be inserted into the definition of the Berry connection (5.13), which in turn gives the transformation properties of the Berry phase (5.14) and the Berry curvature (5.15), from which the behaviour of the Chern number (5.11) follows directly. The results are summarized in table 5.1.

Berryological Quantity	Symbol	$\mathcal{P}$	$\mathcal{T}$	Invariance under Operation $\mathcal{O}$
Lattice Function	$u_{n\boldsymbol{k}}(\boldsymbol{r})$	$u_{n-\boldsymbol{k}}(-\boldsymbol{r})$	$u^*_{n-\boldsymbol{k}}(\boldsymbol{r})$	$\mathcal{O}u_{n\boldsymbol{k}}(\boldsymbol{r}) = e^{i\theta_n(\boldsymbol{k})}u_{n\boldsymbol{k}}(\boldsymbol{r})$
Berry Connection	$\boldsymbol{\mathcal{A}}^{(n)}(\boldsymbol{k})$	$-\boldsymbol{\mathcal{A}}^{(n)}(-\boldsymbol{k})$	$\boldsymbol{\mathcal{A}}^{(n)}(-\boldsymbol{k})$	$\mathcal{O}\boldsymbol{\mathcal{A}}^{(n)}(\boldsymbol{k}) = \boldsymbol{\mathcal{A}}^{(n)}(\boldsymbol{k}) + \nabla_{\boldsymbol{k}}\theta_n(\boldsymbol{k})$
Berry curvature	$\boldsymbol{\mathcal{B}}^{(n)}(\boldsymbol{k})$	$\boldsymbol{\mathcal{B}}^{(n)}(-\boldsymbol{k})$	$-\boldsymbol{\mathcal{B}}^{(n)}(-\boldsymbol{k})$	$\mathcal{O}\boldsymbol{\mathcal{B}}^{(n)}(\boldsymbol{k}) = \boldsymbol{\mathcal{B}}^{(n)}(\boldsymbol{k})$
Berry Phase	γ_n	γ_n	$-\gamma_n$	$\mathcal{O}\gamma_n = \gamma_n + 2\pi z$
Chern Number	c_n	c_n	$-c_n$	$\mathcal{O}c_n = c_n$

Table 5.1: The behaviour of berryological quantities under space inversion $\mathcal{P}$ and time reversal $\mathcal{T}$. The rightmost column gives the condition for invariance under a general operation $\mathcal{O}$ for the respective quantities, dependent on their gauge variance. The Chern number c_n refers to either element of the Chern number triplet (c_{nx}, c_{ny}, c_{nz}).

The rightmost column of table (5.1) gives the condition for invariance of the berryological quantities under any general operation. If then the $\boldsymbol{k}$-dependent Hamiltonian (B19) is invariant under a symmetry operation, this translates to symmetry restrictions on the berryological quantities. From the table, it is then seen that if a system is invariant under time reversal $\mathcal{T}$, the Berry phase must satisfy $-\gamma_n = \gamma_n + 2\pi z$, and so becomes $\gamma_n = \pi z$ for some integer z. Thus, because the Berry phase is gauge invariant modulo 2π, the only possible values of the Berry phase for systems invariant under time reversal are $\gamma_n = 0$ and $\gamma_n = \pi$. Under space inversion symmetry, no such constraint is present.

Consider then the behaviour of the Berry curvature $\boldsymbol{\mathcal{B}}^n(\boldsymbol{k})$ under both space inversion and time reversal, given in table 5.1. The Berry curvature must be even for a crystalline system invariant under space inversion $\mathcal{P}$, and odd for a crystalline system invariant under time reversal $\mathcal{T}$. If then the system is invariant under the combined $\mathcal{PT}$-symmetry, the Berry curvature must be zero at all points where it is defined, as it then satisfies $\boldsymbol{\mathcal{B}}^n(\boldsymbol{k}) = -\boldsymbol{\mathcal{B}}^n(\boldsymbol{k}) = 0$.

If however the Berry phase for some contour in the Brillouin zone is non-zero, it is not possible to define the Berry curvature over the entire Brillouin zone; at some points, the Berry curvature will be singular. In particular, for a two-dimensional system with both space inversion and time reversal symmetry, as time reversal symmetry imposes $\gamma_n = z\pi$, the Berry curvature under the restriction of $\mathcal{PT}$-symmetry need not be zero identically, but can take the form

$$\mathcal{B}^{(n)}_z(\boldsymbol{k}) = \sum_a z_a \pi \delta(\boldsymbol{k} - \boldsymbol{k}_a), \tag{5.17}$$

where $\delta(\boldsymbol{k})$ is the Dirac delta function. Here, the crystal momenta $\boldsymbol{k}_a$ are points in the Brillouin zone where the energy bands are degenerate, leading to the singular behaviour of the Berry curvature. The integers z_a then correspond to the Berry phase $\gamma_n = c_a\pi$ for any contour enclosing solely the momentum $\boldsymbol{k}_a$. Because Berry phases are only defined modulo 2π, the singularities can be categorized depending on z_i is even or odd. In particular, if the number z_a is odd and the energy band structure is linear near the degeneracy, the corresponding crystal momentum $\boldsymbol{k}_a$ is known as a *Weyl point*.

5.3 The Berryology of Two-Level Systems

In general, a quantum two-level system is any system whose Hilbert space of states is two-dimensional. Any state of the system can then be described as a superposition of two orthonormal basis states, hereby denoted $|0\rangle$ and $|1\rangle$.

Only based on the assumption of a two-level system, it is possible to find a general Hamiltonian of the system with a general set of parameters, and in turn calculate the Berryological quantities involved. A particular case for a two-level system is the tightbinding model for graphene, derived in section 4.3.

5.3.1 Description of a General Two-Level System

A general state of a two-level system is denoted $|\psi\rangle = c_0 |0\rangle + c_1 |1\rangle$. Left multiplying by $\langle i|$ and using the orthonormality of the basis states, these coefficients can be expressed $c_i = \langle i|\psi\rangle$. Introduce then the *matrix representation* of quantum mechanics, in which the state of the system is represented by the column vector denoted $\psi = (c_0, c_1) = (\langle 0|\psi\rangle, \langle 1|\psi\rangle)$. The two basis states are then represented by $\psi_0 = (1, 0)$ and $\psi_1 = (0, 1)$ respectively, giving $\psi = c_0\psi_0 + c_1\psi_1$.

Consider then the Hamiltonian $\hat{H}$ of the system, whose eigenvalue equation is given by $\hat{H}|\psi\rangle = E|\psi\rangle$. Left multiplying by either basis state $\langle i|$ and using their completeness relation (1.1), the eigenvalue equation takes the form of a matrix equation $\mathcal{H}\psi = E\psi$, where the *Hamiltonian matrix* is given by

$$\mathcal{H} = \begin{bmatrix} \langle 0|\hat{H}|0\rangle & \langle 0|\hat{H}|1\rangle \\ \langle 1|\hat{H}|0\rangle & \langle 1|\hat{H}|1\rangle \end{bmatrix} \equiv \begin{bmatrix} \mathcal{H}_{00} & \mathcal{H}_{01} \\ \mathcal{H}_{10} & \mathcal{H}_{11} \end{bmatrix}$$

Notice here that $\mathcal{H}_{10} = \mathcal{H}_{01}^*$, making the Hamiltonian matrix a hermitian matrix. The energies E can be calculated as the eigenvalues of this matrix.

In consequence, any two-level system can be described in the matrix formulation of quantum mechanics by the Hamiltonian matrix. Then because the two-dimensional identity matrix and the three Pauli matrices (C8) respectively denoted by $\sigma_0 \equiv I_2$ and $\boldsymbol{\sigma} = (\sigma_x, \sigma_y, \sigma_z)$ span the space of complex (2×2) hermitian matrices, a general two-level Hamiltonian matrix can be expressed

$$\mathcal{H} = h_0\sigma_0 + \boldsymbol{h}\cdot\boldsymbol{\sigma} = \begin{bmatrix} h_0 + h_z & h_x - ih_y \\ h_x + ih_y & h_0 - h_z \end{bmatrix}. \tag{5.18}$$

The vector $\boldsymbol{h} = (h_x, h_y, h_z)$ will in the following be referred to as the *Bloch vector* of the two-level system, with the three components and the scalar h_0 all being real. With the decomposition of the Hamiltonian matrix in terms of the Pauli matrices, the corresponding energy eigenvalues are readily calculated as

$$E_\pm = h_0 \pm |\boldsymbol{h}|. \tag{5.19}$$

Whenever the quantity h_0 is constant, it can be physically interpreted as the zero-point energy of the system, and can be subsumed into the energy eigenvalues without physical consequences. The eigenfunctions corresponding to the two energies are in general independent on the quantity h_0, and can be chosen

$$\psi_+ = \frac{1}{D(\boldsymbol{h})}\begin{bmatrix} h_z + |\boldsymbol{h}| \\ h_x + ih_y \end{bmatrix} \qquad \psi_- = \frac{1}{D(\boldsymbol{h})}\begin{bmatrix} -h_x + ih_y \\ h_z + |\boldsymbol{h}| \end{bmatrix} \tag{5.20}$$

where the normalization constant is given by $D^2(\boldsymbol{h}) = 2|\boldsymbol{h}|[h_z + |\boldsymbol{h}|]$. Notice now that the energy eigenvalues (5.19) of the two-level system are degenerate whenever the Bloch vector $\boldsymbol{h} = 0$, where both energy eigenvalues take on the value $E_\pm = h_0$. Inserting $\boldsymbol{h} = 0$, it is seen that the degeneracy corresponds to a singular behaviour of the eigenfunctions (5.20) of the Hamiltonian matrix.

Introducing spherical coordinates, letting $\boldsymbol{h} = |\boldsymbol{h}|(\sin\eta\cos\xi, \sin\eta\sin\xi, \cos\eta)$ where the polar angle $\eta \in [0, \pi)$ and the angle azimuth $\xi \in [0, 2\pi)$, the two eigenstates take the form

$$\psi_+ = \begin{bmatrix} \cos\left(\frac{\eta}{2}\right) \\ e^{i\xi}\sin\left(\frac{\eta}{2}\right) \end{bmatrix} \quad \psi_- = \begin{bmatrix} e^{i(\pi-\xi)}\sin\left(\frac{\eta}{2}\right) \\ \cos\left(\frac{\eta}{2}\right) \end{bmatrix}$$

For the particular Bloch vector $\boldsymbol{h} = (0, 0, h_z)$, the eigenvectors of the Hamiltonian (5.20) coincide with the originally defined basis vectors, denoted $\psi_+ = (1, 0)$ and $\psi_- = (0, 1)$.

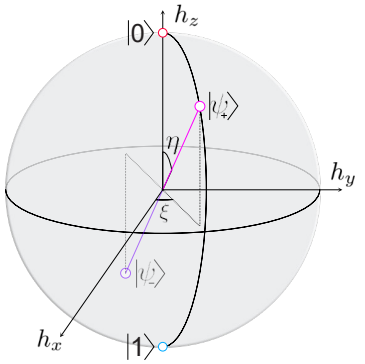

Figure 5.1: The Bloch sphere, visualizing the mapping between the unit sphere spanned by the Bloch unit vector $\hat{\boldsymbol{h}}$ and the two-dimensional Hilbert space of a two-level system. The basis states of the Hilbert space are denoted $|0\rangle$ and $|1\rangle$, and are mapped onto the two poles of the sphere. The eigenstates of the Hamiltonian of the two-level system are denoted $|\psi_\pm\rangle$, mapped onto two antipodal points.

By argument from the spherical representation, there exists a bijective map between the Hilbert space of the two-level system and the unit sphere in three dimensions. This unit sphere is known as the *Bloch sphere*, which is traced out by the normalized Bloch vector $\hat{\boldsymbol{h}} = \boldsymbol{h}/|\boldsymbol{h}|$, and gives a geometrical visualization of the two-level system Hilbert space. The Bloch sphere is shown in figure 5.1, with the two basis states at the poles. The two eigenvectors of the Hamiltonian then map onto two diametrically opposite points on the sphere, with ψ_+ and ψ_- conventionally chosen at the positive and negative h_z-hemisphere, respectively.

5.3.2 Berryological Quantitites for Two-Level Systems

In general, the parameter h_0 and Bloch vector $\boldsymbol{h}$ are dependent on a set of parameters $\boldsymbol{\mathcal{R}}$. This dependence can be assumed continuous, and translates to the Hamiltonian matrix (5.18) and its corresponding eigenvectors (5.20), allowing for a definition of berryological quantities for the two-level system.

Consider the Berry curvature (5.9) of the two-level system, whose sum now consists of only one term. Using the completeness relation (1.1) of the basis states of the two-level system, the Berry curvature is rewritten in terms of the general Hamiltonian matrix (5.18) as a product of two quadratic forms

$$\Omega^{\pm}_{\mu\nu} = -2\,\mathrm{Im}\,\frac{(\psi^{\dagger}_{\pm}[\partial_\mu\mathcal{H}]\psi_{\mp})(\psi^{\dagger}_{\mp}[\partial_\nu\mathcal{H}]\psi_{\pm})}{[E_{\pm}-E_{\mp}]^2}. \tag{5.21}$$

Notice here that $(\psi^{\dagger}_{\mp}[\partial_\mu\mathcal{H}]\psi_{\pm}) = (\psi^{\dagger}_{\pm}[\partial_\mu\mathcal{H}]\psi_{\mp})^*$, and so $\Omega^{-}_{\mu\nu} = -\Omega^{+}_{\mu\nu}$. This is a manifestation of the previously derived result that the total Berry curvature summed over all band indices should be zero (5.12).

In the expression (5.21), the derivative of the Hamiltonian matrix (5.18) becomes $\partial_\mu\mathcal{H} = \partial_\mu h_0\sigma_0 + \partial_\mu\boldsymbol{h}\cdot\boldsymbol{\sigma}$, and the denominator $E_{\pm} - E_{\mp} = \pm 2|\boldsymbol{h}|$. Inserting also the eigenvectors (5.20), the components of the Berry curvature for a general two-level system described by the Bloch vector $\hat{\boldsymbol{h}}$ can be calculated

$$\Omega^{\pm}_{\mu\nu} = \mp\frac{1}{2|\boldsymbol{h}|^3}\boldsymbol{h}\cdot[\partial_\mu\boldsymbol{h}\times\partial_\nu\boldsymbol{h}] = \mp\frac{1}{2}\hat{\boldsymbol{h}}\cdot[\partial_\mu\hat{\boldsymbol{h}}\times\partial_\nu\hat{\boldsymbol{h}}] \tag{5.22}$$

independent on the parameter h_0, where the second equality follows from writing out the derivatives. From this expression, the Berry curvature is singular at any point $\boldsymbol{\mathcal{R}} = \boldsymbol{\mathcal{R}}_0$ in parameter space leaving $\boldsymbol{h}(\boldsymbol{\mathcal{R}}_0) = 0$, corresponding to the previously mentioned degeneracy of the energy eigenvalues (5.19) with $E_{\pm} = h_0$.

The found expression for the Berry curvature of a general two-level system (5.22) yields a particular interpretation of the Chern number (5.11). Recalling the assumption that $\boldsymbol{h}(\boldsymbol{\mathcal{R}})$ varies continuously with the parameter set $\boldsymbol{\mathcal{R}}$, any enclosed surface $\mathcal{S}$ in the parameter space $\boldsymbol{\mathcal{R}}$ will correspond to a closed two-dimensional manifold $\boldsymbol{h}(\mathcal{S})$ drawn by the Bloch vector $\boldsymbol{h}$. Consider then the projection $\hat{\boldsymbol{h}}(\mathcal{S})$ of the initial closed manifold $\boldsymbol{h}(\mathcal{S})$ onto the Bloch sphere of figure 5.1. Upon this projection, the manifold $\hat{\boldsymbol{h}}(\mathcal{S})$ will cover the entire Bloch sphere only if the initial surface $\boldsymbol{h}(\mathcal{S})$ encloses the origin $\boldsymbol{h} = 0$. More precisely, if the initial manifold wraps around the origin B times, the Bloch sphere will correspondingly be covered B times. Thus in general, the closed manifold $\hat{\boldsymbol{h}}(\mathcal{S})$ will subtend a solid angle from the origin given by $4\pi B$. The integer B is known as the *Brouwer degree* of the map $\hat{\boldsymbol{h}}(\boldsymbol{\mathcal{R}})$, thus giving how many times the Bloch sphere is covered by the map. Notice that the Brouwer degree B is a positive or a negative integer whenever the normal vector of the manifold $\boldsymbol{h}(\mathcal{S})$ points away from or towards the origin of the Bloch sphere $\boldsymbol{h} = 0$, respectively.

In viewing the normalized Bloch vector $\hat{\boldsymbol{h}}(\boldsymbol{\mathcal{R}})$ as a map from parameter space to the surface of the Bloch sphere, the expression for the general two-level Berry curvature (5.22) is nothing but half the Jacobian determinant corresponding to the map $\hat{\boldsymbol{h}}(\boldsymbol{\mathcal{R}})$. The Chern number (5.11) is thus readily expressed

$$c_{\pm} = \mp\frac{1}{4\pi}\oint_{\mathcal{S}}\hat{\boldsymbol{h}}\cdot[\partial_\mu\hat{\boldsymbol{h}}\times\partial_\nu\hat{\boldsymbol{h}}]\mathrm{d}s_\mu\wedge\mathrm{d}s_\nu = \mp B. \tag{5.23}$$

Here, the center integral is evaluated as the integral of the map $\hat{\boldsymbol{h}}(\mathcal{S})$ over the Bloch sphere. In consequence, the Chern number corresponding to some surface $\mathcal{S}$ in parameter space gives the Brouwer degree B of the map $\mathcal{S}\mapsto\hat{\boldsymbol{h}}(\mathcal{S})$, which equals the number of times the surface $\hat{\boldsymbol{h}}(\mathcal{S})$ covers the Bloch sphere. Hence, the Chern number is zero unless the surface $\mathcal{S}$ encloses some point of degeneracy $\boldsymbol{\mathcal{R}}_0$ in parameter space for which $\boldsymbol{h}(\boldsymbol{\mathcal{R}}_0) = 0$.

As a result of this interpretation, all surfaces with the same topology enclosing a degeneracy point $\boldsymbol{\mathcal{R}}_0$ in parameter space will give the same Chern number. It is then meaningful to speak of the Chern number as a topological invariant of the degeneracy point itself. Analogous to a magnetic monopole, the degeneracy point $\boldsymbol{\mathcal{R}}_0$ acts as a source or a sink of Berry curvature in parameter space, corresponding to a positive or negative Chern number respectively.

Viewing the Bloch vector $\hat{h}(\boldsymbol{\mathcal{R}})$ as a map from parameter space to the surface of the Bloch sphere and the Berry curvature (5.22) as the Jacobian determinant of this map also leaves a simple interpretation of the Berry phase (5.10). Choosing any closed contour $\mathcal{C}$ in parameter space, corresponding to a closed contour $\hat{\boldsymbol{h}}(\mathcal{C})$ on the surface of the Bloch sphere, the Berry phase readily becomes

$$\gamma_{\pm} = \mp\frac{1}{2}\int_{\mathcal{S}} \hat{\boldsymbol{h}} \cdot [\partial_\mu \hat{\boldsymbol{h}} \times \partial_\nu \hat{\boldsymbol{h}}] \mathrm{d}s_\mu \wedge \mathrm{d}s_\nu = \mp\frac{1}{2}\Omega_{\mathcal{C}}$$

where $\Omega_{\mathcal{C}}$ is the area on the Bloch sphere enclosed by the contour $\hat{\boldsymbol{h}}(\mathcal{C})$.

Another expression for the Berry phase can also be calculated explicitly in terms of the Berry connection (5.2), which for the two-level system also can be rewritten with respect to the eigenvectors of the Hamiltonian matrix (5.20). The components of the Berry connection then becomes

$$\mathcal{A}_\mu^{\pm} = i\psi_{\pm}^\dagger \partial_\mu \psi_{\pm} = \pm\frac{h_y\partial_\mu h_x - h_x \partial_\mu h_y}{2|\boldsymbol{h}|(|\boldsymbol{h}| + h_z)} = \mp\frac{(\boldsymbol{h}\times\partial_\mu \boldsymbol{h})_z}{2|\boldsymbol{h}|(|\boldsymbol{h}| + h_z)}. \tag{5.24}$$

Hence, the Berry connection becomes proportional to the h_z-component of the cross product between the Bloch vector and its derivative. Alternately, in terms of the spherical coordinates of the Bloch sphere, the Berry connection becomes

$$\boldsymbol{\mathcal{A}}^{\pm}(\eta, \xi) = \mp\sin^2\left(\frac{\eta}{2}\right)\nabla_{\boldsymbol{\mathcal{R}}}\xi \tag{5.25}$$

Notice here that both angles are in general dependent on the parameter set $\boldsymbol{\mathcal{R}}$.

Choose then in particular a closed contour $\mathcal{C}$ in parameter space corresponding to a contour on the Bloch sphere $\hat{\boldsymbol{h}}(\mathcal{C})$ at a constant polar angle η. For such contours, by inserting the expression for the Berry connection (5.25), the Berry phase (5.4) can readily be expressed

$$\gamma_{\pm} = \mp\sin^2\left(\frac{\eta}{2}\right)\oint_{\mathcal{C}} \nabla_{\boldsymbol{\mathcal{R}}}\xi(\boldsymbol{\mathcal{R}}) \cdot \mathrm{d}\boldsymbol{\mathcal{R}} = \mp 2\pi\Gamma\sin^2\left(\frac{\eta}{2}\right) = \mp\pi\Gamma\Big(1 - \frac{h_z}{|\boldsymbol{h}|}\Big) \tag{5.26}$$

Here, $\Delta\xi = 2\pi\Gamma$ is the change in the angle azimuth ξ on the Bloch sphere upon moving around the contour in parameter space once, where Γ is the winding number of the contour with respect to the h_z-axis of the Bloch sphere. In consequence, the Berry phase (5.4) for a fixed polar angle η becomes dependent only on the winding number of the contour. In particular, at the Bloch sphere equator with $\eta = \pi/2$, the Berry phase $\gamma_{\pm} = \mp\pi\Gamma$. Notice that this expression for the Berry phase (5.26) is in agreement with the Berry phase corresponding to half the enclosed area on the Bloch sphere, which for a contour at a constant latitude η is given by the formula $\Omega_{\mathcal{C}} = 4\pi\sin^2(\eta/2)$.

5.3.3 The Berryology of Graphene

A particular example for two-levels systems is that of crystals with diatomic primitive unit cells in general, and that of graphene in particular, both of which is investigated in section 4.3. In neglecting the Coulomb interaction between electrons, the Hamiltonian of these systems is written as a sum of single-electron terms, each of which takes the second quantized form $\Psi_{\boldsymbol{k}}^\dagger \mathcal{H}(\boldsymbol{k})\Psi_{\boldsymbol{k}}$ with $\mathcal{H}$ being the Hamiltonian kernel (4.11). The two rows of the Hamiltonian kernel then corresponds to an electron located at either of the two sublattices of the diatomic lattice structure, thus enabling a two-level description.

As can be seen from the expression of the Hamiltonian kernel (4.22), recalling that $\mathcal{H} = h_0\sigma_0 + \boldsymbol{h}\cdot\boldsymbol{\sigma}$ for a general two-level system (5.18), the Bloch vector for a general diatomic crystal take the form $\boldsymbol{h}(\boldsymbol{k}) = (-\operatorname{Re}\phi(\boldsymbol{k}), \operatorname{Im}\phi(\boldsymbol{k}), -\Delta/2)$. Here the structure factor $\phi(\boldsymbol{k})$ depends only on the crystal momentum $\boldsymbol{k}$, whereas the bandgap Δ is a constant of the crystalline system. The parameter space is given by the Brillouin zone of the crystal, denoted $\boldsymbol{\mathcal{R}} = \boldsymbol{k}$.

Let the Brillouin zone be two dimensional, leaving only one component of the Berry curvature (5.8). Inserting the vector $\boldsymbol{h} = (-\operatorname{Re}\phi(\boldsymbol{k}), \operatorname{Im}\phi(\boldsymbol{k}), -\Delta/2)$ into the general expression for the Berry curvature of two-level systems (5.22), the Berry curvature for a two-dimensional diatomic crystal becomes

$$\mathcal{B}_z^\pm = \Omega_{xy}^\pm = \mp\frac{\Delta}{4}\left[\frac{\operatorname{Re}\{\partial_x\phi\}\operatorname{Im}\{\partial_y\phi\} - \operatorname{Im}\{\partial_x\phi\}\operatorname{Re}\{\partial_y\phi\}}{(t^2|\phi|^2 + \frac{\Delta^2}{4})^{\frac{3}{2}}}\right] \tag{5.27}$$

where the partial derivatives $\partial_\mu \equiv \partial/\partial k_\mu$ are with respect to the components of the crystal momentum. Notice here that even though the structure factor is not periodic with the Brillouin zone, but changes by a phase upon a reciprocal lattice translation, the Berry curvature does satisfy $\mathcal{B}_z^\pm(\boldsymbol{k} - \boldsymbol{G}_j) = \mathcal{B}_z^\pm(\boldsymbol{k})$.

Inserting the structure factor for graphene (4.28) into the expression for the Berry curvature (5.27) above leaves the Berry curvature for gapped graphene

$$\mathcal{B}_z^\pm = \mp\frac{\sqrt{3}a^2t^2\Delta}{16}\left[\frac{4\sin\left(\frac{\sqrt{3}a}{2}k_y\right)\cos\left(\frac{3}{2}ak_x\right) - 2\sin\left(\sqrt{3}ak_y\right)}{(t^2[3+2\cos\left(\sqrt{3}ak_y\right)+4\cos\left(\frac{\sqrt{3}}{2}ak_y\right)\cos\left(\frac{3}{2}ak_x\right)]+\frac{\Delta^2}{4})^{\frac{3}{2}}}\right] \tag{5.28}$$

Notice here that the Berry curvature is an odd function of the reciprocal vector $\boldsymbol{k}$, as $\mathcal{B}_z^\pm(-\boldsymbol{k}) = -\mathcal{B}_z^\pm(\boldsymbol{k})$, which is a consequence of the time reversal symmetry of the system as noted by the symmetry restrictions of table 5.1.

The Berry curvature of the conduction band $\mathcal{B}_z^+$ is plotted for different bandgaps in figure 5.2. Comparing the curvature to the energy bands in figure 4.4, it is seen that the Berry curvature is mostly negligible, except near the Brillouin zone corner points $\boldsymbol{K}$ and $\boldsymbol{K}'$ at which the energy bands are at their closest. In particular, with a zero bandgap $\Delta = 0$, the system becomes invariant under space inversion and the Berry curvature vanishes everywhere except at the Brillouin zone corners where it diverges, being ill defined at the degeneracy.

Consider then the Hamiltonian kernel expanded about the Brillouin zone corners at low energies (4.32), giving the Bloch vector $\boldsymbol{h} = (\pm v_f q_x, v_f q_y, -\Delta/2)$, where the signs corresponds to the corner points $\boldsymbol{K}$ and $\boldsymbol{K}'$, respectively. Inserting this into the formula for Berry curvature (5.22) of the conduction band

$$\mathcal{B}_z^+(\boldsymbol{q}) = \mp \frac{v_f^2 \Delta}{4\Big(v_f^2 \boldsymbol{q}^2 + \big(\frac{\Delta}{2}\big)^2\Big)^{\frac{3}{2}}} \tag{5.29}$$

Here, the upper sign corresponds to the corner point $\boldsymbol{K}$ and the lower to $\boldsymbol{K}'$. In the limit $\Delta = 0$, the Berry curvature is again seen to approach identically zero except at the corner points where $\boldsymbol{q} = 0$ and the Berry curvature diverges.

In particular, for a constant energy contour in the Brillouin zone surrounding either of the corner points $\boldsymbol{K}$ and $\boldsymbol{K}'$. Using the Bloch vector of graphene near the corner points, the Berry phase (5.26) of this contour is readily given by [25]

$$\gamma_+ = -\pi\left(1 - \frac{\Delta}{2\sqrt{v_f^2 \boldsymbol{q}^2 + (\frac{\Delta}{2})^2}}\right) \tag{5.30}$$

where now $|\boldsymbol{q}| \neq 0$ is fixed for the particular contour. For pure graphene with $\Delta = 0$, the Berry phase thus attains the non-trivial value $\gamma_+ = -\pi$ for any contour surrounding either of the Brillouin zone corner points. Notice also that for $\Delta \neq 0$, the magnitude of the Berry phase decreases with increasing bandgap Δ.

For $\Delta = 0$ the space inversion symmetry of graphene is restored, and the energy band structure obtains two Weyl points of opposite sign located at the Brillouin zone corner points $\boldsymbol{K}$ and $\boldsymbol{K}'$. These Weyl points are topologically protected by the space inversion and time reversal symmetries of the crystalline system, and so graphene can be categorized as a *symmetry-protected Weyl semimetal*. The topological properties of graphene are precursors to defining the Dirac and Weyl semimetals in three dimensions, being the main topic of chapter 6.

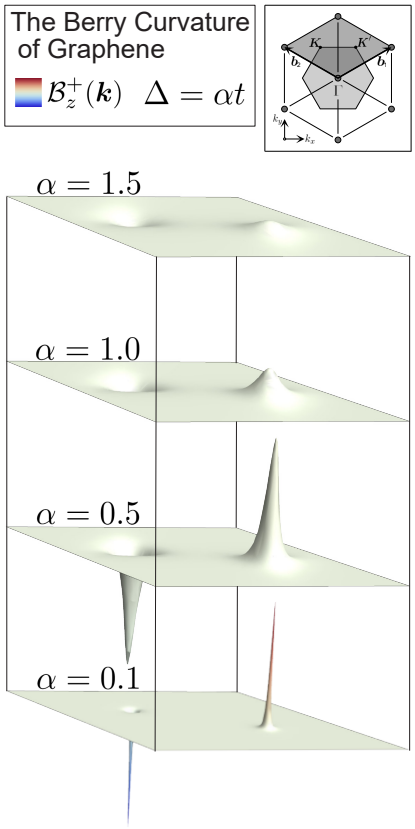

Figure 5.2: The Berry curvature $\mathcal{B}_z^+(\boldsymbol{k})$ of graphene for different values of the ratio $\alpha \equiv \Delta/t$, where Δ is the bandgap and t the tunnelling rate. The height of the peaks located at the Brillouin zone corners $\boldsymbol{K}$ and $\boldsymbol{K}'$ is given by $9/2\alpha^2$. The three upper graphs are drawn using the same scale, whereas the peak for $\alpha = 0.1$ is 25 times higher than for $\alpha = 0.5$.

Chapter 6

Dirac and Weyl Semimetals

In section 4.3, the tightbinding model revealed that the point symmetries of the two-dimensional crystal lattice of pure graphene made the non-relativistic Schrödinger Hamiltonian (4.21) effectively take on the same form as the relativistic Weyl Hamiltonian at low energies. Graphene is a part of a larger class of materials known as *topological semimetals*, in which features of the energy band structure are protected by topology rather than or in combination with symmetry. The following chapter describes the emergence of two particular types of topological semimetals, known as *Dirac* and *Weyl* semimetals.

Common to both Weyl and Dirac semimetals, the energy band structure is completely gapped at the Fermi level, except for at a single point in the Brillouin zone where the energy band structure is twofold and fourfold degenerate respectively, around which the dispersion relation is locally linear. Unlike Weyl semimetals the energy band structure of Dirac semimetals are Kramers degenerate, usually attributed to the crystalline structure being invariant under the $\mathcal{PT}$-symmetry, elaborated on in appendix C. A Weyl semimetal can then be produced from a Dirac semimetal by breaking the $\mathcal{PT}$-symmetry, which lifts the Kramers degeneracy of the band structure and splits the fourfold degenerate Dirac point into two doubly degenerate Weyl nodes.

Weyl semimetals were predicted theoretically in 2011 by Burkov, Hook and Balents [4] and experimentally verified first for the material tantalum arsenide (TaAs) in 2015 by Xu et al. [26]. Also in 2015, Soluyanov et al. [27] extended the classification of Weyl semimetals to include two types: in addition to breaking the $\mathcal{PT}$-symmetry, Weyl Type-II materials also violate the effective Lorentz invariance preserved more or less stringently in Weyl Type-I semimetals. The first verified Weyl Type-II semimetal was lanthanum aluminum germanide (LaAlGe), found experimentally by Xu et al. [28] in 2017.

The following chapter presents the theory of Dirac and Weyl semimetals as given through the several seminal papers on the subjects from recent years. The mathematical concepts behind the classification and symmetry arguments of Weyl semimetals however originates in fermionic quantum field theory, elaborated upon in appendix D, along which the chapter runs parallel.

6.1 Weyl Semimetals

The following section investigates the emergence of Weyl nodes as points of degeneracy for a general energy band structure comprising two energy bands. The section relies heavily on chapter 5 on two-level systems and berryological quantities, from which the topological protection of Weyl nodes originates, and runs parallel to the relativistic derivation of Weyl fermions in appendix D.

6.1.1 The Hamiltonian Kernel of Weyl Semimetals

In order to investigate the properties of Weyl semimetals, introduce similarly to the Hamiltonian matrix of two-level systems (5.18) the *two-band kernel*

$$\mathcal{H}(\boldsymbol{k}) = h_0(\boldsymbol{k})\tau_0 + \boldsymbol{\tau}\cdot\boldsymbol{h}(\boldsymbol{k}) \tag{6.1}$$

where $(\tau_0, \tau_x, \tau_y, \tau_z)$ is a complete set of Pauli matrices (C8) corresponding to some pseudospin degree of freedom, with $h_0(\boldsymbol{k})$ and $\boldsymbol{h}(\boldsymbol{k}) = (h_x(\boldsymbol{k}), h_y(\boldsymbol{k}), h_z(\boldsymbol{k}))$ being four real parameters of the crystalline system. The two-band kernel is a generalization of the graphene Hamiltonian kernel (4.22), which was derived based on the tightbinding approximation. Here however, no assumptions are made on the origin of the pseudospin degree of freedom.

Denoting by $\tau = \pm 1$ the pseudospin index, the two energy eigenvalues corresponding to the two-band kernel (6.1) can be written on the form

$$\varepsilon_\tau(\boldsymbol{k}) = h_0(\boldsymbol{k}) + \tau\sqrt{h_x^2(\boldsymbol{k}) + h_y^2(\boldsymbol{k}) + h_z^2(\boldsymbol{k})}, \tag{6.2}$$

which describe two energy bands of the crystalline system. The energy spectrum is entirely gapped, except for momenta $\boldsymbol{k}_0$ where $h_x(\boldsymbol{k}_0) = h_y(\boldsymbol{k}_0) = h_z(\boldsymbol{k}_0) = 0$. This condition gives three equations for the momentum $\boldsymbol{k}_0$, which without any additional tuning in general requires three independent variables in order to have a solution. Hence, such points of double degeneracy can be expected to exist for the spatial dimension $d = 3$. In this case, as the two-band kernel (6.1) exhausts the basis for two-dimensional hermitian matrices, the degeneracy will in general be stable to small perturbations to the system parameters [5].

Consider then the expansion of the two-band kernel (6.1) to linear order about the degeneracy at $\boldsymbol{k}_0$, with the momentum $\boldsymbol{q} \equiv \boldsymbol{k} - \boldsymbol{k}_0$ being denoted by

$$\mathcal{H}(\boldsymbol{q}) = (\varepsilon_0 + \hbar\boldsymbol{v}_0\cdot\boldsymbol{q})\tau_0 + (\hbar\boldsymbol{v}_x\cdot\boldsymbol{q})\tau_x + (\hbar\boldsymbol{v}_y\cdot\boldsymbol{q})\tau_y + (\hbar\boldsymbol{v}_z\cdot\boldsymbol{q})\tau_z. \tag{6.3}$$

Here the parameter $\varepsilon_0 = h_0(\boldsymbol{k}_0)$, while the effective velocities $\boldsymbol{v}_\mu = (v_{\mu x}, v_{\mu y}, v_{\mu z})$ are defined as the gradients $\hbar\boldsymbol{v}_\mu = \nabla_{\boldsymbol{k}} h_\mu(\boldsymbol{k})\big|_{\boldsymbol{k}=\boldsymbol{k}_0}$; recall here the matrix elements of the velocity operator (3.10) in the Bloch basis. Unless the effective velocities $\boldsymbol{v}_i$ for $i \in \{x, y, z\}$ are linearly dependent due to additional symmetries, the degeneracy point located at $\boldsymbol{q} = 0$ is a *Weyl node*, with

$$\varepsilon_\tau(\boldsymbol{q}) = \varepsilon_0 + \hbar\boldsymbol{v}_0\cdot\boldsymbol{q} + \tau\sqrt{(\hbar\boldsymbol{v}_x\cdot\boldsymbol{q})^2 + (\hbar\boldsymbol{v}_y\cdot\boldsymbol{q})^2 + (\hbar\boldsymbol{v}_z\cdot\boldsymbol{q})^2} \tag{6.4}$$

being locally linear around the point of degeneracy. The shape of the energy dispersion around the Weyl node is known as a *Weyl cone*, depicted in figure 6.1. The effect of the effective velocities $\boldsymbol{v}_0$ and $\boldsymbol{v}_i$ is to tilt the Weyl cone or alter its shape respectively without changing its location in the energy band spectrum, and the former vector is known as the *tilting vector*. If the energy at the Weyl node ε_0 lies near or at the Fermi level μ of the fermionic system, the material is said to be a *Weyl semimetal*. For simplicity, assume both the reference energy $\varepsilon_0 = 0$ and the tilting vector $\boldsymbol{v}_0 = 0$; a non-zero tilting of the Weyl cone is investigated in the subsequent subsection.

If the Fermi-level μ lies near the Weyl node, the *Fermi surface* defined by the equation $\varepsilon_\tau(\boldsymbol{k}) - \mu = 0$ takes the shape of an ellipsoid in momentum space. Consider then a linear transformation of the crystal momentum, given by

$$\boldsymbol{v}_i \cdot \boldsymbol{q} = v_{ix}q_x + v_{iy}q_y + v_{iz}q_z = v_F\kappa_i, \tag{6.5}$$

for each of the three effective velocities $\boldsymbol{v}_i$. Here, the introduced parameter v_F is an isotropic effective velocity. Denoting by $\mathcal{V}$ the matrix with elements v_{ij}, the transformation can be written on the form $\mathcal{V}\boldsymbol{q} = v_F\boldsymbol{\kappa}$, where the transformed crystal momentum is denoted by $\boldsymbol{\kappa} = (\kappa_1, \kappa_2, \kappa_3)$. Because the transformation is linear, the corresponding Jacobian matrix is independent on the crystal momentum and given by $\mathcal{V}/v_F$, with the Jacobian determinant $\det \mathcal{V}/v_F^3$ where

$$\det \mathcal{V} = \boldsymbol{v}_x \cdot (\boldsymbol{v}_y \times \boldsymbol{v}_z) \tag{6.6}$$

The transformation of the crystal momentum renders the Fermi surface spherical, with the transformed energy bands $\varepsilon_s(\boldsymbol{\kappa}) = sv_F|\boldsymbol{\kappa}|$ being dependent only on the magnitude of the transformed momentum $|\boldsymbol{\kappa}| \equiv \kappa$. The condition that the three effective velocities $\boldsymbol{v}_i$ are linearly independent here corresponds to a non-zero determinant $\det \mathcal{V} \neq 0$, such that the inverse transformation $\boldsymbol{q} = v\mathcal{V}^{-1}\boldsymbol{\kappa}$ is well defined. For $\det \mathcal{V} = 0$, the Fermi surface becomes unbounded in some direction, leaving the transformation ill defined.

In particular, for the isotropic case $v_{ij} = \delta_{ij}v_F$, the defined transformation of the crystal momentum (6.5) is the identity transform, with $\boldsymbol{\kappa} = \boldsymbol{q}$. In this case, the Hamiltonian kernel (6.3) becomes a three dimensional analogue to the effective Hamiltonian kernel of graphene (4.32), and the parameter v_F can be interpreted as the effective velocity of the electrons at the Fermi level. The Hamiltonian kernel is then mathematically identical to the Weyl Hamiltonian (D17) of relativistic fermionic quantum theory, as derived from the condition of Lorentz invariance in appendix D, and can be written on the form

$$\mathcal{H}(\boldsymbol{\kappa}) = \hbar v_F(\boldsymbol{\kappa} \cdot \boldsymbol{\tau}). \tag{6.7}$$

The Fermi velocity v_F here acts as an effective speed of light. The equivalence with the Weyl Hamiltonian is the reason for the nomenclature surrounding the class of materials known as Weyl semimetals. The electrons described by the Weyl Hamiltonian kernel (6.3) thus effectively behave as if they were ultrarelativistic, but with a different value for the speed of light in different directions.

6.1.2 The Tilting Vector and Weyl Type II Semimetals

In appendix D, the Weyl Hamiltonian (D17) describing massless Weyl fermions was derived on the basis of Lorentz invariance. For systems in solid state physics however, the Lorentz invariance exhibited by the systems investigated is merely an effective Lorentz invariance due to the symmetries of the systems, and is not a constraint from an underlying principle of the physical theory. This allows for a nonzero tilting vector $\boldsymbol{v}_0$ in the Weyl Hamiltonian kernel (6.3), and the corresponding energy bands can be expressed on the form

$$\varepsilon_\tau(\boldsymbol{q}) = \boldsymbol{v}_0 \cdot \boldsymbol{q} + \tau \sqrt{\sum_i (\hbar \boldsymbol{v}_i \cdot \boldsymbol{q})^2} \equiv T(\boldsymbol{q}) + \tau U(\boldsymbol{q}) \tag{6.8}$$

The tilting term clearly breaks the effective Lorentz invariance, being proportional to the momentum itself. Considering in particular isotropic effective velocities $v_{ij} = \delta_{ij} v_F$ and a tilting vector $\boldsymbol{v}_0 = (v_t, 0, 0)$, the corresponding Weyl cones are portrayed in figure 6.1 for different values of the tilting parameter v_t.

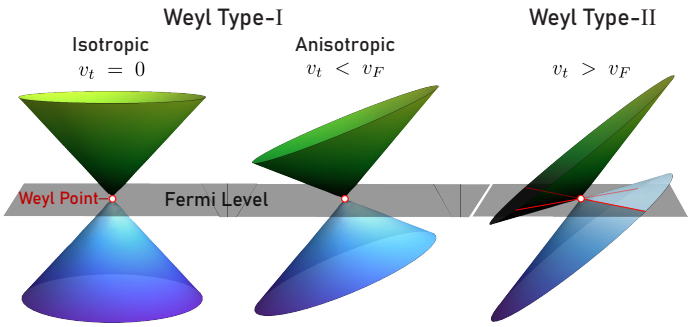

Figure 6.1: The distinction between Weyl nodes of Type-I and Type-II, with the Fermi level displayed as a translucent plane. In the leftmost figure an isotropic Weyl cone with an effective Fermi velocity v_F is shown. The effective Lorentz invariance is then increasingly broken by a tilting parameter v_t. At the critical point $v_t = v_F$, the Weyl cone tilts partially through the Fermi level, and the node transitions from a Weyl Type-I node to a Weyl Type-II node.

Due to the tilting vector $\boldsymbol{v}_t$, Weyl semimetals can be categorized into two types [27]. For Weyl Type-I semimetals, the Fermi level crosses the Weyl cone only at the Weyl node, as shown in figure 6.1. If however there exists a direction $\hat{\boldsymbol{q}}$ for which the tilting vector dominates, meaning $|T(\hat{\boldsymbol{q}})| > |U(\hat{\boldsymbol{q}})|$ for the energy band structure (6.8), the Weyl cone tilts through the Fermi level and the Weyl node is rendered a contact point between electron and hole pockets in the energy band structure. If such a direction exists, the Weyl node is of Type-II.

The tilting of the Weyl cone is analogous to the tilt of the light cone in general relativity near massive objects. Consequently, materials comprising both Weyl Type-I and Weyl Type-II materials have been proposed as solid state systems able to simulate analogues of black hole horizons, Hawking radiation and other astronomical phenomena known from general relativity [29].

6.1.3 Topological Analysis of Weyl Semimetals

Consider the isotropic Weyl Hamiltonian kernel (6.7), for which the Bloch vector becomes $\boldsymbol{h}(\boldsymbol{\kappa}) = \hbar v_F \boldsymbol{\kappa}$. Inserting this into the formula for the Berry curvature of a two-level system (5.21), which is related to the Berry curvature vector of the Brillouin zone (5.15) through $\mathcal{B}_\lambda = \frac{1}{2}\varepsilon_{\lambda\mu\nu}\Omega_{\mu\nu}$, the Berry curvature for the isotropic Weyl semimetal can be caltulated

$$\boldsymbol{\mathcal{B}}^\tau(\boldsymbol{\kappa}) = -\tau \, \mathrm{sgn}[v_F] \frac{\boldsymbol{\kappa}}{2|\boldsymbol{\kappa}|^3} \tag{6.9}$$

where $\mathrm{sgn}[v_F]$ denotes the sign of the Fermi velocity v_F. Hence, in the isotropic case the Weyl node located at $\boldsymbol{\kappa} = 0$ acts as a Berry curvature monopole in momentum space. The divergence of the Berry curvature readily becomes

$$\nabla_{\boldsymbol{\kappa}} \cdot \boldsymbol{\mathcal{B}}^\tau(\boldsymbol{\kappa}) = -2\pi\tau \, \mathrm{sgn}[v_F]\delta(\boldsymbol{\kappa}), \tag{6.10}$$

where $\delta(\boldsymbol{\kappa})$ is the Dirac delta function. In consequence, the Chern number (5.11) of any enclosed surface $\mathcal{S}$ in momentum space will be zero unless the surface encloses the Weyl node, for which the divergence theorem gives

$$c_\tau(v_F) = \frac{1}{2\pi} \oiint_{\mathcal{S}} \boldsymbol{\mathcal{B}}^\tau(\boldsymbol{\kappa}) \cdot \mathrm{d}\boldsymbol{\mathcal{S}} = \frac{1}{2\pi} \iiint_{\mathcal{Z}} \nabla_{\boldsymbol{\kappa}} \cdot \boldsymbol{\mathcal{B}}^\tau(\boldsymbol{\kappa}) \mathrm{d}\mathcal{Z} = -\tau \, \mathrm{sgn}[v_F] \tag{6.11}$$

where $\mathcal{Z}$ is the momentum space volume enclosed by the surface $\mathcal{S}$.

From the expression of the Berry curvature (6.9), the Chern number (6.11) can be interpreted as the *topological charge* of the Weyl node, which acts either as a sink or a source of Berry curvature depending on the sign of the Chern number. Furthermore, the Chern number is decided by the sign of the effective velocity v_F, which also gives the sign in front of the isotropic Weyl Hamiltonian kernel (6.7). Compared to the Weyl Hamiltonian (D17), the Chern number is then also analogous to the chirality of the Weyl fermions of relativistic fermionic theory. Thus, the electronic states near the Weyl node in the positive energy band $\tau = +1$ are effectively described as Weyl fermions with chirality $-\mathrm{sgn}[v_F]$.

Reconsider the linear transformation of the crystal momentum (6.5), which transforms the non-isotropic Weyl Hamiltonian kernel (6.7) to the isotropic Weyl Hamiltonian kernel (6.3). From this transformation, it is readily shown that the Chern number for the non-isotropic case can be expressed [5]

$$c_\tau = -\tau \, \mathrm{sgn}[\boldsymbol{v}_1 \cdot (\boldsymbol{v}_2 \times \boldsymbol{v}_3)] \tag{6.12}$$

Hence, the Chern number corresponding to any Weyl node will take on either of the values $c_\tau = \pm 1$ for both isotropic and the non-isotropic Weyl semimetals.

Recall that the Brillouin zone takes the topological shape of a 3-torus, meaning the Brillouin zone boundary becomes a single point. Hence, an integration over the entire boundary and thus the net Chern number (6.11) of the Brillouin zone will leave zero. Weyl nodes must therefore come in pairs of opposite Chern number, and can only be eliminated through pairwise annihilation with Weyl nodes of opposite chirality. Weyl nodes are therefore said to be *topologically protected*, leaving stable band degeneracies even in the absence of symmetry.

6.2 Dirac Semimetals

As stated in the chapter introduction, a *Dirac semimetal* is a material for which the energy bands are doubly degenerate and fully gapped, except at a single point of the Brillouin zone known as a *Dirac point* where a fourfold degeneracy persists. The section at hand introduces the conventions needed for mathematically describing Dirac semimetals. The Kramers degeneracy of the energy band structure is usually attributed to an imposed $\mathcal{PT}$-symmetry of the system, as described in appendix (C), from which a general form of the Hamiltonian kernel for Dirac semimetals can be derived.

6.2.1 Conditions for the Dirac Hamiltonian Kernel

In order to describe a fourfold degeneracy in the energy band spectrum, the Hamiltonian kernel $\mathcal{H}(\boldsymbol{k})$ of the given crystalline system must be at least of size (4×4), corresponding to a set of discrete quantum numbers with a total of four components. For many electronic systems, two of the components are related to the electron spin, manifested by the set of Pauli matrices (C8) denoted by $\boldsymbol{\sigma} = (\sigma_x, \sigma_y, \sigma_z)$ and σ_0, with the fourth Pauli matrix being the unit matrix conventionally added to complete the basis of (2×2) hermitian matrices.

The remaining two components comprise a pseudospin degree of freedom, denoted by τ as for the Weyl Hamiltonian kernel (6.3). Alike the spin components, the pseudospin components can be represented by a set of Pauli matrices and the unit matrix, conventionally denoted by $\boldsymbol{\tau} = (\tau_x, \tau_y, \tau_z)$ and τ_0 in order to separate the spin and pseudospin degrees of freedom.

The set of matrices $(\sigma_0, \boldsymbol{\sigma})$ and $(\tau_0, \boldsymbol{\tau})$ can be combined using the Kronecker product to obtain a basis for the set of hermitian (4×4) matrices, with basis elements on the form $\tau_\mu \otimes \sigma_\nu \equiv \tau_\mu \sigma_\nu$; the notational differentiation between the two sets of Pauli matrices renders the explicit Kronecker product redundant. The resulting sixteen matrices can be arranged as a Clifford algebra (D13), with four of the matrices serving as the Dirac matrices (D3) of appendix D, depending on the chosen representation. The arrangement corresponding to the Weyl representation of the Dirac matrices is given in table D.1.

In conclusion, a general Hamiltonian kernel (4.11) describing four energy bands, here by named the *four-band kernel*, can be expressed on the form

$$\mathcal{H}(\boldsymbol{k}) = \sum_{\mu,\nu} h_{\mu\nu}(\boldsymbol{k}) \tau_\mu \sigma_\nu, \tag{6.13}$$

where $h_{\mu\nu}(\boldsymbol{k})$ are real parameters dependent only on the crystal momentum $\boldsymbol{k}$ with indices $\mu, \nu \in \{0, x, y, z\}$. Further constraints can then be put on the particular parameters using the symmetries of the system at hand.

Assume in particular the pseudospin degree of freedom is spatial in nature, as is the case for the tightbinding model of chapter 4. As elaborated upon in appendix C, the operation of time reversal does not affect the spatial and by assumption the pseudospin degree of freedom, while the spin is reversed. In the conventional representation (C10), the time reversal operator acting on the

spin and pseudospin bases becomes given by $\mathcal{T} = \tau_0 \otimes (i\sigma_y)\mathcal{K} \equiv i\sigma_y\mathcal{K}$, with $\mathcal{K}$ being complex conjugation; the matrix τ_0 acting on the pseudospin basis is written implicitly, being the unit matrix. Notice that the time reversal operator incidentally takes on the same form as in relativistic fermionic theory (D23).

Likewise, the operation of space inversion (C12) affects only the pseudospin degree of freedom while preserving the spin, and so the part of the parity operator $\mathcal{P}$ acting on the spin basis is simply the unit matrix σ_0. In which way spatial inversion acts on the pseudospin basis will depend on the physical interpretation of the pseudospin degree of freedom. In order to exemplify a representation for the parity operator, consider a crystalline system within the tightbinding approximation of chapter 4, where the pseudospin degree of freedom is an orbital degree of freedom. In general, there are only two ways in which the primitive unit cell harbours the possibility of being invariant under spatial inversion: the electron orbitals must either transform into themselves or into each other. Furthermore, the spatial shape of the electron orbitals must also be invariant under space inversion, with either even or odd intrinsic parities. If the orbitals transforms into themselves, the parity operator acting on the pseudospin basis can take on the forms $\mathcal{P} = \pm\tau_0$ and $\mathcal{P} = \pm\tau_z$ if the orbitals have the same and opposite parities respectively. If instead the orbitals transform into each other, the parity operator can likewise take the forms $\mathcal{P} = \pm\tau_x$, again depending on the intrinsic parities of the orbitals; this is the case of graphene, which can be ascertained from the hexagonal lattice portrayed in figure 4.3. It should be noted that the particular representation however does not necessarily render the Hamiltonian invariant under the parity operator; for graphene, the symmetry is broken whenever the two lattice sites inhibits different on-site energies.

Under the combined $\mathcal{PT}$-symmetry the crystal momentum is invariant, and so the corresponding invariance of the Hamiltonian kernel (6.13) does not restrict the form of the coefficients $h_{\mu\nu}(\boldsymbol{k})$. However, the particular representation of the $\mathcal{PT}$-operator will discard some of the terms due to its action on the spin and pseudospin spaces. With $\mathcal{T} = i\sigma_y\mathcal{K}$, then for the different representations of the parity operator, the Hamiltonian takes on the forms

$$\begin{aligned}
\mathcal{P} = \pm\tau_z: &\quad \mathcal{H}(\boldsymbol{k}) = h_{00} + \tau_x(\boldsymbol{\sigma}\cdot\boldsymbol{h}_x) + h_{y0}\tau_y + h_{z0}\tau_z \\
\mathcal{P} = \pm\tau_0: &\quad \mathcal{H}(\boldsymbol{k}) = h_{00} + \tau_y(\boldsymbol{\sigma}\cdot\boldsymbol{h}_y) + h_{z0}\tau_z + h_{x0}\tau_x \\
\mathcal{P} = \pm\tau_x: &\quad \mathcal{H}(\boldsymbol{k}) = h_{00} + \tau_z(\boldsymbol{\sigma}\cdot\boldsymbol{h}_z) + h_{x0}\tau_x + h_{y0}\tau_y
\end{aligned} \tag{6.14}$$

where the vectors $\boldsymbol{h}_i = (h_{ix}, h_{iy}, h_{iz})$ and the momentum independence is written implicitly. Notice that all terms are diagonalized with respect to the spin degree of freedom, except the terms pertaining to σ_x and σ_y. These two terms model spin inversion processes, often generated through spin-orbit coupling [11].

Notice that the three different representations of the four-band kernel (6.14) are related by unitary rotation in pseudospin space. Furthermore, the representation corresponding to $\mathcal{P} = \pm\tau_x$ is equivalent to the Weyl representation of the Dirac matrices, investigated in appendix D. In order to simplify the analysis, consider therefore the Hamiltonian kernel corresponding to $\mathcal{P} = \pm\tau_x$, rewritten

$$\begin{aligned}\mathcal{H}(\boldsymbol{k}) &= h_0 I_4 + \tau_z \otimes (\boldsymbol{\sigma}\cdot\boldsymbol{h}) + \tau_x \otimes (h_4\sigma_0) + \tau_y \otimes (h_5\sigma_0) \\ &= \begin{bmatrix} h_0 + \boldsymbol{\sigma}\cdot\boldsymbol{h} & h_4 - ih_5 \\ h_4 + ih_5 & h_0 - \boldsymbol{\sigma}\cdot\boldsymbol{h} \end{bmatrix}\end{aligned} \tag{6.15}$$

where the vector $\boldsymbol{h} = (h_1, h_2, h_3)$ and all coefficients are dependent on the crystal momentum; $h_j = h_j(\boldsymbol{k})$. In the following, it is convenient to introduce the five dimensional parameter vector $\boldsymbol{H} = (h_1, h_2, h_3, h_4, h_5)$, in terms of which the energy eigenvalues of the Hamiltonian kernel are readily expressed

$$\varepsilon_{\tau\sigma}(\boldsymbol{k}) = h_0 + \tau\sqrt{h_1^2 + h_2^2 + h_3^2 + h_4^2 + h_5^2} = h_0 + \tau|\boldsymbol{H}|. \tag{6.16}$$

Here, $\tau = \pm 1$ is the pseudospin index. The energy band structure is independent on the spin index $\sigma = \pm 1$ and hence doubly degenerate over the entire Brillouin zone, being an effect of the imposed $\mathcal{PT}$-symmetry. The degeneracy becomes four-fold at any region of the Brillouin zone where crystal momenta $\boldsymbol{k}_0$ renders the parameter vector $\boldsymbol{H}(\boldsymbol{k}_0) = 0$. For a three-dimensional crystal, such a four-fold degeneracy will in general not be guaranteed unless two of the parameter vector elements of $\boldsymbol{H} = (h_1, h_2, h_3, h_4, h_5)$ are identically zero.

The $\mathcal{PT}$-invariant four-band kernel (6.15) can similarly to the Weyl Hamiltonian kernel (6.3) be expanded around the fourfold degenerate point $\boldsymbol{k}_0$ of the Brillouin zone with $\boldsymbol{q} \equiv \boldsymbol{k} - \boldsymbol{k}_0$ to give the *Dirac Hamiltonian kernel*

$$\begin{aligned}\mathcal{H}(\boldsymbol{k}) = \varepsilon_0 + \hbar\boldsymbol{v}_0\cdot\boldsymbol{q} + \tau_z\sigma_x(\boldsymbol{\Delta}_1\cdot\boldsymbol{q}) + \tau_z\sigma_y(\boldsymbol{\Delta}_2\cdot\boldsymbol{q}) \\ + \tau_x(\hbar\boldsymbol{v}_1\cdot\boldsymbol{q}) + \tau_y(\hbar\boldsymbol{v}_2\cdot\boldsymbol{q}) + \tau_z\sigma_z(\hbar\boldsymbol{v}_3\cdot\boldsymbol{q})\end{aligned} \tag{6.17}$$

where the vectors $\boldsymbol{v}_i$ are analogous to the effective velocities of the Weyl Hamiltonian kernel (6.3), while the parameters $\boldsymbol{\Delta}_m \equiv \nabla_{\boldsymbol{k}} h_m(\boldsymbol{k})\big|_{\boldsymbol{k}=\boldsymbol{k}_0}$ for $m \in \{1, 2\}$ are parameter vectors $\boldsymbol{\Delta}_m = (\Delta_{m1}, \Delta_{m2}, \Delta_{m3})$ modelling spin-orbit coupling.

In particular, when the spin reversal parameters $\boldsymbol{\Delta}_1 = \boldsymbol{\Delta}_2 = 0$, the Dirac Hamiltonian kernel (6.17) decouples into two Weyl Hamiltonian kernels (6.1) with Bloch vectors given by $\boldsymbol{g}_\pm(\boldsymbol{q}) = \hbar(\boldsymbol{v}_1\cdot\boldsymbol{q}, \boldsymbol{v}_2\cdot\boldsymbol{q}, \pm\boldsymbol{v}_3\cdot\boldsymbol{q})$. From the expression of the Chern number for Weyl semimetals (6.12), these two Weyl Hamiltonians are seen to describe Weyl fermions of opposite chirality. Furthermore, if instead the effective velocities $\boldsymbol{v}_1 = \boldsymbol{v}_2 = 0$, the Dirac Hamiltonian kernel will similarly decouple into two Weyl Hamiltonian kernels on the form

$$\mathcal{H}_W^\pm(\boldsymbol{q}) = \pm\big[\sigma_x(\boldsymbol{\Delta}_1\boldsymbol{q}) + \sigma_y(\boldsymbol{\Delta}_2\boldsymbol{q}) + \sigma_z(\hbar\boldsymbol{v}_1\boldsymbol{q})\big] \tag{6.18}$$

where the two degrees of freedom are related to the spin basis σ rather than the pseudospin basis τ. In both cases the fourfold degenerate Dirac point is seen to be created from two superposed Weyl nodes of opposite chirality. Hence, the total Chern number (5.11) corresponding to a Dirac point is zero.

In fact, seeing that the Dirac Hamiltonian kernel (D8) is invariant under the combined $\mathcal{PT}$-symmetry, the Berry curvature (5.15) of Dirac semimetals is

identically zero. Dirac points are therefore unlike Weyl nodes not topologically protected, and may split into two separated Weyl nodes upon small perturbations. In conclusion, Dirac semimetals are dependent on rigid symmetries in order to be stable other than the imposed $\mathcal{PT}$-symmetry. The different physical phenomena responsible for producing Dirac points in real systems allows for a categorization of Dirac semimetals [3]. An example of symmetry protected Dirac points is found in the antiferromagnetic Dirac semimetal CuMnAs [11], for which the emergence of Dirac points is investigated in chapter 8.

6.2.2 The Isotropic Dirac Hamiltonian Kernel

Until this point, the four-band Hamiltonian kernels (6.14) have been assumed invariant only under the combined $\mathcal{PT}$-symmetry. Consider then a four-band system invariant under both time reversal $\mathcal{T}$ and space inversion $\mathcal{P}$ separately. In this case, the different parameters $h_{\mu\nu}(\boldsymbol{k})$ will be either even or odd under inversion of the direction of the crystal momentum $\boldsymbol{k}$. As an example, consider the four-band Hamiltonian kernel (6.15) with the representation of the parity operator being $\mathcal{P} = \pm\tau_x$. From application of the parity operator, it is seen that the different parameters must satisfy $h_j(-\boldsymbol{k}) = h_j(\boldsymbol{k})$ for $j \in \{0, 4\}$ and $h_j(-\boldsymbol{k}) = -h_j(\boldsymbol{k})$ for $j \in \{1, 2, 3, 5\}$. Seeing that the combined $\mathcal{PT}$-operator by assumption leaves the Hamiltonian kernel invariant, a similar application of the time reversal operator $\mathcal{T} = i\sigma_y\mathcal{K}$ leaves the same conditions on the parameters as the parity operator. Hence, if the system is invariant under space inversion and time reversal separately, both the even parameter $h_4(\boldsymbol{k})$ and the linear tilting term of the parameter $h_0(\boldsymbol{k})$ will be left out of the linearized Dirac Hamiltonian kernel (6.17), while the remaining parameters still may leave a locally linear dispersion around a point of fourfold degeneracy.

Finally, the reason for the name of Dirac point is due to the similarity between the Dirac Hamiltonian kernel (6.17) and the Dirac Hamiltonian (D8) of relativistic quantum theory. In particular, with the parameters $h_0 = h_5 = 0$ and $h_4 = m$, and assuming an isotropic linearization $h_i(\boldsymbol{q}) = -\hbar v_F q_i$ for the remaining parameters, the four-band kernel (6.15) linearized around the Dirac point $\boldsymbol{q}$ becomes equivalent to the relativistic Dirac Hamiltonian, written

$$\mathcal{H}_D(\boldsymbol{q}) = -\tau_z(\hbar v_F \boldsymbol{\sigma}\cdot\boldsymbol{q}) + m\tau_x = \begin{bmatrix} -\hbar v_F\boldsymbol{\sigma}\cdot\boldsymbol{q} & m \\ m & \hbar v_F\boldsymbol{\sigma}\cdot\boldsymbol{q} \end{bmatrix}. \tag{6.19}$$

Similarly to the isotropic Weyl Hamiltonian kernel (6.7), the effective velocity v_F here takes on the role of an effective speed of light. From the preceding discussion, this Hamiltonian kernel is invariant under both time reversal $\mathcal{T}$ and space inversion $\mathcal{P}$ separately, as derived also in appendix D on the basis of Lorentz invariance. Due to the rest mass term m however, not to be confused with the electron mass, the energy band structure will be completely gapped in the entire Brillouin zone. Only for $m = 0$ will the Hamiltonian kernel decouple into two Weyl Hamiltonian kernels (6.18), and the energy band structure becomes locally linear around the emerging fourfold degenerate Dirac point.

6.3 Weyl Nodes from Symmetry Breaking

Recall that the Dirac Hamiltonian kernel (6.17) under the correct assumptions decouples into two Weyl Hamiltonian kernels (6.3), meaning the fourfold degenerate Dirac point can be interpreted as two superposed Weyl nodes. Because the Weyl nodes are topologically protected, these cannot be removed from the energy band structure for small perturbations. Hence, under certain perturbations the Dirac point may split into two Weyl nodes, corresponding to a transition of a topological semimetal from the Dirac to the Weyl type.

In the following, the isotropic Dirac Hamiltonian kernel (6.19) will serve as a basis for investigating the emergence of Weyl nodes from Dirac points under time reversal and space inversion symmetry breaking perturbations. The resulting energy band structures are the same as derived by Burkow, Hook and Balents [4], with figures inspired by Armitage, Mele and Vishwanath [5].

The section ends with a discussion of magnetic order in a crystalline system with a diatomic primitive unit cell, in order to exemplify the origin of the different types of perturbations. Magnetic order also allows for a classification of ferromagnetic and antiferromagnetic topological semimetals, one of which is the material CuMnAs investigated in chapter 8.

6.3.1 The Breaking of Time Reversal Symmetry

Consider first breaking the time reversal symmetry of the Dirac Hamiltonian kernel (6.19) while preserving the space inversion symmetry. From the transformation properties of the Clifford algebra in table D.1, the matrices satisfying these conditions are the relativistic spin matrix $\boldsymbol{\Sigma} = \tau_0\boldsymbol{\sigma}$ and $\gamma^5\boldsymbol{\gamma} = -\tau_x\boldsymbol{\sigma}$. The time reversal symmetry of the Dirac Hamiltonian kernel is thus broken with

$$\mathcal{H}(\boldsymbol{q}) = \mathcal{H}_D(\boldsymbol{q}) + \tau_0(\boldsymbol{\sigma}\cdot\boldsymbol{b}) + \tau_x(\boldsymbol{\sigma}\cdot\boldsymbol{z}) = \begin{bmatrix} \boldsymbol{\sigma}\cdot(\boldsymbol{b}-\boldsymbol{q}) & m+\boldsymbol{\sigma}\cdot\boldsymbol{z} \\ m+\boldsymbol{\sigma}\cdot\boldsymbol{z} & \boldsymbol{\sigma}\cdot(\boldsymbol{b}+\boldsymbol{q}) \end{bmatrix} \tag{6.20}$$

where the parameter vectors $\boldsymbol{b}$ and $\boldsymbol{z}$ physically can be interpreted as Zeeman fields, whose components can be taken as internal or external variables.

The energy eigenvalues of the current Hamiltonian kernel (6.20) does not in general attain an easily analyzable form. However, analytical expressions for the energy can be found for specific choices for the mass m and the Zeeman fields $\boldsymbol{b}$ and $\boldsymbol{z}$. Consider first the case $\boldsymbol{z} = 0$, for which the energy eigenvalues

$$\varepsilon_{\tau\sigma}(\boldsymbol{q}, m; \boldsymbol{b}) = \tau\sqrt{\boldsymbol{q}^2 + m^2 + \boldsymbol{b}^2 + 2\sigma\sqrt{(\boldsymbol{b}\cdot\boldsymbol{q})^2 + \boldsymbol{b}^2 m^2}} \tag{6.21}$$

where again $\sigma = \pm 1$ and $\tau = \pm 1$ are the spin and pseudospin indices. Here, the introduction of the Zeeman field $\boldsymbol{b}$ lifts the Kramers degeneracy of the original Dirac Hamiltonian kernel $\mathcal{H}_D(\boldsymbol{q})$, giving four energy bands in total. For $|\boldsymbol{b}| > m$, the four bands touch pairwise in two Weyl nodes located at $\boldsymbol{q} = \pm\hat{\boldsymbol{b}}\sqrt{\boldsymbol{b}^2 - m^2}$ in the direction of the Zeeman field $\hat{\boldsymbol{b}} = \boldsymbol{b}/|\boldsymbol{b}|$, respectively. The energy spectrum is fully gapped whenever $|\boldsymbol{b}| < m$, where the mass dominates the Zeeman term.

Consider next the case $\boldsymbol{b} = 0$. The energy bands are likewise calculated

$$\varepsilon_{\tau\sigma}(\boldsymbol{q}, m; \boldsymbol{z}) = \tau\sqrt{\boldsymbol{q}^2 + m^2 + \boldsymbol{z}^2 + 2\sigma\sqrt{|\boldsymbol{z} \times \boldsymbol{q}|^2 + \boldsymbol{z}^2 m^2}} \tag{6.22}$$

The analytical expression for the energy bands are almost identical to the previous case, but with the scalar product exchanged for the vector product. In this case, when $|\boldsymbol{z}| > m$ two of the bands touch along a circle with radius $\boldsymbol{q}^2 = \boldsymbol{z}^2 - m^2$ known as a *nodal loop*, lying in the plane defined by $\boldsymbol{z} \cdot \boldsymbol{q} = 0$.

Letting for simplicity $m = 0$, the energy bands for the two cases $\boldsymbol{b} = 0$ and $\boldsymbol{z} = 0$ are shown in figure 6.2, displaying the Weyl nodes and the nodal loop respectively, together with the fourfold degenerate Dirac point for $\boldsymbol{z} = \boldsymbol{b} = 0$. If the Fermi level of the material lies near a Weyl node or a nodal loop, the material is categorized as a Weyl semimetal or a *line nodal semimetal*, respectively [4].

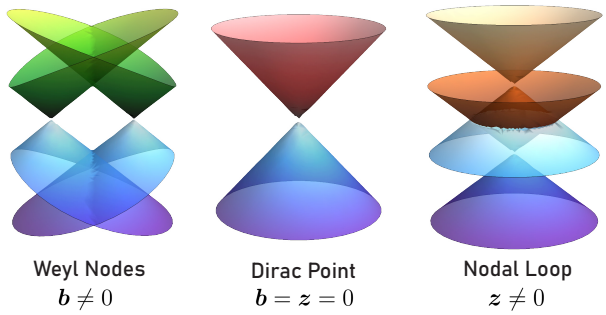

Figure 6.2: The central figure displays a Kramers degenerate Dirac cone. Introducing the Zeeman field $\boldsymbol{b}$ breaking time reversal symmetry, the Kramers degeneracy is lifted and the Dirac point is split horizontally into two Weyl nodes in the left figure. Alternately, introducing the field $\boldsymbol{z}$, the Dirac cone is split vertically and the energy bands meet at a nodal loop.

Consider then both of the Zeeman fields $\boldsymbol{b}$ and $\boldsymbol{z}$ to be nonzero, while assuming a mass $m = 0$. The four energy bands are then readily calculated

$$\varepsilon_{\tau\sigma}(\boldsymbol{q}; \boldsymbol{b}, \boldsymbol{z}) = \tau\sqrt{\boldsymbol{q}^2 + \boldsymbol{b}^2 + \boldsymbol{z}^2 + 2\sigma\sqrt{(\boldsymbol{b} \cdot \boldsymbol{q})^2 + |\boldsymbol{z} \times \boldsymbol{q}|^2 + (\boldsymbol{b} \cdot \boldsymbol{z})^2}}. \tag{6.23}$$

For simplicity, consider in particular the case $\boldsymbol{z} \times \boldsymbol{b} = 0$, such that the fields become parallel with $(\boldsymbol{b} \cdot \boldsymbol{z})^2 = \boldsymbol{b}^2\boldsymbol{z}^2$. The band structure may then exhibit either two Weyl nodes or a nodal loop depending on the relative magnitude of the two fields. If the field $\boldsymbol{b}$ dominates, with $|\boldsymbol{b}| > |\boldsymbol{z}|$, there are two Weyl nodes located at $\boldsymbol{q} = \pm\hat{\boldsymbol{b}}\sqrt{\boldsymbol{b}^2 - \boldsymbol{z}^2}$. If the other field dominates however, with $|\boldsymbol{b}| < |\boldsymbol{z}|$, there will instead be a nodal loop with radius $\boldsymbol{q}^2 = \boldsymbol{z}^2 - \boldsymbol{b}^2$ lying in the plane defined by $\boldsymbol{z} \cdot \boldsymbol{q} = 0$.

Finally, assume both Zeeman fields $\boldsymbol{b}$ and $\boldsymbol{z}$ and the mass m are all nonzero. In that case an analytical expression for the energy bands can be found as long as the Zeeman fields are perpendicular, satisfying $\boldsymbol{b} \cdot \boldsymbol{z} = 0$, for which

$$\varepsilon_{\tau\sigma}(\boldsymbol{q}, m; \boldsymbol{b}, \boldsymbol{z}) = \tau\sqrt{\boldsymbol{q}^2 + m^2 + \boldsymbol{b}^2 + \boldsymbol{z}^2 + 2\sigma\sqrt{(\boldsymbol{b}\cdot\boldsymbol{q})^2 + |\boldsymbol{z}\times\boldsymbol{q}|^2 + (\boldsymbol{b}^2+\boldsymbol{z}^2)m^2}} \tag{6.24}$$

If the mass term dominates over the fields, with $\boldsymbol{b}^2 + \boldsymbol{z}^2 < m^2$, the energy spectrum will be fully gapped. For $\boldsymbol{b}^2 + \boldsymbol{z}^2 > m^2$ however, the energy bands touch at two Weyl nodes located at $\boldsymbol{q} = \pm\hat{\boldsymbol{b}}\sqrt{\boldsymbol{b}^2 + \boldsymbol{z}^2 - m^2}$.

6.3.2 The Breaking of Space Inversion Symmetry

In order to break the space inversion symmetry of the Dirac Hamiltonian (D8) while preserving the time reversal symmetry, the only suitable hermitian matrices of table D.1 are $\gamma^5 = -\tau_z \otimes \sigma_0$ and $i\gamma^\mu = -\tau_y \otimes \boldsymbol{\sigma}$. Adding these symmetry breaking terms to the Dirac Hamiltonian kernel $\mathcal{H}_D(\boldsymbol{q})$, the total Hamiltonian

$$\mathcal{H}(\boldsymbol{q}) = \mathcal{H}_D(\boldsymbol{q}) + \tau_y(\boldsymbol{\sigma}\cdot\boldsymbol{w}) + \lambda\tau_z = \begin{bmatrix} -\boldsymbol{\sigma}\cdot\boldsymbol{q} + \lambda & m - i\boldsymbol{\sigma}\cdot\boldsymbol{w} \\ m + i\boldsymbol{\sigma}\cdot\boldsymbol{w} & \boldsymbol{\sigma}\cdot\boldsymbol{q} - \lambda \end{bmatrix} \tag{6.25}$$

where now the scalar λ and the vector $\boldsymbol{w}$ are introduced as parameters of the system. The energy band spectrum of the system can then be calculated to be

$$\varepsilon_{\tau\sigma}(\boldsymbol{q}, m; \boldsymbol{w}, \lambda) = \tau\sqrt{\boldsymbol{q}^2 + m^2 + \boldsymbol{w}^2 + \lambda^2 + 2\sigma\sqrt{\lambda^2\boldsymbol{q}^2 + |\boldsymbol{w}\times\boldsymbol{q}|^2}} \tag{6.26}$$

Here, the energy spectrum is fully gapped whenever $m \neq 0$. For $m = 0$ however, two of the bands touch at a nodal loop defined by $\boldsymbol{q}^2 = \boldsymbol{w}^2 + \lambda^2$ and $\boldsymbol{q}\cdot\boldsymbol{w} = 0$.

Under the current analysis there are then no Weyl nodes appearing if only the space inversion symmetry is broken. From topological arguments, Weyl nodes must be generated in pairs of different Chern number, with each Weyl node pair representing a source and a sink of Berry curvature. Recall then the transformation properties of the Berry curvature, given in table 5.1. If space inversion symmetry is broken whereas time reversal symmetry is preserved, the Berry curvature must be an even function of the crystal momentum $\boldsymbol{k}$. In that case, two Weyl nodes located at the momenta $\boldsymbol{k}_0$ and $-\boldsymbol{k}_0$ must have the same Chern number. Thus in general, if only the space inversion symmetry is broken there must be a minimum of four Weyl nodes in the system in order to have a net Chern number of zero. The Hamiltonian under consideration however is dependent linearly on its parameters and only describe four degrees of freedom, and so cannot produce four points at which the energy bands are degenerate.

Finally, it should be noted that all introduced parameters in the preceding calculations are assumed independent on the crystal momentum. Hence, it should be clear that the discussion on the generation of Weyl nodes from Dirac points is not exhaustive, and holds only when the dependence on crystal momentum lies entirely within the Dirac Hamiltonian kernel (6.19).

6.3.3 Classifications of Magnetic Order

From relativistic quantum theory, the spin of electrons in the classical limit generate a magnetic moment which couple to the spin of other particles. For crystalline systems in particular, the spins of itinerant electrons may couple to the magnetic moment generated by the localized spins of electrons in lower energy orbitals of the underlying lattice. In most materials however the spin structure of the underlying crystal lattice is disordered both spatially and temporally, and the effect of the coupling between the spins levels out at the macroscopic scale.

If the system is magnetically ordered, the material can be classified according to the symmetries of the spin structure. For *ferromagnetic* materials, the spins tend to align in the same direction throughout the material, giving rise to a net *uniform magnetization* per spin $\boldsymbol{m}$ which serves as an order parameter for the system. If instead neighbouring spins tend to align in opposite directions, the material is said to be *antiferromagnetic*. In the antiferromagnetic case, the material is magnetically ordered but without a net magnetization, and the order parameter is instead given by the *staggered magnetization*, conventionally termed the *Néel vector* and denoted by $\boldsymbol{n}$.

In the following, a diatomic crystalline system is considered where the localized spins of the two atomic nuclei of the unit cell are denoted by $\boldsymbol{S}_A$ and $\boldsymbol{S}_B$, as shown in figure 6.3. Assuming the representation of the parity operator is given by $\mathcal{P} = \pm\tau_x$, the itinerant electrons of the system will then couple to the localized spins through the exchange interaction [30]

$$\begin{aligned}\mathcal{H}_J &= \frac{J}{2}\Big[(\tau_0 + \tau_z) \otimes (\boldsymbol{\sigma} \cdot \boldsymbol{S}_A) + (\tau_0 - \tau_z) \otimes (\boldsymbol{\sigma} \cdot \boldsymbol{S}_B)\Big] \\ &= J\Big[\tau_0 \otimes \boldsymbol{\sigma} \cdot \boldsymbol{m} + \tau_z \otimes \boldsymbol{\sigma} \cdot \boldsymbol{n}\Big]\end{aligned} \tag{6.27}$$

where $\boldsymbol{\tau}$ and $\boldsymbol{\sigma}$ are sets of Pauli matrices (C8) corresponding to the orbital and spin degrees of freedom respectively, and J is an assumed isotropic coupling strength. The uniform and staggered magnetizations are here related to the two spins through $\boldsymbol{m} = (\boldsymbol{S}_A + \boldsymbol{S}_B)/2$ and $\boldsymbol{n} = (\boldsymbol{S}_A - \boldsymbol{S}_B)/2$ respectively. The following classification scheme for magnetic order is illustrated in figure 6.3.

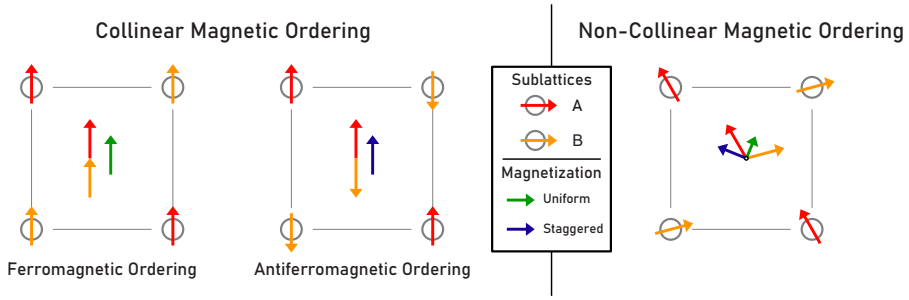

Figure 6.3: The different classifications of magnetic order, shown for a diatomic square crystal lattice where the spin related to the atomic orbitals provide the two sublattices.

If the spins are aligned with $\boldsymbol{S}_A = \boldsymbol{S}_B = \boldsymbol{m}$ and $\boldsymbol{n} = 0$ the system is fully ferromagnetic. Similarly, if instead the spins are anti-aligned with $\boldsymbol{m} = 0$ and $\boldsymbol{S}_A = -\boldsymbol{S}_B = \boldsymbol{n}$ the system is fully antiferromagnetic. In both cases, all spins are arranged in the same direction, and the spin structure is said to be *collinear*. In the *non-collinear* case, both the uniform and the staggered magnetizations are non-zero. Notice that for a general polyatomic primitive unit cell, the net magnetization $\boldsymbol{m}$ can be zero even in the non-collinear case [31].

From appendix C the quantum spin is inverted under the time reversal symmetry $\mathcal{T}$, while being unaffected by the space inversion symmetry $\mathcal{P}$. Considering then the different spin structures of figure 6.3, ferromagnetic ordering is seen to break the time reversal symmetry which would otherwise be present in the absence of spin. The ferromagnetic ordering does however not affect the space inversion symmetry, seeing that the spins are equivalent on all lattice sites; a system invariant under space inversion without magnetic ordering will also be invariant under space inversion with ferromagnetic ordering. For the antiferromagnetic ordering, both the time reversal symmetry and the space inversion symmetry are broken due to the magnetic ordering. If however the crystal lattice is invariant under space inversion without the magnetic ordering, the system will be invariant under the combined $\mathcal{PT}$-symmetry.

Consider then adding the exchange coupling (6.27) to the general $\mathcal{PT}$-invariant four-band kernel (6.15), which then takes the form

$$\mathcal{H}(\boldsymbol{k}) = h_0(\boldsymbol{k})I_4 + \tau_z \boldsymbol{\sigma} \cdot (\boldsymbol{h}(\boldsymbol{k}) + J\boldsymbol{n}) + h_4(\boldsymbol{k})\tau_x + h_5(\boldsymbol{k})\tau_y + J\boldsymbol{\sigma} \cdot \boldsymbol{m}. \quad (6.28)$$

The uniform magnetization $\boldsymbol{m}$ is here seen to be equivalent to the Zeeman field $\boldsymbol{b}$ introduced in order to break the time reversal symmetry (6.20) of the Dirac Hamiltonian kernel (6.19). Hence, the uniform magnetization lifts the Kramers degeneracy of the energy band structure, and so Dirac semimetals excludes ferromagnetic order; the energy band structure of a ferromagnetic crystalline system cannot harbour Dirac points. Weyl semimetals however can be ferromagnetic, and in general also antiferromagnetic as long as the $\mathcal{PT}$-symmetry is broken.

In order to investigate the effect of the Néel vector $\boldsymbol{n}$ on the four-band system, consider an antiferromagnetic system with $\boldsymbol{m} = 0$, for which the energy bands can be calculated from the Hamiltonian kernel (6.28) to be

$$\varepsilon_{\tau\sigma}(\boldsymbol{k}; \boldsymbol{n}) = h_0(\boldsymbol{k}) + \tau\sqrt{\big(\boldsymbol{h}(\boldsymbol{k}) + J\boldsymbol{n}\big)^2 + h_4^2(\boldsymbol{k}) + h_5^2(\boldsymbol{k})} \quad (6.29)$$

As foretold by the $\mathcal{PT}$-invariance of the antiferromagnetic coupling term, the energy band structure remains Kramers degenerate under the perturbation. Assume then that the two parameters $h_4 = h_5 = 0$ identically, and that the energy band structure harbours a Dirac point as explained in section 6.2. In this case, the effect of the Néel vector is solely to move the location of the Dirac point in the Brillouin zone. If instead the spin reversal parameters $h_1 = h_2 = 0$ identically, the Néel vector will in general open a gap in the energy band spectrum, removing the assumed Dirac point. Thus, the effect of the antiferromagnetic exchange coupling will depend on the physical origin of the Dirac point.

Part III

Optical Conductivity of Novel Quantum Materials

Chapter 7

Conductivity Calculations for Two-Band Systems

In this chapter, the theoretical machinery regarding the calculation of conductivity derived in Part I of the thesis is used to derive a conductivity tensor for a general energy band structure comprising two bands. A calculation using the resulting formula is then exemplified through the conductivity calculation of a Rashba ferromagnet, as previously performed by Qaiumzadeh and Titov [32].

The chapter can be regarded a prelude to the calculations of chapter 8, where a conductivity formula is derived for a general Kramers degenerate four-band system. The resulting expressions for the conductivity tensors in the two cases will be directly analogous, and a purpose of the current chapter is to introduce the nomenclature and methodology used in the final calculations of the thesis, in a setting where the conductivity tensor is known.

A main demonstration of the calculations is the direct dependence of the conductivity tensor on the Berry curvature tensor, defined and derived for a general two-level system in chapter 5. For topologically non-trivial systems with a finite Berry curvature, the topology of the Hilbert spaces of Bloch functions thus result in the emergence of the anomalous Hall conductivity, where the transverse components of the conductivity tensor are nonzero.

7.1 The Two-Band Conductivity Formula

Consider a crystalline system in the tightbinding approximation, where the mutual Coulomb interactions between the electrons in the system are neglected such that the Hamiltonian takes the form of a single-particle operator. In particular, consider two energy bands of the system, assumed related to some pseudospin degree of freedom denoted by τ. The system then allows for a two-level description, whose general characteristics were investigated in section 5.3, with the two-band Hamiltonian kernel written

$$\mathcal{H}(\boldsymbol{k}) = h_0(\boldsymbol{k})\tau_0 + \boldsymbol{h}(\boldsymbol{k}) \cdot \boldsymbol{\tau} \tag{7.1}$$

where τ_0 is the (2×2) identity matrix and $\boldsymbol{\tau}$ denote the Pauli matrices (C8). The vector $\boldsymbol{h}(\boldsymbol{k}) = (h_x(\boldsymbol{k}), h_y(\boldsymbol{k}), h_z(\boldsymbol{k}))$ is the Bloch vector, which together with the zero-point energy $h_0(\boldsymbol{k})$ constitute four real parameters of the system. The two $\boldsymbol{k}$-dependent eigenvalues of the Hamiltonian kernel constitute two energy bands, written in terms of the four real parameters $h_0(\boldsymbol{k})$ and $\boldsymbol{h}(\boldsymbol{k})$ as

$$\varepsilon_\pm(\boldsymbol{k}) = h_0(\boldsymbol{k}) \pm |\boldsymbol{h}(\boldsymbol{k})|, \tag{7.2}$$

assumed to vary differentiably with respect to the d components of $\boldsymbol{k}$. From the two-band Hamiltonian kernel (7.1) a specific Kubo formula for conductivity (3.33) for two-band systems can be derived.

7.1.1 The Two-Band Matsubara Autocorrelation Function

The two-point Matsubara Green functions of the two-band system can be calculated from the equation of motion for the matrix of Green functions (2.44)

$$\mathcal{G}(\boldsymbol{k}, i\nu_n) = \big[i\hbar\nu_n - (\mathcal{H}(\boldsymbol{k}) - \mu)\big]^{-1} = \frac{[i\hbar\nu_n - (h_0(\boldsymbol{k}) - \mu)] + \boldsymbol{h}\cdot\boldsymbol{\tau}}{[i\hbar\nu_n - \xi_+(\boldsymbol{k})][i\hbar\nu_n - \xi_-(\boldsymbol{k})]}.$$

Here, the denominator is the determinant of the matrix $i\hbar\nu_n I_2 - (\mathcal{H}(\boldsymbol{k}) - \mu)$ written as the product of its two eigenvalues, where $\xi_s = \varepsilon_s - \mu$ with μ being the chemical potential. Through a partial fraction decomposition the matrix of Green functions is readily expressed as a sum over band indices s as

$$\mathcal{G}(\boldsymbol{k}, i\nu_n) = \frac{1}{2}\sum_{s=\pm}\left(1 + s\frac{\boldsymbol{\tau}\cdot\boldsymbol{h}(\boldsymbol{k})}{|\boldsymbol{h}(\boldsymbol{k})|}\right)\frac{1}{i\hbar\nu_n - \xi_s(\boldsymbol{k})} \tag{7.3}$$

where the unit Bloch vector in the following is denoted by $\hat{\boldsymbol{h}} = \boldsymbol{h}/|\boldsymbol{h}|$.

Considering the uniform case, where the modulations of the applied electric field are much larger than the interatomic distances within the crystal, the current density matrices (3.14) can be calculated as the derivative

$$\mathcal{J}_i(\boldsymbol{k}) = -\frac{e}{\hbar}\frac{\partial\mathcal{H}(\boldsymbol{k})}{\partial k_i} = -\frac{e}{\hbar}\partial_i h_0(\boldsymbol{k})I_2 - \frac{e}{\hbar}\partial_i\boldsymbol{h}(\boldsymbol{k})\cdot\boldsymbol{\tau} \tag{7.4}$$

where e is the charge of the electron and the notation $\partial_i \equiv \partial/\partial k_i$ is adopted.

Inserting the two-band matrix of Green functions (7.3) and the current density matrices (7.4) into the Matsubara autocorrelation function (3.41) gives

$$\begin{aligned}\pi_{il}(i\omega_m) &= \frac{1}{\beta}\int \frac{\mathrm{d}^d k}{(2\pi)^d}\sum_{\nu_n}\mathrm{Tr}\{\mathcal{J}_i(\boldsymbol{k})\mathcal{G}(\boldsymbol{k}, i\nu_n + i\hbar\omega_m)\mathcal{J}_l(\boldsymbol{k})\mathcal{G}(\boldsymbol{k}, i\nu_n)\} \\ &= \frac{e^2}{2\hbar^2\beta}\int \frac{\mathrm{d}^d k}{(2\pi)^d}\sum_{\nu_n}\sum_{s_1=\pm}\sum_{s_2=\pm}\cdot \\ &\quad\cdot\frac{1}{2}\,\mathrm{Tr}\left\{\frac{[\partial_i h_0 I_2 + \partial_i \boldsymbol{h}\cdot\boldsymbol{\tau}][I_2 + s_1\hat{\boldsymbol{h}}\cdot\boldsymbol{\tau}][\partial_l h_0 I_2 + \partial_l \boldsymbol{h}\cdot\boldsymbol{\tau}][I_2 + s_2\hat{\boldsymbol{h}}\cdot\boldsymbol{\tau}]}{[i\hbar\nu_n - \xi_{s_1}][i\hbar\nu_n + i\hbar\omega_m - \xi_{s_2}]}\right\}\end{aligned}$$

Here, the calculation involves a trace over multiple products of identity and Pauli matrices (C8). Using the relation for the product of Pauli matrices (C9), all the Pauli matrix products reduce to sums over identity and Pauli matrices. Then, as the trace over Pauli matrices $\mathrm{Tr}\{\boldsymbol{\tau}\} = 0$, only the coefficients of the identity matrix remains. The trace can then readily be expressed

$$\begin{aligned}&\frac{1}{2}\,\mathrm{Tr}\Big\{[\partial_i h_0 I_2 + \partial_i \boldsymbol{h}\cdot\boldsymbol{\tau}][I_2 + s_1\hat{\boldsymbol{h}}\cdot\boldsymbol{\tau}][\partial_l h_0 I_2 + \partial_l \boldsymbol{h}\cdot\boldsymbol{\tau}][I_2 + s_2\hat{\boldsymbol{h}}\cdot\boldsymbol{\tau}]\Big\} \\ &\quad= (1 + s_1 s_2)\partial_i h_0 \partial_l h_0 + (s_1 + s_2)[\partial_i h_0(\hat{\boldsymbol{h}}\cdot\partial_l \boldsymbol{h}) + (\hat{\boldsymbol{h}}\cdot\partial_i \boldsymbol{h})\partial_l h_0] \\ &\qquad+ 2s_1 s_2(\hat{\boldsymbol{h}}\cdot\partial_i \boldsymbol{h})(\hat{\boldsymbol{h}}\cdot\partial_l \boldsymbol{h}) + (1 - s_1 s_2)\partial_i \boldsymbol{h}\partial_l \boldsymbol{h} + i(s_2 - s_1)\hat{\boldsymbol{h}}(\partial_i \boldsymbol{h}\times\partial_l \boldsymbol{h}).\end{aligned}$$

Performing the sums over band indices s_1 and s_2, and noticing that the derivative $\partial_i|\boldsymbol{h}| = \hat{\boldsymbol{h}}\cdot\partial_i \boldsymbol{h}$, the Matsubara autocorrelation function can be expressed

$$\begin{aligned}\pi_{il}(i\omega_m) \equiv\ \pi_{il}^{\mathrm{intra}}(i\omega_m) + \pi_{il}^{\mathrm{inter}}(i\omega_m)\ &=\ \frac{e^2}{\hbar^2\beta}\int\frac{\mathrm{d}^d k}{(2\pi)^d}\sum_{\nu_n}\sum_{s} \\ \left[\frac{(\partial_i\varepsilon_s)(\partial_l\varepsilon_s)}{(i\hbar\nu_n - \xi_s)(i\hbar\nu_n + i\hbar\omega_m - \xi_s)}\right.&+\left.\frac{(\hat{\boldsymbol{h}}\times\partial_i \boldsymbol{h})\cdot(\hat{\boldsymbol{h}}\times\partial_l \boldsymbol{h}) - is\hat{\boldsymbol{h}}\cdot(\partial_i \boldsymbol{h}\times\partial_l \boldsymbol{h})}{(i\hbar\nu_n - \xi_s)(i\hbar\nu_n + i\hbar\omega_m - \xi_{-s})}\right]\end{aligned} \tag{7.5}$$

The autocorrelation function is here split into an *intraband* and an *interband* contribution, describing the transport properties of electrons within and between the two energy bands, respectively. Notice in particular that the form of the intraband terms are identical to the autocorrelation function for a single band (3.42). By the analysis of section 3.3, the intraband autocorrelation function

$$\Pi_{il}^{\mathrm{intra}}(\omega) = \frac{e^2\omega}{\omega + i\eta}\int\frac{\mathrm{d}^d k}{(2\pi)^d}\sum_{s}\frac{\partial_i\varepsilon_s(\boldsymbol{k})}{\hbar}\frac{\partial_l\varepsilon_s(\boldsymbol{k})}{\hbar}\big[n_F(\varepsilon_s - \hbar\omega) - n_F(\varepsilon_s)\big]. \tag{7.6}$$

where $n_F(\varepsilon)$ is the Fermi-Dirac distribution (1.34).

7.1.2 The Two-Band Interband Autocorrelation Function

Consider the interband term of the two-band Matsubara autocorrelation function (7.5) describing the excitation of electrons between the two energy bands,

$$\pi_{il}^{\text{inter}}(i\omega_m) = \frac{e^2}{\hbar^2\beta}\int\frac{\mathrm{d}^d k}{(2\pi)^d}\sum_{\nu_n}\sum_{s}\frac{(\hat{\boldsymbol{h}}\times\partial_i\boldsymbol{h})\cdot(\hat{\boldsymbol{h}}\times\partial_l\boldsymbol{h}) - is\hat{\boldsymbol{h}}\cdot(\partial_i\boldsymbol{h}\times\partial_l\boldsymbol{h})}{(i\hbar\nu_n-\xi_s)(i\hbar\nu_n+i\hbar\omega_m-\xi_{-s})}. \quad (7.7)$$

In order to simplify notation under calculations, introduce here the tensors

$$\begin{aligned}\Xi_{il}(\boldsymbol{k}) &\equiv (\hat{\boldsymbol{h}}\times\partial_i\boldsymbol{h})\cdot(\hat{\boldsymbol{h}}\times\partial_l\boldsymbol{h}) = \partial_i\boldsymbol{h}\cdot\partial_l\boldsymbol{h} - \partial_i|\boldsymbol{h}|\partial_l|\boldsymbol{h}| \\ \Omega_{il}(\boldsymbol{k}) &\equiv \frac{1}{2|\boldsymbol{h}|^3}\boldsymbol{h}\cdot(\partial_i\boldsymbol{h}\times\partial_l\boldsymbol{h}).\end{aligned} \quad (7.8)$$

In the following, the first tensor $\Xi_{il}(\boldsymbol{k})$ will be referred to as the *interband tensor*, while the second tensor is related to the Berry curvature tensor (5.21) of band s through $\Omega_{il}^{(s)}(\boldsymbol{k}) \equiv -s\Omega_{il}(\boldsymbol{k})$. Furthermore, the second Matsubara frequency summation rule (2.38) can be applied directly to give the expression

$$\frac{1}{\beta}\sum_{\nu_n}\frac{1}{(i\hbar\nu_n-\xi_s)(i\hbar\nu_n+i\hbar\omega_m-\xi_{-s})} = \frac{n_F(\varepsilon_s)-n_F(\varepsilon_{-s}-i\hbar\omega_m)}{\varepsilon_s-\varepsilon_{-s}+i\hbar\omega_m},$$

where the Fermi-Dirac distribution satisfies $n_F(\varepsilon - i\hbar\omega_m) = n_F(\varepsilon)$. Inserting also the exact form of the energy functions (7.2) then leaves

$$\pi_{il}^{\text{inter}}(i\omega_m) = \frac{e^2}{\hbar^2}\int\frac{\mathrm{d}^d k}{(2\pi)^d}\cdot\sum_{s}\big[n_F(\varepsilon_s)-n_F(\varepsilon_{-s})\big]\frac{\Xi(\boldsymbol{k}) - is|\boldsymbol{h}|^2\Omega_{il}(\boldsymbol{k})}{2s|\boldsymbol{h}|+i\hbar\omega_m}$$

Performing the analytical continuation of the interband Matsubara autocorrelation function then gives the interband current density autocorrelation function

$$\Pi_{il}^{\text{inter}}(\omega) = \frac{e^2}{\hbar^2}\int\frac{\mathrm{d}^d k}{(2\pi)^d}\big[n_F(\varepsilon_+)-n_F(\varepsilon_-)\big]\sum_{s}\frac{s\Xi(\boldsymbol{k}) - i|\boldsymbol{h}|^2\Omega_{il}(\boldsymbol{k})}{2s|\boldsymbol{h}|+\hbar\omega+i\eta} \quad (7.9)$$

where the sum over bands has been moved past the Fermi-Dirac distributions.

The interband current density autocorrelation function (7.9) can thus be split into two parts, denoted by the two tensors

$$\begin{aligned}\Pi_{il}^{\Xi}(\omega) &= \frac{e^2}{\hbar^2}\int\frac{\mathrm{d}^d k}{(2\pi)^d}\big[n_F(\varepsilon_+)-n_F(\varepsilon_-)\big]\sum_{s}\frac{s\Xi_{il}(\boldsymbol{k})}{2s|\boldsymbol{h}|+\hbar\omega+i\eta} \\ \Pi_{il}^{\Omega}(\omega) &= \frac{e^2}{i\hbar^2}\int\frac{\mathrm{d}^d k}{(2\pi)^d}\big[n_F(\varepsilon_+)-n_F(\varepsilon_-)\big]\sum_{s}\frac{2|\boldsymbol{h}|^2\Omega_{il}(\boldsymbol{k})}{2s|\boldsymbol{h}|+\hbar\omega+i\eta},\end{aligned} \quad (7.10)$$

By definition the diagonal terms of the Berry curvature (5.8) are zero, and so the term $\Pi^{\Omega}_{il}(\omega)$ only contributes to the transverse conductivity. Furthermore, seeing that the interband and Berry curvature tensors (7.8) are symmetric and antisymmetric respectively, the corresponding conductivity tensors (3.33) will also be symmetric and antisymmetric, with $\sigma^{\Xi}_{il}(\omega) = \sigma^{\Xi}_{li}(\omega)$ and $\sigma^{\Omega}_{il}(\omega) = -\sigma^{\Omega}_{li}(\omega)$.

In calculations of the interband autocorrelation function (7.9), the Sokhotski-Plemelj theorem [33] states that when residing within an integral, the factor

$$\frac{1}{2s|\boldsymbol{h}| + \hbar\omega + i\eta} = -i\pi\delta(2s|\boldsymbol{h}| + \hbar\omega) + \mathrm{P}\frac{1}{2s|\boldsymbol{h}| + \hbar\omega} \tag{7.11}$$

where P signifies the action of taking the principal value of the surrounding integral. Here, seeing that the frequency $\omega > 0$, the delta function will only leave a contribution for $s = -1$. Furthermore, because the vector $|\boldsymbol{h}|$ is in general dependent on both the magnitude and the direction of the crystal momentum $\boldsymbol{k}$, the delta function will leave an integration over the surface in the Brillouin zone for which the equation $\hbar\omega - 2|\boldsymbol{h}(\boldsymbol{k})| = 0$ holds.

Finally, in the zero temperature limit the Fermi-Dirac distribution $n_F(\varepsilon)$ approaches the Heaviside function $\Theta(\mu - \varepsilon)$, for which the difference

$$\lim_{T\to 0}\Big[n_F(\varepsilon_+) - n_F(\varepsilon_-)\Big] = \Theta(\mu - \varepsilon_+) - \Theta(\mu - \varepsilon_-). \tag{7.12}$$

Hence, in the zero temperature limit, seeing that $\varepsilon_+ > \varepsilon_-$ for any value of $\boldsymbol{k}$, the Fermi-Dirac distributions in the interband autocorrelation function (7.9) enforces the constraint $\varepsilon_-(\boldsymbol{k}) < \mu < \varepsilon_+(\boldsymbol{k})$. The constraint allows for a natural physical interpretation: the direct optical transition of an electron from the valence band $\varepsilon_-(\boldsymbol{k})$ to the conduction band $\varepsilon_+(\boldsymbol{k})$ requires the former to be filled and the latter to be empty at the specific momentum $\boldsymbol{k}$, which at zero temperature is the case only if the Fermi-level μ lies in between the two bands.

7.1.3 The Anomalous Hall Conductivity

The direct current interband conductivity tensor (3.34) can then be calculated

$$\sigma^{\mathrm{inter}}_{il}(\omega) = i\frac{\partial\Pi^{\mathrm{inter}}_{il}}{\partial\omega}\bigg|_{\omega=0} = \frac{e^2}{\hbar}\int\frac{\mathrm{d}^d k}{(2\pi)^d}\big[n_F(\varepsilon_-) - n_F(\varepsilon_+)\big]\frac{\boldsymbol{h}\cdot(\partial_i\boldsymbol{h}\times\partial_l\boldsymbol{h})}{2|\boldsymbol{h}|^3}.$$

where the sum over s cancels the part $\Pi^{\Xi}_{il}(\boldsymbol{k})$ and leavs a factor of two for $\Pi^{\Omega}_{il}(\omega)$. Recalling that the Berry curvature (5.21) is defined $\Omega^{(s)}_{il}(\boldsymbol{k}) \equiv -s\Omega_{il}(\boldsymbol{k})$ for band s, the two-band direct current interband conductivity becomes

$$\sigma^{\mathrm{inter}}_{il} = \frac{e^2}{\hbar}\int\frac{\mathrm{d}^d k}{(2\pi)^d}\sum_s n_F(\varepsilon_s)\,\Omega^{(s)}_{il} \tag{7.13}$$

This is the expression for the *anomalous Hall conductivity* [34], which is a consequence of the topology of the Brillouin zone. The anomalous Hall conductivity is a contribution to the transverse conductivity, as the diagonal terms of the Berry curvature (5.8) are zero from their definition.

7.2 Conductivity of a Rashba Ferromagnet

The present section rederives the conductivity tensor for a Rashba ferromagnet, as performed in the article by Qaiumzadeh and Titov [32]. The section initiates with a description of the Rashba system, whose effective Hamiltonian operator is invariant under continuous translation invariance. The calculations are therefore performed in the momentum representation (B6), and not in the Bloch basis (B18) as for systems where the translation invariance is discrete.

7.2.1 System Description of the Rashba Ferromagnet

Consider a two dimensional ferromagnet with Rashba spin-orbit coupling, whose Hamiltonian operator disregarding disorder effects takes the form [32]

$$\hat{\mathfrak{h}}(\hat{\boldsymbol{p}}) = \frac{\hat{\boldsymbol{p}}^2}{2m}\sigma_0 + \alpha_R(\hat{\boldsymbol{p}} \times \boldsymbol{\sigma})_z + M\sigma_z, \tag{7.14}$$

where $\hat{\boldsymbol{p}} = (\hat{p}_x, \hat{p}_y)$ denotes the two dimensional momentum operator and m is the electron mass. The parameter α_R here describes the strength of the Rashba spin-orbit coupling, and M gives the ferromagnetic exchange energy for the magnetization perpendicular to the material plane. The set of Pauli matrices $(\sigma_0, \boldsymbol{\sigma})$ represents the electron spin degree of freedom.

For the case at hand, the Hamiltonian operator $\hat{\mathfrak{h}}(\hat{\boldsymbol{p}})$ describing a single electron is only dependent on the momentum operator $\hat{\boldsymbol{p}}$ of the electron. The Hamiltonian kernel $\mathcal{H}(\boldsymbol{p})$ can then readily be calculated as the matrix elements of the Hamiltonian operator with respect to the eigenstates $|\boldsymbol{p}\rangle$ of the momentum operator (B6), with the corresponding momentum eigenvalue denoted by $\boldsymbol{p}$. Thus, the Hamiltonian kernel for the Rashba ferromagnet becomes

$$\mathcal{H}(\boldsymbol{p}) = \langle \boldsymbol{p}| \, \hat{\mathfrak{h}}(\hat{\boldsymbol{p}}) \, |\boldsymbol{p}\rangle = \frac{\boldsymbol{p}^2}{2m}\sigma_0 + \alpha_R(\boldsymbol{p} \times \boldsymbol{\sigma})_z + M\sigma_z. \tag{7.15}$$

Compared with the general two-band Hamiltonian kernel (7.1), the Bloch vector for the Rashba ferromagnet becomes $\boldsymbol{h}(\boldsymbol{p}) = (-\alpha_R p_y, \alpha_R p_x, M)$ and the parameter $h_0(\boldsymbol{p}) = \boldsymbol{p}^2/2m$, with the corresponding energies (7.2)

$$\varepsilon_s(\boldsymbol{p}) = \frac{\boldsymbol{p}^2}{2m} + s\sqrt{\alpha_R^2 \boldsymbol{p}^2 + M^2} \tag{7.16}$$

Notice here that the energy spectrum is dependent only on the magnitude of the momentum $|\boldsymbol{p}| = p$. The energy bands are plotted in figure 7.1.

From the analysis of section 3.1, the momentum representation of the current density matrices (3.8) can then be calculated from the Hamiltonian kernel (7.15) as $\boldsymbol{\mathcal{J}}(\boldsymbol{p}) = -e\nabla_{\boldsymbol{p}}\mathcal{H}(\boldsymbol{p}) = -\frac{e\boldsymbol{p}}{m}\sigma_0 - e\alpha_R(\hat{z} \times \boldsymbol{\sigma})$, where $\hat{z}$ is the unit vector in the z-direction and e is the unit charge. The derivation of the conductivity formulae for a general two-band Hamiltonian kernel in section 7.1 can then similarly be performed for the Rashba Hamiltonian kernel (7.15), with the crystal momentum exchanged for the fully conserved linear momentum $\boldsymbol{p}$.

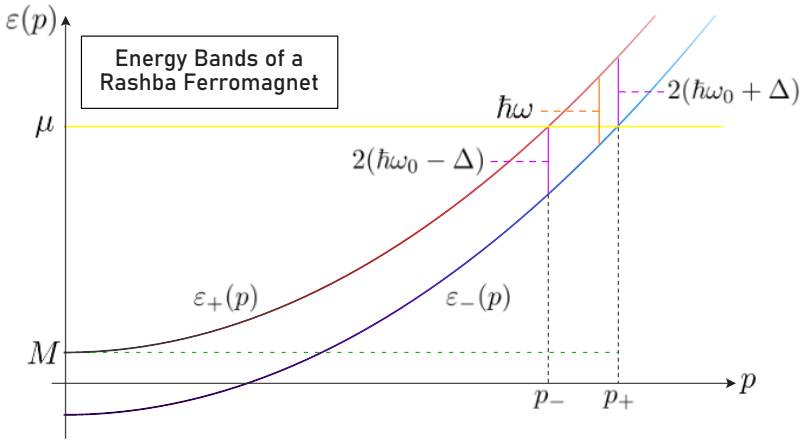

Figure 7.1: The two energy bands of a Rashba ferromagnet with spin-orbit coupling as a function of the magnitude of the momentum p, with a Fermi level μ larger than the ferromagnetic exchange energy M. The frequency ω corresponds to a direct optical transition from $\varepsilon_-(p)$ to $\varepsilon_+(p)$ under the condition $\varepsilon_-(p) < \mu < \varepsilon_+(p)$. The coupling strength of the Rashba spin-orbit coupling is denoted by Δ, and the parameter $\hbar\omega_0 = \sqrt{\Delta^2 + 2\Delta\mu + M^2}$. Notice that with zero spin-orbit coupling $\Delta = 0$, the optical frequency $\hbar\omega = 2M$, equal to the resulting constant gap between the energy bands. The energy bands are plotted for the parameter values $\mu = 3.3\,\text{eV}$, $M = 0.4\,\text{eV}$ and $\Delta = 0.1\,\text{eV}$, as given by Qaiumzadeh and Titov [32].

Let then the conduction band $\varepsilon_+(\boldsymbol{p})$ be vacant while an electron occupies a state in the valence band with energy $\varepsilon_-(\boldsymbol{p})$ for a specific momentum $\boldsymbol{p}$, imposing the condition $\varepsilon_-(\boldsymbol{p}) < \mu < \varepsilon_+(\boldsymbol{p})$ on the Fermi level μ. From the expression of the energy bands (7.16), this condition is satisfied for any momentum with a magnitude satisfying $p_- < p < p_+$, where the bounds are defined through

$$p_\pm^2 = 2m(\Delta + \mu \pm \hbar\omega_0) \tag{7.17}$$

Here, the introduced parameters $\Delta = m\alpha_R^2$ and $\omega_0^2 = (\Delta^2 + 2\mu\Delta + M^2)/\hbar^2$. The notation is related to the interaction between an imposed photon and an electron occupying the state with the energy $\varepsilon_-(\boldsymbol{p})$. For a direct optical transition from the lower to the upper energy band to occur at the specific momentum $\boldsymbol{p}$, the frequency of the photon must satisfy $\hbar\omega = \varepsilon_+(\boldsymbol{p}) - \varepsilon_-(\boldsymbol{p})$, which in combination with the condition on the Fermi level can be written

$$\hbar\omega_0 - \Delta < \frac{\hbar\omega}{2} < \hbar\omega_0 + \Delta. \tag{7.18}$$

Ascertaining that the mass m and the Fermi level μ both are positive quantities, the introduced parameters here satisfies $\hbar\omega_0 > \Delta$ by definition. Notice also that with no Rashba spin-orbit interaction $\alpha_R = 0$, the condition means any optical transitions between the bands must occur at the frequency $\hbar\omega = 2M$ corresponding to the then constant separation between the two bands. In this

way, the spin-orbit interaction allows for a wider interval of frequencies for which an optical transition between the two bands can occur.

The following calculations of the conductivity tensor for the two dimensional Rashba ferromagnet will involve the introduced parameters Δ and ω_0. Furthermore, the calculations assumes the optical transitions occurs at the upper part of the energy spectrum, where both energy bands satisfies $\varepsilon_s(\boldsymbol{p}) > M$. This imposes the additional restriction $\mu > M$, which translates to $\Delta + \mu > \hbar\omega_0$. These restrictions on the parameters are rendered implicit in the following calculations.

7.2.2 The Rashba Ferromagnet Intraband Conductivity

Consider the intraband term of the Matsubara autocorrelation function (7.5) for a general two-band system. By the analysis provided in section 3.3, in the limit $\mu \gg \omega$ the corresponding intraband conductivity tensor can be calculated

$$\sigma_{il}^{\text{intra}}(\omega) = \frac{e^2}{\eta - i\omega} \int \frac{\mathrm{d}^d p}{(2\pi)^d} \sum_s \frac{\partial \varepsilon_s}{\partial p_i} \frac{\partial \varepsilon_s}{\partial p_l} \frac{\partial n_F(\varepsilon_s)}{\partial \mu}. \tag{7.19}$$

For the case at hand, the energy band spectrum $\varepsilon_s(\boldsymbol{p}) = \varepsilon_s(p)$ is independent on the direction of the momentum. Using the derived conductivity formula for single isotropic energy bands (3.51) then gives the expression

$$\sigma_{il}^{\text{intra}}(\omega) = \frac{\delta_{il}}{4\pi} \frac{e^2}{\eta - i\omega} \sum_s \sum_a p_0^{sa} \left| \frac{\partial \varepsilon_s}{\partial p}(p_0^{sa}) \right|. \tag{7.20}$$

where the current dimension $d = 2$ has been inserted. Here, the momenta p_0^{sa} are the solutions to the equations $\varepsilon_s(p_0^{sa}) - \mu = 0$ for $s = \pm 1$. These equations are solved for the momentum bounds previously defined (7.17), with $p_\pm$ being the solution for band $s = \mp$ respectively, confirmed visually by figure 7.1. Inserting the derivative of the energy bands (7.16), the conductivity readily becomes

$$\sigma_{il}^{\text{intra}}(\omega) = \frac{\delta_{il}}{\pi} \frac{e^2}{\eta - i\omega} \Big[\Delta + \mu - \frac{M^2 \Delta}{M^2 + 2\mu\Delta} \Big] = \frac{\delta_{il}}{\pi} \frac{\mu e^2}{\eta - i\omega} \frac{\hbar^2\omega_0^2 + \Delta^2}{\hbar^2\omega_0^2 - \Delta^2}. \tag{7.21}$$

In the last expression, it is seen that the conductivity increases with an increasing Rashba spin-orbit coupling parameter Δ, which alters the slope of the energy bands near the Fermi level. Furthermore, it should here be noted that the expression is derived for a Fermi level $\mu > M$, where both of the energy bands cross the Fermi level and hence contributes to the intraband conductivity. Inserting then first $M = 0$ followed by $\mu = 0$, the intraband conductivity is still seen to be finite and proportional to the Rashba coupling strength Δ. Furthermore, for $\Delta = 0$, the intraband conductivity becomes proportional to the Fermi level μ, independent on the ferromagnetic exchange energy M.

7.2.3 The Rashba Ferromagnet Interband Conductivity

The interband contribution to the conductivity tensor (7.9) is expressed in terms of the interband and Berry curvature tensors (7.8), which for the Bloch vector $\boldsymbol{h}(\boldsymbol{p}) = (-\alpha_R p_y, \alpha_R p_x, M)$ of the Rashba ferromagnet can be expressed

$$\begin{aligned} \Xi_{il}(\boldsymbol{p}) &= \alpha_R^2 \delta_{il} - \frac{\alpha_R^4 p_i p_l}{\alpha_R^2 \boldsymbol{p}^2 + M^2} = \Xi_{li}(\boldsymbol{p}) \\ \Omega_{xy}(\boldsymbol{p}) &= \frac{M\alpha_R^2}{2(\alpha_R^2 \boldsymbol{p}^2 + M^2)^{3/2}} = -\Omega_{yx}(\boldsymbol{p}). \end{aligned} \tag{7.22}$$

Furthermore, at zero temperature the Fermi-Dirac distributions take the form of Heaviside functions enforcing the constraint $\varepsilon_- < \mu < \varepsilon_+$. In terms of the previously defined momentum bounds (7.17), the difference

$$\Theta(\mu - \varepsilon_+(p)) - \Theta(\mu - \varepsilon_-(p)) = -\Theta([p_+^2 - p^2][p^2 - p_-^2]), \tag{7.23}$$

enforcing the constraint $p_- < p < p_+$ as seen in figure 7.1; the momenta in the final Heaviside function are squared for easier calculations in the following.

Consider first the interband contribution corresponding to the tensor $\Xi_{il}(\boldsymbol{p})$. Using the Sokhotski-Plemelj theorem (7.11), the autocorrelation function (7.10)

$$\begin{aligned} \Pi_{il}^{\Xi}(\omega) = & -e^2 \int \frac{\mathrm{d}^2 p}{(2\pi)^2} \Theta([p_+^2 - \boldsymbol{p}^2][\boldsymbol{p}^2 - p_-^2]) \left(\alpha_R^2 \delta_{il} - \frac{\alpha_R^4 p_i p_l}{\alpha_R^2 \boldsymbol{p}^2 + M^2} \right) \\ & \sum_s \left[-i\pi s \delta(\hbar\omega + 2s|\boldsymbol{h}|) + \frac{s}{2s|\boldsymbol{h}| + \hbar\omega} \right] \end{aligned}$$

Notice here that the only dependence on the direction of $\boldsymbol{p}$ lies in the second factor. Converting to spherical coordinates and performing the integral over the solid angle (3.50), the resulting integral can be expressed

$$\begin{aligned} \Pi_{il}^{\Xi}(\omega) = & -\delta_{il} \frac{\alpha_R^2 e^2}{4\pi} \int \mathrm{d}p \; p \Theta([p_+^2 - p^2][p^2 - p_-^2]) \left(2 - \frac{\alpha_R^2 p^2}{\alpha_R^2 p^2 + M^2} \right) \\ & \sum_s \left[-i\pi s \delta(\hbar\omega + 2s|\boldsymbol{h}(p)|) + \frac{1}{2|\boldsymbol{h}(p)| + s\hbar\omega} \right] \end{aligned} \tag{7.24}$$

Hence, the autocorrelation function $\Pi_{il}^{\Xi}(\omega)$ contributes only to the diagonal elements of the interband conductivity tensor. Recalling then that the other contribution $\Pi_{il}^{\Omega}(\omega)$ only contributes to the transverse elements of the conductivity tensor, the transverse components satisfies $\Pi_{ii}^{\mathrm{inter}}(\omega) = \Pi_{ii}^{\Xi}(\omega)$. Notice also that the delta function only gives a contribution for $s = -1$.

In consequence, the real and imaginary parts of the transverse elements of the interband autocorrelation function can be expressed

$$\begin{aligned}
\operatorname{Im}\Pi_{ii}^{\text{inter}}(\omega) &= -\frac{\alpha_R^2 e^2}{4}\int \mathrm{d}p\; p\;\Theta([p_+^2-p^2][p^2-p_-^2])\frac{\alpha_R^2 p^2+2M^2}{\alpha_R^2 p^2+M^2}\delta(\omega-2|\boldsymbol{h}(p)|)\\
\operatorname{Re}\Pi_{ii}^{\text{inter}}(\omega) &= -\frac{\alpha_R^2 e^2}{4\pi}\int_{p_-}^{p_+}\mathrm{d}p\; p\frac{\alpha_R^2 p^2+2M^2}{\alpha_R^2 p^2+M^2}\left[\frac{1}{2|\boldsymbol{h}(p)|+\hbar\omega}+\frac{1}{2|\boldsymbol{h}(p)|-\hbar\omega}\right]
\end{aligned}$$

Here, the Heaviside function was used to change the bounds of the integral of the real part. For the imaginary part, the remaining delta function

$$\delta(\hbar\omega-2|\boldsymbol{h}(p)|)=\frac{\delta(p-p_0)}{\left|2\frac{\partial|\boldsymbol{h}(p)|}{\partial p}(p_0)\right|}\qquad\qquad p_0=\frac{1}{\alpha_R}\sqrt{\frac{\hbar^2\omega^2}{4}-M^2}\tag{7.25}$$

where p_0 is the solution to the equation $\hbar\omega-2|\boldsymbol{h}(p)|=0$. Introducing also the substitution $u=|\boldsymbol{h}(p)|=\sqrt{\alpha_R^2p^2+M^2}$, the real and imaginary parts becomes

$$\begin{aligned}
\operatorname{Im}\Pi_{ii}^{\text{inter}}(\omega) &= -\frac{\alpha_R^2 e^2}{4}p_0\Theta([p_+^2-p_0^2][p_0^2-p_-^2])\frac{\alpha_R^2 p_0^2+2M^2}{\alpha_R^2 p_0^2+M^2}\cdot\frac{\hbar\omega}{4\alpha_R^2 p_0}\\
\operatorname{Re}\Pi_{ii}^{\text{inter}}(\omega) &= -\frac{\alpha_R^2 e^2}{4\pi}\int_{u_-}^{u_+}\mathrm{d}u\; u\left(1+\frac{M^2}{u^2}\right)\left[\frac{1}{2u+\omega}+\frac{1}{2u-\omega}\right]
\end{aligned}$$

where the bounds $u_\pm=\hbar\omega_0\pm\Delta$. Inserting the expressions for p_0 and $p_\pm$ in the imaginary part, performing the remaining integral for the real part, and introducing the parameter

$$\lambda=\frac{1}{\hbar\omega\Delta}\left(\frac{\hbar^2\omega^2}{4}-\hbar^2\omega_0^2+\Delta^2\right)\tag{7.26}$$

the interband autocorrelation function (7.9) can thus be written on the form

$$\begin{aligned}
\operatorname{Im}\Pi_{ii}^{\text{inter}}(\omega) &= -\frac{\hbar\omega e^2}{16}\left(1+\frac{4M^2}{\hbar^2\omega^2}\right)\Theta(1-\lambda^2)\\
\operatorname{Re}\Pi_{ii}^{\text{inter}}(\omega) &= -\frac{\hbar\omega e^2}{2\pi}\left[\frac{1}{8}\left(1+\frac{4M^2}{\hbar^2\omega^2}\right)\ln\left|\frac{1+\lambda}{1-\lambda}\right|+\frac{\Delta}{\hbar\omega}\right]
\end{aligned}\tag{7.27}$$

Notice here that the imaginary part is finite only for $|\lambda|<1$, which can be rewritten to the frequency condition (7.18) derived previously.

From the expression of the Rashba ferromagnet interband autocorrelation function (7.27), the real and imaginary parts of the corresponding conductivity tensor (3.33) are readily calculated. Noticing here that $\operatorname{Im}\Pi_{ii}^{\text{inter}}(0)=0$ by virtue of the Heaviside function, and calculating $\operatorname{Re}\Pi_{ii}^{\text{inter}}(0)=2\mu\Delta^2/(\hbar^2\omega_0^2-\Delta^2)$ in the zero frequency limit, the diagonal elements of the interband conductivity tensor for the Rashba ferromagnet (7.14) can be expressed

$$\begin{aligned}
\operatorname{Re}\sigma_{ii}^{\mathrm{inter}}(\omega) &= \frac{\hbar e^2}{16}\left(1+\frac{4M^2}{\hbar^2\omega^2}\right)\Theta(1-\lambda^2) \\
\operatorname{Im}\sigma_{ii}^{\mathrm{inter}}(\omega) &= \frac{\hbar e^2}{2\pi}\left[\frac{1}{8}\left(1+\frac{4M^2}{\hbar^2\omega^2}\right)\ln\left|\frac{1-\lambda}{1+\lambda}\right| - \frac{\Delta}{\hbar\omega}\left(1-\frac{2\Delta\mu}{\hbar^2\omega_0^2-\Delta^2}\right)\right]
\end{aligned} \tag{7.28}$$

Inserting the zero magnetization limit $M = 0$, the expressions for the conductivity are seen to reduce to the results found by Magarill et al. [35].

Consider then the part of the interband autocorrelation function (7.9) corresponding to the Berry curvature tensor $\Omega_{il}(\boldsymbol{p})$. From the previous discussion, the transverse elements of the interband autocorrelation function

$$\begin{aligned}
\Pi_{xy}^{\mathrm{inter}}(\omega) = \Pi_{xy}^{\Omega}(\omega) = ie^2\int\frac{\mathrm{d}^2p}{(2\pi)^2}\Theta([p_+^2-\boldsymbol{p}^2][\boldsymbol{p}^2-p_-^2])\frac{M\alpha_R^2}{\sqrt{\alpha_R^2\boldsymbol{p}^2+M^2}} \\
\sum_s\Big[-i\pi\delta(\hbar\omega+2s|\boldsymbol{h}(p)|)+\frac{1}{2s|\boldsymbol{h}(p)|+\hbar\omega}\Big]
\end{aligned}$$

Here, the other transverse component is given by $\Pi_{yx}^{\mathrm{inter}}(\omega) = -\Pi_{xy}^{\mathrm{inter}}(\omega)$.

As in the derivation of the diagonal elements (7.27), the delta function only gives a contribution (7.25) for $s = -1$. Performing also the integral directly for the second part, the transverse interband autocorrelation function becomes

$$\Pi_{xy}^{\mathrm{inter}}(\omega) = \frac{e^2M}{4}\Theta(1-\lambda^2) + i\frac{e^2M}{4\pi}\ln\left|\frac{1+\lambda}{1-\lambda}\right|, \tag{7.29}$$

where all frequency dependence lies within the parameter λ, introduced previously (7.26). In this case, both the real and imaginary parts leave $\Pi_{xy}^{\mathrm{inter}}(0) = 0$, and so the transverse interband conductivity for the Rashba ferromagnet

$$\sigma_{xy}^{\mathrm{inter}}(\omega) = \sigma_{xy}^{\mathrm{inter}}(\omega) = \frac{e^2M}{4\pi\omega}\ln\left|\frac{1-\lambda}{1+\lambda}\right| + i\frac{e^2M}{4\omega}\Theta(1-\lambda^2) \tag{7.30}$$

Seeing that the intraband term (7.21) is diagonal, the resulting expression gives the entire contribution to the transverse conductivity of the Rashba ferromagnet, being the alternate current anomalous Hall conductivity of the Rashba ferromagnet [32]. Inserting the direct current limit $\omega = 0$, the direct current anomalous Hall conductivity (7.13) becomes

$$\sigma_{xy} = \frac{\hbar e^2}{2\pi}\frac{M\Delta}{M^2+2\mu\Delta} \tag{7.31}$$

Hence, in the zero magnetization limit $M = 0$, there is no transverse conductivity in either the direct current or the alternate current cases. In this limit, the Hamiltonian kernel (7.15) is rendered invariant under time reversal, and the Berry curvature tensor of the system (7.22) becomes zero. In conclusion, for the Rashba ferromagnet, a nonzero transverse conductivity is reliant on the Berry curvature being nonzero, both in the alternate and direct current cases.

Chapter 8

Conductivity Calculations for Dirac Semimetals

In the final chapter of main contents of the thesis, the cumulation of all previous chapters, a formula for the conductivity tensor for a general Kramers degenerate four-band system is calculated and then specialized to the case of a Dirac semimetal as introduced in chapter 6. The calculations are first performed for two superposed Weyl nodes where spin-orbit coupling is neglected, where an analytical expression is achievable in the zero temperature limit. Then, the spin-orbit coupling is treated as a perturbative interaction between the superposed Weyl nodes, and the conductivity tensor calculated to second order in the emerging spin reversal parameters.

Finally, the formulae are used to predict features of the conductivity tensor of the orthorhombic phase of the antiferromagnetic Dirac semimetal CuMnAs, whose energy band structure has been analyzed by Tang et al. [11]. In this regard, the symmetry protection of the Dirac points for the particular material is investigated in order to exemplify the symmetry protection of Dirac nodes, and in particular to discuss the effect of reorientation of the magnetic moments in the antiferromagnetically ordered crystal structure.

The calculations suggests the orthorhombic phase of CuMnAs will inhibit a Hall conductivity, which unlike the anomalous Hall conductivity introduced in chapter 7 is symmetric in the conductivity tensor indices. The emergence of the symmetric Hall conductivity is dependent on a non-zero optical frequency, and cannot be attributed to the Berry curvature which is identically zero due to the imposed Kramers degeneracy. Instead, the symmetric Hall effect appears to originate in particular features of the anisotropy of the Fermi surface related to the directions of the effective velocities nearby the Dirac point.

8.1 Conductivity Neglecting Spin-Orbit Coupling

The following section derives conductivity formulae from the general Dirac Hamiltonian kernel (6.17) investigated in chapter 6. In particular, the section initiates with the calculation of a general current density autocorrelation function for a Kramers degenerate four-band system, and then specializes to a conductivity calculation for two superposed Weyl nodes.

8.1.1 Kramers Degenerate Four-Band Conductivity

Recall the Kramers degenerate Hamiltonian four-band kernels (6.14) devised in chapter 6, and consider in particular the representation

$$\mathcal{H}(\boldsymbol{k}) = h_0(\boldsymbol{k}) + \tau_y \boldsymbol{\sigma} \cdot \boldsymbol{h}(\boldsymbol{k}) + \tau_z h_4(\boldsymbol{k}) + \tau_x h_5(\boldsymbol{k}) \tag{8.1}$$

where the vector $\boldsymbol{h}(\boldsymbol{k}) = (h_1(\boldsymbol{k}), h_2(\boldsymbol{k}), h_3(\boldsymbol{k}))$ is analogous to a Bloch vector (5.18), and τ and σ denote a pseudospin and a spin related degree of freedom respectively. The Hamiltonian kernel is exhaustive for all Kramers degenerate four-band system; all $\mathcal{PT}$-invariant perturbations can for any four-band system be incorporated in the parameters $h_j(\boldsymbol{k})$. The Hamiltonian kernel corresponds to the representation of the parity operator $\mathcal{P} = \pm\tau_0$, and are related to the other derived representations of chapter 6 through a rotation in pseudospin space. Hence, the calculations performed in the following for the particular representation will apply for any Kramers degenerate four-band system with a spin related and a spatial pseudospin degree of freedom.

Due to the imposed $\mathcal{PT}$-invariance the four energy bands are pairwise Kramers degenerate, and can be labelled by a band index $s = \pm 1$. Defining the five dimensional parameter vector $\boldsymbol{H}(\boldsymbol{k}) = (h_1(\boldsymbol{k}), h_2(\boldsymbol{k}), h_3(\boldsymbol{k}), h_4(\boldsymbol{k}), h_5(\boldsymbol{k}))$, the two pairs of Kramers degenerate energy bands can be expressed on the form

$$\varepsilon_s(\boldsymbol{k}) = h_0(\boldsymbol{k}) + s|\boldsymbol{H}(\boldsymbol{k})|. \tag{8.2}$$

Notice here the similarity with the non-degenerate two-band system (6.1) investigated in chapter 7, the analogy of which will be apparent in the following.

Recall the expression for the Matsubara autocorrelation function (3.41) for a spatially uniform imposed electric field, rewritten here for convenience as

$$\pi_{il}(i\omega_m) = \frac{1}{\hbar\beta} \int \frac{\mathrm{d}^d k}{(2\pi)^d} \sum_{\nu_n} \mathrm{Tr}\{\mathcal{J}_i(\boldsymbol{k}) \mathcal{G}(\boldsymbol{k}, i\nu_n + i\omega_m) \mathcal{J}_l(\boldsymbol{k}) \mathcal{G}(\boldsymbol{k}, i\nu_n)\}.$$

The matrix of Matsubara Green functions (2.44) is calculated as the inverse matrix $\mathcal{G}(\boldsymbol{k}) = [i\hbar\nu_n - (\mathcal{H}(\boldsymbol{k}) - \mu)]^{-1}$, where ν_n is a fermionic Matsubara frequency (2.15) and μ is the Fermi-level of the system. Inserting the Hamiltonian kernel (8.1) under consideration, the Green matrices can readily be expressed

$$\mathcal{G}(\boldsymbol{k}, i\nu_n) = \frac{1}{2} \sum_{s=\pm} \left(I + \frac{\tau_y \boldsymbol{\sigma} \cdot \boldsymbol{h} + \tau_z h_4 + \tau_x h_5}{s|\boldsymbol{H}|} \right) \frac{1}{i\hbar\nu_n - \xi_s} \tag{8.3}$$

with $\xi_s(\boldsymbol{k}) = \varepsilon_s(\boldsymbol{k}) - \mu$, the result being analogous to the matrix of Green functions of a general two-band system (7.3). Furthermore, the current density matrices (3.14) are defined as derivatives with respect to the crystal momentum $\mathcal{J}_i(\boldsymbol{k}) = -e\partial_i\mathcal{H}(\boldsymbol{k})/\hbar$, where the notation $\partial_i = \partial/\partial k_i$ is adopted. The calculation of the Matsubara autocorrelation function thus involves the trace

$$\begin{aligned}
&\frac{1}{4}\,\mathrm{Tr}\Big\{[\partial_i\mathcal{H}]\Big[I + \frac{\tau_y\boldsymbol{\sigma}\cdot\boldsymbol{h} + \tau_z h_4 + \tau_x h_5}{s_1|\boldsymbol{H}|}\Big][\partial_l\mathcal{H}]\Big[I + \frac{\tau_y\boldsymbol{\sigma}\cdot\boldsymbol{h} + \tau_z h_4 + \tau_x h_5}{s_2|\boldsymbol{H}|}\Big]\Big\} \\
&\quad = (1 + s_1 s_2)\partial_i h_0 \partial_l h_0 + (s_1 + s_2)[\partial_i h_0(\hat{\boldsymbol{H}}\cdot\partial_l\boldsymbol{H}) + (\hat{\boldsymbol{H}}\cdot\partial_i\boldsymbol{H})\partial_l h_0] \\
&\qquad + 2s_1 s_2(\hat{\boldsymbol{H}}\cdot\partial_i\boldsymbol{H})(\hat{\boldsymbol{H}}\cdot\partial_l\boldsymbol{H}) + (1 - s_1 s_2)\partial_i\boldsymbol{H}\cdot\partial_l\boldsymbol{H}.
\end{aligned}$$

where the band indices s_1 and s_2 originates from the expression for the Green matrix (8.3). Performing the sums over the band indices, the Matsubara autocorrelation function for the Kramers degenerate four-band kernel (8.1) becomes

$$\begin{aligned}
\pi_{il}(i\omega_m) = \pi_{il}^{\mathrm{intra}}(i\omega_m) + \pi_{il}^{\mathrm{inter}}(i\omega_m) = \frac{2}{\hbar^3\beta}\int\frac{\mathrm{d}^d k}{(2\pi)^d}\sum_{\nu_n}\sum_{s}\cdot \\
\left[\frac{(\partial_i\varepsilon_s)(\partial_l\varepsilon_s)}{(i\hbar\nu_n - \xi_s)(i\hbar\nu_n - i\hbar\omega_m - \xi_s)} + \frac{(\partial_i\boldsymbol{H})\cdot(\partial_l\boldsymbol{H}) - (\hat{\boldsymbol{H}}\cdot\partial_i\boldsymbol{H})(\hat{\boldsymbol{H}}\cdot\partial_l\boldsymbol{H})}{(i\hbar\nu_n - \xi_s)(i\hbar\nu_n + i\hbar\omega_m - \xi_{-s})}\right].
\end{aligned} \tag{8.4}$$

The expression is analogous to the two-level autocorrelation function (7.5), with the two-level Bloch vector exchanged for the five dimensional parameter vector $\boldsymbol{H}(\boldsymbol{k})$. Here however, there is no term involving the Berry curvature (5.15), as the Berry curvature of the energy band structure is identically zero due to the imposed $\mathcal{PT}$-symmetry. Notice also how the extra factor of two compared to the two-band case reflects the double degeneracy of the energy band structure.

Hence, the Matsubara autocorrelation function (8.4) for the Kramers degenerate four-band system is split into an intraband term $\pi_{il}^{\mathrm{intra}}(i\omega_m)$ and an interband term $\pi_{il}^{\mathrm{inter}}(i\omega_m)$, describing the electronic transport properties within and between the pair of doubly degenerate energy bands respectively. Notice that the calculated intraband term (8.4) is simply the sum of two terms being equivalent to the Matsubara autocorrelation function for a single energy band (3.42). Performing the analytical continuation $i\omega_m \to \omega + i\eta$ and summing over the Matsubara frequencies using the second Matsubara frequency summation rule (2.38), the intraband current density autocorrelation function becomes

$$\Pi_{il}^{\mathrm{intra}}(\omega) = \frac{2e^2}{\hbar}\frac{1}{\omega + i\eta}\int\frac{\mathrm{d}^d k}{(2\pi)^d}\sum_{s}\frac{\partial_i\varepsilon_s(\boldsymbol{k})}{\hbar}\frac{\partial_l\varepsilon_s(\boldsymbol{k})}{\hbar}\big[n_F(\varepsilon_s - \hbar\omega) - n_F(\varepsilon_s)\big] \tag{8.5}$$

analogous to the current density autocorrelation function for a single energy band (3.44) of section 3.3. Here, the infinitesimal η is interpreted as a phenomenological scattering rate, without which the interband conductivity is divergent in the direct current limit. Hence, the intraband conductivity is dependent on impurities in the crystal lattice in order to be finite, and is as

such not intrinsic to the ideal crystalline system. The function $n_F(\varepsilon)$ is the Fermi-Dirac distribution (1.34). In particular, for the zero temperature limit the Fermi-Dirac distribution approaches a Heaviside function, and the difference $\Theta(\mu-\varepsilon)-\Theta(\mu-\varepsilon+\hbar\omega)$ enforces the integrals to attain boundaries defined through $\mu < \varepsilon_s(\boldsymbol{k}) < \mu+\hbar\omega$. For values of energies outside of these boundaries, the electron will optically transition to a bandgap or to another band. Such a transition is either forbidden or incorporated by the interband part of the autocorrelation function.

In order to simplify notation for the interband term of the derived Matsubara autocorrelation function (8.4), introduce the *interband tensor*

$$\Xi_{il}(\boldsymbol{k}) = \partial_i \boldsymbol{H} \cdot \partial_l \boldsymbol{H} - \partial_i |\boldsymbol{H}| \partial_l |\boldsymbol{H}|, \tag{8.6}$$

which is analogous to the interband tensor of the two-level system (7.8) but with the three-dimensional Bloch vector exchanged for the five-dimensional parameter vector $\boldsymbol{H}$. In terms of the interband tensor the interband autocorrelation function can after using the second Matsubara frequency summation rule (2.38) and performing the analytical continuation $i\omega_m \to \omega + i\eta$ be expressed

$$\Pi_{il}^{\text{inter}}(\omega) = \frac{2e^2}{\hbar^2} \int \frac{\mathrm{d}^d k}{(2\pi)^d} \big[n_F(\varepsilon_+) - n_F(\varepsilon_-) \big] \sum_s \frac{s \Xi_{il}(\boldsymbol{k})}{2s|\boldsymbol{H}| + \hbar\omega + i\eta}, \tag{8.7}$$

again analogous to the two-band result (7.9). From the expression of the interband tensor the interband conductivity tensor will be symmetric, satisfying $\sigma_{il}^{\text{inter}}(\omega) = \sigma_{li}^{\text{inter}}(\omega)$. However, an exact formula for the interband conductivity (3.33) will depend on the direct current limit of the interband autocorrelation function, which is dependent on the exact form of the remaining integral.

8.1.2 Conductivity of Two Superposed Weyl Nodes

Recall the Dirac semimetals investigated in section 6.2, and consider the general Dirac semimetal Hamiltonian kernel (6.17) linearized around the Dirac point, which upon neglecting the tilting term corresponding to $h_0(\boldsymbol{k})$ and the spin-orbit coupling terms can be expressed in the current representation (8.1) as

$$\mathcal{H}_0(\boldsymbol{k}) = \tau_y \sigma_z (\hbar \boldsymbol{v}_2 \cdot \boldsymbol{k}) + \tau_z (\hbar \boldsymbol{v}_3 \cdot \boldsymbol{k}) + \tau_x (\hbar \boldsymbol{v}_1 \cdot \boldsymbol{k}). \tag{8.8}$$

Here, the three vectors $\boldsymbol{v}_i = (v_{i1}, v_{i2}, v_{i3})$ are interpreted as effective velocities, giving the gradient of the different terms of the Hamiltonian kernel (8.1) near the Dirac point. The zero label is introduced in order to differentiate between the cases with and without spin-orbit coupling, the former of which will be investigated in the next subsection. From the analysis of chapter 6, the effective Hamiltonian kernel here describes two superposed Weyl nodes (6.3) of opposite chirality, with the corresponding Kramers degenerate energy band structure

$$\varepsilon_s^0(\boldsymbol{k}) = s\sqrt{(\hbar \boldsymbol{v}_2 \cdot \boldsymbol{k})^2 + (\hbar \boldsymbol{v}_3 \cdot \boldsymbol{k})^2 + (\hbar \boldsymbol{v}_1 \cdot \boldsymbol{k})^2} \tag{8.9}$$

near the Dirac point where again the band index $s = \pm 1$. Notice that the linearization presumes the effective velocities $\boldsymbol{v}_i$ are linearly independent. Under the assumption of a positive Fermi level $\mu > 0$, the Fermi surface defined by $\varepsilon_+^0(\boldsymbol{k}) = \mu$ then takes the shape of an ellipsoid in momentum space. If in particular the parameters satisfies $v_{ij} = v_F \delta_{ij}$, the energy bands becomes isotropic, taking the form $\varepsilon_s^0(\boldsymbol{k}) = s\hbar v_F |\boldsymbol{k}|$ corresponding to a spherical Fermi surface.

Recall the crystal momentum transformation (6.5) relating the isotropic and non-isotropic Weyl semimetals. For simplicity, the isotropic Fermi velocity v_F can without loss of generality be subsumed into the transformed momentum elements κ_i, leaving the transformation rewritten on the form

$$\boldsymbol{v}_i \cdot \boldsymbol{k} = v_{i1} k_x + v_{i2} k_y + v_{i3} k_z = \kappa_i, \tag{8.10}$$

with $i \in \{1, 2, 3\}$. The transform can be written on matrix form as $\mathcal{V}\boldsymbol{k} = \boldsymbol{\kappa}$, where $\mathcal{V}$ is the matrix with elements v_{ij} and the transformed crystal momentum is denoted by $\boldsymbol{\kappa} = (\kappa_1, \kappa_2, \kappa_3)$. The corresponding Jacobian matrix of the transformation is independent on the crystal momentum and given by $\det \mathcal{V} = \boldsymbol{v}_1 \cdot (\boldsymbol{v}_2 \times \boldsymbol{v}_3)$. The inverse transformation and its geometric interpretation is considered in the following subsection.

The momentum transform allows for a calculation of the conductivity tensor (3.33) of two superposed Weyl nodes, hereby denoted $\sigma_{0;il}(\omega)$ when spin-orbit coupling is neglected. Reconsider then the intraband autocorrelation function (8.5) for a general Kramers degenerate four-band system, which after inserting the dimensionality $d = 3$ in the zero temperature limit can be expressed

$$\Pi_{0;il}^{\text{intra}}(\omega) = \frac{2e^2}{\hbar} \frac{1}{\omega + i\eta} \int \frac{\mathrm{d}^3 k}{(2\pi)^3} \sum_s \frac{\partial_i \varepsilon_s^0(\boldsymbol{k})}{\hbar} \frac{\partial_l \varepsilon_s^0(\boldsymbol{k})}{\hbar} \big[\Theta(\mu - \varepsilon_s + \hbar\omega) - \Theta(\mu - \varepsilon_s)\big]$$

The intraband autocorrelation function can here be calculated exactly using the momentum transform (8.10), in terms of which the derivatives of the energy

$$\partial_i \varepsilon_s^0(\boldsymbol{k}) = \sum_j \frac{\partial \kappa_j}{\partial k_i} \frac{\partial \varepsilon_s^0}{\partial \kappa_j} = s\hbar \sum_j v_{ji} \frac{\kappa_j}{\kappa} \tag{8.11}$$

where $v_{ji} = \partial \kappa_j / \partial k_i$ from the definition of the transformation and the isotropic energy bands are given by $\varepsilon_s^0(\kappa) = s\hbar\kappa$. Inserting also the determinant of the transform $\det \mathcal{V}^{-1} = 1/\det \mathcal{V}$, the intraband autocorrelation function becomes

$$\Pi_{0;il}^{\text{intra}}(\omega) = \frac{2e^2}{\omega + i\eta} \int \frac{\mathrm{d}^3 \kappa}{(2\pi)^3} \sum_s \frac{\Theta(\mu - s\hbar\kappa + \hbar\omega) - \Theta(\mu - s\hbar\kappa)}{\det \mathcal{V}} \sum_{j,m} v_{ji} v_{ml} \frac{\kappa_j}{\kappa} \frac{\kappa_m}{\kappa}.$$

Here under the assumptions $\mu > 0$ and $\omega > 0$, the integral only gains a contribution for $s = +1$ due to the Heaviside functions; for the unconsidered case $\mu < -\omega$ the integral likewise gains a contribution only for $s = -1$, while both terms give a contribution for $-\omega < \mu < 0$. Introducing here spherical coordinates for the transformed crystal momentum $\boldsymbol{\kappa} = \kappa(\sin\theta\cos\phi, \sin\theta\sin\phi, \cos\theta)$,

and noticing that $\kappa_j/\kappa \equiv (\hat{\boldsymbol{\kappa}})_j$ is dependent only on the direction of the transformed momentum, the integral can be split into two parts as

$$\Pi^{\text{intra}}_{0;il}(\omega) = \frac{2e^2}{\omega + i\eta}\frac{1}{\hbar \det \mathcal{V}} \int_{\mu/\hbar}^{\mu/\hbar+\omega} \frac{\mathrm{d}\kappa}{(2\pi)^3}\kappa^2 \sum_{j,m} v_{ji} v_{ml} \int \mathrm{d}\Omega\, (\hat{\boldsymbol{\kappa}})_j (\hat{\boldsymbol{\kappa}})_m.$$

The integral over the solid angle (3.50) is calculated in section 3.3 and given by

$$\int \mathrm{d}\Omega\, (\hat{\boldsymbol{\kappa}})_j (\hat{\boldsymbol{\kappa}})_m = \frac{4\pi}{3}\delta_{jm}, \tag{8.12}$$

proportional to the Kronecker delta δ_{jm}. Integrating also over the magnitude of the transformed momentum using the delta function finally leaves

$$\Pi^{\text{intra}}_{0;il}(\omega) = \frac{e^2}{\omega + i\eta}\frac{(\hbar\omega)^3 + 3(\hbar\omega)^2\mu + 3\hbar\omega\mu^2}{9\pi^2\hbar^3} \sum_j \frac{v_{ji}v_{jl}}{\hbar \boldsymbol{v}_1 \cdot (\boldsymbol{v}_2 \times \boldsymbol{v}_3)} \tag{8.13}$$

where the determinant $\det \mathcal{V} = \boldsymbol{v}_1 \cdot (\boldsymbol{v}_2 \times \boldsymbol{v}_3)$ has been inserted. Hence, the direct current limit of the intraband autocorrelation function leaves $\Pi^{\text{intra}}_{0;il}(0) = 0$, and so the intraband conductivity tensor becomes $\sigma^{\text{intra}}_{0;il}(\omega) = i\Pi^{\text{intra}}_{0;il}(\omega)/\omega$, giving

$$\sigma^{\text{intra}}_{0;il}(\omega) = \frac{e^2}{\eta - i\omega}\frac{\hbar^2\omega^2 + 3\hbar\omega\mu + 3\mu^2}{9\pi^2\hbar^2} \sum_j \frac{v_{ji}v_{jl}}{\hbar \boldsymbol{v}_1 \cdot (\boldsymbol{v}_2 \times \boldsymbol{v}_3)} \tag{8.14}$$

Here, for a zero phenomenological scattering rate the last term gives rise to a singularity in the conductivity tensor in the direct current limit. For the two other terms however, the zero scattering limit can be taken without any singularities appearing, giving rise to terms constant and linear with respect to the optical frequency ω. For a Fermi level $\mu = 0$ when only the zero dimensional Dirac point at the boundary of the two Kramers degenerate bands lies at the Fermi level, only the former linear term independent on the Fermi level remains.

Consider next the interband current-density autocorrelation function (8.7), which in the zero temperature limit in $d = 3$ dimensions can be expressed

$$\Pi^{\text{inter}}_{0;il}(\omega) = \frac{2e^2}{\hbar^2}\int \frac{\mathrm{d}^3k}{(2\pi)^3}\big[\Theta(\mu - \varepsilon^0_+) - \Theta(\mu - \varepsilon^0_-)\big] \sum_s \frac{s\Xi^0_{il}(\boldsymbol{k})}{2s|\boldsymbol{H}_0| + \hbar\omega + i\eta} \tag{8.15}$$

For the Dirac Hamiltonian kernel (8.8) neglecting spin-orbit coupling, the five-dimensional parameter vector can after the momentum transform (8.10) be written in terms of the transformed momentum as $\boldsymbol{H}_0(\boldsymbol{\kappa}) = (0, 0, \hbar\kappa_2, \hbar\kappa_3, \hbar\kappa_1)$. The corresponding interband tensor (8.6) can thus be calculated

$$\Xi^0_{il}(\boldsymbol{\kappa}) = \hbar^2\big(\partial_i\boldsymbol{\kappa}\cdot\partial_l\boldsymbol{\kappa} - \partial_i|\boldsymbol{\kappa}|\partial_l|\boldsymbol{\kappa}|\big) = \hbar^2\Big(\sum_j v_{ji}v_{jl} - \sum_{j,m} v_{ji}\frac{\kappa_j}{\kappa}v_{ml}\frac{\kappa_m}{\kappa}\Big). \tag{8.16}$$

Hence, the interband tensor becomes dependent only on the direction of the transformed momentum, as $\Xi^0_{il}(\boldsymbol{\kappa}) = \Xi^0_{il}(\hat{\boldsymbol{\kappa}})$. Performing then the momentum transform (8.10) with the Jacobian determinant $1/\det\mathcal{V}$ and inserting spherical coordinates, the interband autocorrelation function (8.15) then becomes

$$\Pi^{\text{inter}}_{0;il}(\omega) = -\frac{2e^2}{\hbar^2}\int\frac{\mathrm{d}\kappa}{(2\pi)^3}\frac{\kappa^2}{\det\mathcal{V}}\sum_s\frac{s\Theta(\hbar\kappa-\mu)}{2s\hbar\kappa+\hbar\omega+i\eta}\int\mathrm{d}\Omega\;\Xi^0_{il}(\hat{\boldsymbol{\kappa}}),$$

where the two Heaviside functions have been combined to a single function as $\Theta(\mu–\hbar\kappa)–\Theta(\mu+\hbar\kappa) = –\Theta(\hbar\kappa–\mu)$, which holds in general for $\kappa > 0$. Using here the derived solid angle integral (8.12) over two components of the unit vector, the solid angle integral over the interband tensor (8.16) readily becomes

$$\int\mathrm{d}\Omega\;\Xi^0_{il}(\hat{\boldsymbol{\kappa}}) = \frac{8\pi}{3}\hbar^2\sum_j v_{ji}v_{jl}. \tag{8.17}$$

Furthermore, in the limit of zero scattering where the phenomenological scattering rate $\eta \to 0$, the Sokhotski-Plemelj theorem (7.11) states that the factor

$$\lim_{\eta\to0}\frac{1}{2s\hbar\kappa+\hbar\omega+i\eta} = -i\pi\delta(2s\hbar\kappa+\hbar\omega)+\mathrm{P}\frac{1}{2s\hbar\kappa+\hbar\omega} \tag{8.18}$$

where P signifies the action of taking the Cauchy principal value of the surrounding integral. For $\mu > 0$ the emerging dirac delta functions only give a contribution for $s = -1$, leaving the interband autocorrelation function

$$\Pi^{\text{inter}}_{0;il}(\omega) = -\frac{2e^2}{3\pi^2}\sum_j\frac{v_{ji}v_{jl}}{\det\mathcal{V}}\int\mathrm{d}\kappa\kappa^2\Theta(\hbar\kappa-\mu)\cdot\left(i\pi\delta(2\hbar\kappa-\hbar\omega)+\frac{1}{2\hbar\kappa+\hbar\omega}+\frac{1}{2\hbar\kappa-\hbar\omega}\right).$$

The integrand can thus be split into a real and an imaginary part. Inserting the determinant $\det\mathcal{V} = \boldsymbol{v}_1\cdot(\boldsymbol{v}_2\times\boldsymbol{v}_3)$ and integrating over the delta function, the imaginary part of the interband autocorrelation function becomes

$$\operatorname{Im}\Pi^{\text{inter}}_{0;il}(\omega) = -\frac{e^2\omega^2}{12\pi}\sum_j\frac{v_{ji}v_{jl}}{\hbar\boldsymbol{v}_1\cdot(\boldsymbol{v}_2\times\boldsymbol{v}_3)}\Theta\Big(\frac{\hbar\omega}{2}-\mu\Big). \tag{8.19}$$

For the real part, notice that the remaining integral diverges. This divergence is an artefact of the linearization of the Hamiltonian kernel (8.8) around the Dirac point, and can in the effective model be amended by imposing an upper cutoff $\kappa_c \equiv \hbar^2\omega_c^2/4$ on the integration. Performing the integration then leaves

$$\operatorname{Re}\Pi^{\text{inter}}_{0;il}(\omega) = \frac{e^2}{12\pi^2\hbar^3}\sum_j\frac{v_{ji}v_{jl}}{\det\mathcal{V}}\left[4\mu^2-\hbar^2\omega_c^2-\hbar^2\omega^2\ln\left|\frac{\hbar^2(\omega_c^2-\omega^2)}{4\mu^2-\hbar^2\omega^2}\right|\right] \tag{8.20}$$

Notice that only the logarithmic term is dependent on the optical frequency ω.

From the imaginary (8.19) and the real (8.20) parts of the interband current density autocorrelation function, the interband conductivity tensor (3.33) is readily calculated as $\sigma^{\text{inter}}_{0;il}(\omega) = i[\Pi^{\text{inter}}_{0;il}(\omega) - \Pi^{\text{inter}}_{0;il}(0)]/\omega$, giving

$$\begin{aligned}
\operatorname{Re}\sigma^{\text{inter}}_{0;il}(\omega) &= \frac{e^2\omega}{12\pi}\left[\sum_j \frac{v_{ji}v_{jl}}{\hbar \boldsymbol{v}_1\cdot(\boldsymbol{v}_2\times\boldsymbol{v}_3)}\right]\Theta\Big(\frac{\hbar\omega}{2}-\mu\Big) \\
\operatorname{Im}\sigma^{\text{inter}}_{0;il}(\omega) &= \frac{e^2\omega}{12\pi^2}\left[\sum_j \frac{v_{ji}v_{jl}}{\hbar \boldsymbol{v}_1\cdot(\boldsymbol{v}_2\times\boldsymbol{v}_3)}\right]\ln\left|\frac{\hbar^2\omega^2-4\mu^2}{\hbar^2\omega^2-\hbar^2\omega_c^2}\right|
\end{aligned} \tag{8.21}$$

Notice here that the imaginary part of the interband conductivity tensor is dependent on the introduced cutoff frequency ω_c. The cutoff frequency can usually be found in terms of other system parameters through calculating the conductivity when considering the particular crystal lattice structure, using a full tightbinding model corresponding to the linearized Hamiltonian kernel (8.8).

From the calculated expressions, the contributions to the conductivity from both the intraband (8.14) and the interband (8.21) conductivity tensors become proportional to a tensor of sums dependent only on the elements of the effective velocity vectors $\boldsymbol{v}_i$. In the following, these *effective velocity sums* will be denoted

$$\mathfrak{V}_{il} = \sum_j \frac{v_{ji}v_{jl}}{\hbar \boldsymbol{v}_1\cdot(\boldsymbol{v}_2\times\boldsymbol{v}_3)} \tag{8.22}$$

In particular, for the isotropic case $v_{ij} = v_F\delta_{ij}$ the sums can be evaluated

$$\text{Isotropic}: \qquad \mathfrak{V}_{il} = \sum_j \frac{v_{ji}v_{jl}}{\hbar \boldsymbol{v}_1\cdot(\boldsymbol{v}_2\times\boldsymbol{v}_3)} = \frac{\delta_{il}}{\hbar v_F} \tag{8.23}$$

Thus for the isotropic case, the transverse terms of the conductivity tensor are zero. The longitudinal terms of the interband conductivity (8.21) here match the results of Kargarian et al. [9], which calculated the Kubo conductivity for an isotropic Weyl semimetal with broken time reversal symmetry (6.20). In their paper, it was also found that the introduced cutoff frequency ω_c was effectively proportional to $\hbar v_F/a$, where a is the interatomic distance within the crystal lattice. For the Weyl semimetal however, the broken time reversal symmetry leads to a nonzero Berry curvature, leading to an anomalous Hall contribution to the transverse components of the conductivity tensor.

For the anisotropic Dirac semimetal however, the transverse components of the conductivity can be nonzero even if the Berry curvature is zero identically. For this Kramers degenerate system however, the anomalous Hall conductivity is symmetric with respect to its indices and disappears at zero optical frequency, unlike the direct current anomalous Hall conductivity (7.13) related to the Berry curvature devised in chapter 7. Hence, for Dirac semimetals in general, an anomalous Hall conductivity can for finite frequencies be generated if the effective velocities pertaining to the Dirac point are anisotropic.

8.1.3 Geometric Considerations of the Fermi Surface

Recall the momentum transformation (8.10) relating the isotropic to the non-isotropic Dirac semimetals, which can be written on the matrix form $\mathcal{V}\boldsymbol{k} = \boldsymbol{\kappa}$ where the transformation matrix is given by the effective velocities $\boldsymbol{v}_i$ as

$$\mathcal{V} = \begin{bmatrix} \boldsymbol{v}_1 \\ \boldsymbol{v}_2 \\ \boldsymbol{v}_3 \end{bmatrix} = \begin{bmatrix} v_{11} & v_{12} & v_{13} \\ v_{21} & v_{22} & v_{23} \\ v_{31} & v_{32} & v_{33} \end{bmatrix}. \tag{8.24}$$

In order for the inverse transform to be well defined the determinant must satisfy $\det \mathcal{V} \neq 0$, corresponding to the three effective velocity vectors $\boldsymbol{v}_i$ being linearly independent. The inverse transformation matrix is then readily expressed

$$\mathcal{V}^{-1} = \frac{1}{\boldsymbol{v}_1 \cdot (\boldsymbol{v}_2 \times \boldsymbol{v}_3)} \begin{bmatrix} (\boldsymbol{v}_2 \times \boldsymbol{v}_3) & (\boldsymbol{v}_3 \times \boldsymbol{v}_1) & (\boldsymbol{v}_1 \times \boldsymbol{v}_2) \end{bmatrix} \tag{8.25}$$

where the determinant $\det \mathcal{V} = \boldsymbol{v}_1 \cdot (\boldsymbol{v}_2 \times \boldsymbol{v}_3) = \boldsymbol{v}_3 \cdot (\boldsymbol{v}_1 \times \boldsymbol{v}_2) = \boldsymbol{v}_2 \cdot (\boldsymbol{v}_3 \times \boldsymbol{v}_1)$.

From the expressions of the energy bands (8.9), the Fermi-surface is defined through $\varepsilon_+(\boldsymbol{k}) = \mu$ under the assumption of a positive Fermi level $\mu > 0$. Assuming the effective velocities $\boldsymbol{v}_i$ are linearly independent, the Fermi surface for two superposed Weyl nodes thus takes the shape of an ellipsoid in momentum space. The transformation (8.24) is then geometrically interpreted as the affine transformation between the spherical and ellipsoid Fermi surfaces. The inverse transformation (8.25) reshapes the Fermi surface from spherical to the specific non-isotropic ellipsoid shape corresponding to the particular effective velocities $\boldsymbol{v}_i$. Hence, the ellipsoidal Fermi surface can be parametrized in spherical coordinates by $\boldsymbol{k}_F(\theta, \phi) = \boldsymbol{u}_1 \sin(\theta)\cos(\phi) + \boldsymbol{u}_2 \sin(\theta)\sin(\phi) + \boldsymbol{u}_3 \cos(\theta)$, where the vectors $\boldsymbol{u}_\lambda$ are the column vectors of the inverse transformation $\mathcal{V}^{-1}$, written

$$\boldsymbol{u}_\lambda = \sum_{\mu\nu} \frac{\varepsilon_{\mu\nu\lambda}}{2\boldsymbol{v}_1 \cdot (\boldsymbol{v}_2 \times \boldsymbol{v}_3)} (\boldsymbol{v}_\mu \times \boldsymbol{v}_\nu) \tag{8.26}$$

It should be noted that the parametrization of the Fermi surface is unique only if the inverse $\mathcal{V}^{-1}$ is symmetric and positive definite. The Fermi surface with its parametrization vectors is visualized in figure 8.1, where the effect of anisotropy on the Fermi surface is exemplified. If the effective velocities are linearly dependent, the determinant of the transformation becomes zero. In this case the Fermi surface will be unbounded, leaving both the momentum transformation and the linearization of the Hamiltonian kernel (8.8) ill defined.

In terms of the parametrization vectors (8.26) of the Fermi surface, the inverse momentum transform $\boldsymbol{k} = \mathcal{V}^{-1}\boldsymbol{\kappa}$ is readily expressed

$$k_j = \sum_\lambda u_{\lambda j}\kappa_\lambda = \sum_{\mu\nu\lambda} \frac{\varepsilon_{\mu\nu\lambda}}{2\boldsymbol{v}_1 \cdot (\boldsymbol{v}_2 \times \boldsymbol{v}_3)} (\boldsymbol{v}_\mu \times \boldsymbol{v}_\nu)_j \kappa_\lambda. \tag{8.27}$$

Furthermore, by definition of the momentum transform (8.24) and its inverse (8.25), the effective velocities $\boldsymbol{v}_i$ and the parametrization vectors $\boldsymbol{u}_\lambda$ satisfies

$$\sum_{\lambda} v_{\lambda i} u_{\lambda p} = \sum_{\mu\nu\lambda} \frac{\varepsilon_{\mu\nu\lambda}}{2\boldsymbol{v}_1 \cdot (\boldsymbol{v}_2 \times \boldsymbol{v}_3)} (\boldsymbol{v}_\mu \times \boldsymbol{v}_\nu)_p v_{\lambda i} = \delta_{ip}. \tag{8.28}$$

If the effective velocity vectors $\boldsymbol{v}_i$ are mutually orthogonal, the parametrization vectors $\boldsymbol{u}_\lambda$ will also be mutually orthogonal and define the vertices of the ellipsoidal Fermi surface, as exemplified by figure 8.1.

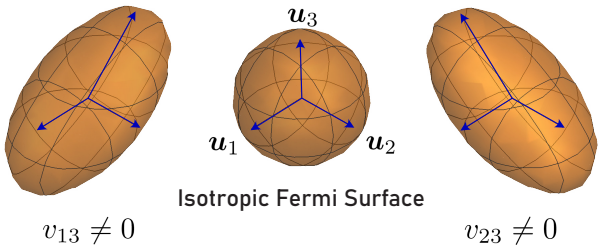

Figure 8.1: An exemplification of the effect of the nondiagonal elements of the effective velocity vectors $\boldsymbol{v}_i$. In the central figure the spherical Fermi surface of a Dirac semimetal with an isotropic energy dispersion around the Dirac point is portrayed, with $v_{ij} = v_F \delta_{ij}$. The parametrization vectors of the Fermi surface $\boldsymbol{u}_\lambda$ are coloured in blue. On the left and right respectively the corresponding Fermi surfaces with $v_{13} \neq 0$ and $v_{23} \neq 0$ are shown, being the parameters of the third column of the transformation matrix comprised of the elements v_{ij}. Notice that the anisotropy only affects the third parametrization vector $\boldsymbol{u}_3$.

Reconsider then the introduced effective velocity sums (8.22). In relation to the matrix of effective velocity elements (8.24), the effective velocity sums are seen to be given by the inner products of the columns $\mathfrak{v}_i = (v_{1i}, v_{2i}, v_{3i})$ as

$$\mathfrak{V}_{il} = \sum_{j} \frac{v_{ji} v_{jl}}{\det \mathcal{V}} = \frac{\mathfrak{v}_i \cdot \mathfrak{v}_l}{\mathfrak{v}_1 \cdot (\mathfrak{v}_2 \times \mathfrak{v}_3)}. \tag{8.29}$$

where the determinant has been written in terms of the columns rather than the rows of $\mathcal{V}$. Hence, if the columns of the momentum transformation matrix $\mathcal{V}$ are mutually orthogonal, the effective velocity sums are zero. In this case, the inverse transformation matrix (8.25) is composed of an orthogonal matrix followed by a diagonal matrix. The inverse transformation then rotates or mirrors the spherical Fermi surface about the origin, followed by a compression along the axes. It is then possible to find another set of parametrization vectors of the ellipsoid Fermi surface which are orthogonal. Although not complete, the geometrical analysis gives an inkling towards the relation between the effective velocity sums and the anisotropy of the Fermi surface.

In conclusion, the transverse components of the conductivity tensor of the two superposed Weyl nodes will be nonzero only if the ellipsoidal Fermi surface cannot be parametrized by an orthogonal set of parametrization vectors. Hence, the appearance of the symmetric anomalous Hall conductivity is tightly related to the geometrical shape, and in particular the anisotropy, of the Fermi surface.

8.2 Spin-Orbit Coupling Corrections

The rather simplistic calculation of the conductivity for two superposed Weyl nodes of the previous subsection is solely based on the momentum transformation (8.10) relating the non-isotropic to the isotropic Weyl semimetals. Such a transformation is possible seeing that there are three effective velocities and three dimensions of reciprocal space. Consider instead the Dirac Hamiltonian kernel (6.17) including spin-orbit coupling, given by

$$\mathcal{H}(\boldsymbol{k}) = \tau_y\sigma_z(\hbar\boldsymbol{v}_2\cdot\boldsymbol{k})+\tau_z(\hbar\boldsymbol{v}_3\cdot\boldsymbol{k})+\tau_x(\hbar\boldsymbol{v}_1\cdot\boldsymbol{k})+\tau_y\sigma_x(\boldsymbol{\Delta}_1\cdot\boldsymbol{k})+\tau_y\sigma_y(\boldsymbol{\Delta}_2\cdot\boldsymbol{k}). \quad (8.30)$$

Here, the two parameter vectors $\boldsymbol{\Delta}_m = (\Delta_{m1}, \Delta_{m2}, \Delta_{m3})$ relate to spin reversal processes, and can be interpreted to originate as an interaction between the two superposed Weyl nodes. The corresponding energy bands are given by

$$\varepsilon_s(\boldsymbol{k}) = s\sqrt{(\hbar\boldsymbol{v}_1\cdot\boldsymbol{k})^2 + (\hbar\boldsymbol{v}_2\cdot\boldsymbol{k})^2 + (\hbar\boldsymbol{v}_3\cdot\boldsymbol{k})^2 + (\boldsymbol{\Delta}_1\cdot\boldsymbol{k})^2 + (\boldsymbol{\Delta}_2\cdot\boldsymbol{k})^2} \quad (8.31)$$

Due to the spin reversal parameter vectors $\boldsymbol{\Delta}_m = (\Delta_{m1}, \Delta_{m2}, \Delta_{m3})$, there is in three dimensional space no longer a well defined transformation analogous to the used momentum transform (8.10) relating the energy band structure to a corresponding isotropic energy band structure.

Instead, the calculations can be simplified by assuming the spin-orbit coupling interaction is weak, and the conductivity tensor calculated using perturbation theory. The conductivity tensor can then be written on the form $\sigma_{il}(\omega) = \sigma_{0;il}(\omega) + \delta\sigma_{il}(\omega)$, where $\sigma_{0;il}(\omega)$ is the conductivity disregarding the spin-orbit coupling, calculated in the previous subsection. In order to simplify notation, reconsider the current density autocorrelation function (8.4), which is proportional to some integral on the form

$$\Pi_{il}(\omega) \propto \int \frac{d^3k}{(2\pi)^3} \sum_s \mathscr{I}_{il;s}(\Delta) \quad (8.32)$$

where the integrand $\mathscr{I}_{il;s}$ is dependent on the spin reversal parameters Δ_{mp} and implicitly on the crystal momentum $\boldsymbol{k}$ and the optical frequency ω. Recall here that the current density autocorrelation function (8.4) is even with respect to its indices, satisfying $\Pi_{il}(\omega) = \Pi_{li}(\omega)$. In consequence, expanding the integrand of the autocorrelation function (8.32) in orders of the spin reversal parameters Δ_{mp}, the first order term will leave zero. This can also be confirmed by noticing that the energy band structure (8.31) is dependent only on squares of the spin reversal parameters. Expanding the integrand to second order with respect to the spin reversal parameters, the correction term compared to the case without spin-orbit coupling (8.8) can be written on the form

$$\delta\Pi_{il}(\omega) \propto \int \frac{d^3k}{(2\pi)^3} \sum_s \left(\sum_{p,q} \sum_{m,n} \frac{\partial^2 \mathscr{I}_{il;s}}{\partial\Delta_{mp}\partial\Delta_{nq}}\Big|_{\Delta=0} \Delta_{mp}\Delta_{nq} \right), \quad (8.33)$$

where the case with zero spin-orbit coupling is symbolically written as $\Delta = 0$. Notice here that the indices $m, n \in \{1, 2\}$, whereas $p, q \in \{1, 2, 3\}$.

8.2.1 The Intraband Spin-Orbit Coupling Correction

Consider then the general intraband autocorrelation function (8.5) for a Kramers degenerate four-band system. From the previous discussion, the second order spin-orbit coupling correction to the intraband term can be expressed

$$\delta\Pi_{il}^{\text{intra}}(\omega) = \frac{2e^2}{\omega + i\eta}\frac{1}{\hbar^3}\int \frac{\mathrm{d}^3k}{(2\pi)^3}\sum_s\Big(\sum_{p,q}\sum_{m,n}\frac{\partial^2 \mathscr{J}_{il;s}^{\text{intra}}}{\partial\Delta_{mp}\partial\Delta_{nq}}\Big|_{\Delta=0}\Delta_{mp}\Delta_{nq}\Big). \tag{8.34}$$

Here, the intraband integrand can be written in terms of the energy functions $\varepsilon_s(\boldsymbol{k})$ of the system with spin-orbit interactions (8.31) as

$$\mathscr{J}_{il;s}^{\text{intra}}(\Delta) = \partial_i\varepsilon_s\partial_l\varepsilon_s\big[\Theta(\mu - \varepsilon_s + \hbar\omega) - \Theta(\mu - \varepsilon_s)\big] \tag{8.35}$$

in the zero temperature limit. With the derivative of a Heaviside function being a corresponding delta function, the derivative of the intraband integrand with respect to the spin reversal parameters is readily calculated

$$\begin{aligned}\frac{\partial^2 \mathscr{J}_{il;s}^{\text{intra}}}{\partial\Delta_{mp}\partial\Delta_{nq}}\Big|_{\Delta=0} &= -\partial_i\varepsilon_s^0\partial_l\varepsilon_s^0\frac{\partial^2\varepsilon_s}{\partial\Delta_{mp}\partial\Delta_{nq}}\Big|_{\Delta=0}\big[\delta(\mu-\varepsilon_s^0+\hbar\omega)-\delta(\mu-\varepsilon_s^0)\big]\\ &+\Big(\frac{\partial^2\partial_i\varepsilon_s}{\partial\Delta_{mp}\partial\Delta_{nq}}\Big|_{\Delta=0}\partial_l\varepsilon_s^0-\partial_i\varepsilon_s^0\frac{\partial^2\partial_l\varepsilon_s}{\partial\Delta_{mp}\partial\Delta_{nq}}\Big|_{\Delta=0}\Big)\big[\Theta(\mu-\varepsilon_s^0+\hbar\omega)-\Theta(\mu-\varepsilon_s^0)\big]\end{aligned}$$

where the energies neglecting spin-orbit coupling (8.9) are denoted by $\varepsilon_s^0(\boldsymbol{k})$. The derivatives of the energies (8.31) including spin-orbit coupling becomes

$$\begin{aligned}\frac{\partial^2\varepsilon_s}{\partial\Delta_{mp}\partial\Delta_{nq}}\Big|_{\Delta=0} &= \frac{\delta_{mn}}{\varepsilon_s^0}k_pk_q\\ \frac{\partial^2\partial_i\varepsilon_s}{\partial\Delta_{mp}\partial\Delta_{nq}}\Big|_{\Delta=0} &= \delta_{mn}\Big(\delta_{ip}\frac{k_q}{\varepsilon_s^0}+\frac{k_p}{\varepsilon_s^0}\delta_{iq}-\frac{k_p}{\varepsilon_s^0}\frac{k_q}{\varepsilon_s^0}\partial_i\varepsilon_s^0\Big)\end{aligned} \tag{8.36}$$

The second order spin-orbit coupling correction to the integrand of the intraband autocorrelation function can readily be expressed

$$\begin{aligned}\frac{\partial^2 \mathscr{J}_{il;s}^{\text{intra}}}{\partial\Delta_{mp}\partial\Delta_{nq}}\Big|_{\Delta=0} &= -\delta_{nm}\partial_i\varepsilon_s^0\partial_l\varepsilon_s^0\frac{k_pk_q}{\varepsilon_s^0}\big[\delta(\mu-\varepsilon_s^0+\hbar\omega)-\delta(\mu-\varepsilon_s^0)\big]\\ &+\delta_{nm}\Big[\Big(\delta_{ip}\frac{k_q}{\varepsilon_s^0}+\frac{k_p}{\varepsilon_s^0}\delta_{iq}\Big)\partial_l\varepsilon_s^0+\partial_i\varepsilon_s^0\Big(\frac{k_q}{\varepsilon_s^0}\delta_{lp}+\frac{k_p}{\varepsilon_s^0}\delta_{lq}\Big)\\ &\qquad-2\partial_i\varepsilon_s^0\partial_l\varepsilon_s^0\frac{k_p}{\varepsilon_s^0}\frac{k_q}{\varepsilon_s^0}\Big]\big[\Theta(\mu-\varepsilon_s^0+\hbar\omega)-\Theta(\mu-\varepsilon_s^0)\big].\end{aligned} \tag{8.37}$$

The resulting expression is written only in terms of components of the crystal momentum k_p and the energy functions $\varepsilon_s^0(\boldsymbol{k})$ in the absence of spin-orbit

coupling (8.9), making it viable to use the inverse momentum transform (8.27) which leaves the isotropic energy bands $\varepsilon_s^0(\kappa) = s\hbar\kappa$. Notice that under the assumption $\mu > 0$, only the positive energy band $s = +1$ will give a contribution due to the delta and Heaviside functions. Performing the momentum transformation in the expression for the second order spin-orbit correction to the intraband autocorrelation function (8.34) then leaves

$$\begin{aligned}\delta\Pi_{il}^{\text{intra}}(\omega) = \frac{2e^2}{\omega + i\eta}\sum_{p,q,m}\frac{\Delta_{mp}\Delta_{mq}}{\hbar^3\det\mathcal{V}}\int\frac{\mathrm{d}\kappa}{(2\pi)^3}\kappa^2\Bigg(\big[\Theta(\mu-\hbar\kappa+\hbar\omega)-\Theta(\mu-\hbar\kappa)\big] \\ \Bigg[\sum_{\lambda j}\Big[\big(\delta_{ip}u_{\lambda q}+u_{\lambda p}\delta_{iq}\big)\hbar v_{jl}+\hbar v_{ji}\big(\delta_{lp}u_{\lambda q}+u_{\lambda p}\delta_{lq}\big)\Big]\frac{\kappa_\lambda}{\hbar\kappa}\frac{\kappa_j}{\kappa} \\ -2\Big(\hbar^2\sum_{j,k}v_{ji}v_{kl}\frac{\kappa_j}{\kappa}\frac{\kappa_k}{\kappa}\Big)\sum_{\lambda\rho}u_{\lambda p}u_{\rho q}\frac{\kappa_\lambda}{\hbar\kappa}\frac{\kappa_\rho}{\hbar\kappa}\Bigg] \\ -\hbar\kappa\big[\delta(\mu-\hbar\kappa+\hbar\omega)-\delta(\mu-\hbar\kappa)\big]\Big(\hbar^2\sum_{jk}v_{ji}v_{kl}\frac{\kappa_j}{\kappa}\frac{\kappa_k}{\kappa}\Big)\sum_{\lambda\rho}u_{\lambda p}u_{\rho q}\frac{\kappa_\lambda}{\hbar\kappa}\frac{\kappa_\rho}{\hbar\kappa}\Bigg)\end{aligned}$$

where $\boldsymbol{u}_\lambda$ are the parametrization vectors (8.26) of the ellipsoidal Fermi surface. Notice here that the integrand is dependent on the transformed momentum mostly through terms on the form $\kappa_j/\kappa = (\hat{\boldsymbol{\kappa}})_j$, which are only dependent on the direction of the momentum and not its magnitude. Converting to spherical coordinates, the integral over the solid angle can be calculated separately. In particular, the integration over four components of the unit vector becomes

$$\int\mathrm{d}\Omega\ \ (\hat{\boldsymbol{\kappa}})_j(\hat{\boldsymbol{\kappa}})_k(\hat{\boldsymbol{\kappa}})_\lambda(\hat{\boldsymbol{\kappa}})_\delta = \frac{4\pi}{15}(\delta_{jk}\delta_{\lambda\delta}+\delta_{j\lambda}\delta_{k\delta}+\delta_{j\delta}\delta_{k\lambda}) \tag{8.38}$$

while the solid angle integral over two components (8.12) has been expressed previously. Inserting the resulting Kronecker deltas leaves two types of contractions (8.28) between the effective velocities $\boldsymbol{v}_j$ and the parametrization vectors $\boldsymbol{u}_\lambda$. Using also the Heaviside and delta functions to calculate the integral over the magnitude of the transformed crystal momentum, the second order spin-orbit coupling correction to the intraband autocorrelation function becomes

$$\begin{aligned}\delta\Pi_{il}^{\text{intra}}(\omega) = \frac{2e^2}{\omega+i\eta}\sum_{mpq}\frac{\Delta_{mp}\Delta_{mq}}{(2\pi)^3\hbar^3\det\mathcal{V}}\frac{\hbar^3\omega^3+3\hbar^2\omega^2\mu+\hbar\omega\mu^2}{\hbar^3} \\ \Bigg(\frac{8\pi}{45}\Big[4(\delta_{ip}\delta_{lq}+\delta_{iq}\delta_{pl})-\Big(\sum_j v_{ji}v_{jl}\Big)\Big(\sum_\lambda u_{\lambda p}u_{\lambda q}\Big)\Big] \\ +\frac{4\pi}{15}\Big[\delta_{ip}\delta_{lq}+\delta_{iq}\delta_{pl}+\Big(\sum_j v_{ji}v_{jl}\Big)\Big(\sum_\lambda u_{\lambda p}u_{\lambda q}\Big)\Big]\Bigg)\end{aligned}$$

Fusing the spin reversal parameters with the various terms using the sums over momentum indices, the second order spin-orbit coupling correction to the intraband autocorrelation function can finally be written on the form

$$\begin{aligned}\delta\Pi_{il}^{\text{intra}}(\omega) = \frac{e^2}{\omega+i\eta}\frac{1}{9\pi^2\hbar^3}\big[\hbar^3\omega^3+3\hbar^2\omega^2\mu+3\hbar\omega\mu^2\big] \\ \left[2\sum_m \frac{\Delta_{mi}\Delta_{ml}}{\hbar^3\boldsymbol{v}_1\cdot(\boldsymbol{v}_2\times\boldsymbol{v}_3)} - \left(\sum_j \frac{v_{ji}v_{jl}}{\hbar\boldsymbol{v}_1\cdot(\boldsymbol{v}_2\times\boldsymbol{v}_3)}\right)\sum_{m\lambda}\left(\frac{\boldsymbol{\Delta}_m\cdot\boldsymbol{u}_\lambda}{\hbar}\right)^2\right]\end{aligned} \tag{8.39}$$

Hence, in the direct current limit the correction to the intraband autocorrelation function becomes $\delta\Pi_{il}^{\text{intra}}(0) = 0$, and so the second order spin-orbit coupling correction to the intraband conductivity (8.14) can be calculated

$$\begin{aligned}\delta\sigma_{il}^{\text{intra}}(\omega) = \frac{e^2}{\eta-i\omega}\frac{\hbar^2\omega^2+3\hbar\omega\mu+3\mu^2}{9\pi^2\hbar^2} \\ \left[2\sum_m \frac{\Delta_{mi}\Delta_{ml}}{\hbar^3\boldsymbol{v}_1\cdot(\boldsymbol{v}_2\times\boldsymbol{v}_3)} - \left(\sum_j \frac{v_{ji}v_{jl}}{\hbar\boldsymbol{v}_1\cdot(\boldsymbol{v}_2\times\boldsymbol{v}_3)}\right)\sum_{m\lambda}\left(\frac{\boldsymbol{\Delta}_m\cdot\boldsymbol{u}_\lambda}{\hbar}\right)^2\right]\end{aligned} \tag{8.40}$$

The spin-orbit coupling correction is thus seen to take a similar form as the intraband conductivity tensor without spin-orbit coupling (8.14). Notice in particular the dependence on the effective velocity sums (8.22).

8.2.2 The Interband Spin-Orbit Coupling Correction

Consider next the interband term (8.7), whose integrand can be written

$$\mathcal{J}_{il;s}^{\text{inter}}(\Delta) = \big[n_F(\varepsilon_+) - n_F(\varepsilon_-)\big]\frac{s\Xi_{il}(\boldsymbol{k})}{2\varepsilon_s+\hbar\omega+i\eta}. \tag{8.41}$$

The derivative with respect to the spin reversal parameters then becomes

$$\begin{aligned}\frac{\partial^2\mathcal{J}_{il;s}^{\text{inter}}}{\partial\Delta_{mp}\partial\Delta_{nq}}\bigg|_{\Delta=0} = \left[\frac{\partial^2\varepsilon_+}{\partial\Delta_{mp}\partial\Delta_{nq}}\frac{\partial n_F}{\partial\varepsilon_+} - \frac{\partial^2\varepsilon_-}{\partial\Delta_{mp}\partial\Delta_{nq}}\frac{\partial n_F}{\partial\varepsilon_-}\right]\bigg|_{\Delta=0}\frac{s\Xi_{il}^0(\boldsymbol{k})}{2\varepsilon_s^0+\hbar\omega+i\eta} \\ + s\frac{\partial^2\Xi_{il}(\boldsymbol{k})}{\partial\Delta_{mp}\partial\Delta_{nq}}\bigg|_{\Delta=0}\frac{n_F(\varepsilon_+^0)-n_F(\varepsilon_-^0)}{2\varepsilon_s^0+\hbar\omega+i\eta} - \frac{\partial^2\varepsilon_s}{\partial\Delta_{mp}\partial\Delta_{nq}}\bigg|_{\Delta=0}\frac{2[n_F(\varepsilon_+^0)-n_F(\varepsilon_-^0)]s\Xi_{il}^0(\boldsymbol{k})}{(2\varepsilon_s^0+\hbar\omega+i\eta)^2}\end{aligned}$$

where again the energy functions $\varepsilon_s(\boldsymbol{k})$ and $\varepsilon_s^0(\boldsymbol{k})$ denote the doubly degenerate energy bands with (8.31) and without (8.9) spin-orbit coupling. Inserting the zero temperature limit, the Fermi-Dirac distribution approach a Heaviside function $n_F(\varepsilon_s) = \Theta(\mu-\varepsilon_s)$. With the two energy bands $\varepsilon_\pm$ strictly positive and strictly negative respectively, the difference of the Heaviside functions can then be written $\Theta(\mu-\varepsilon_+^0)-\Theta(\mu-\varepsilon_-^0) = -\Theta(\varepsilon_+^0-\mu)$ for $\mu > 0$. The derivatives

then approach delta functions, which for $\mu > 0$ only gives a contribution for $s = +1$. Furthermore, the derivative of the interband tensor (8.6) becomes

$$\begin{aligned}\frac{\partial^2 \Xi_{il}(\boldsymbol{k})}{\partial \Delta_{mp} \partial \Delta_{nq}}\bigg|_{\Delta=0} &= \delta_{mn}(\delta_{ip}\delta_{lq} + \delta_{iq}\delta_{lp}) \\ &\quad - \frac{\partial^2 \partial_i |\boldsymbol{H}|}{\partial \Delta_{mp} \partial \Delta_{nq}}\bigg|_{\Delta=0} \partial_l |\boldsymbol{H}_0| - \partial_i |\boldsymbol{H}_0| \frac{\partial^2 \partial_l |\boldsymbol{H}|}{\partial \Delta_{mp} \partial \Delta_{nq}}\bigg|_{\Delta=0}\end{aligned} \tag{8.42}$$

Notice here that $|\boldsymbol{H}(\boldsymbol{k})| = \varepsilon_+(\boldsymbol{k})$ for the case at hand. Inserting then the derivatives of the energy functions (8.36), the second order spin-orbit correction to the interband current density autocorrelation function becomes

$$\begin{aligned}\delta\Pi_{il}^{\text{inter}}(\omega) &= \frac{2e^2}{\hbar^2} \int \frac{d^3k}{(2\pi)^3} \sum_s \bigg(\sum_{p,q} \sum_{m,n} \frac{\partial^2 \mathcal{J}_{il;s}^{\text{inter}}}{\partial \Delta_{mp} \partial \Delta_{nq}}\bigg|_{\Delta=0} \Delta_{mp}\Delta_{nq} \bigg) \\ &= -\frac{2e^2}{\hbar^2} \sum_{p,q} \sum_m \Delta_{mp}\Delta_{mq} \int \frac{d^3k}{(2\pi)^3} \sum_s \bigg[\frac{s\Xi_{il}^0(\boldsymbol{k})\delta(\mu - \varepsilon_+^0)}{2\varepsilon_s^0 + \hbar\omega + i\eta} \frac{k_p k_q}{\varepsilon_+^0} \\ &\quad - \frac{2s\Xi_{il}^0(\boldsymbol{k})\Theta(\varepsilon_+^0 - \mu)}{(2\varepsilon_s^0 + \hbar\omega + i\eta)^2} \frac{k_p k_q}{\varepsilon_s^0} + \frac{s\Theta(\varepsilon_+^0 - \mu)}{2\varepsilon_s + \hbar\omega + i\eta} \bigg(\delta_{ip}\delta_{lq} + \delta_{iq}\delta_{lp} \\ &\quad - \Big(\delta_{ip}\frac{k_q}{\varepsilon_+^0} + \frac{k_p}{\varepsilon_+^0}\delta_{iq}\Big)\partial_l\varepsilon_+^0 - \partial_i\varepsilon_+^0\Big(\delta_{lp}\frac{k_q}{\varepsilon_+^0} + \frac{k_p}{\varepsilon_+^0}\delta_{lq}\Big) + 2\partial_i\varepsilon_+^0\partial_l\varepsilon_+^0 \frac{k_p}{\varepsilon_+^0}\frac{k_q}{\varepsilon_+^0} \bigg) \bigg]\end{aligned}$$

Seeing that the expression is dependent only on the energy function and components of the momentum, it is viable to perform the inverse momentum transformation (8.27), which leaves the energy bands isotropic with $\varepsilon_s(\boldsymbol{\kappa}) = s\hbar\kappa$. Inserting then the derivatives of the isotropic energy functions (8.11) and the inverse momentum transformation (8.27), the second order spin-orbit correction to the interband current density autocorrelation function is readily expressed

$$\begin{aligned}\delta\Pi_{il}^{\text{inter}}(\omega) &= -\frac{2e^2}{\hbar^2} \sum_{p,q} \sum_m \frac{\Delta_{mp}\Delta_{mq}}{\det \mathcal{V}} \bigg[\int \frac{\mathrm{d}^3\kappa}{(2\pi)^3} \sum_{\lambda\rho} u_{\lambda p} u_{\rho q} \Xi_{il}^0(\boldsymbol{\kappa}) \frac{\kappa_\lambda}{\hbar\kappa} \frac{\kappa_\rho}{\hbar\kappa} \\ &\quad \cdot \bigg(\hbar\kappa\delta(\hbar\kappa - \mu)\Big[\frac{1}{2\hbar\kappa + \hbar\omega + i\eta} + \frac{1}{2\hbar\kappa - \hbar\omega - i\eta}\Big] \\ &\qquad - 2\hbar\kappa\Theta(\hbar\kappa - \mu)\Big[\frac{1}{(2\hbar\kappa + \hbar\omega + i\eta)^2} + \frac{1}{(2\hbar\kappa - \hbar\omega - i\eta)^2}\Big] \bigg) \\ &\quad + \int \frac{\mathrm{d}^3\kappa}{(2\pi)^3} \Theta(\hbar\kappa - \mu)\Big[\frac{1}{2\hbar\kappa + \hbar\omega + i\eta} + \frac{1}{2\hbar\kappa - \hbar\omega - i\eta}\Big] \\ &\qquad \cdot \bigg(\big(\delta_{ip}\delta_{lq} + \delta_{iq}\delta_{lp}\big) + 2\sum_{jm} \hbar v_{ji} \hbar v_{ml} \frac{\kappa_j}{\kappa}\frac{\kappa_m}{\kappa} \sum_{\lambda\rho} u_{\lambda p} u_{\rho q} \frac{\kappa_\lambda}{\hbar\kappa}\frac{\kappa_\rho}{\hbar\kappa} \\ &\quad - \sum_\lambda \Big[\big(\delta_{ip}u_{\lambda q}\frac{\kappa_\lambda}{\hbar\kappa} + u_{\lambda p}\frac{\kappa_\lambda}{\hbar\kappa}\delta_{iq}\big)\hbar v_{jl}\frac{\kappa_j}{\kappa} + \hbar v_{ji}\frac{\kappa_j}{\kappa}\big(\delta_{lp}u_{\lambda q}\frac{\kappa_\lambda}{\hbar\kappa} + u_{\lambda p}\frac{\kappa_\lambda}{\hbar\kappa}\delta_{lq}\big) \Big] \bigg) \bigg]\end{aligned}$$

where $\boldsymbol{v}_j$ and $\boldsymbol{u}_\lambda$ are the effective velocity vectors and the parametrization vectors (8.26) of the ellipsoidal Fermi surface, respectively.

Recall that the isotropic interband tensor (8.16) is dependent only on the magnitude of the transformed momentum, as $\Xi^0_{il}(\boldsymbol{\kappa}) = \Xi^0_{il}(\hat{\boldsymbol{\kappa}})$, and notice that all terms of the correction are dependent only on the magnitude κ or the direction $\boldsymbol{\kappa}_j/\kappa = (\hat{\boldsymbol{\kappa}})_i$ of the transformed crystal momentum. Hence, converting to spherical coordinates the integrals can be split into integrals over the magnitude and the direction of the transformed crystal momentum separately. In the zero scattering limit, the Sokhotski-Plemelj-Fox theorem [33] then gives the factors

$$\lim_{\eta\to 0}\int \frac{F(x)}{(x - x_0 \mp i\eta)^{n+1}}\mathrm{d}x = \mathrm{P}\int \frac{F(x)}{(x-x_0)^{n+1}}\mathrm{d}x \pm \frac{i\pi}{n!}\frac{\mathrm{d}^n F}{\mathrm{d}x^n}\bigg|_{x=x_0} \tag{8.43}$$

where P represents the Cauchy principal value of the integral. The Sokhotski-Plemelj-Fox theorem is a generalization of the Sokhotski-Plemelj theorem (7.11), and reduces to the latter for $n = 0$, giving for the first and third terms

$$\lim_{\eta\to 0}\frac{1}{2\hbar\kappa + s\hbar\omega + is\eta} = -is\pi\delta(2\kappa + s\hbar\omega) + \mathrm{P}\frac{1}{2\hbar\kappa + s\hbar\omega} \tag{8.44}$$

Likewise, for the second term the Sokhotski-Plemelj-Fox theorem gives

$$\lim_{\eta\to 0}\frac{1}{(2\hbar\kappa + s\hbar\omega + is\eta)^2} = \mathrm{P}\frac{1}{(2\hbar\kappa + s\hbar\omega)^2} + is\pi\delta'(2\kappa + s\hbar\omega), \tag{8.45}$$

where $\delta'(x)$ is the distributional derivative of the delta function. The expression can also be derived by explicit differentiation of the Sokhotski-Plemelj theorem (8.44). Thus, for the second term the magnitude integral

$$\begin{aligned}\lim_{\eta\to 0}\int \mathrm{d}\kappa \frac{\kappa^3\Theta(\hbar\kappa - \mu)}{(2\hbar\kappa + s\hbar\omega + is\eta)^2} &= \mathrm{P}\int \mathrm{d}\kappa \frac{\kappa^3\Theta(\hbar\kappa - \mu)}{(2\hbar\kappa - s\hbar\omega)^2} \\ &\quad - \frac{is\pi}{4\hbar^4}\Big(\frac{\hbar\omega}{2}\Big)^3\delta\Big(-\frac{s\hbar\omega}{2} - \mu\Big) - \frac{3is\pi}{4\hbar^4}\Big(\frac{\hbar\omega}{2}\Big)^2\Theta\Big(-\frac{s\hbar\omega}{2} - \mu\Big)\end{aligned}$$

In both cases, the action of taking the Cauchy principal value avoids the singularities present at $\varepsilon^0_s = \hbar\omega/2$ for the case $s = -1$. In the following, in order to simplify notation the symbol P representing the Cauchy principal value is rendered implicit. Notice also that the appearing delta and Heaviside functions only gives a contribution for $s = +1$ under the assumption $\mu > 0$.

Hence, after converting to spherical coordinates and using the Sokhotski-Plemelj-Fox theorem (8.43), the second order spin-orbit coupling correction to the interband autocorrelation function becomes

$$\delta\Pi_{il}^{\text{inter}}(\omega) = -\frac{2e^2}{(2\pi)^3\hbar^2}\sum_{p,q}\sum_{m}\frac{\Delta_{mp}\Delta_{mq}}{\det\mathcal{V}}\Bigg[\sum_{\lambda\rho}u_{\lambda p}u_{\rho q}\int \mathrm{d}\Omega\;\Xi_{il}^{0}(\hat{\boldsymbol{\kappa}})\frac{\kappa_\lambda}{\hbar\kappa}\frac{\kappa_\rho}{\hbar\kappa}$$
$$\cdot\Bigg(\int \mathrm{d}\kappa\;\hbar\kappa^3\delta(\hbar\kappa-\mu)\Big[\frac{1}{2\hbar\kappa+\hbar\omega}+\frac{1}{2\hbar\kappa-\hbar\omega}+i\pi\delta(2\hbar\kappa-\hbar\omega)\Big]$$
$$-2\int \mathrm{d}\kappa\;\hbar\kappa^3\Theta(\hbar\kappa-\mu)\Big[\frac{1}{(2\hbar\kappa+\hbar\omega)^2}+\frac{1}{(2\hbar\kappa-\hbar\omega)^2}\Big]$$
$$-\frac{i\pi}{2\hbar^3}\Big(\frac{\hbar\omega}{2}\Big)^3\delta\Big(\frac{\hbar\omega}{2}-\mu\Big)-\frac{3i\pi}{2\hbar^3}\Big(\frac{\hbar\omega}{2}\Big)^2\Theta\Big(\frac{\hbar\omega}{2}-\mu\Big)\Bigg)$$
$$+\Bigg(4\pi\big(\delta_{ip}\delta_{lq}+\delta_{iq}\delta_{lp}\big)+2\sum_{jm}v_{ji}v_{ml}\sum_{\lambda\rho}u_{\lambda p}u_{\rho q}\int \mathrm{d}\Omega\frac{\kappa_j}{\kappa}\frac{\kappa_m}{\kappa}\frac{\kappa_\lambda}{\kappa}\frac{\kappa_\rho}{\kappa}$$
$$-\sum_{\lambda}\Big[\big(\delta_{ip}u_{\lambda q}+u_{\lambda p}\delta_{iq}\big)v_{jl}+v_{ji}\big(\delta_{lp}u_{\lambda q}+u_{\lambda p}\delta_{lq}\big)\Big]\int \mathrm{d}\Omega\frac{\kappa_j}{\kappa}\frac{\kappa_\lambda}{\kappa}\Bigg)$$
$$\cdot\int \mathrm{d}\kappa\;\kappa^2\Theta(\hbar\kappa-\mu)\Big[\frac{1}{2\hbar\kappa+\hbar\omega}+\frac{1}{2\hbar\kappa-\hbar\omega}+i\pi\delta(2\hbar\kappa-\hbar\omega)\Big]\Bigg]$$

Notice here that the two delta function divergences cancel exactly. For the third integral, the solid angle integrals over two (8.12) and four (8.38) components of the unit vector can be inserted directly. From the expression of the interband tensor (8.16) with zero spin-orbit coupling, the remaining solid angle integral

$$\int \mathrm{d}\Omega\;\Xi_{il}^{0}(\hat{\boldsymbol{\kappa}})\frac{\kappa_\lambda}{\kappa}\frac{\kappa_\rho}{\kappa}=\frac{16\pi\hbar^2}{15}\delta_{\lambda\rho}\sum_{j}v_{ji}v_{jl}-\frac{4\pi\hbar^2}{15}\big(v_{\lambda i}v_{\rho l}+v_{\rho i}v_{\lambda l}\big).\qquad(8.46)$$

The three integrals over the magnitude κ however are divergent, being an artefact of the linearization of the energy band structure around the Dirac point in the continuum limit. Introducing then the momentum cutoff $\kappa_c=\hbar\omega_c/2$, all integrals are readily calculated and the correction term expressed

$$\delta\Pi_{il}^{\text{inter}}(\omega) = -\frac{2e^2}{(2\pi)^3\hbar^2}\sum_{p,q}\sum_{m}\frac{\Delta_{mp}\Delta_{mq}}{\hbar^3\det\mathcal{V}}\Bigg[\Big(\frac{4\mu^4}{4\mu^2-\hbar^2\omega^2}-\frac{3i\pi}{2}\Big(\frac{\hbar\omega}{2}\Big)^2\Theta\Big(\frac{\hbar\omega}{2}-\mu\Big)$$
$$-\frac{1}{8}\Big[3\hbar^2\omega^2\ln\Big|\frac{\hbar^2\omega_c^2-\hbar^2\omega^2}{4\mu^2-\hbar^2\omega^2}\Big|+\frac{2\hbar^4\omega^4}{\hbar^2\omega^2-\hbar^2\omega_c^2}-\frac{2\hbar^4\omega^4}{\hbar^2\omega^2-4\mu^2}+\hbar^2\omega_c^2-4\mu^2\Big]\Big)$$
$$\frac{4\pi}{15}\Big[4\Big(\sum_j v_{ji}v_{jl}\Big)\Big(\sum_\lambda u_{\lambda p}u_{\lambda q}\Big)-\big(\delta_{ip}\delta_{lq}+\delta_{iq}\delta_{lp}\big)\Big]$$
$$+\frac{1}{8}\Bigg(\hbar^2\omega^2\ln\Big|\frac{\hbar^2\omega_c^2-\hbar^2\omega^2}{4\mu^2-\hbar^2\omega^2}\Big|+\hbar^2\omega_c^2-4\mu^2+i\pi\hbar^2\omega^2\Theta(\frac{\hbar\omega}{2}-\mu)\Bigg)$$
$$\frac{4\pi}{15}\Big[2\Big(\sum_j v_{ji}v_{jl}\Big)\Big(\sum_\lambda u_{\lambda p}u_{\lambda q}\Big)+7\big(\delta_{ip}\delta_{lq}+\delta_{iq}\delta_{lp}\big)\Big]\Bigg]$$

Inserting here the determinant $\det \mathcal{V} = \boldsymbol{v}_1 \cdot (\boldsymbol{v}_2 \times \boldsymbol{v}_3)$, in order to compactify the expressions it is viable to introduce the *spin reversal parameter sums*

$$\mathfrak{Q}_{il} = \sum_m \frac{\Delta_{mi}\Delta_{ml}}{\hbar^3 \boldsymbol{v}_1 \cdot (\boldsymbol{v}_2 \times \boldsymbol{v}_3)} \tag{8.47}$$

analogous to the effective velocity sums (8.22) defined previously. Furthermore, the expressions for the corrections are seen to be dependent on a sum independent on the conductivity tensor indices, hereby named the *warping sum*

$$\mathfrak{X} = \sum_{m\lambda} \left(\frac{\boldsymbol{\Delta}_m \cdot \boldsymbol{u}_\lambda}{\hbar} \right)^2 = \frac{1}{2} \sum_{m\mu\nu} \left(\frac{\boldsymbol{\Delta}_m \cdot (\boldsymbol{v}_\mu \times \boldsymbol{v}_\nu)}{\hbar \boldsymbol{v}_1 \cdot (\boldsymbol{v}_2 \times \boldsymbol{v}_3)} \right)^2 . \tag{8.48}$$

where the latter equality can be derived from inserting the expression for the parametrization vectors (8.26). Because the parametrization vectors $\boldsymbol{u}_\lambda$ by assumption span reciprocal space, the warping sum will be nonzero as long as any of the spin reversal parameters Δ_{mp} are nonzero.

Gathering similar terms, the spin-orbit coupling correction to the interband autocorrelation function is written in terms of the warping sum $\mathfrak{X}$, the effective velocity sums $\mathfrak{V}_{il}$ and the spin reversal parameter sums $\mathfrak{Q}_{il}$ as

$$\begin{aligned}
\delta\Pi_{il}^{\text{inter}}(\omega) = -\frac{e^2}{15\pi^2\hbar^2} \Bigg[& -\frac{5i\pi}{8}\hbar^2\omega^2\Theta\Big(\frac{\hbar\omega}{2} - \mu\Big)\Big[2\mathfrak{X}\mathfrak{V}_{il} - 4\mathfrak{Q}_{il}\Big] \\
& - \frac{5}{8}\left(\hbar^2\omega^2 \ln\left|\frac{\hbar^2\omega_c^2 - \hbar^2\omega^2}{4\mu^2 - \hbar^2\omega^2}\right| + \hbar^2\omega_c^2 - 4\mu^2\right)\Big[2\mathfrak{X}\mathfrak{V}_{il} - 4\mathfrak{Q}_{il}\Big] \\
& + \left(\frac{4\mu^4}{4\mu^2 - \hbar^2\omega^2} - \frac{1}{4}\frac{\hbar^4\omega^4(\hbar^2\omega_c^2 - 4\mu^2)}{(\hbar^2\omega^2 - \hbar^2\omega_c^2)(\hbar^2\omega^2 - 4\mu^2)}\right)\Big[4\mathfrak{X}\mathfrak{V}_{il} - 2\mathfrak{Q}_{il}\Big]
\end{aligned}$$

The second order spin-orbit correction to the interband conductivity tensor can then be calculated as $\delta\sigma_{il}^{\text{inter}}(\omega) = (\delta\Pi_{il}^{\text{inter}}(\omega) - \delta\Pi_{il}^{\text{inter}}(0))/i\omega$, which gives

$$\begin{aligned}
\operatorname{Re}\delta\sigma_{il}^{\text{inter}}(\omega) &= \frac{e^2\omega}{12\pi}\Theta\Big(\frac{\hbar\omega}{2} - \mu\Big)\Big[2\mathfrak{Q}_{il} - \mathfrak{X}\mathfrak{V}_{il}\Big] \\
\operatorname{Im}\delta\sigma_{il}^{\text{inter}}(\omega) &= \frac{e^2\omega}{12\pi^2}\left(\ln\left|\frac{\hbar^2\omega^2 - 4\mu^2}{\hbar^2\omega^2 - \hbar^2\omega_c^2}\right|\Big[2\mathfrak{Q}_{il} - \mathfrak{X}\mathfrak{V}_{il}\Big]\right. \\
&\qquad \left. + \frac{2}{5}\frac{\hbar^2\omega_c^2}{\hbar^2\omega^2 - \hbar^2\omega_c^2}\Big[\mathfrak{Q}_{il} - 2\mathfrak{X}\mathfrak{V}_{il}\Big]\right)
\end{aligned} \tag{8.49}$$

Compared to the interband conductivity tensor (8.21) in the absence of spin-orbit coupling, the second order spin-orbit coupling correction is seen to renormalize the effective velocity sums (8.22). Furthermore, the imaginary part of the correction introduces a new dependency of the conductivity tensor on the optical frequency ω, dependent on the cutoff frequency ω_c.

8.2.3 The Total Conductivity Tensor

Combining the intraband conductivity tensor $\sigma^{\text{intra}}_{0;il}(\omega)$ neglecting spin-orbit coupling (8.14) with the corresponding spin-orbit coupling correction (8.34), the intraband conductivity tensor to second order in spin-orbit coupling becomes

$$\sigma^{\text{intra}}_{il}(\omega) = \frac{e^2}{\eta - i\omega} \frac{\hbar^2\omega^2 + 3\hbar\omega\mu + 3\mu^2}{9\pi^2\hbar^2} \left[\Big(1 - \mathfrak{X}\Big)\mathfrak{V}_{il} + 2\mathfrak{Q}_{il} \right] \tag{8.50}$$

Likewise, the real and imaginary parts of the interband conductivity tensor neglecting spin-orbit coupling (8.21) can be combined with the corresponding correction (8.49) to give the interband conductivity tensor to second order

$$\begin{aligned} \text{Re}\, \sigma^{\text{inter}}_{il}(\omega) &= \frac{e^2\omega}{12\pi} \Theta\Big(\frac{\hbar\omega}{2} - \mu\Big) \left[\Big(1 - \mathfrak{X}\Big)\mathfrak{V}_{il} + 2\mathfrak{Q}_{il} \right] \\ \text{Im}\, \sigma^{\text{inter}}_{il}(\omega) &= \frac{e^2\omega}{12\pi^2} \left[\ln\left| \frac{\hbar^2\omega^2 - 4\mu^2}{\hbar^2\omega^2 - \hbar^2\omega_c^2} \right| \left[\Big(1 - \mathfrak{X}\Big)\mathfrak{V}_{il} + 2\mathfrak{Q}_{il} \right] \right. \\ &\qquad \left. + \frac{2}{5} \frac{\hbar^2\omega_c^2}{\hbar^2\omega^2 - \hbar^2\omega_c^2} \Big[\mathfrak{Q}_{il} - 2\mathfrak{X}\mathfrak{V}_{il} \Big] \right] \end{aligned} \tag{8.51}$$

Hence, to second order in the spin reversal parameters both the interband and intraband conductivity tensors become dependent on the effective velocity sums (8.22), the warping sum (8.48) and the spin reversal parameter sums (8.47) through a term $(1 - \mathfrak{X})\mathfrak{V}_{il} + 2\mathfrak{Q}_{il}$. The warping sum $\mathfrak{X}$ is interpreted as an effect of the change in shape of the Fermi surface due to the spin-orbit coupling interaction compared to the case with zero spin-orbit coupling. The spin reversal parameter sums however does not allow for a simple geometrical interpretation, but are seen to give rise to transverse components of the conductivity tensor as long as the components Δ_{mi} and Δ_{ml} are nonzero for some indices m and $i \neq l$.

The calculation for the conductivity tensor corresponding to the Dirac Hamiltonian kernel has thus been reduced to calculating the effective velocity sums (8.22), the spin-orbit coupling sums (8.47) and the warping sum (8.48), determined by the effective velocities $\boldsymbol{v}_i$ and the spin reversal parameters $\boldsymbol{\Delta}_m$. In particular, the ellipsoidal Fermi surface does not allow for a parametrization where the parametrization vectors are orthogonal, or several components of the spin reversal parameters are nonzero simultaneously, the conductivity tensor will contain finite nondiagonal elements corresponding to a symmetric anomalous Hall conductivity. However, all the intrinsic terms which are not dependent on a nonzero scattering are dependent on a nonzero optical frequency ω to be finite. Hence, a Dirac semimetal will in general inhibit a symmetric anomalous Hall effect for nonzero optical frequencies, even if the Berry curvature of the material is zero due to the imposed $\mathcal{PT}$-symmetry of the system.

8.3 Dirac Fermions in an Antiferromagnetic Semimetal

An important example of a recently investigated Dirac semimetal is the material *CuMnAs*, formed by various atomic compositions of copper, manganese and arsenic in different crystal structures dependent on the stochiometry of the composition. Below the Néel temperature of the specific structure [36] the manganese atoms of the primitive unit cell are antiferromagnetically ordered, making CuMnAs an example of an antiferromagnetic Dirac semimetal. The following section displays the crystal structure of CuMnAs, and briefly recites the construction of an effective four-band model based on symmetry arguments as performed by Tang et al. [11]. The resulting effective Dirac Hamiltonian kernel is then combined with the general conductivity formulae for a Dirac semimetal derived in the previous section in order to exemplify the results and predict the electronic transport properties of an experimentally realizable material.

8.3.1 Symmetry Considerations of CuMnAs

The crystal structure of the compound CuMnAs is sensitive to the exact relative composition of the copper, manganese and arsenic atoms, with three different structural phases reported [36]. Stochiometric CuMnAs crystallizes in an orthorhombic structure with four formula units in the primitive unit cell. If instead the compound is manganese deficient compared to the stochiometric case the crystal lattice arranges in a tetragonal structure with two formula units in the unit cell. For both structures the manganese atoms are antiferromagnetically ordered and the crystal lattice invariant under the $\mathcal{PT}$-symmetry, as shown in figure 8.2. The energy band structures of both the tetragonal and the orthorhombic phases of CuMnAs are able to harbour Dirac points close to the Fermi level, and are hence classified as antiferromagnetic Dirac semimetals [37]. In the following, the analysis will only consider the stochiometric orthorhombic phase, as studied by Tang et al. [11]. An analysis of the tetragonal phase is investigated by Šmejkal et al. [38] and briefly recited in the next subsection.

As portrayed by figure 8.2 the orthorhombic CuMnAs crystal structure contains four manganese atoms labelled Mn1 to Mn4. In the ground state of the crystalline system, the localized magnetic moments of the manganese atoms point in the positive z-direction for Mn1 and Mn2, and in the negative z-direction for Mn3 and Mn4. Counting the spin degree of freedom, the tight-binding approach represented in chapter 4 will correspond to the construction of eight Bloch sums (4.8) denoted by $|\chi_{\alpha\varsigma}(\boldsymbol{k})\rangle$, where $\boldsymbol{k}$ is the crystal momentum, α the site index of the manganese atoms and ς the physical spin index of the electron; the symbol σ attains another meaning in the following.

From the analysis performed by Tang et al. [11], the orthorhombic CuMnAs crystal lattice is invariant under the screw-axis symmetry S_{2z}, being a rotation of π radians about the z-axis followed by a translation $T_{\boldsymbol{\rho}}$ with the translation vector $\boldsymbol{\rho} = (\frac{1}{2}, 0, \frac{1}{2})$ given in lattice units. Hence, performing the operation twice leaves $S_{2z}^2 = -T_{\hat{\boldsymbol{z}}}$, where $\hat{\boldsymbol{z}} = (0, 0, 1)$ is the lattice unit vector in the z-direction and the negative sign originates in the full rotation of the localized magnetic

moments. Furthermore, from its definition in real space the S_{2z} symmetry acts on the crystal momentum of reciprocal space as $S_{2z} : \boldsymbol{k} \to (-k_x, -k_y, k_z)$.

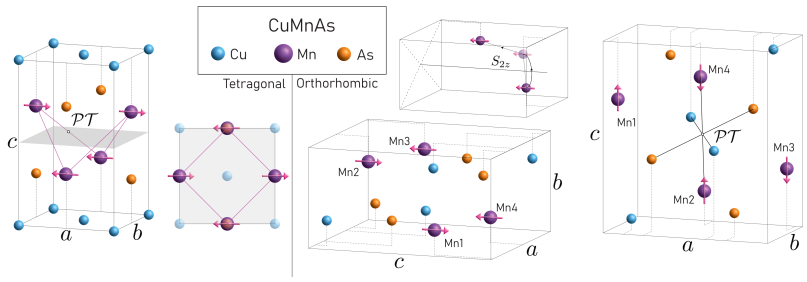

Figure 8.2: The primitive unit cells of tetragonal and orthorhombic CuMnAs, with lattice parameters given by $a = b = 0.3800\,\text{nm}$ and $c = 0.6318\,\text{nm}$ for the tetragonal and $a = 0.6586\,\text{nm}$, $b = 0.3867\,\text{nm}$ and $c = 0.7320\,\text{nm}$ for the orthorhombic phase, with the two phases having two and four structural formulae per unit cell respectively. The manganese nuclei are antiferromagnetically ordered, with spin directions given by the arrows. The figure also displays the $\mathcal{PT}$-symmetry of the two crystal structures, and the S_{2z}-symmetry for the orthorhombic phase. The figures are based on the lattice parameters provided by Mündelein and Schuster [39], and inspired by Uhlířová et al. [36] and Šmejkal et al. [38].

The Bloch eigenstates of the Hamiltonian operator of orthorhombic CuMnAs can thus be chosen as simultaneous eigenstates with S_{2z}, which can also be constructed from the Bloch sums $|\chi_{\alpha\varsigma}(\boldsymbol{k})\rangle$. Consider then the action of the S_{2z} symmetry on the Bloch sums. Seeing that the Bloch sums satisfies the Bloch theorem (B16) and noticing from figure 8.2 that the manganese atoms are moved to different unit cells under the screw-axis symmetry S_{2z}, then

$$\begin{aligned}
S_{2z}\,|\chi_{1\varsigma}(\boldsymbol{k})\rangle &= \varsigma i e^{-ik_x}\,|\chi_{2\varsigma}(-k_x,-k_y,k_z)\rangle \\
S_{2z}\,|\chi_{2\varsigma}(\boldsymbol{k})\rangle &= \varsigma i e^{-ik_x}e^{-ik_z}\,|\chi_{1\varsigma}(-k_x,-k_y,k_z)\rangle \\
S_{2z}\,|\chi_{3\varsigma}(\boldsymbol{k})\rangle &= \varsigma i e^{-ik_z}\,|\chi_{4\varsigma}(-k_x,-k_y,k_z)\rangle \\
S_{2z}\,|\chi_{4\varsigma}(\boldsymbol{k})\rangle &= \varsigma i\,|\chi_{3\varsigma}(-k_x,-k_y,k_z)\rangle
\end{aligned} \tag{8.52}$$

where the sign $\varsigma = \pm 1$ again originates in the rotation of the spin degree of freedom. In consequence, eigenstates of the S_{2z} operator can be constructed as

$$\begin{aligned}
|\Phi_+(\boldsymbol{k})\rangle &= a_+\big[\,|\chi_{1+}(\boldsymbol{k})\rangle + e^{-ik_x}e^{ik_z/2}\,|\chi_{2+}(-k_x,-k_y,k_z)\rangle\,\big] \\
&\quad + b_+\big[e^{ik_z/2}\,|\chi_{3+}(\boldsymbol{k})\rangle + |\chi_{4+}(-k_x,-k_y,k_z)\rangle\,\big] \\
|\Phi_-(\boldsymbol{k})\rangle &= a_-\big[\,|\chi_{1+}(\boldsymbol{k})\rangle - e^{-ik_x}e^{ik_z/2}\,|\chi_{2+}(-k_x,-k_y,k_z)\rangle\,\big] \\
&\quad + b_-\big[-e^{ik_z/2}\,|\chi_{3+}(\boldsymbol{k})\rangle + |\chi_{4+}(-k_x,-k_y,k_z)\rangle\,\big]
\end{aligned} \tag{8.53}$$

satisfying the eigenvalue equations $S_{2z}\,|\Phi_\pm(\boldsymbol{k})\rangle = \pm ie^{-ik_z/2}\,|\Phi_\pm(\boldsymbol{k})\rangle$. Notice that these are then eigenstates of $S_{2z}^2 = -T_{\hat{\boldsymbol{z}}}$ satisfying the eigenvalue equation $S_{2z}^2\,|\Phi_\pm(\boldsymbol{k})\rangle = -e^{ik_z}\,|\Phi_\pm(\boldsymbol{k})\rangle$, being a consequence of the Bloch theorem (B16).

Furthermore, the crystal lattice is invariant under the $\mathcal{PT}$-symmetry, making all energy bands Kramers degenerate. From figure 8.2, the manganese atoms Mn1 and Mn3 are seen to be partners under space inversion, and so their corresponding Bloch sums satisfies $\mathcal{P}\,|\chi_{1\varsigma}(\boldsymbol{k})\rangle = |\chi_{3\varsigma}(-\boldsymbol{k})\rangle$. Likewise, the Bloch sums of the lattice sites Mn2 and Mn4 are related by $\mathcal{P}\,|\chi_{2\varsigma}(\boldsymbol{k})\rangle = |\chi_{4\varsigma}(-\boldsymbol{k})\rangle$. In conclusion, with the time reversal operator $\mathcal{T}$ reversing the direction of the spin, the $\mathcal{PT}$-operator acts on the eigenstates (8.53) of the S_{2z} operator as

$$\begin{aligned}
\mathcal{PT}\,|\Phi_+(\boldsymbol{k})\rangle &= a_+^* e^{-ik_z/2}\big[e^{ik_z/2}\,|\chi_{3-}(\boldsymbol{k})\rangle + e^{ik_x}\,|\chi_{4-}(-k_x,-k_y,k_z)\rangle\,\big] \\
&\quad + b_+^* e^{-ik_z/2}\big[\,|\chi_{1-}(\boldsymbol{k})\rangle + e^{ik_z/2}\,|\chi_{2-}(-k_x,-k_y,k_z)\rangle\,\big] \\
\mathcal{PT}\,|\Phi_-(\boldsymbol{k})\rangle &= a_-^* e^{-ik_z/2}\big[e^{ik_z/2}\,|\chi_{3-}(\boldsymbol{k})\rangle - e^{ik_x}\,|\chi_{4-}(-k_x,-k_y,k_z)\rangle\,\big] \\
&\quad + b_-^* e^{-ik_z/2}\big[\,|\chi_{1-}(\boldsymbol{k})\rangle - e^{ik_z/2}\,|\chi_{2-}(-k_x,-k_y,k_z)\rangle\,\big]
\end{aligned} \tag{8.54}$$

From Kramers theorem, demonstrated in appendix C, the states $\mathcal{PT}\,|\Phi_\pm\rangle$ are distinct from the eigenstates $|\Phi_\pm\rangle$ of the S_{2z} operator. Furthermore, from the definition of the S_{2z} screw-axis symmetry, the $\mathcal{PT}$ and S_{2z} operators do not commute but satisfies the relation $S_{2z}(\mathcal{PT}) = T_{2\boldsymbol{\rho}}(\mathcal{PT})S_{2z}$. Using then the eigenvalue equation $S_{2z}\,|\Phi_\pm(\boldsymbol{k})\rangle = \pm ie^{-ik_z/2}\,|\Phi_\pm(\boldsymbol{k})\rangle$, the states $\mathcal{PT}\,|\Phi_\pm(\boldsymbol{k})\rangle$ are also eigenstates of the operator S_{2z}, satisfying the eigenvalue equation

$$S_{2z}(\mathcal{PT}\,|\Phi_\pm\rangle) = \mp ie^{-ik_x}e^{-ik_z/2}\mathcal{PT}\,|\Phi_\pm\rangle \tag{8.55}$$

which is readily confirmed by directly applying the S_{2z} operator.

Recall then that the screw-axis symmetry acts on the crystal momentum as $S_{2z} : \boldsymbol{k} \to (-k_x, -k_y, k_z)$. Hence, there are four high symmetry lines in the Brillouin zone invariant under the operation S_{2z}, given in lattice units by $k_x, k_y \in \{0, \pi\}$. Notice then that in the planes defined by $k_x = 0$ and $k_x = \pi$, the $\mathcal{PT}$-partners of the eigenstates (8.53) of the S_{2z} operator satisfies

$$\begin{aligned}
S_{2z}(\mathcal{PT}\,|\Phi_\pm(0,k_y,k_z)\rangle &= \mp ie^{-ik_z/2}\mathcal{PT}\,|\Phi_\pm(0,k_y,k_z)\rangle \\
S_{2z}(\mathcal{PT}\,|\Phi_\pm(\pi,k_y,k_z)\rangle &= \pm ie^{-ik_z/2}\mathcal{PT}\,|\Phi_\pm(\pi,k_y,k_z)\rangle\,,
\end{aligned} \tag{8.56}$$

and are thus eigenstates of the S_{2z} operator with eigenvalues opposite of and equal to $|\Phi_\pm(\boldsymbol{k})\rangle$, respectively. As argued by Tang et al. [11], the assignment of equal eigenvalues to $\mathcal{PT}$-partners will in general lead any band crossing to be stable. Hence, for orthorhombic CuMnAs any band crossing in the plane $k_x = 0$ will be unstable, while band crossings in the plane $k_x = \pi$ will be stable to perturbations. These band crossings are furthermore expected to take place along the high symmetry lines where also $k_y = 0$ or $k_y = \pi$, being the regions of the Brillouin zone invariant under the S_{2z} symmetry.

Finally, notice that the four states $|\Phi_\pm(\boldsymbol{k})\rangle$ and $\mathcal{PT}\,|\Phi_\pm(\boldsymbol{k})\rangle$ are Bloch states, being linear combinations of Bloch sums (4.8). The eigenstates of the Hamiltonian operator can then be written as linear combinations of these four states. The S_{2z} symmetry thus groups the original eight Bloch sums $\chi_{\alpha\varsigma}(\boldsymbol{k})$ into pairs,

effectively reducing the dimensionality of the Hamiltonian kernel to (4×4). The states $|\Phi_+\rangle$ and $|\Phi_-\rangle$ are here interpreted as orbital states corresponding to a pseudospin basis denoted τ, while the $\mathcal{PT}$-partners $|\Phi_+\rangle$ and $\mathcal{PT}|\Phi_+\rangle$ correspond to a spin-related *antiferromagnetic basis* denoted by σ.

In particular, in the plane $k_x = \pi$ the S_{2z} symmetry can be represented by $S_{2z} = ie^{-ik_z/2}\tau_z$, with its eigenvalues along the diagonal. Furthermore, seeing that $(\mathcal{PT})^2 = -1$ from the antiunitarity of the time reversal operator, the $\mathcal{PT}$ symmetry can likewise be represented by $\mathcal{PT} = i\sigma_y\mathcal{K}$. The representation of the $\mathcal{PT}$ operator here mathematically corresponds to the representation of the parity operator $\mathcal{P} = \pm\tau_0$ investigated in chapter 4. Here however, the $\mathcal{P}$ and $\mathcal{T}$ operators does not have a definite representation in the orbital and antiferromagnetic bases, in that the basis states $|\Phi_\pm\rangle$ and $\mathcal{PT}|\Phi_\pm(\boldsymbol{k})\rangle$ unlike the original Bloch sums $\chi_{\alpha\varsigma}(\boldsymbol{k})$ are not related by the $\mathcal{P}$ or $\mathcal{T}$ operations separately.

Hence, along the high symmetry line of the Brillouin zone defined by $k_x = \pi$ and $k_y = 0$, the Hamiltonian kernel of CuMnAs takes the same form as the general Hamiltonian kernel (6.13) investigated in section 8.1, where the $\mathcal{PT}$-symmetry has been enforced. Imposing the S_{2z} symmetry then leaves

$$\begin{aligned} S_{2z}\mathcal{H}(\boldsymbol{k})S_{2z}^{-1} =& h_0(-k_x,-k_y,k_z) - \tau_y\boldsymbol{\sigma}\cdot\boldsymbol{h}(-k_x,-k_y,k_z) \\ &+ \tau_z h_4(-k_x,-k_y,k_z) - \tau_x h_5(-k_x,-k_y,k_z) = \mathcal{H}(\boldsymbol{k}), \end{aligned}$$

Hence, invariance under S_{2z} imposes the condition $h_j(\boldsymbol{k}) = h_j(-k_x,-k_y,k_z)$ for $j \in \{0,4\}$ and $h_j(\boldsymbol{k}) = -h_j(-k_x,-k_y,k_z)$ for $j \in \{1,2,3,5\}$. Thus, at the line itself where $k_x = \pi$ and $k_y = 0$, the only remaining terms are $h_0(\pi,0,k_z)$ and $h_4(\pi,0,k_z)$. Hence, with only the parameter $h_4(\pi,0,k_z)$ remaining with k_z arbitrary, there will in general be some point where the energy bands (8.31) touch at a fourfold degenerate point. Shifting the origin to and expanding the parameters linearly around this point then leaves the Hamiltonian kernel

$$\begin{aligned} \mathcal{H}_o(\boldsymbol{k}) = (\hbar v_{11}k_x + \hbar v_{12}k_y)\tau_x + \hbar v_{33}k_z\tau_z + (\hbar v_{21}k_x + \hbar v_{22}k_y)\tau_y\sigma_z \\ +(\Delta_{11}k_x + \Delta_{12}k_y)\tau_y\sigma_x + (\Delta_{21}k_x + \Delta_{22}k_y)\tau_y\sigma_y, \end{aligned} \tag{8.57}$$

being on the same form as the general Dirac Hamiltonian kernel (8.8) with the effective velocities $\boldsymbol{v}_1 = (v_{11}, v_{12}, 0)$, $\boldsymbol{v}_2 = (v_{21}, v_{22}, 0)$ and $\boldsymbol{v}_3 = (0, 0, v_{33})$, and the spin reversal parameters $\boldsymbol{\Delta}_1 = (\Delta_{11}, \Delta_{12}, 0)$ and $\boldsymbol{\Delta}_2 = (\Delta_{21}, \Delta_{22}, 0)$. In conclusion, the S_{2z} symmetry allows for the presence of Dirac points in the energy band structure of orthorhombic CuMnAs.

Along the other high symmetry lines where the Dirac points are not protected by the S_{2z} symmetry, the Dirac points will vanish upon the introduction of spin-orbit coupling [11], rendering the derived Hamiltonian kernel (8.57) invalid. In general, a more rigorous and careful investigation of the crystal symmetries is needed in order to confirm the emergence of Dirac points when more than three terms of the Dirac Hamiltonian kernel (8.30) are nonzero.

8.3.2 Discussion on Reorientation of Magnetic Moments

Consider the tetragonal phase of CuMnAs as portrayed in figure 8.2 and analyzed by Šmejkal et al. [38]. Unlike the orthorhombic phase, the tetragonal crystal lattice contains only two manganese atoms in the unit cell, and so an effective four-band model can in the tightbinding approach be derived directly from the Bloch sums (4.8) corresponding to the manganese atoms. In this case, the pseudospin degree of freedom τ corresponds directly to the states $|\chi_{a+}\rangle$ and $|\chi_{b+}\rangle$ of the two sublattices, while the spin related degree of freedom σ is exactly the physical spin degree of freedom, corresponding to $|\chi_{a+}\rangle$ and $|\chi_{a-}\rangle$. The full tightbinding Hamiltonian kernel of tetragonal CuMnAs is given by [38]

$$\begin{aligned}\mathcal{H}_t(\boldsymbol{k}) = &-t_2(\cos k_x \cos k_y) - 2t_1 \cos\frac{k_x}{2}\cos\frac{k_y}{2} \\ &+ \Delta\tau_z(\sigma_y \sin k_x - \sigma_x \sin k_y) + \tau_z J_n \boldsymbol{\sigma}\cdot\boldsymbol{n}.\end{aligned} \tag{8.58}$$

where t_1 and t_2 describe intersublattice and intrasublattice tunnelling rates and Δ denotes the strength of the intrasublattice spin-orbit coupling strength respectively, and the final term gives explicitly the antiferromagnetic exchange coupling (6.27) with a coupling strength J_n in terms of the Néel vector $\boldsymbol{n}$. The representation of the Hamiltonian kernel corresponds to the parity operator $\mathcal{P} = \tau_x$, seeing from figure 8.2 that space inversion exchanges the two sublattices.

In the analysis performed by Šmejkal et al. [38], and similar to the discussion of section 6.3, the tetragonal phase of CuMnAs (8.58) harbours two Dirac points along the edge of the Brillouin zone when the Néel vector lies either in the x or in the y directions. Hence, the existence of Dirac points at different regions of the Brillouin zone can be controlled through a reorientation of the Néel vector. Such a reorientation can be performed by applying a current through the material, effectuated by the appearance of a spin-orbit torque. The change in the direction of the magnetic moments on the two sublattices is perpendicular to the direction of the applied current and the direction of the magnetic moments themselves.

For the orthorhombic phase of CuMnAs however, the primitive unit cell contains four localized magnetic moments, and so a single Néel vector is not in general defined. Recall then the eigenstates 8.53 of the S_{2z} operator, where the manganese atoms with the same direction of the localized magnetic moments are paired by the S_{2z} symmetry. Due to this pairing, a Néel vector for the orthorhombic phase of CuMnAs can be defined similarly to the tetragonal phase, as the difference between the magnetic moments of the two pairs. Here however, the exchange coupling (6.27) does not allow for a simple representation as for the Hamiltonian kernel of tetragonal CuMnAs (8.58), due to the particular construction of the τ and σ bases. Instead, the volatility of the Dirac points from the reorientation of the Néel vector can be discussed from symmetry arguments.

In the analysis performed by Tang et al. [11] on which the derivation of the orthorhombic CuMnAs Hamiltonian kernel (8.57) is based, the entire space group of orthorhombic CuMnAs is considered, which besides the space inversion symmetry $\mathcal{P}$ and the screw-axis rotation symmetry S_{2z} is generated also by the

unconsidered gliding mirror reflection R_y, composed of a reflection in the y-plane followed by a translation of half a lattice unit in the y-direction; the invariance under R_y can be verified visually by figure 8.2. With zero spin-orbit coupling, both of the symmetries are preserved. In this case, the analysis [11] reveals a fourfold degenerate *Dirac nodal line* on the high symmetry plane defined by $k_y = 0$, which is invariant under the gliding mirror reflection R_y.

When R_y is broken and only the S_{2z} symmetry is preserved, the Dirac nodal line becomes gapped except at four fourfold degenerate zero dimensional points. Two of these points lie on the high symmetry line defined by $k_x = \pi$ and $k_y = 0$, and are from the preceding discussion protected by the S_{2z} symmetry. The other pair lies within the bulk of the Brillouin zone and are not symmetry protected from perturbations. If the S_{2z} and R_y symmetries are simultaneously broken, the energy spectrum becomes fully gapped near the Fermi surface, and the material transitions to a semiconducting phase [37].

For the case with spin-orbit coupling, the localized magnetic moments on the manganese atoms enters into the Hamiltonian of the system. Seeing that the point group symmetries affect the magnetic moments $\boldsymbol{s}$ through rotation and reflection as $S_{2z} : \boldsymbol{s} \to (-s_x, -s_y, s_z)$ and $R_y : \boldsymbol{s} \to (-s_x, s_y, -s_z)$ respectively, the preservation of the symmetries will depend on the orientation of the magnetic moments. In particular, for the ground state of orthorhombic CuMnAs where the spins are aligned in the z-direction, the R_y symmetry is broken while the S_{2z} symmetry is still preserved. In this case, the pair of Dirac points lying at the high symmetry line will be preserved, while the pair lying within the bulk of the Brillouin zone will obtain a gap [37]. If the spins are aligned along any other axis however the S_{2z} symmetry will be broken, and the entire energy band spectrum will be gapped near the Fermi surface.

In conclusion, the derived Hamiltonian kernel for orthorhombic CuMnAs (8.57) is only valid when the localized magnetic moments and hence the Néel vector are aligned in the z-direction. In this case, the effect of the exchange coupling (6.27) is simply to move the location of the Dirac point along the z-axis on the high symmetry line of S_{2z} without affecting the shape of the Hamiltonian kernel itself. If the localized magnetic moments are aligned in any other direction, the effective Hamiltonian kernel will no longer be valid.

8.3.3 Orthorhombic CuMnAs Conductivity Predictions

Reconsider the derivations of section 8.1, where the intraband (8.14) and interband (8.21) conductivity tensors was calculated for a general Dirac semimetal neglecting spin-orbit coupling, followed by second order intraband (8.34) and interband (8.49) spin-orbit coupling corrections. The conductivity formulae are all dependent on a sum over the components of the effective velocities (8.22). For the effective Hamiltonian kernel (8.57) of orthorhombic CuMnAs nearby the Dirac point, the determinant of the momentum transform (8.10) takes the form

$$\det \mathcal{V} = \boldsymbol{v}_3 \cdot (\boldsymbol{v}_1 \times \boldsymbol{v}_2) = v_{33}(v_{11}v_{22} - v_{12}v_{21}). \tag{8.59}$$

Hence, the condition $\det \mathcal{V} \neq 0$ here translates to $v_{11}v_{22} \neq v_{12}v_{21}$ and $v_{33} \neq 0$. The corresponding effective velocity sums (8.22) can be calculated

$$\begin{aligned} \mathfrak{V}_{11} &= \frac{v_{11}^2 + v_{21}^2}{\hbar v_{33}(v_{11}v_{22} - v_{12}v_{21})} & \mathfrak{V}_{12} &= \frac{v_{11}v_{12} + v_{21}v_{22}}{\hbar v_{33}(v_{11}v_{22} - v_{12}v_{21})} \\ \mathfrak{V}_{22} &= \frac{v_{12}^2 + v_{22}^2}{\hbar v_{33}(v_{11}v_{22} - v_{12}v_{21})} & \mathfrak{V}_{33} &= \frac{v_{33}}{\hbar(v_{11}v_{22} - v_{12}v_{21})} \\ & & \mathfrak{V}_{13} &= \mathfrak{V}_{23} = 0 \end{aligned} \tag{8.60}$$

Likewise, with $\boldsymbol{\Delta}_1 = (\Delta_{11}, \Delta_{12}, 0)$ and $\boldsymbol{\Delta}_2 = (\Delta_{21}, \Delta_{22}, 0)$ the corresponding spin-orbit coupling sums (8.47) and the warping sum (8.48) readily becomes

$$\begin{aligned} \mathfrak{Q}_{11} &= \frac{\Delta_{11}^2 + \Delta_{21}^2}{\hbar^3 v_{33}(v_{11}v_{22} - v_{12}v_{21})} & \mathfrak{Q}_{12} &= \frac{\Delta_{11}\Delta_{12} + \Delta_{21}\Delta_{22}}{\hbar^3 v_{33}(v_{11}v_{22} - v_{12}v_{21})} \\ \mathfrak{Q}_{22} &= \frac{\Delta_{12}^2 + \Delta_{22}^2}{\hbar^3 v_{33}(v_{11}v_{22} - v_{12}v_{21})} & \mathfrak{Q}_{13} &= \mathfrak{Q}_{23} = \mathfrak{Q}_{33} = 0 \\ \mathfrak{X} &= \frac{(\boldsymbol{\Delta}_1 \times \boldsymbol{v}_1)^2 + (\boldsymbol{\Delta}_1 \times \boldsymbol{v}_2)^2 + (\boldsymbol{\Delta}_2 \times \boldsymbol{v}_1)^2 + (\boldsymbol{\Delta}_2 \times \boldsymbol{v}_2)^2}{\hbar^2 (v_{11}v_{22} - v_{12}v_{21})^2} \end{aligned} \tag{8.61}$$

where the cross products $\boldsymbol{\Delta}_m \times \boldsymbol{v}_j = (0, 0, \Delta_{m1}v_{j2} - \Delta_{m2}v_{j1})$ for $j, m \in \{1, 2\}$.

Hence, from the expressions of the effective velocity sums (8.60) and the spin-orbit coupling sums (8.61), the conductivity tensor of orthorhombic CuMnAs should satisfy $\sigma_{xz}(\omega) = \sigma_{yz}(\omega) = 0$, while all other components gain nonzero contributions. Thus, the material should in general feature a finite symmetric Hall conductivity $\sigma_{xy}(\omega) = \sigma_{yx}(\omega)$ for nonzero optical frequencies ω.

The conductivity predictions are dependent on the preservation of the S_{2z} symmetry of the orthorhombic CuMnAs lattice, the condition for which the Hamiltonian kernel (8.57) is valid. When a current is passed through the material, the localized magnetic moments on the manganese atoms may reorient in a different direction due to spin-orbit coupling. Hence, if a current is applied in the x or y-directions, the following reorientation of the localized magnetic moments breaks the S_{2z} symmetry, and the Dirac point is removed from the energy band spectrum. In conclusion, the supposed Hall effect in the xy-plane will only be valid if the current is weak enough to not reorient the localized magnetic moments of the manganese atoms. However, such a reorientation is dependent on the presence of a spin-orbit torque, and would be outside the regime of the linear Kubo formalism, on which the calculations are based.

Chapter 9

Outlook

This final chapter briefly introduces the prospects of the future research following the results of the thesis. In particular, the chapter recites particular derived formulae which allows for numerical calculations of the conductivity tensor, and presents formulae which quantifies the optical phenomena related to the conductivity of a material.

From knowledge of the conductivity of a material, it is possible to infer optical effects caused by the interactions between electromagnetic waves and matter. In particular, the change in polarization angle and ellipticity of a beam of light being transmitted through or reflected off a material surface can be predicted based directly on the conductivity formula, constituting the Faraday and Kerr magneto-optical effects. Apart from being a useful method for probing the electronic properties of matter, the Faraday effect is important historically in being the first experimental verification of the connection between light and electromagnetism, as observed by Michael Faraday in 1845.

9.1 Numerical Conductivity Calculations

The main goal of the thesis has been to calculate and interpret analytical formulae for the conductivity tensor of different crystalline systems. In this pursuit, it is necessary to introduce specific assumptions and simplifications for the calculations to be fruitful. In particular, the conductivity tensors obtained have all been evaluated in the zero temperature limit, and in the limit of zero scattering.

In realistic materials as compared to the ideal crystal structures considered, scattering of electrons originate in impurities of the crystal lattice, being irregularities in the otherwise regular lattice structure in the form of extraneous elements or locally broken symmetries. A general approach to incorporate scattering in solid state calculations is to exchange the non-interactive ideal Matsubara Green functions $\mathcal{G}(i\nu_n)$ with *impurity averaged* Green functions [8], which to lowest order corresponds to exchanging the phenomenological scattering rate η with a corresponding parameter dependent on the sign of the Matsubara frequency as $\eta_n = \eta\ \mathrm{sgn}(\nu_n)$. In this case however, the derived Matsubara frequency summation rules (2.37) cannot be applied directly, and the calculation will usually proceed using an analytical continuation in complex frequency space in order to calculate frequency summations. Hence, the calculation of the Matsubara autocorrelation function (3.41) with a finite scattering is a much more subtle task than the corresponding calculation in the zero scattering limit.

However, as demonstrated, parts of the conductivity tensor may originate in other physical processes than scattering, and are hence important to the intrinsic physics of the particular crystalline system under investigation. Considering the zero scattering limit, an important result of the thesis is to obtain general conductivity formulae for two-band systems in chapter 7 and $\mathcal{PT}$-invariant four-band systems in chapter 8, being dependent only on the Hamiltonian kernel (4.11) of the system. Importantly, the derivation of the formulae involves performing the Matsubara frequency summation of the Matsubara autocorrelation function (3.41), leaving only an integral over the crystal momentum $\boldsymbol{k}$.

Of particular importance are the conductivity calculations for a general $\mathcal{PT}$-invariant four-band system, whose Hamiltonian kernel can be represented by

$$\mathcal{H}(\boldsymbol{k}) = h_0(\boldsymbol{k}) + \tau_y \boldsymbol{\sigma} \cdot \boldsymbol{h}(\boldsymbol{k}) + \tau_z h_4(\boldsymbol{k}) + \tau_x h_5(\boldsymbol{k}), \tag{9.1}$$

where $\boldsymbol{h} = (h_1, h_2, h_3)$. It should here be noted that the particular representation and interpretation of the τ and σ bases is nonessential; the importance lies within the imposed $\mathcal{PT}$-symmetry, which leaves six terms in the Hamiltonian kernel. The five latter terms are here combined to form the five dimensional parameter vector $\boldsymbol{H}(\boldsymbol{k}) = (h_1(\boldsymbol{k}), h_2(\boldsymbol{k}), h_3(\boldsymbol{k}), h_4(\boldsymbol{k}), h_5(\boldsymbol{k}))$, in terms of which the Kramers degenerate energy bands of the system can be written

$$\varepsilon_s(\boldsymbol{k}) = h_0 + s\sqrt{h_1^2 + h_2^2 + h_3^2 + h_4^2 + h_5^2} = h_0 + |\boldsymbol{H}|. \tag{9.2}$$

Here, $s = \pm 1$ is a band index labelling each Kramers degenerate pair of energy bands. The current density autocorrelation function (3.31) then split into one term originating in transport within each Kramers degenerate pair of energy

bands, and one term describing optical transitions between the pairs. For the interband autocorrelation function, a novel quantity aptly named the *interband tensor* was introduced, given by

$$\Xi_{il}(\boldsymbol{k}) = \partial_i \boldsymbol{H} \cdot \partial_l \boldsymbol{H} - \partial_i |\boldsymbol{H}| \partial_l |\boldsymbol{H}|, \tag{9.3}$$

In terms of the five dimensional parameter vector $\boldsymbol{H}$, the energy bands ε_s and the interband tensor Ξ_{il}, the intraband (8.5) and interband (7.9) current density autocorrelation functions was found to be given by the integrals

$$\begin{aligned} \Pi_{il}^{\text{intra}}(\omega) &= \frac{2e^2}{\hbar} \frac{1}{\omega + i\eta} \int \frac{\mathrm{d}^d k}{(2\pi)^d} \sum_s \frac{\partial_i \varepsilon_s(\boldsymbol{k})}{\hbar} \frac{\partial_l \varepsilon_s(\boldsymbol{k})}{\hbar} \big[n_F(\varepsilon_s) - n_F(\varepsilon_s - \hbar\omega) \big] \\ \Pi_{il}^{\text{inter}}(\omega) &= \frac{2e^2}{\hbar^2} \int \frac{\mathrm{d}^d k}{(2\pi)^d} \big[n_F(\varepsilon_+) - n_F(\varepsilon_-) \big] \sum_s \frac{s \Xi_{il}(\boldsymbol{k})}{2s|\boldsymbol{H}| + \hbar\omega + i\eta}. \end{aligned} \tag{9.4}$$

Under the assumptions of linear response theory as discussed in section 3.2, in the zero scattering limit and neglecting the influence of other bands present in the energy band spectrum, these formulae describe the electric transport properties of an ensemble of non-interactive electrons exactly. For effective models the integrals are most readily calculated in the continuum limit, where the Brillouin zone for simplicity is extended to infinity. The corresponding conductivity tensor is then given by the formula

$$\sigma_{il}(\omega) = \frac{\Pi_{il}(\omega) - \Pi_{il}(0)}{i\omega}. \tag{9.5}$$

The second term here originates in a diamagnetic contribution to the current density operator (3.17), which in general cancels the possible divergencies of the current density autocorrelation function.

The derived formulae for the current density autocorrelation function (9.4) are temperature dependent through the Fermi-Dirac distributions $n_F(\varepsilon)$. For nonzero temperatures, the formulae can be calculated numerically to find the temperature dependence of the conductivity tensor in the zero scattering limit.

Finally, the reader should be aware that in some literature the diamagnetic contribution is excluded for a linear dispersion [9], in the belief that the electromagnetic vector potential couple to the crystal momentum $\boldsymbol{k}$. In the semiclassical Kubo formalism of chapter 3 however, the minimal coupling principle affects only the momentum operator $\hat{\boldsymbol{p}}$, and the appearance of a diamagnetic term cannot be read from the Hamiltonian kernel (4.11) itself. On physical grounds, if the electromagnetic vector potential does not vary in time, the electric field is zero and no current is induced. This effect is accounted for by subtracting the zero frequency component of the current density autocorrelation function [40]. It can also be argued that a diamagnetic term must exist in order to cancel the gradient part of the conductivity tensor in the zero frequency limit, which is necessary for the conductivity to be a gauge invariant quantity [41].

9.2 Experimental Predictions of the Formulae

From the calculated conductivity tensor, it is possible to predict optical effects exhibited by the interaction between the particular material and the electromagnetic field. In general, the interaction between electromagnetic waves and matter is highly dependent on the electronic structure of the matter, thus making it viable to probe the electronic properties of a material through studying the interaction with light. The Faraday and Kerr effects in particular are examples of *magneto-optical effects*, in which the electromagnetic interaction is especially affected by the magnetic state of the material. The setup for measuring the Faraday and Kerr effects are shown in figure 9.1, where a linearly polarized beam of light with initial frequency ω is incident on some material.

For linearly polarized light the projection of the electric field along the axis of propagation oscillates in a straight line. In general however the electric field component will over time trace out an ellipse, known as the *polarization ellipse*. The polarization angle θ gives the orientation of the ellipse, whereas the ellipticity ϵ gives the ratio between the major and minor axes of the ellipse. If the ellipticity is unity, the beam of light is said to be circularly polarized.

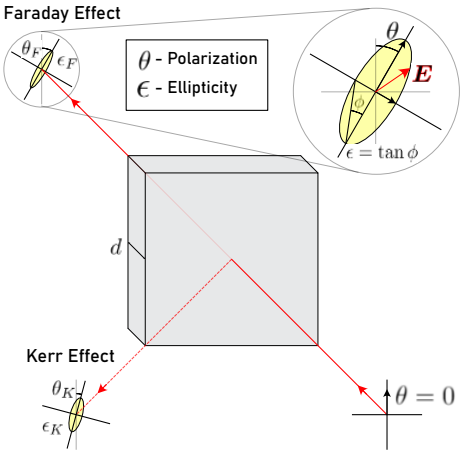

Figure 9.1: Diagrammatic representation of the Faraday and Kerr effects. A perpendicularly incident beam of linearly polarized light with polarization angle $\theta = 0$ is partially reflected from and transmitted through some material of thickness d. The electronic and magnetic properties of the material affects the ellipticity ϵ and the polarization angle of the reflected and transmitted beams, comprising the Kerr and Faraday effects, respectively. The figure also shows the polarization ellipse traced out by the oscillating electric field component $\boldsymbol{E}$.

When light is transmitted through the bulk or reflected from the surface of a material, both the polarization angle and the ellipticity of the beam may be affected by the material. If the optical response is linear, meaning the reflected and transmitted beams oscillate at the same frequency ω as the initial beam, the change in the polarization angle and ellipticity is known as *the Faraday effect* for the transmitted beam and *the Kerr effect* for the reflected beam. The experimental setup for measuring both effects is depicted in figure 9.1, which also portrays the polarization ellipse.

The change in the polarization angle comprising the Faraday effect is a result of the material having different indices of refraction for right- and left-circularly polarized light, denoted $n_\pm$. Assuming the beam of light is incident perpendicularly on the material surface along the z-axis, these indices of refraction can be calculated from the components of the conductivity tensor as [10]

$$n_{\pm}^2 = \epsilon_{\pm} = 1 + \frac{4\pi i}{\omega}\sigma_{\pm} \tag{9.6}$$

where the optical conductivity for left and right circularly polarized light

$$\sigma_{\pm} = \frac{1}{2}\Big[\sigma_{xx} + \sigma_{yy} \pm i\big(\sigma_{yx} - \sigma_{xy}\big)\Big] \tag{9.7}$$

Whenever $n_+ \neq n_-$, the right- and left-circularly polarized components of the beam of light will move at different speeds, hence changing the ellipticity of the beam cyclically with the transmission length through the material. This effect is known as *circular dichroism*, and can be quantified by the parameter

$$D_c = \frac{\operatorname{Re}\sigma_+ - \operatorname{Re}\sigma_-}{\operatorname{Re}\sigma_+ + \operatorname{Re}\sigma_-} \tag{9.8}$$

Consider then a material with thickness d, corresponding to the transmission length through the material. Assuming the material comprise a thin film, the *Faraday angle* corresponding to the change in the polarization angle upon transmission through the material is then given by [10]

$$\theta_F + i\epsilon_F = \frac{\omega d}{2c}(n_+ - n_-) \tag{9.9}$$

where c is the speed of light in a vacuum. The formula also gives the *Faraday ellipticity* ϵ_F, which is connected to the absorption of light upon transmission.

The magneto-optical Kerr effect likewise observes the change in the polarization angle if an incident linearly polarized beam of light. Unlike the Faraday effect however, the Kerr effect can be measured for different geometries, dependent on the direction of the magnetization of the material with respect on the incident angle of the light beam. In particular, for the *polar Kerr effect* the magnetization and the incident beam of light are both oriented normal to the interface. For a magnetic bulk material, the *polar Kerr rotation angle* is connected to the components of the conductivity tensor as [42]

$$\theta_K + i\epsilon_K = \frac{-\sigma_{xy}}{\sigma_o\sqrt{1 + i(4\pi/\omega)\sigma_o}}. \tag{9.10}$$

Here, the conductivity σ_o depends on the symmetries of the crystal lattice [42]. For an orthorhombic system in particular, then $\sigma_o = (\sigma_{xx} + \sigma_{xy})/2$.

Summary and Conclusion

The first part of the thesis investigated the quantum physical theories underpinning the calculation of optical conductivity in the Kubo formalism, considering perturbations to a crystalline system with low degree of disorder at equilibrium in the regime of linear response theory. Of particular importance was the introduction of the Matsubara autocorrelation function, from which the conductivity tensor was obtained through an analytical continuation in the complex frequency plane. The mathematical machinery devised was then used to derive particular conductivity formulae for topological semimetals, whose emergence and topological analysis was investigated in the second part of the thesis.

In particular, in the third part of the thesis a conductivity formula for a Kramers degenerate four-band system was calculated in the low disorder regime. From the obtained formula, an analytical expression for the conductivity tensor of two superposed Weyl nodes was calculated in the zero temperature limit. The resulting conductivity tensor witnessed the emergence of a symmetric Hall effect, presumably caused by geometrical features of the anisotropy of the Fermi surface nearby the Dirac point. Adding spin-orbit coupling as a perturbative interaction to second order between the Weyl nodes manifested in a set of spin reversal parameters, the conductivity tensor gained a renormalization term originating in the warping of the Fermi surface due to the spin-orbit coupling, and another source for a symmetric Hall conductivity dependent directly on the spin reversal parameters. Furthermore, the intrinsic symmetric Hall effect discovered is only apparent for a nonzero optical frequency of the applied electric field.

Applied to the antiferromagnetic semimetal CuMnAs, the calculated conductivity tensor predicts a symmetric Hall effect in the plane perpendicular to the localized magnetic moments in the ground state of the orthorhombic phase of the material. The results are assumed to hold under the confinement of linear response theory, where the applied electric current is weak enough to not break the symmetry protection of the Dirac points. The symmetric Hall effect is assumed experimentally detectable through different magneto-optical effects such as circular dichroism, on which further research must be conducted.

Appendices

Appendix A

Dynamical Pictures in Quantum Mechanics

The theoretical framework of quantum mechanics allows for the mathematical computation of physical observables O by assigning to each observable the corresponding operator $\hat{O}$. If a system is described by the quantum state $|\psi\rangle$, the expectation value of the physical observable O in that state can then be expressed as an inner product on the form $\langle\hat{O}\rangle = \langle\psi|\,\hat{O}\,|\psi\rangle$. It is only expectation values on this form that can be measured experimentally. For the expectation value to be a real quantity, the operators of observables are then constrained to be self-adjoint, or *hermitian* operators, satisfying $\hat{O}^\dagger = \hat{O}$.

Many physical systems are *dynamical systems*, in that the physical observables $\langle\hat{O}\rangle = \langle\psi|\,\hat{O}\,|\psi\rangle$ are time dependent. For dynamical systems, this dependence on time translates to the states $|\psi\rangle$ and the operators $\hat{O}$ describing the system. However, because only the expectation values themselves are observable, there is no univocal way of distributing the time dependence between the states and the operators; any apportions of time dependence leading to the same expectation values are physically equivalent. Even so, some prescriptions turn out to be more advantageous than others, depending on the system at hand. This is the mathematical origin of *dynamical pictures* in quantum mechanics.

In this appendix, the most common dynamical pictures are presented, namely the *Schrödinger picture*, the *Heisenberg picture* and the *Dirac picture*, the latter also known as the *interaction picture*. The formalism of this appendix is adamant to the definitions of Green functions in chapter 2 and to linear response theory in chapter 3. The investigation of these dynamical pictures additionally derives fundamental results from the theory of quantum physics, and also introduces the concept of time ordering which is used in the Matsubara method of chapter 2.

A.1 The Schrödinger and Heisenberg Pictures

From the epigraph of this appendix, there are in particular two dynamical pictures which naturally follows. In the Schrödinger picture, all time dependence is allotted the quantum state $|\psi_S\rangle = |\psi_S(t)\rangle$, whereas operators $\hat{O}_S$ carries no implicit time dependence. On the contrary, in the Heisenberg picture the time dependence of the system is fully encoded in the operators $\hat{O}_H = \hat{O}_H(t)$, whereas the states $|\psi_H\rangle$ themselves are time independent. The Schrödinger and Heisenberg pictures are the main dynamical pictures of quantum mechanics from which all other pictures will be intermediate.

A.1.1 Time Evolution and the Schrödinger Equation

Consider a quantum mechanical system initially prepared in the state $|\psi_S(0)\rangle$ at a time $t = 0$. In the Schrödinger picture, evolution of the system from the initial state to a state $|\psi_S(t)\rangle$ at a time $t > 0$ is then modelled using the *evolution operator* $\hat{U}(t, t')$, time translating the state as $|\psi_S(t)\rangle = \hat{U}(t, 0)\,|\psi_S(0)\rangle$. The evolution of the system between any two times t and t' is readily given

$$|\psi_S(t)\rangle = \hat{U}(t, t')\,|\psi_S(t')\rangle\,, \tag{A1}$$

where $\hat{U}(t, t') \equiv \hat{U}(t, 0)\hat{U}(0, t')$ defines the group property of the evolution operator. From this definition, the evolution operator satisfies $\hat{U}(t, t) = \hat{I}$. Furthermore, for the state vector normalization $\langle\psi_S(t)|\psi_S(t)\rangle = 1$ to be preserved for all times t, the evolution operator must be unitary, and hence satisfy $\hat{U}^\dagger(t, t') = \hat{U}^{-1}(t, t') = \hat{U}(t', t)$, the last equality following by definition.

By the assumption of physical continuity, the state $|\psi_S(t)\rangle$ is restricted to be differentiable with respect to time. This restriction is transferred to the evolution operator (A1), guaranteeing the existence of the limit

$$\lim_{t' \to t} \frac{\hat{U}(t, t') - I}{t' - t} = \hat{u}(t) \equiv \frac{1}{i\hbar}\hat{H}(t)$$

By the property $\hat{U}^\dagger(t, t') = \hat{U}(t', t)$, this limit is an anti-hermitian operator, satisfying $\hat{u}^\dagger(t) = -\hat{u}(t)$. Thus, from its definition, the operator $\hat{H}(t)$ is likewise a hermitian operator. Then by differentiation, the equation governing the time evolution of quantum states (A1) is recast into the *Schrödinger equation*

$$i\hbar\frac{\mathrm{d}\,|\psi_S\rangle}{\mathrm{d}t} = \hat{H}\,|\psi_S\rangle\,. \tag{A2}$$

The hermitian operator $\hat{H}$ is identified as the *Hamiltonian operator* of the system, being the quantum mechanical analogue of the classical Hamiltonian function. In the following of this subappendix, it will be assumed that the Hamiltonian operator is independent on time, such that the evolution operator becomes homogeneous in time, satisfying $\hat{U}(t, t') = \hat{U}(t - t')$. Systems with a time dependent Hamiltonian will be treated in the next subappendix on the Dirac picture, where a time dependent perturbation is added to the system.

Using the Schrödinger equation (A2), it is now viable to calculate an explicit form of the evolution operator in terms of the Hamiltonian operator $\hat{H}$. By inserting the expression for the time evolution of the state (A1) into the Schrödinger equation, the equation of state for the evolution operator becomes

$$i\hbar \frac{\mathrm{d}\hat{U}(t,t')}{\mathrm{d}t} = \hat{H}\hat{U}(t,t'). \tag{A3}$$

Because the Hamiltonian is assumed to carry no explicit time dependence, the equation of state for the evolution operator gives directly

$$\hat{U}(t,t') = \hat{U}(t-t') = e^{-i\hat{H}(t-t')/\hbar}. \tag{A4}$$

The Hamiltonian operator is thus seen to be the generator of time translations.

A.1.2 The Heisenberg Equation

Recall that the average of any observable $\langle \hat{O} \rangle$ must be independent on the dynamical picture, thus giving $\langle \psi_S(t)| \hat{O}_S |\psi_S(t)\rangle = \langle \psi_H| \hat{O}_H(t) |\psi_H\rangle$. From the definition of the evolution operator (A1), the time independent states of the Heisenberg picture are related to the states in the Schrödinger picture as

$$|\psi_H\rangle = \hat{U}^\dagger(t,0)\,|\psi_S(t)\rangle = |\psi_S(0)\rangle\,, \tag{A5}$$

whereas operators in the Heisenberg picture are related to the corresponding time independent operators in the Schrödinger picture through

$$\hat{O}_H(t) = \hat{U}^\dagger(t,0)\hat{O}_S\hat{U}(t,0) = e^{i\hat{H}t/\hbar}\hat{O}_S e^{-i\hat{H}t/\hbar}, \tag{A6}$$

where the evolution operator is given in the Schrödinger picture (A16).

Recall now that operators in the Schrödinger picture does not carry any implicit time dependence. By taking the derivative of the general Heisenberg operator (A6), and using the expression for the general evolution operator of the Schrödinger picture (A4), the time evolution of Heisenberg operators becomes governed by the *Heisenberg equation of motion*

$$\frac{\mathrm{d}\hat{O}_H}{\mathrm{d}t} = \hat{U}^\dagger(t,0)\left(\frac{i}{\hbar}\Big[\hat{H},\hat{O}_S\Big] + \frac{\partial \hat{O}_S}{\partial t}\right)\hat{U}(t,0) = \frac{i}{\hbar}\Big[\hat{H},\hat{O}_H\Big] + \left(\frac{\partial \hat{O}_S}{\partial t}\right)_H. \tag{A7}$$

Notice then that when the Hamiltonian $\hat{H}$ is independent on time, it commutes with the evolution operator (A4), and hence leaves both the Hamiltonian and the evolution operator independent on the dynamical picture used.

Finally, it should be noted that the unitary transformation between the Schrödinger and Heisenberg pictures besides preserving observable averages, also preserves eigenvalues; if λ is an eigenvalue of $\hat{O}_S$ with eigenstate $|\psi_S(t)\rangle$, it is also an eigenvalue of $\hat{O}_H(t)$ with eigenstate $|\psi_H\rangle$. This is evident from the relation between the states (A5) and the operators (A6).

A.2 The Dirac Picture

Consider now a system in which the Hamiltonian can be separated into a time independent unperturbed part $\hat{H}_0$, and a time dependent perturbation $\hat{V}_S(t)$, giving the Schrödinger picture Hamiltonian $\hat{H}_S = \hat{H}_0 + \hat{V}_S(t)$. Due to the time dependent perturbation the full Hamiltonian will not be independent on the dynamical picture used, elucidated by the subscript.

For such systems, it turns out advantageous to distribute time dependence between both operators $\hat{O}_I = \hat{O}_I(t)$ and states $|\psi_I\rangle = |\psi_I(t)\rangle$. Specifically, the evolution of the operators is governed by the unperturbed Hamiltonian, whereas the rest of the time dependence is allotted the states. This particular distribution of time dependence characterises the *Dirac picture*, otherwise known as the *interaction picture* whenever the perturbation $\hat{V}_S$ model interactions between different parts of the system not included in the unperturbed Hamiltonian $\hat{H}_0$.

A.2.1 Modified Schrödinger and Heisenberg Equations

Operators in the Dirac picture are connected to the time independent operators in the Schrödinger picture through the unperturbed part of the Hamiltonian,

$$\hat{O}_I(t) = e^{i\hat{H}_0 t/\hbar}\hat{O}_S e^{-i\hat{H}_0 t/\hbar} \tag{A8}$$

whereas the quantum states evolves by a modified evolution operator

$$|\psi_I(t)\rangle = \hat{U}_I(t,t')\,|\psi_I(t')\rangle\,. \tag{A9}$$

The modified evolution operator $\hat{U}_I(t,t')$ is connected to the evolution operator of the Schrödinger picture defined through the equation of state (A3) as

$$\hat{U}_I(t,t') = e^{i\hat{H}_0 t/\hbar}\hat{U}(t,t')e^{-i\hat{H}_0 t'/\hbar}. \tag{A10}$$

Due to the explicit time dependence of the Hamiltonian operator $\hat{H}$, the evolution operator $\hat{U}(t,t')$ is no longer given by the homogeneous evolution operator (A4). Notice also that the second exponential here is unity for $\hat{U}_I(t,0)$.

Repurposing the derivation of the Schrödinger equation (A2), the time evolution of states in the Dirac picture can through differentiation of its definition (A9) be recast into a modified Schrödinger equation

$$i\hbar\frac{\mathrm{d}\,|\psi_I\rangle}{\mathrm{d}t} = \hat{V}_I(t)\,|\psi_I\rangle\,, \tag{A11}$$

where the evolution operator equation of state (A3) was used. Notice that the operator $\hat{V}_I(t)$ appearing here is the perturbation term $\hat{V}_S(t)$ in the Dirac picture (A8). Likewise, the Heisenberg equation (A7) has the modified analogue

$$\frac{\mathrm{d}\hat{O}_I}{\mathrm{d}t} = \frac{i}{\hbar}\Big[\hat{H}_0, \hat{O}_I\Big] + \left(\frac{\partial\hat{O}_S}{\partial t}\right)_I. \tag{A12}$$

Recall here that the unperturbed part of the Hamiltonian $\hat{H}_0$ is independent on the dynamical picture seeing that it commutes with itself.

A.2.2 Dyson Series and the Time Ordering Operator

Inserting the modified evolution operator (A9) into the modified Schrödinger equation (A11) gives the modified equation of state of the Dirac picture

$$i\hbar\frac{\mathrm{d}\hat{U}_I(t,t')}{\mathrm{d}t} = \hat{V}_I(t)\hat{U}_I(t,t'). \tag{A13}$$

Integrating the equation (A3) from t' to t, the equation of state for the modified evolution operator is recast into an integral equation on the form

$$\hat{U}_I(t,t') = \hat{I} - \frac{i}{\hbar}\int_{t'}^{t}\mathrm{d}t_1\hat{V}_I(t_1)\hat{U}_I(t_1,t'). \tag{A14}$$

This integral equation can be iterated up to any order in the perturbation $V_I(t)$ to give an arbitrarily accurate expression for $\hat{U}_I(t,t')$. At iteration n, inserting $\hat{U}(t_n,t') = \hat{I}$, the integral equation (A14) gives the approximated operator

$$\hat{U}_I(t,t') = \hat{I} + \sum_{k=1}^{n}\Big(-\frac{i}{\hbar}\Big)^k\int_{t'}^{t}\mathrm{d}t_1\hat{V}_I(t_1)\int_{t_0}^{t_1}\mathrm{d}t_2\hat{V}_I(t_2)\cdots\int_{t_0}^{t_{k-1}}\mathrm{d}t_k\hat{V}_I(t_k)$$

It must here be noted that the perturbation term in general does not commute with itself evaluated at different times; $[\hat{V}_I(t_k),\hat{V}_I(t_l)] \neq 0$. This leaves the integration over the operators non-trivial.

Introduce then the *time ordering operator* $\hat{\mathrm{T}}$, which arranges operators according to descending time arguments. In particular, for n time dependent operators $\hat{O}_i(t)$, their time ordered product is defined

$$\hat{\mathrm{T}}\{\hat{O}_1(t_1)\cdots\hat{O}_n(t_n)\} = \sum_p\theta(t_{p_1}\leq\cdots\leq t_{p_n})\zeta^P\hat{O}_{p_1}(t_{p_1})\cdots\hat{O}_{p_n}(t_{p_n}) \tag{A15}$$

The sign factor $\zeta^P = (\pm1)^P$, where P is the number of permutations needed to achieve the specific ordering from the original expression; the upper and lower signs corresponds to bosonic and fermionic operators, respectively.

Using the time ordering operator (A15), the iterated integral

$$\int_{t_0}^{t}\mathrm{d}t_1\hat{V}_I(t_1)\cdots\int_{t_0}^{t_{k-1}}\mathrm{d}t_k\hat{V}_I(t_k) = \frac{1}{k!}\int_{t_0}^{t}\mathrm{d}t_1\cdots\int_{t_0}^{t}\mathrm{d}t_k\hat{\mathrm{T}}\{\hat{V}_I(t_1)\cdots\hat{V}_I(t_k)\}.$$

The equality is made tenable by considering the boundaries of the integrals: on the left, the integration domain is over a single of the $k!$ congruent simplexes of the k-dimensional hypercube, whereas the right expression integrates over the entire hypercube itself, with all upper limits being t.

In this last expression, the time ordering operator can be put outside of the integrals, leaving a product of k integrals on the same form. By letting $n\to\infty$ the evolution operator is readily expressed as the exponential operator

$$\hat{U}_I(t,t') = \hat{\mathrm{T}}\sum_{k=0}^{\infty}\frac{1}{k!}\Big(-\frac{i}{\hbar}\int_{t'}^{t}\mathrm{d}\tau\hat{V}_I(\tau)\Big)^k = \hat{\mathrm{T}}\exp\Big(-\frac{i}{\hbar}\int_{t'}^{t}\mathrm{d}\tau\hat{V}_I(\tau)\Big) \quad \text{(A16)}$$

This expansion is known as the *Dyson series* for the evolution operator. Introducing also the anti-time-ordering operator $\hat{\bar{\mathrm{T}}}$, arranging operators according to ascending time arguments, the adjoint of the evolution operator (A16) is likewise expressed as the anti-time-ordered exponential operator

$$\hat{U}_I^{\dagger}(t,t') = \hat{U}_I(t',t) = \hat{\bar{\mathrm{T}}}\exp\Big(\frac{i}{\hbar}\int_{t'}^{t}\mathrm{d}\tau\hat{V}_I(\tau)\Big) \quad \text{(A17)}$$

This derivation holds for any time dependent Hamiltonian. Hence, the Dyson series (A16) can be viewed as a generalization of the evolution operator for a time independent Hamiltonian (A4).

Comparing the modified Schrödinger (A11) and Heisenberg (A12) equations to their original counterparts, a natural transition from the Dirac picture to the Schrödinger and Heisenberg pictures follows. Recall that the Hamiltonian of interest when applying the Dirac picture is comprised of a free Hamiltonian and a perturbation term, denoted $\hat{H}_I = \hat{H}_0 + \hat{V}_I$. In order to obtain the original Schrödinger equation (A2) and time independent operators, let $\hat{H}_0 = 0$. The remaining operator $\hat{V}_I = \hat{H}$ then serves as the Hamiltonian for the Schrödinger picture. Likewise for the Heisenberg picture, let $\hat{V}_I = 0$. The states then become time independent, while the time evolution of operators becomes governed by the Hamiltonian operator $\hat{H} = \hat{H}_0$ through the Heisenberg equation (A7).

Appendix B

Crystal Structures and Bloch Wavefunctions

In a vacuum, electrons are quantum mechanically described by plane waves extended over the entirety of space. For an aggregate of matter however, being a collection of neutrally charged atoms, the underlying atomic nuclei generate a positive potential field effectively modulating the plane wave behaviour of the electron. The form of the underlying potential is determined by the arrangement of the positively charged atomic nuclei inside the material, and so electronic properties of a material thus become highly dependent on atomic structure.

For many materials the atomic structure can be approximated by a perfectly periodic lattice, and the crystalline system becomes translationally invariant for a set of discrete translations. Considering then a single electron residing on the underlying crystal lattice, it is possible on the assumption of discrete translation invariance to gain insight into the general shape of the wavefunction of the electron and the properties of the corresponding energy eigenvalue equation.

The purpose of this appendix is to introduce the mathematical description of lattices and translations, and to use these mathematical tools for extracting information about the single-electron states in periodic crystalline structures. The appendix initiates with the description of the position representation of quantum mechanics, which connects the following material to the discussion on Hilbert spaces and quantum states of chapter 1. The chapter then introduces the Bloch functions of the Brillouin zone resulting from discrete translation invariance, giving the foundation for defining the berryological quantities of crystalline systems in chapter 5. Eventually, it will be shown that individual electrons residing on a crystal structure can be described by a linear combination of atomic orbitals, being the theoretical basis for the tightbinding model of chapter 4. The appendix at hand thus derives many important results from solid state physics, providing the main background for several chapters.

The derivations, relations and nomenclature of the appendix is inspired by the introductory book by Vanderbilt [24].

B.1 The Position and Momentum Operators

In chapter 1, the mathematical formalism underpinning quantum mechanics was investigated, with general quantum states being described by Hilbert space vectors $|\psi\rangle$. These vectors can be expanded in any complete basis of the corresponding Hilbert space. In particular, for particles moving in configuration space dependent on the spatial coordinate $\boldsymbol{r}$, the Hilbert subspace corresponding to the spatial degrees of freedom is spanned by the position states $|\boldsymbol{r}\rangle$. These vectors comprise an uncountably infinite and continuous basis set, orthonormalized to satisfy $\langle \boldsymbol{r}_1|\boldsymbol{r}_2\rangle = \delta(\boldsymbol{r}_1 - \boldsymbol{r}_2)$ and satisfying the completeness relation

$$\int \mathrm{d}^d r \, |\boldsymbol{r}\rangle \langle \boldsymbol{r}| = \hat{I}, \tag{B1}$$

analogous to the discrete completeness relation (1.1) derived in section 1.1. The position basis states $|\boldsymbol{r}\rangle$ are the eigenstates of the *position operator vector* $\hat{\boldsymbol{r}}$, defined through the eigenvalue equation $\hat{\boldsymbol{r}}\,|\boldsymbol{r}\rangle = \boldsymbol{r}\,|\boldsymbol{r}\rangle$.

The continuously related components of the state $|\psi\rangle$ expanded in the position basis are collectively known as the *wavefunction* corresponding to $|\psi\rangle$, denoted by $\psi(\boldsymbol{r}) \equiv \langle \boldsymbol{r}|\psi\rangle$. For systems where the only degrees of freedom are spatial in nature, the wavefunction incorporates the same complete information as the state vector. Describing quantum systems in terms of the wavefunction $\psi(\boldsymbol{r})$ rather than the state vector $|\psi\rangle$ defines the *position representation* of quantum mechanics, which is particularly convenient for describing spatial distributions and symmetries in regards to particular quantum states.

From the Born rule, the state vector $|\psi\rangle$ should be normalized to unity. Using the completeness relation of the position basis (B1), this condition translates to

$$\langle \psi|\psi\rangle = \int \mathrm{d}^d r |\psi(\boldsymbol{r})|^2 = 1. \tag{B2}$$

Hence, wavefunctions are in general square integrable, and thus an element of the Lebesgue space of square integrable functions, being the only Hilbert space among the Lebesgue spaces [15]. Using again the completeness relation, this allows for the definition of the inner product between wavefunctions, defined by

$$\langle \psi_1|\psi_2\rangle = \int \mathrm{d}^d r \; \psi_1^*(\boldsymbol{r})\psi_2(\boldsymbol{r}), \tag{B3}$$

where the asterisk denotes complex conjugation. This property of the space of wavefunctions is inherited from the original Hilbert space of quantum states.

Introduce the *translation operator* $\hat{T}_{\boldsymbol{x}}$ acting on space by translating each vector $\boldsymbol{r}$ by $\boldsymbol{x}$, corresponding to a shift in the origin. Application of the translation operator on an element of the position basis gives $\hat{T}_{\boldsymbol{x}}\,|\boldsymbol{r}\rangle = |\boldsymbol{r} + \boldsymbol{x}\rangle$. From this definition, translation operators evidently satisfies $\hat{T}_{\boldsymbol{x}_1}\hat{T}_{\boldsymbol{x}_2} = \hat{T}_{\boldsymbol{x}_1+\boldsymbol{x}_2}$, and so all translation operators commute; the group of all translation operators is an abelian group. With $\boldsymbol{x} = 0$ corresponding to the unity operator, the inverse of translation operators is then naturally given by $\hat{T}_{\boldsymbol{x}}^{-1} = \hat{T}_{-\boldsymbol{x}}$. Furthermore,

from the definition of the adjoint operator (C4) and seeing that the inner product $\langle \boldsymbol{r}_1 | \boldsymbol{r}_2 + \boldsymbol{x} \rangle = \langle \boldsymbol{r}_1 - \boldsymbol{x} | \boldsymbol{r}_2 \rangle$, the adjoint of the translation operator satisfies $\hat{T}_{\boldsymbol{x}}^\dagger = \hat{T}_{-\boldsymbol{x}} = \hat{T}_{\boldsymbol{x}}^{-1}$. In consequence, translation operators are unitary operators and can be written on the form $\hat{T}_{\boldsymbol{x}} = e^{-i\boldsymbol{x}\cdot\hat{\boldsymbol{p}}/\hbar}$ where $\hbar$ is Plancks constant and $-i\hat{\boldsymbol{p}}/\hbar$ is the generator of translations with $\hat{\boldsymbol{p}}$ being hermitian by construction.

Consider the application of the translation operator and the position operator on an element of the position eigenbasis, which satisfies $\hat{T}_{\boldsymbol{x}} \hat{\boldsymbol{r}} \, | \boldsymbol{r} \rangle = \boldsymbol{r} \, | \boldsymbol{r} + \boldsymbol{x} \rangle$ and $\hat{\boldsymbol{r}} \hat{T}_{\boldsymbol{x}} \, | \boldsymbol{r} \rangle = (\boldsymbol{r} + \boldsymbol{x}) \, | \boldsymbol{r} + \boldsymbol{x} \rangle$. Subtracting these two relations, the commutation relation between the position and translation operators becomes $[\hat{\boldsymbol{r}}, \hat{T}_{\boldsymbol{x}}] = \boldsymbol{x}$. In particular, assume $\boldsymbol{x}$ is an infinitesimal distance, such that the translation operator can be written in terms of the generator $\hat{\boldsymbol{p}}$ as $\hat{T}_{\boldsymbol{x}} = 1 - i\boldsymbol{x} \cdot \hat{\boldsymbol{p}}/\hbar + \mathcal{O}(\boldsymbol{x}^2)$. The commutation relation between the elements $\hat{r}_i$ of the position operator and $\hat{p}_j$ of the generator of translations thus becomes

$$[\hat{r}_i, \hat{p}_j] = i\hbar\delta_{ij}. \tag{B4}$$

This is the *canonical commutation relation* of elementary quantum mechanics. The quantum mechanical commutator corresponds to the classical Poisson bracket of the observables represented by the quantum operators, from which the generator of translations $\hat{\boldsymbol{p}}$ can be interpreted as the *momentum operator*.

Similarly to the eigenstates of the position operator, the continuously connected eigenstates of the momentum operator can be defined through the eigenvalue equation $\hat{\boldsymbol{p}} \, | \boldsymbol{p} \rangle = \boldsymbol{p} \, | \boldsymbol{p} \rangle$, orthonormalized with $\langle \boldsymbol{p}_1 | \boldsymbol{p}_2 \rangle = \delta(\boldsymbol{p}_2 - \boldsymbol{p}_1)$. The inner product between any two quantum states can then be expanded

$$\langle \psi_1 | \psi_2 \rangle = \int \mathrm{d}^d p \; \psi_1^*(\boldsymbol{p}) \psi_2(\boldsymbol{p}) \tag{B5}$$

where $\psi(\boldsymbol{p}) = \langle \boldsymbol{p} | \psi \rangle$ is the *momentum wavefunction*. Using the momentum wavefunction $\psi(\boldsymbol{p})$ to describe the quantum state $|\psi\rangle$ constitute the *momentum representation* of quantum mechanics, analogous to the position representation.

In the position representation, the translation operator acts on wavefunctions as $\hat{T}_{\boldsymbol{x}} \psi(\boldsymbol{r}) = \langle \boldsymbol{r} | \, \hat{T}_{\boldsymbol{x}} \, | \psi \rangle = \psi(\boldsymbol{r} - \boldsymbol{x})$. Hence, expanding the wavefunction and momentum operators to linear order in the displacement $\boldsymbol{x}$, the momentum operator takes the form $\hat{\boldsymbol{p}} = -i\hbar\nabla$ in the position representation of quantum mechanics. The position representation wavefunction corresponding to the momentum operator eigenstate $|\boldsymbol{p}\rangle$ can thus be chosen

$$\chi_{\boldsymbol{p}}(\boldsymbol{r}) = \langle \boldsymbol{r} | \boldsymbol{p} \rangle = \frac{1}{(2\pi\hbar)^{d/2}} e^{i\boldsymbol{r}\cdot\boldsymbol{p}/\hbar}. \tag{B6}$$

Hence, using the continuous completeness relation (B1) of the momentum eigenstates $|\boldsymbol{p}\rangle$, any wavefunction can be expressed on the form

$$\psi(\boldsymbol{r}) = \int \frac{\mathrm{d}^d p}{(2\pi\hbar)^{d/2}} \psi(\boldsymbol{p}) e^{i\boldsymbol{r}\cdot\boldsymbol{p}/\hbar}. \tag{B7}$$

The position and momentum representations of quantum mechanics are thus mathematically related by a symmetric Fouriér transform.

B.2 The Bloch Theorem and Energy Bands

In this section, the *Bloch theorem* is derived on the basis of discrete translation invariance, being one of the main results of solid state physics. The Bloch theorem puts restrictions on the possible quantum wavefunctions describing particles in a periodic spatial potential, from which the section initiates.

B.2.1 Real and Reciprocal Lattice Structures

In solid state physics, a *crystal* is a structure of atoms in space built up in a periodic lattice, hereafter termed the *crystal lattice*. The crystal lattice can be separated into equal unit cells, the smallest of which are *primitive unit cells* spanned by primitive lattice vectors $\boldsymbol{a}_l$. The crystal lattice is then spanned by translating the primitive unit cell throughout a *Bravais lattice*, which for a d-dimensional crystal is mathematically described by a set of *lattice vectors*

$$\boldsymbol{R}_i = \boldsymbol{R}_{\{z_l\}} = \sum_{l=1}^{d} z_l \boldsymbol{a}_l, \qquad z_l \in \mathbb{Z}, \tag{B8}$$

where $i = \{z_l\}$ is the unique set of integer weights for each lattice vector. Finite lattices are then described by limiting the range of the weights z_l. For simplicity, it is in the following assumed that the crystal lattice is of infinite extent.

The primitive unit cell may contain one or more lattice points, and its total volume is denoted by V_C. Apart from the volume and number of lattice points, the choice of a primitive unit cell is otherwise arbitrary. However, there is only one choice that retains all symmetries of the entire lattice: the *Wigner-Seitz cell*. The Wigner-Seitz cell is defined as the locus of points in space closer to a lattice point than to all neighbouring lattice points. Its construction is explained by figure B.1.

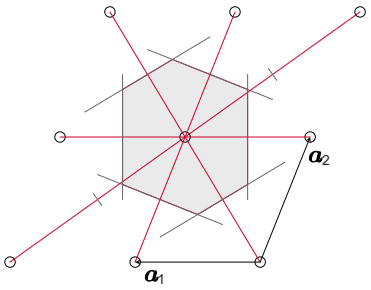

Figure B.1: Construction of the Wigner-Seitz cell of a Bravais lattice with primitive lattice vectors $\boldsymbol{a}_1$ and $\boldsymbol{a}_2$. The red lines connecting lattice points are bisected, and the enclosed grey area constitute the cell.

Denote by $\boldsymbol{r}$ the position vector in d-dimensional space. Seeing that the crystal structure is infinite in extent and periodic, the lattice is homogeneous at the level of primitive unit cells. In consequence, any local property of the crystal described by a field $f(\boldsymbol{r})$ should be invariant under the symmetries of the crystal lattice. In particular, any physically observable field defined on the lattice should be invariant under discrete lattice translations, and so must satisfy $f(\boldsymbol{r} - \boldsymbol{R}_i) = f(\boldsymbol{r})$.

The Fouriér transform of such a field, chosen asymmetric, can be written

$$\tilde{f}(\boldsymbol{k}) = \int \mathrm{d}^d r f(\boldsymbol{r}) e^{-i\boldsymbol{k}\cdot\boldsymbol{r}} = \sum_i e^{i\boldsymbol{k}\cdot\boldsymbol{R}_i} \int_{V_C} \mathrm{d}^d r f(\boldsymbol{r}) e^{-i\boldsymbol{k}\cdot\boldsymbol{r}} \tag{B9}$$

where $\boldsymbol{k}$ is a reciprocal vector in Fouriér space, usually named *reciprocal space*. Here, the sum over lattice vectors $\boldsymbol{R}_i$ is known as the *lattice sum*, and the final integral is over the primitive unit cell within the volume V_C. Being a sum of terms distributed along the complex unit circle, the lattice sum and hence the Fouriér coefficient $\tilde{f}(\boldsymbol{k})$ is zero except for reciprocal vectors $\boldsymbol{k} \equiv \boldsymbol{G}_j$ satisfying

$$e^{i\boldsymbol{G}_j \cdot \boldsymbol{R}_i} = 1 \qquad \text{or} \qquad \boldsymbol{G}_j \cdot \boldsymbol{R}_i = 2\pi z, \quad z \in \mathbb{Z}. \tag{B10}$$

This condition on the reciprocal vectors defines the *reciprocal lattice* of the crystal, spanned by the reciprocal lattice vectors $\boldsymbol{G}_j$ defined similarly to the real space lattice vectors (B8). The reciprocal lattice is therefore itself a Bravais lattice, whose primitive reciprocal lattice vectors $\boldsymbol{b}_m$ can be defined through

$$\boldsymbol{a}_l \cdot \boldsymbol{b}_m = 2\pi\delta_{lm} \tag{B11}$$

in order to satisfy their defining condition (B10). Notice that the reciprocal lattice is defined with respect to the underlying Bravais lattice of the crystal lattice, and so will only have one reciprocal lattice point per unit cell.

The Wigner-Seitz cell of the reciprocal lattice is known as the *First Brillouin Zone*, and has a volume given by $(2\pi)^d/V_C$. Just as fields over real space $\boldsymbol{r}$ are completely determined by their properties in the Wigner-Seitz cell, fields over reciprocal space $\boldsymbol{k}$ are determined by their properties in the Brillouin zone. As such, most properties of crystals need only be considered in the Wigner-Seitz cell or the Brillouin zone in order to be determined completely.

All reciprocal vectors $\boldsymbol{k}$ are connected to a reciprocal vector $\boldsymbol{k}'$ in the Brillouin zone through some reciprocal lattice vector $\boldsymbol{G}_j$ through $\boldsymbol{k} = \boldsymbol{k}' + \boldsymbol{G}_j$. In consequence, the inverse Fouriér transform of a reciprocal field $\tilde{g}(\boldsymbol{k})$ periodic over the reciprocal lattice can be expressed in terms of a reciprocal lattice sum,

$$g(\boldsymbol{r}) = \int \frac{\mathrm{d}^d k}{(2\pi)^d} \tilde{g}(\boldsymbol{k}) e^{i\boldsymbol{k}\cdot\boldsymbol{r}} = \sum_j e^{i\boldsymbol{G}_j\cdot\boldsymbol{r}} \int_{\mathrm{BZ}} \frac{\mathrm{d}^d k}{(2\pi)^d} \tilde{g}(\boldsymbol{k}) e^{i\boldsymbol{k}\cdot\boldsymbol{r}}. \tag{B12}$$

This is nonzero only for $\boldsymbol{r} = \boldsymbol{R}_i$, analogous to the Fouriér transform itself (B9).

From the Fouriér transform (B9) and its inverse (B12), mathematical relations between the real and reciprocal lattices can be derived. In particular, considering the inverse Fouriér transform of $\tilde{g}(\boldsymbol{k}) = e^{-i\boldsymbol{k}\cdot\boldsymbol{R}_j}$ and the Fouriér transform of $f(\boldsymbol{r}) = e^{i\boldsymbol{k}'\cdot\boldsymbol{r}}$ gives the two important orthogonality relations

$$V_C \int_{\mathrm{BZ}} \frac{\mathrm{d}^d k}{(2\pi)^d} e^{i\boldsymbol{k}\cdot(\boldsymbol{R}_i - \boldsymbol{R}_j)} = \delta_{ij} \qquad \sum_i e^{i(\boldsymbol{k}-\boldsymbol{k}')\cdot\boldsymbol{R}_i} = \frac{(2\pi)^d}{V_C}\delta(\boldsymbol{k}-\boldsymbol{k}'). \tag{B13}$$

Here, δ_{ij} is the Kronecker delta and $\delta(\boldsymbol{k})$ the Dirac delta function.

B.2.2 Bloch Functions and the Bloch Theorem

The atoms comprising the crystal lattice are composed of atomic nuclei and their surrounding electrons. Because the electron mass m is very light compared to the mass of the nuclei, the crystal lattice can be considered fixed with respect to the electrons of the material. In consequence, most dynamical properties of aggregates of matter are determined by their electronic structure.

Consider then a single electron moving in a potential $U(\boldsymbol{r})$ generated by the underlying atomic nuclei of the aggregate. Assuming the atomic nuclei are arranged in a crystal lattice, the potential becomes lattice periodic, satisfying $U(\boldsymbol{r}-\boldsymbol{R}_i)=U(\boldsymbol{r})$. Assuming the electron carries a non-relativistic momentum $\boldsymbol{p}$, the Hamiltonian operator describing the single electron can be written in terms of the position operator $\hat{\boldsymbol{r}}$ and the momentum operator $\hat{\boldsymbol{p}}$ as

$$\hat{\mathfrak{h}}=\frac{\hat{\boldsymbol{p}}^2}{2m}+\hat{U}(\hat{\boldsymbol{r}}), \tag{B14}$$

Here, the former term represents the kinetic energy of the electron, while the latter describes the interaction between the electron and the crystal lattice. In particular, in the position representation (B1) the matrix elements of the Hamiltonian becomes diagonal and takes the form

$$\mathfrak{h}=\langle \boldsymbol{r}|\,\hat{\mathfrak{h}}\,|\boldsymbol{r}\rangle=-\frac{\hbar^2}{2m}\nabla^2+U(\boldsymbol{r}), \tag{B15}$$

with the momentum operator being represented by $\hat{\boldsymbol{p}}=-i\hbar\nabla$. The eigenfunctions $\psi(\boldsymbol{r})$ of the Hamiltonian in the position representation are the wavefunctions corresponding to the eigenstates $|\psi\rangle$ of the Hamiltonian operator (B14), and satisfies the eigenvalue equation $\mathfrak{h}\psi(\boldsymbol{r})=\varepsilon\psi(\boldsymbol{r})$ where ε is the energy of the electronic state described by the quantum state $|\psi\rangle$.

Because of the potential term, the single-electron Hamiltonian (B14) does not commute with the momentum operator $\hat{\boldsymbol{p}}$, and so electronic states with a defined momentum cannot be constructed. However, due to the crystal structure the Hamiltonian is invariant under discrete lattice translations, and hence satisfies the commutation $[\mathfrak{h},T_{\boldsymbol{R}_i}]=0$. Simultaneous eigenfunctions between the discrete translation and Hamiltonian operators can then be constructed. Because translation operators are unitary, their eigenvalues lie along the complex unit circle. Hence, the eigenfunctions of the Hamiltonian operator can be chosen to satisfy the discrete translation operator eigenvalue equation $T_{\boldsymbol{R}_i}\psi(\boldsymbol{r})=e^{i\kappa}\psi(\boldsymbol{r})$. The eigenvalue parameter κ must respect the abelian group structure of the translation operators. Denoting by κ_l the parameter corresponding to translation by the primitive lattice vector $\boldsymbol{a}_l$, then for any lattice vector (B8),

$$T_{\boldsymbol{R}_i}\psi(\boldsymbol{r})=e^{i\sum_l z_l\kappa_l}\psi(\boldsymbol{r})=e^{i\boldsymbol{k}\cdot\boldsymbol{R}_i}\psi(\boldsymbol{r}).$$

Here, $\boldsymbol{k}$ is a linear combination of the primitive reciprocal lattice vectors (B11) $\boldsymbol{b}_m$ with weights $\kappa_m/2\pi$, and is as such a vector residing in reciprocal space.

The eigenfunctions of the single-electron Hamiltonian operator (B14) can thus be labelled by their eigenvalues from the lattice translation operator given

implicitly through the reciprocal vectors $\boldsymbol{k}$. This labelling is however not unique: any two vectors connected by a reciprocal lattice vector as $\boldsymbol{k}' = \boldsymbol{k} + \boldsymbol{G}_j$ will give the same eigenvalue, evident from the defining relation of the reciprocal lattice (B10). In conclusion, all distinct eigenfunctions of the single-electron Hamiltonian (B14) can be labelled by reciprocal vectors $\boldsymbol{k}$ lying in the Brillouin zone of the reciprocal lattice of the crystal structure, and will satisfy

$$\psi_{\boldsymbol{k}}(\boldsymbol{r} - \boldsymbol{R}_i) = e^{i\boldsymbol{k}\cdot\boldsymbol{R}_i}\psi_{\boldsymbol{k}}(\boldsymbol{r}) \qquad \psi_{\boldsymbol{k}-\boldsymbol{G}_j}(\boldsymbol{r}) = \psi_{\boldsymbol{k}}(\boldsymbol{r}). \tag{B16}$$

Define then the *lattice periodic function* $u_{\boldsymbol{k}}(\boldsymbol{r}) = e^{-i\boldsymbol{k}\cdot\boldsymbol{r}}\psi_{\boldsymbol{k}}(\boldsymbol{r})$, which from the derived relations will be periodic with the underlying crystal lattice and satisfy

$$u_{\boldsymbol{k}}(\boldsymbol{r} - \boldsymbol{R}_i) = u_{\boldsymbol{k}}(\boldsymbol{r}) \qquad u_{\boldsymbol{k}-\boldsymbol{G}_j}(\boldsymbol{r}) = e^{i\boldsymbol{G}_j\cdot\boldsymbol{r}}u_{\boldsymbol{k}}(\boldsymbol{r}). \tag{B17}$$

The eigenfunctions of the Hamiltonian thus takes the form of *Bloch functions*,

$$\psi_{\boldsymbol{k}}(\boldsymbol{r}) = e^{i\boldsymbol{k}\cdot\boldsymbol{r}}u_{\boldsymbol{k}}(\boldsymbol{r}). \tag{B18}$$

This is the Bloch theorem: In a periodic crystal structure, the electronic wave function will be a plane wave modulated by a lattice periodic function. Here, the vector $\boldsymbol{k}$ is not equivalent to the momentum of the electrons, but gives rise to the *crystal momentum* $\hbar\boldsymbol{k}$. Unlike the physical momentum, the crystal momentum is only conserved up to a reciprocal lattice vector $\boldsymbol{G}_j$, which is an effect of the discrete translation symmetry of the lattice.

Recall that the Bloch function (B18) are eigenfunctions of the single-electron Hamiltonian (B15), now satisfying $\mathfrak{h}\psi_{\boldsymbol{k}} = \epsilon_{\boldsymbol{k}}\psi_{\boldsymbol{k}}$. Upon inserting the Bloch function (B18) into this eigenvalue equation, it is seen that the lattice periodic function $u_{\boldsymbol{k}}(\boldsymbol{r})$ are eigenfunctions of the crystal momentum dependent Hamiltonian $\mathfrak{h}(\boldsymbol{k}) \equiv e^{i\boldsymbol{k}\cdot\boldsymbol{r}}\mathfrak{h}e^{-i\boldsymbol{k}\cdot\boldsymbol{r}}$ with the same energy eigenvalue $\epsilon_{\boldsymbol{k}}$, satisfying

$$\mathfrak{h}(\boldsymbol{k})u_{n\boldsymbol{k}}(\boldsymbol{r}) = \Big[\frac{\hbar^2}{2m}\big(-i\nabla + \boldsymbol{k}\big)^2 + U(\boldsymbol{r})\Big]u_{n\boldsymbol{k}}(\boldsymbol{r}) = \epsilon_{n\boldsymbol{k}}u_{n\boldsymbol{k}}(\boldsymbol{r}). \tag{B19}$$

For a particular value of $\boldsymbol{k}$ there is a countably infinite family of solutions $u_{n\boldsymbol{k}}(\boldsymbol{r})$ to this equation, each with a different eigenvalue $\epsilon_{n\boldsymbol{k}}$. This is the mathematical origin of *energy bands*, with each solution in the family being labelled by the discrete *band index* n. Each energy band $\epsilon_{n\boldsymbol{k}}$ is continuous with respect to the reciprocal vector $\boldsymbol{k}$, and as the Bloch functions (B18) are periodic with the reciprocal lattice the bands must be bounded both from above and from below.

From here on, the Bloch states (B18) are thus labelled by the band index n and the crystal momentum $\boldsymbol{k}$, as $\psi_{n\boldsymbol{k}}(\boldsymbol{r})$. These are the quantum numbers labelling the possible wavefunctions of a single electron residing in a crystal lattice, corresponding to the eigenvalues of the single-electron Hamiltonian (B14) and the discrete translation operator respectively. Additionally, if the crystal lattice has a spin structure, the electronic spin will be added as a third quantum number describing the possible states. The quantum spin is investigated in appendix C, along with the prospect of Kramers degeneracy for energy bands.

B.2.3 Bloch Function Inner Products

The Bloch wavefunctions are the position representation of the abstract Bloch state vectors $|\psi_{n\boldsymbol{k}}\rangle$, related by the projection $\psi_{n\boldsymbol{k}}(\boldsymbol{r}) = \langle \boldsymbol{r}|\psi_{n\boldsymbol{k}}\rangle$. Likewise, the lattice periodic function $u_{n\boldsymbol{k}}(\boldsymbol{r})$ correspond to state vectors $|u_{n\boldsymbol{k}}\rangle$. Notice then that the Bloch functions $\psi_{n\boldsymbol{k}}(\boldsymbol{r})$ and the lattice periodic functions $u_{n\boldsymbol{k}}(\boldsymbol{r})$ are the eigenfunctions of different Hamiltonians $\mathfrak{h}$ and $\mathfrak{h}(\boldsymbol{k})$, and hence the state vectors $|\psi_{n\boldsymbol{k}}\rangle$ and $|u_{n\boldsymbol{k}}\rangle$ are elements of different Hilbert spaces. Furthermore, because the Hamiltonian of the lattice periodic functions $\mathfrak{h}(\boldsymbol{k})$ is dependent on the crystal momentum $\boldsymbol{k}$, the state vectors $|u_{n\boldsymbol{k}}\rangle$ are unlike Bloch state vectors elements of different Hilbert spaces for each value of $\boldsymbol{k}$. For a particular value of $\boldsymbol{k}$, the Hilbert spaces of Bloch and lattice periodic functions are related by the exponential transform $|\psi_{n\boldsymbol{k}}\rangle = e^{i\boldsymbol{k}\cdot\hat{\boldsymbol{r}}}\,|u_{n\boldsymbol{k}}\rangle$, where $\hat{\boldsymbol{r}}$ is the position operator.

Due to the lattice periodic function $u_{n\boldsymbol{k}}(\boldsymbol{r})$, the Bloch functions (B18) evidently describe electronic states extended over the entire crystal structure. In consequence, the inner product between Bloch functions must be defined as an integral over the entire lattice (B3). The lattice periodic functions however need only to be described in a single primitive unit cell, with the inner product of the Hilbert space corresponding to the crystal momentum $\boldsymbol{k}$ being defined by

$$\langle u_{n\boldsymbol{k}}|u_{m\boldsymbol{k}}\rangle = \frac{1}{V_C}\int_{V_C} \mathrm{d}^d r\; u^*_{n\boldsymbol{k}}(\boldsymbol{r})u_{m\boldsymbol{k}}(\boldsymbol{r}). \tag{B20}$$

Here, the subscript V_C signifies integration over the primitive unit cell. Using the second orthogonality relation of the crystal lattice (B13), the inner product between Bloch states of different crystal momenta $\boldsymbol{k}$ and $\boldsymbol{q}$, which unlike the lattice periodic functions are part of the same Hilbert space, can then be expressed in terms of an integral over their corresponding lattice periodic functions as

$$\langle \psi_{n\boldsymbol{k}}|\psi_{m\boldsymbol{q}}\rangle = \int \mathrm{d}^d r\; \psi^*_{n\boldsymbol{k}}(\boldsymbol{r})\psi_{m\boldsymbol{q}}(\boldsymbol{r}) = (2\pi)^d\delta(\boldsymbol{k}-\boldsymbol{q})\,\langle u_{n\boldsymbol{k}}|u_{m\boldsymbol{k}}\rangle\,. \tag{B21}$$

where the subscripts $\boldsymbol{k}$ and $\boldsymbol{q}$ are set equal by virtue of the delta function. Unlike the full Bloch functions, the lattice periodic functions need only be square integrable over the primitive unit cell, and so can be made to comprise an orthonormal set satisfying $\langle u_{n\boldsymbol{k}}|u_{m\boldsymbol{k}}\rangle = \delta_{nm}$ for every choice of the crystal momentum $\boldsymbol{k}$. Hence, the Bloch functions of different quantum numbers n and $\boldsymbol{k}$ can be chosen to be orthogonal over the entire crystal lattice.

Seeing that the Bloch functions (B18) and the lattice periodic functions are related by a phase factor, a normalization condition is naturally defined

$$\int_{V_C} \mathrm{d}^d r|\psi_{n\boldsymbol{k}}(\boldsymbol{r})|^2 = \int_{V_C} \mathrm{d}^d r|u_{n\boldsymbol{k}}(\boldsymbol{r})|^2 = 1. \tag{B22}$$

Hence, the normalization condition of the Bloch functions is independent on the definition of their inner product (B21). The normalization condition also gives a physical explanation of the absolute square of the Bloch functions as the electron density over the crystal lattice, which is lattice periodic and indeed extends over all of space for an electron described by a single Bloch function.

B.3 Localized Wannier Orbitals

Instead of describing the electrons as Bloch states extended over the entire crystal structure, it is often more convenient to describe the electrons as bound in *localized molecular orbitals* corresponding to individual primitive unit cells in the crystal lattice. These electronic states are known as *Wannier orbitals*, and can be mathematically described using the Bloch functions derived from the discrete translation invariance of the lattice. The Wannier orbitals are more or less localized around each unit cell, and constitute the theoretical background for a rigorous derivation of the tightbinding model in chapter 4.

Upon imposing the normalization condition (B22) on the Bloch functions $\psi_{n\boldsymbol{k}}(\boldsymbol{r})$, the *Wannier function* of band n and lattice site $\boldsymbol{R}_i$ is defined as an integral over the Brillouin zone given by

$$w_{ni}(\boldsymbol{r}) = V_C \int_{\mathrm{BZ}} \frac{\mathrm{d}^d k}{(2\pi)^d}\, e^{-i\boldsymbol{k}\cdot\boldsymbol{R}_i} \psi_{n\boldsymbol{k}}(\boldsymbol{r}). \tag{B23}$$

The Wannier wavefunction denoted $w_{ni}(\boldsymbol{r})$ describes a *Wannier orbital* localized around lattice site $\boldsymbol{R}_i$. For Wannier states the quantum number n thus takes on the role of labelling different electronic orbitals, as opposed to its role for Bloch functions (B18) where n denotes the energy band index.

Using here the defining property of the Bloch functions (B16), it is clear that the Wannier functions satisfies $w_{ni}(\boldsymbol{r} - \boldsymbol{R}_j) = w_{n,i+j}(\boldsymbol{r})$. In consequence, it suffices to define only one Wannier function $w_{n0} \equiv w_n$ for each orbital type n. The Wannier function at lattice site i is then a translated version of this orbital

$$w_{ni}(\boldsymbol{r}) = w_n(\boldsymbol{r} - \boldsymbol{R}_i). \tag{B24}$$

This description is possible because the lattice vectors $\boldsymbol{R}_i$ are spanning a homogeneous Bravais lattice, meaning the surrounding lattice is identical at every lattice site, leading to identical but translated electronic orbitals.

From the definition of the Wannier functions (B23) and the orthonormality of the Bloch functions (B21), the Wannier functions are square integrable and constitute an orthonormal set over the entire crystal lattice, satisfying

$$\int \mathrm{d}^d r\; w_{ni}(\boldsymbol{r}) w_{mj}(\boldsymbol{r}) = \delta_{nm}\delta_{ij}, \tag{B25}$$

where the first orthogonality relation of the crystal lattice (B13) was used. From the second orthogonality relation, the Bloch functions (B18) can then be retrieved from the Wannier functions (B23) through the inverse transform

$$\psi_{n\boldsymbol{k}}(\boldsymbol{r}) = \sum_i e^{i\boldsymbol{k}\cdot\boldsymbol{R}_i} w_{ni}(\boldsymbol{r}) \tag{B26}$$

Hence, the Bloch function of band index n can be interpreted as the collective wavefunction of the Wannier functions of orbital index n translated to every primitive unit cell of the crystal lattice. Notice that the sum is over the entire lattice and satisfies the defining relation of the Bloch functions (B16).

In this formulation of the Wannier orbitals it is assumed that the Bloch functions are smooth and periodic over the entire Brillouin zone. This is however only viable for isolated, non-degenerate energy bands that are separated from all other energy bands. A degeneracy in the energy band structure will usually translate to a singularity in the Bloch functions at the degeneracy point, which in turn results in delocalization of the corresponding single-band Wannier function. However, it is possible to construct *multiband Wannier functions* by a linear, unitary combination of the Bloch functions from degenerate bands [24], thus avoiding the inconvenience. This topic will not be covered further in the thesis.

Appendix C

Time Reversal Symmetry

In theoretical physics, *time reversal* of a system is the operation of reversing the direction of time, denoted by the operator

$$\mathcal{T} : t \longmapsto -t. \tag{C1}$$

Classically, variables are either invariant or negated under the act of reversing the direction of time: the position of a particle $\boldsymbol{r}$ is invariant upon time reversal, whereas the linear momentum $\boldsymbol{p}$ is negated due to the reversal of velocity.

Many physical laws are invariant under time reversal, meaning the formulae governing the dynamics of physical systems remain valid upon reversing the direction of time. This property of physical laws is known as *time reversal symmetry*, being the symmetry behind the conservation of energy. Arguments based on time reversal symmetry are important to the description of many physical systems, and is used in chapters 5 and 6 as a tool for discovering the properties of topological materials.

In the following appendix, the consequences of time reversal symmetry is investigated for quantum mechanical systems. Of special importance is the proof of *Kramers degeneracy*, which states that fermionic systems invariant under time reversal will be doubly degenerate. The appendix also introduces the Pauli matrices, which appear in the two-level Hamiltonian matrix of chapter 5, the orbital basis of chapter 4 and in the Weyl representation of the Dirac matrices in appendix D.

The appendix on time reversal symmetry is based on the textbook by Bernevig [23] and the article on hidden antiunitary symmetry by Hou and Chen [43].

C.1 Properties of Antiunitary Operators

Let a quantum mechanical system be described by the state vector $|\psi\rangle$, whose time reversed analogue is described by the reversed state vector $\mathcal{T}|\psi\rangle \equiv |\mathcal{T}\psi\rangle$. If the system is invariant under time reversal, the amplitude square should be conserved, meaning $|\langle\mathcal{T}\psi|\mathcal{T}\psi\rangle| = |\langle\psi|\psi\rangle|$. According to the Wigner theorem, time reversal $\mathcal{T}$ will then correspond to either a unitary or an antiunitary operator.

Consider then some physical process in which an initial state $|\psi\rangle$ turns into a final state $|\phi\rangle$, where the amplitude of the process is calculated as the inner product $\langle\phi|\psi\rangle$. When the arrow of time is reversed, the final and initial states will interchange, such that $|\mathcal{T}\psi\rangle$ becomes the final state and vice versa. In consequence, the time reversal operator will satisfy

$$\langle\mathcal{T}\phi|\mathcal{T}\psi\rangle = \langle\psi|\phi\rangle = \langle\phi|\psi\rangle^* . \tag{C2}$$

The time reversal operator is therefore an *antiunitary* operator.

Being an antiunitary operator, the time reversal operator can always be expressed $\mathcal{T} = U\mathcal{K}$, where $\mathcal{K}$ is the operator for complex conjugation. In this way, the time reversal operator will be an *antilinear* operator, satisfying

$$\mathcal{T}(a|\psi\rangle + b|\phi\rangle) = a^*|\mathcal{T}\psi\rangle + b^*|\mathcal{T}\phi\rangle . \tag{C3}$$

Due to the complex conjugation, the definitions of the adjoint operators $U^\dagger$ and $\mathcal{T}^\dagger$ are different for unitary and antiunitary operators, given respectively by

$$\langle U\phi|\psi\rangle = \langle\phi|U^\dagger\psi\rangle \qquad\qquad \langle\mathcal{T}\phi|\psi\rangle = \langle\phi|\mathcal{T}^\dagger\psi\rangle^* \tag{C4}$$

From the antiunitarity constraint of the time reversal operator (C2), the inverse $\mathcal{T}^{-1} = \mathcal{T}^\dagger$, with the proper definition of the adjoint for antiunitary operators.

Consider then the square of the time reversal operator, which by its antiunitarity (C2) satisfies $\langle\mathcal{T}^2\phi|\mathcal{T}^2\psi\rangle = \langle\phi|\psi\rangle$. For this to hold for any two state vectors, the square of the time reversal operator must satisfy $\mathcal{T}^2 = \pm 1$.

C.2 Time Reversal in Spinful Systems

The components of the quantum mechanical spin-operator $\boldsymbol{S} = (S_x, S_y, S_z)$ of a general spinful system are generated by the commutation relation

$$[S_i, S_j] = i\varepsilon_{ijk}S_k \tag{C5}$$

For the dynamics of spinful systems to be invariant under time reversal, the time reversed spin-operator $\mathcal{T}\boldsymbol{S}\mathcal{T}^\dagger$ must also satisfy the commutation relation. Due to the antilinearity (C3) of the time reversal operator however, using also that $\mathcal{T}\mathcal{T}^\dagger = I$, applying the time reversal operator on the commutation relation above yields $[\mathcal{T}S_i\mathcal{T}^\dagger, \mathcal{T}S_j\mathcal{T}^\dagger] = -i\varepsilon_{ijk}\mathcal{T}S_k\mathcal{T}^\dagger$. The original commutation relation is regained if the spin operator is negated under time reversal, satisfying

$$\mathcal{T}\boldsymbol{S}\mathcal{T}^\dagger = -\boldsymbol{S}. \tag{C6}$$

As such, the direction of the spin is flipped under time reversal, consistent with the spin being regarded as analogous to angular momentum. This can be taken as a conventional constraint on the time reversal operator.

It is customary to choose the eigenstates of the S_z operator as the basis state vectors of the Hilbert space of spin states. In that case, the spin flip under time reversal can be implemented by a rotation of π radians around an arbitrary axis perpendicular to the z-axis. The prevalent convention is to choose a rotation around the y-axis, fixing the time reversal operator for spinful systems as

$$\mathcal{T} = e^{i\pi S_y/\hbar}\mathcal{K} \tag{C7}$$

where S_y being the y-component of the spin is the generator of rotations around the y-axis. For a standard spin representation, the S_y component is purely imaginary, such that the square $\mathcal{T}^2 = e^{2\pi i S_y/\hbar}$. In consequence, the time reversal parity $\mathcal{T}^2 = 1$ corresponds to particles of integer spin, or bosons, while $\mathcal{T}^2 = -1$ corresponds to particles of half-integer spin, or fermions.

For a spin-$\frac{1}{2}$ system in particular, the Hilbert space of quantum states is two dimensional. In the matrix representation of quantum mechanics, the spin operator can be represented using the *Pauli matrices* as $\boldsymbol{S} = \hbar\boldsymbol{\sigma}/2$, with

$$\sigma_x = \begin{bmatrix} 0 & 1 \\ 1 & 0 \end{bmatrix} \qquad \sigma_y = \begin{bmatrix} 0 & -i \\ i & 0 \end{bmatrix} \qquad \sigma_z = \begin{bmatrix} 1 & 0 \\ 0 & -1 \end{bmatrix} \tag{C8}$$

The Pauli matrices are all unitary and hermitian, satisfying $\boldsymbol{\sigma}^{-1} = \boldsymbol{\sigma}^\dagger = \boldsymbol{\sigma}$. In addition to obeying the spin commutation relation (C5), the Pauli matrices also satisfies a Clifford algebra in the form of an anticommutation relation:

$$\begin{gathered} [\sigma_i, \sigma_j] = i\varepsilon_{ijk}\sigma_k \qquad \{\sigma_i, \sigma_j\} = 2\delta_{ij} \\ \sigma_i\sigma_j = \delta_{ij} \ + i\varepsilon_{ijk}\sigma_k. \end{gathered} \tag{C9}$$

In the lower equation, the two relations have been added to form a general expression for the product of any two Pauli matrices.

Inserting the matrix $\sigma_y/2$ into the general formula for the time reversal operator of spinful systems (C7), the time reversal operator for spin-$\frac{1}{2}$ systems

$$\mathcal{T} = i\sigma_y\mathcal{K}. \tag{C10}$$

This expression explicitly confirms the general form $\mathcal{T} = U\mathcal{K}$ of an antiunitary operator, where now $U = i\sigma_y$ is a unitary and anti-hermitian operator, readily satisfying $U^{-1} = U^\dagger = -U$ from the unitarity and hermiticity of σ_y.

Finally, it should be noted that the spin component S_y in the general expression for the time reversal operator (C7) denotes the y-component of the total spin in the system. Hence, for a system of several fermions, the spin component $S_y = \sum_i S_{iy}$, being the sum of the y-component of all individual fermions in the system. Thus, squaring the time reversal operator will leave $\mathcal{T}^2 = 1$ if there is an even and $\mathcal{T}^2 = -1$ if there is an odd number of fermions in the system. For bosonic systems however, the total spin will always be of integer value, and so the property $\mathcal{T}^2 = 1$ holds independent on the number of bosonic particles.

C.3 Kramers Degeneracy

Consider a system of half integer spin, such that the time reversal operator satisfies $\mathcal{T}^2 = -1$, and denote by $|\psi\rangle$ an eigenstate of the Hamiltonian $\hat{H}$ of the system with a corresponding eigenvalue E. Assume then the system is invariant under time reversal, such that the Hamiltonian commutes with the time reversal operator: $[\hat{H}, \mathcal{T}] = 0$. In that case, the time reversed state vector satisfies $\hat{H}(\mathcal{T}|\psi\rangle) = \mathcal{T}\hat{H}|\psi\rangle = E\mathcal{T}|\psi\rangle$, and so $\mathcal{T}|\psi\rangle$ is also an eigenstate with the same eigenvalue E as the eigenstate $|\psi\rangle$.

Assume then the spectrum of the Hamiltonian $\hat{H}$ is non-degenerate. In that case, the state vector $\mathcal{T}|\psi\rangle$ must be equal to $|\psi\rangle$ up to a phase. In consequence, the state $|\psi\rangle$ will also be an eigenstate of $\mathcal{T}$, satisfying the eigenvalue equation $\mathcal{T}|\psi\rangle = e^{i\theta}|\psi\rangle$. Consider then the state given by $|\phi\rangle = e^{i\theta/2}|\psi\rangle$. Using the antilinearity (C3) of the time reversal operator, the state satisfies $\mathcal{T}|\phi\rangle = |\phi\rangle$. Applying the time reversal operator twice thus leaves $\mathcal{T}^2|\phi\rangle = |\phi\rangle$, in contradiction with the assumption that $\mathcal{T}^2 = -1$. Alternately, using directly the assumption $\mathcal{T}^2 = -1$ with the antiunitarity (C2) of the time reversal operator, then $\langle\psi|\mathcal{T}\psi\rangle = \big\langle\mathcal{T}\psi\big|\mathcal{T}^2\psi\big\rangle^* = -\langle\mathcal{T}\psi|\psi\rangle^* = -\langle\psi|\mathcal{T}\psi\rangle$, and so $\langle\psi|\mathcal{T}\psi\rangle = 0$. Thus, the original and time reversed state vectors are orthogonal, and so cannot be linearly dependent. This however holds only if $\mathcal{T}^2 = -1$.

In consequence, for systems which are invariant under time reversal where the time reversal operator satisfies $\mathcal{T}^2 = -1$, each eigenvalue E of the Hamiltonian operator $\hat{H}$ will be doubly degenerate, with $|\psi\rangle$ and $\mathcal{T}|\psi\rangle$ being orthogonal eigenstates of the same eigenvalue. This statement is known as Kramers theorem, and the degeneracy exhibited is known as *Kramers degeneracy*.

The reverse theorem is also true [43]: any two-fold degeneracy of a quantum system must be protected by a symmetry corresponding to an antiunitary operator Υ with its square being $\Upsilon^2 = -1$. In order to prove the theorem, consider a Hamiltonian with two distinct eigenstates $|\psi\rangle$ and $|\phi\rangle$ with the same eigenvalue E, such that the system exhibits a two-fold degeneracy. Define the operator

$$\Upsilon = \big(\,|\phi\rangle\langle\mathcal{K}\psi| - |\psi\rangle\langle\mathcal{K}\phi|\,\big)\mathcal{K}, \tag{C11}$$

where the operator $\mathcal{K}$ corresponds to complex conjugation. Under the prevailing assumptions, the two states have been shown to be orthogonal, and assuming the states are normed to unity the condition $\Upsilon^2 = -1$ is readily verified using the completeness relation (1.1) of the two states. Likewise, the operator satisfies $\Upsilon^\dagger\Upsilon = I$, and so is an antiunitary operator due to the complex conjugation.

Finally, from its definition the operator directly satisfies $\Upsilon|\psi\rangle = |\phi\rangle$ and $\Upsilon|\phi\rangle = -|\psi\rangle$. Recalling that both states corresponds to the same eigenvalue of the Hamiltonian, the operator then satisfies the commutation relation $[\Upsilon, H] = 0$. In consequence, if a quantum system exhibits a two-fold degeneracy, there exists an antiunitary operator with its square being $\Upsilon^2 = -1$ under which the system is invariant. As such, any two-fold degeneracy is protected by a symmetry corresponding to an antiunitary operator, of which the Kramers degeneracy protected by time reversal symmetry is one example.

C.4 The Combined $\mathcal{PT}$-Symmetry

An important symmetry in most branches of physics is the *space inversion symmetry*, with the corresponding *parity operator* defined through

$$\mathcal{P} : \boldsymbol{r} \longmapsto -\boldsymbol{r}, \tag{C12}$$

where $\boldsymbol{r}$ is the position vector in any number of dimensions. Any quantity transforming as the position vector will be odd under the parity transform.

In quantum mechanics in particular, the parity operator is unitary and acts on quantum states $\psi(\boldsymbol{r})$ of the position representation. Because applying the operator twice leaves the spatial degrees of freedom invariant, the parity operator must satisfy $\mathcal{P}^2\psi(\boldsymbol{r}) = e^{i\theta}\psi(\boldsymbol{r})$, where θ is an undetectable phase corresponding to the state $\psi(\boldsymbol{r})$. Usually the phase can in general be chosen $\theta = 0$, such that the parity operator acts on quantum states as $\mathcal{P}\psi(\boldsymbol{r}) = \pm\psi(-\boldsymbol{r})$. Here, the two signs corresponds to the *intrinsic parity* of the particular state.

In solid state physics, the energy band structure of crystalline systems may be dependent on the electron spin degree of freedom σ, with individual energy bands labelled as $\varepsilon_\sigma(\boldsymbol{k})$ with $\boldsymbol{k}$ being the crystal momentum. From the previous sections both the electron momentum $\boldsymbol{k}$ and spin σ will change direction under time reversal $\mathcal{T}$, whereas space inversion $\mathcal{P}$ reverses only the momentum. Hence, the energy bands are affected by the two operations as $\mathcal{T}\varepsilon_\sigma(\boldsymbol{k}) = \varepsilon_{-\sigma}(-\boldsymbol{k})$ and $\mathcal{P}\varepsilon_\sigma(\boldsymbol{k}) = \varepsilon_\sigma(-\boldsymbol{k})$ respectively, which applied in succession leaves

$$\mathcal{PT}\varepsilon_\sigma(\boldsymbol{k}) = \varepsilon_{-\sigma}(\boldsymbol{k}). \tag{C13}$$

The latter expression gives the transformation of the energy bands under the combined time reversal and space inversion symmetry, conventionally termed the *$\mathcal{PT}$-symmetry*. If the system is invariant under the $\mathcal{PT}$-symmetry, the energy bands thus satisfy $E_\sigma(\boldsymbol{k}) = E_{-\sigma}(\boldsymbol{k})$; the energy bands of crystalline systems invariant under the combined space inversion and time reversal symmetry are independent on the spin index, and hence doubly degenerate over the entire Brillouin zone. The double degeneracy is a continuous Kramers degeneracy, as derived for general antiunitary operators in the previous subappendix.

It should be noted that the Kramers degeneracy induced by the $\mathcal{PT}$-symmetry will also hold for systems where both the space inversion symmetry $\mathcal{P}$ and the time reversal symmetry $\mathcal{T}$ are broken individually, as long as their combined symmetry is preserved. Even more generally, for crystalline systems with energy bands labelled as $E_\sigma(\boldsymbol{k})$, the Kramers degeneracy of energy bands will be present for any system invariant under any antiunitary operation which reverses the spin while preserving the crystal momentum.

Appendix D

Fermions in Relativistic Quantum Theory

In chapter 6, a class of crystalline solid state systems known as topological semimetals are investigated, where the electronic dispersion relation is linear around particular points of the Brillouin zone. The resulting effective low-energy description of the electrons is analogous to the Einstein energy-momentum relation for massless fermions in high energy physics known as *Weyl fermions*.

In quantum field theory, spin-$\frac{1}{2}$ fermions are described by the relativistic Dirac equation and can be classified as either Dirac, Majorana or Weyl fermions. Disregarding neutrinos being of Majorana type, all elementary fermions of the standard model of particle physics have been found to be Dirac fermions. The following appendix investigates the mathematical description of relativistic spin-$\frac{1}{2}$ particles from the perspective of relativistic quantum mechanics, where the description of the behaviour of quantum states are constrained to preserve the underlying symmetries of spacetime as described by the theory of relativity. The resulting quantum theory of Dirac, Weyl and Majorana fermions follows mainly the derivation of Kachelrieß [44]. Conventional to quantum field theory, natural units will be used with a Planck constant and speed of light $\hbar = c = 1$.

In order to properly classify Majorana, Dirac and Weyl fermions, the relativistic theory of the coupling between the fermionic and the electromagnetic fields must also be introduced. The coupling constant being the *electromagnetic charge* then makes it viable to define the operation of *charge conjugation*, which in turn will be highly connected to the time reversal symmetry. The related minimal coupling principle is furthermore used to derived the electric current density in chapter 3. The final sections on charge conjugation, time reversal and space inversion is based on the arguments from Lahiri and Pall [45].

D.1 Lorentz Invariance and the Dirac Equation

In the special theory of relativity, the dimensions of space and time combines to form the four-dimensional *Minkowski space*, describing the geometrical properties of flat spacetime. A symmetry of Minkowski space is defined as any operation under which the speed of light remains invariant. Disregarding translational invariance in both space and time, the remaining point symmetries constitute the *Lorentz group*, whose elements are known as *Lorentz transforms*. In general, Lorentz transforms may involve time reversal or space inversion.

Any *proper Lorentz transform* can be subdivided into a circular rotation of space and a hyperbolic rotation incorporating time, the latter known as a *Lorentz boost*. The Lie algebra of the proper Lorentz group contains three generators for rotations $\boldsymbol{J}$ and three generators for Lorentz boosts $\boldsymbol{K}$, satisfying

$$[J_i, J_j] = i\varepsilon_{ijk}J_k, \qquad [J_i, K_j] = i\varepsilon_{ijk}K_k, \qquad [K_i, K_j] = -i\varepsilon_{ijk}J_k.$$

This allows for a decomposition of the proper Lorentz group into two separate groups with mutually commuting generators defined $\boldsymbol{J}^{\pm} = (\boldsymbol{J} \pm i\boldsymbol{K})/2$. These representations of the Lorentz group are labelled by a pair of labels (j^-, j^+), with the dimensionality of the representation being $(2j^- + 1)(2j^+ + 1)$.

The two smallest non-trivial representations are $(1/2, 0)$ and $(0, 1/2)$, where the generators can be given by the Pauli matrices (C8) as $\boldsymbol{J} = -i\boldsymbol{K} \equiv \boldsymbol{\sigma}/2$ and $\boldsymbol{J} = i\boldsymbol{K} \equiv \boldsymbol{\sigma}/2$ respectively, both being two-dimensional. The states transforming under these two representations are the left- and right chiral *Weyl spinors*, which transform under a general Lorentz transformation Λ as

$$\begin{aligned} (1/2, 0): &\qquad \phi_L \to S_L(\Lambda)\phi_L = e^{-\frac{1}{2}i\boldsymbol{\sigma}\cdot\boldsymbol{\alpha} - \frac{1}{2}\boldsymbol{\sigma}\cdot\boldsymbol{\eta}}\phi_L \\ (0, 1/2): &\qquad \phi_R \to S_R(\Lambda)\phi_R = e^{-\frac{1}{2}i\boldsymbol{\sigma}\cdot\boldsymbol{\alpha} + \frac{1}{2}\boldsymbol{\sigma}\cdot\boldsymbol{\eta}}\phi_R \end{aligned} \tag{D1}$$

Here $\boldsymbol{\alpha}$ are the circular rotation angles, while $\boldsymbol{\eta} = \eta\hat{\boldsymbol{n}}$ are the components of the rapidity of the Lorentz boost being connected to the energy E and rest mass m of the particle through $\tanh\eta = E/m$. Considering only a Lorentz boost, which is a shift from the rest frame of the particle to a frame where the particle has a four-momentum p, the Lorentz transformations can then be written as

$$\phi_L(p) = \frac{E + m - \boldsymbol{\sigma}\cdot\boldsymbol{p}}{\sqrt{2m(E+m)}}\phi_L(0) \qquad\qquad \phi_R(p) = \frac{E + m + \boldsymbol{\sigma}\cdot\boldsymbol{p}}{\sqrt{2m(E+m)}}\phi_R(0).$$

The Weyl spinors thus transform similarly under a Lorentz boost, but for a sign which disappears in the rest frame, where $\boldsymbol{p} = 0$. Set therefore $\phi_L(0) = \phi_R(0)$. The two spinors are then connected through the relation

$$(E \mp \boldsymbol{\sigma}\cdot\boldsymbol{p})\phi_{R/L}(p) = m\phi_{L/R}(p). \tag{D2}$$

Hence, for a rest mass $m \neq 0$ the equation for the Weyl spinors are coupled.

Defining $\sigma^\mu = (1, \boldsymbol{\sigma})$ and $\overline{\sigma}^\mu = (1, -\boldsymbol{\sigma})$, where the index runs over the four spacetime coordinates, the (4×4) *gamma matrices* in the Weyl representation

$$\gamma^\mu = \begin{bmatrix} 0 & \sigma^\mu \\ \overline{\sigma}^\mu & 0 \end{bmatrix}. \tag{D3}$$

Defining also the *Dirac spinor* $\psi = (\phi_L,\, \phi_R)$, the relation connecting the Weyl spinors (D2) can then be written more compactly as the *Dirac equation*

$$(\gamma^\mu p_\mu - m)\psi(p) = 0 \qquad \text{or} \qquad (i\gamma^\mu \partial_\mu - m)\psi(x) = 0 \tag{D4}$$

The latter expression gives the Dirac equation in coordinate space, by letting the canonical four-momentum $p^\mu = (E, p_x, p_y, p_z) \to i\partial^\mu = i(\partial_t, \partial_x, \partial_y, \partial_z)$.

The Dirac equation (D4) is the equation of state for relativistic fermions with rest mass m, where the Dirac spinor is a four-component spinor. Notice that even though Dirac spinors have four components, Dirac spinors are not four-vectors; Dirac spinors are defined through their unique transformation properties under Lorentz transforms.

By the definition in terms of Weyl spinors, Dirac spinors transform under the representation $(1/2, 0) \oplus (0, 1/2)$ of the proper Lorentz group as

$$S(\Lambda)\psi = S_L(\Lambda) \oplus S_R(\Lambda)\psi = e^{-\frac{1}{4} i\omega_{\mu\nu}\sigma^{\mu\nu}}\psi, \tag{D5}$$

where the elements $\omega_{\mu\nu}$ parameterizes the transform, and the six generators of the proper Lorentz transform are given by the independent elements of the antisymmetric tensor $\sigma^{\mu\nu}/2$, written in terms of the gamma matrices (D3) as

$$\sigma^{\mu\nu} \equiv \frac{i}{2}[\gamma^\mu, \gamma^\nu]. \tag{D6}$$

The parameters are related to the circular rotation angles and the rapidity components as $\alpha_k = \varepsilon_{kij}\omega_{ij}$ and $\eta_k = \omega_{k0}$. Notice that the scalar $\psi^\dagger\psi$ will not be Lorentz invariant, as Lorentz boosts are not unitary transformations. Conserved quantities are instead often expressed in terms of the *Dirac adjoint* $\overline{\psi} = \psi^\dagger\gamma^0$, for which the corresponding scalar $\overline{\psi}\psi$ indeed becomes Lorentz invariant.

Upon a Lorentz transform (D5), the derivative $\partial_\mu \to \Lambda_\mu{}^\nu \partial_\nu$. For the Dirac equation (D4) to be Lorentz invariant, the gamma matrices must then satisfy

$$S^{-1}(\Lambda)\gamma^\mu \Lambda_\mu{}^\nu S(\Lambda) = \gamma^\nu. \tag{D7}$$

It should be noted that the gamma matrices (D3) contrary to their spacetime index does not comprise a four-vector, while the contraction between the gamma matrices and a four-vector is Lorentz invariant when combined with a spinor.

The physical interpretation of the four components of the Dirac spinor $\psi(p)$ will depend on the representation of the gamma matrices (D3). In general however, the four components corresponds to four degrees of freedom describing a fermion and its corresponding *anti-fermion*, both with two spin degrees of freedom. In the following, the Weyl representation for the gamma matrices will be used, being the favourable representation for investigating chirality.

D.2 Dirac Hamiltonian and Clifford Algebra

From the Dirac equation of motion (D4), a Hamiltonian matrix can be inferred from comparison with the Schrödinger equation (A2) from quantum theory. Expanding the contraction $i\gamma^\mu\partial_\mu = i\gamma^0\partial_t - i\gamma^k\partial_k$, left multiplying by γ^0 and isolating the time component of the derivative, the *Dirac Hamniltonian*

$$i\partial_t\psi = (i\gamma^0\gamma^k\partial_k + \gamma^0 m)\psi \equiv H_D\psi.$$

In particular, recalling the original introduction of the gamma matrices (D3), the Weyl representation of the Dirac Hamiltonian becomes

$$H_D = \gamma^0\gamma^k p_k + \gamma^0 m = \begin{bmatrix} -\boldsymbol{\sigma}\cdot\boldsymbol{p} & mI_2 \\ mI_2 & \boldsymbol{\sigma}\cdot\boldsymbol{p} \end{bmatrix}, \tag{D8}$$

The energy eigenvalues of this Hamiltonian are given by $E^2 = \boldsymbol{p}^2 + m^2$, which is the Einstein energy-momentum relation of special relativity.

The derivation of the Dirac equation (D4) and the Dirac Hamiltonian (D8) considers in particular the Weyl representation of the gamma matrices (D3). However, any unitary transformation of the gamma matrices will provide an equal physical description, and so the Weyl representation is not unique to the physics described. From the constraints enforced by the transformation properties under Lorentz transforms, it is yet possible to find general properties of the gamma matrices independent on the representation.

In particular, the gamma matrices are constrained such that the Dirac Hamiltonian (D8) will reproduce the momentum-relation $p^\mu p_\mu = E^2 - \boldsymbol{p}^2 = m^2$. Squaring the Dirac Hamiltonian, the gamma matrices must readily satisfy

$$\{\gamma^\mu, \gamma^\nu\} = 2\eta^{\mu\nu} I_4, \tag{D9}$$

being their general defining relation. Due to the appearance of the Minkowski metric $\eta^{\mu\nu}$, the spacetime index of the gamma matrices can be raised or lowered as for four-vectors. From this it follows that the gamma matrices must satisfy $(\gamma^0)^2 = I_4$ and $(\gamma^k)^2 = -I_4$. Furthermore, the Dirac Hamiltonian (D8) must be hermitian, meaning the zeroth gamma matrix is hermitian satisfying $(\gamma^0)^\dagger = \gamma^0$ whereas the remaining three must satisfy $(\gamma^k)^\dagger = \gamma^0\gamma^k\gamma^0$, or combined

$$(\gamma^\mu)^\dagger = \gamma^0\gamma^\mu\gamma^0. \tag{D10}$$

Hence, by the anticommutation relation (D9), the space component gamma matrices are anti-hermitian, satisfying $(\gamma^k)^\dagger = -\gamma^k$.

The anticommutation relation of the gamma matrices (D9) defines a *Clifford algebra*, with a basis generated by the gamma matrices constructed by considering all possible products of gamma matrices. Because the gamma matrices satisfies $(\gamma^0)^2 = I_4$ and $(\gamma^k)^2 = -I_4$, the only product of four gamma matrices to consider can be defined as a fifth gamma matrix, in the Weyl representation

$$\gamma^5 \equiv i\gamma^0\gamma^1\gamma^2\gamma^3 = \begin{bmatrix} -I_2 & 0 \\ 0 & I_2 \end{bmatrix}, \tag{D11}$$

where the imaginary unit makes it hermitian. From the anticommutation relation of gamma matrices (D9), the fifth gamma matrix has the properties

$$(\gamma^5)^2 = I_4 \qquad \{\gamma^\mu, \gamma^5\} = 0. \tag{D12}$$

Having introduced the fifth gamma matrix γ^5, all products of three gamma matrices can be expressed in terms of the four matrices $\gamma^\mu\gamma^5$. Finally, any product of two gamma matrices can be written in terms of the antisymmetric tensor $\sigma^{\mu\nu}$ as defined (D6). Combining all elements, the sixteen basis elements of the matrix representation of the Clifford algebra thus becomes

$$\Gamma = \{I_4, \gamma^5, \gamma^\mu, \gamma^\mu\gamma^5, \sigma^{\mu\nu}\}. \tag{D13}$$

These sixteen matrices are linearly independent, and so span the set of all complex (4×4) matrices, to which the Clifford algebra is isomorphic.

D.3 Helicity and Chirality

Recall that the Pauli matrices (C8) are proportional to the matrix representation of the components of the non-relativistic spin operator, given by $\boldsymbol{S} = \boldsymbol{\sigma}/2$. In terms of elements of the Clifford algebra (D13), the components of the *relativistic quantum mechanical spin operator* can similarly be defined

$$\Sigma^k \equiv \frac{1}{2} i\varepsilon_{kij}\sigma^{ij} = \gamma^5\gamma^0\gamma^k = \begin{bmatrix} \sigma^k & 0 \\ 0 & \sigma^k \end{bmatrix}. \tag{D14}$$

The Dirac Hamiltonian does not in general commute with the components of the spin operator (D14); the spin is only conserved in the rest frame of the particle, where $\boldsymbol{p} = 0$. Define then the *helicity operator*, given by

$$\Sigma_{\boldsymbol{p}} = \frac{\boldsymbol{\Sigma} \cdot \boldsymbol{p}}{|\boldsymbol{p}|}. \tag{D15}$$

The helicity operator measures the projection of the spin onto the axis along the direction of momentum $\boldsymbol{p}$. From the expression of the Dirac Hamiltonian (D8), it is readily confirmed that the matrices commute, reflecting that there is no angular momentum along the axis of motion. The simultaneous eigenfunctions of the Dirac Hamiltonian and helicity operator are termed *helicity eigenstates*. For massive particles helicity is however a frame dependent quantity, as the sign of the momentum $\boldsymbol{p}$ may invert when applying a Lorentz boost.

The fifth gamma matrix (D11) is an involutory matrix, satisfying $(\gamma^5)^2 = I_4$, making it viable to define projection operators P_L and P_R onto its eigenspace. For any Dirac spinor ψ, eigenspinors of γ^5 can be constructed as

$$\psi_L \equiv P_L\psi = \frac{1}{2}(1 - \gamma^5)\psi \qquad \psi_R \equiv P_R\psi = \frac{1}{2}(1 + \gamma^5)\psi. \tag{D16}$$

If ψ is a solution to the Dirac equation (D4), the projected states ψ_L and ψ_R are known as *left- and right-chiral states*, being eigenspinors of γ^5 with eigenvalues

∓ 1, respectively. In the Weyl representation in particular, the Dirac spinor was given in terms of the Weyl spinors as $\psi = (\phi_L, \phi_R)$. From the Weyl representation of the fifth gamma matrix (D11), it is then seen that the left and right chiral states (D16) in the Weyl representation can be identified with the Weyl spinors as $\psi_L = (\phi_L, 0)$ and $\psi_R = (0, \phi_R)$. In consequence, the chiral fields follow the same transformation rules under Lorentz transforms (D1) as Weyl spinors, and hence transform separately under a Lorentz boost. Thus, chirality is a Lorentz invariant property independent on the representation of the gamma matrices. However, the matrix γ^5 does not commute with the Dirac Hamiltonian (D8), and so chirality is not in general a conserved quantity; the mass term couple the time evolution of left- and right-chiral fields, meaning the chirality of a state will in general vary over time.

Helicity and chirality can in a sense be seen as complementary quantum numbers, with the former being conserved and frame-dependent whereas the latter is unconserved and Lorentz invariant. For fermions with a zero rest mass $m = 0$ however, helicity is also Lorentz invariant, and from the Weyl representation of the Dirac Hamiltonian (D8) and the fifth gamma matrix (D11), it is readily seen that chirality becomes a conserved quantity.

Reconsider then the Dirac Hamiltonian (D8) in the Weyl representation, which for a vanishing rest mass $m = 0$ decouples into two *Weyl Hamiltonians*

$$H_W^{\mp} = \mp \boldsymbol{\sigma} \cdot \boldsymbol{p} \tag{D17}$$

These Hamiltonians correspond to the left- and right-chiral Weyl spinors ϕ_R and ϕ_L, and hence describe relativistic massless *Weyl fermions* with chirality ∓ 1 respectively. Reconsider then the Dirac equation (D4), which for massless fermions with energy $E = |\boldsymbol{p}|$ can be written on the form $\gamma^k p_k \psi = \gamma^0 |\boldsymbol{p}| \psi$. Multiplying this equation with the matrix $\gamma^5 \gamma^0$, and recalling the definition of the helicity operator (D15) and relativistic spin matrix (D14), the Dirac equation for massless fermions can be written $\Sigma_{\boldsymbol{p}} \psi = \gamma^5 \psi$. In consequence, for massless Weyl fermions the helicity and chirality quantum numbers coincide.

D.4 Charge Conjugation and Majorana Fermions

The electromagnetic field is a massless spin-1 field described by the electromagnetic four-potential A_μ. The observable electric and magnetic fields are governed by the Maxwell equation $\partial_\mu F^{\mu\nu} = j^\nu$, where the electromagnetic currents are denoted j^ν and the electromagnetic field-strength tensor is defined

$$F_{\mu\nu} = \partial_\mu A_\nu - \partial_\nu A_\mu \tag{D18}$$

The four-potential and field-strength are thus seen to be analogous to the Berry connection (5.2) and the Berry curvature (5.8), discussed in chapter 5. Similar to these berryological quantities, the electromagnetic field-strength tensor is invariant under a gauge transform of the four-potential $A_\mu \to A_\mu + \partial_\mu \Lambda$.

The Dirac spinors couple to the electromagnetic field through the minimal coupling prescription. The coupling modifies the Dirac equation (D4) as

$$[i\gamma^\mu(\partial_\mu + iqA_\mu) - m]\psi = 0. \tag{D19}$$

Here, q is the electromagnetic charge or coupling strength of the fermion. For a Dirac fermion both the charge q and rest mass m are nonzero.

Define then the *charge conjugated* spinor $\psi^c = \mathcal{C}\psi$, being a solution to the Dirac equation with the electromagnetic coupling (D19), but with a negated charge $q^c = -q$ compared to the spinor ψ. Charge conjugating the spinor twice should bring back the original spinor, and so $\mathcal{C}^2 = I$. The operator $\mathcal{C}$ is therefore known as the *charge conjugation involution*, as the inverse operator $\mathcal{C}^{-1} = \mathcal{C}$.

For the coupled Dirac equation (D19) to be invariant under a gauge transformation of the four-potential, the spinor and its charge conjugation must transform as $\psi \to e^{iq\Lambda}\psi$ and $\psi^c \to e^{-iq\Lambda}\psi^c$, respectively. The change in the sign of the exponent can be assumed a consequence of a complex conjugation. However, the complex conjugated spinor ψ^* does not satisfy the same Lorentz transformation properties as the spinor ψ, as complex conjugating the Lorentz transformation of Dirac spinors (D5) leaves in the exponent $i(\sigma^{\mu\nu})^* \neq -i\sigma^{\mu\nu}$.

Conjecture therefore the charge conjugated spinor $\psi^c = C(\gamma^0)^T\psi^* = C\overline{\psi}^T$, where the *charge conjugation matrix* C is a unitary matrix changing the representation of the gamma matrices. For the charge conjugated Dirac spinor ψ^c to inherit the Lorentz transformation properties of the spinor ψ, the matrix C is constrained to satisfy $C(\gamma^0)^T(\sigma^{\mu\nu})^* = -\sigma^{\mu\nu}C(\gamma^0)^T$, or $C^{-1}\sigma^{\mu\nu}C = -(\sigma^{\mu\nu})^T$. This property will be guaranteed if the charge conjugation matrix satisfies

$$C^{-1}\gamma^\mu C = -(\gamma^\mu)^T. \tag{D20}$$

By transposing the anticommutation relation (D9) of the gamma matrices, the matrices $-(\gamma^\mu)^T$ also satisfies the Clifford algebra. Thus, for any representation of the gamma matrices the charge conjugation matrix C will be well defined.

Charge conjugation thus affects Dirac spinors as $\psi^c = \mathcal{C}\psi = C(\gamma^0)^T\psi^*$. Using then that $\mathcal{C}^2 = I$, it is readily shown that the charge conjugation matrix satisfies $C^{-1} = (\gamma^0)^T C^*\gamma^0$. The charge conjugation matrix is also unitary with $C^\dagger = C^{-1}$, and by definition (D20) will satisfy $C^{-1}\gamma^0 C = -(\gamma^0)^T$. Combining these formulae, the charge conjugation matrix will be antisymmetric in any representation of the gamma matrices, satisfying $C^T = -C$.

Because the operator $\mathcal{C}$ satisfies $\mathcal{C}^2 = I$, its eigenvalues are ± 1. In particular, the eigenspinors corresponding to unity will be *Majorana spinors*, being their own charge conjugates. Spinors satisfying the Majorana condition $\psi^c = \psi$ describe *Majorana fermions*, having a nonzero rest mass m but a zero charge $q = 0$. In that case, fermions and antifermions cannot be distinguished, and half of the degrees of freedom compared to the charged Dirac field disappears.

In particular, the Weyl representation (D3) of the charge conjugation matrix conventionally takes the form $C = i\gamma^2\gamma^0$, such that charge conjugated spinors $\psi^c = i\gamma^2\psi^*$. Recalling that $\psi = (\phi_L, \phi_R)$ in the Weyl representation, the Weyl spinors will transform under charge conjugation as

$$\phi_L^c = i\sigma^2\phi_R^* \qquad\qquad \phi_R^c = -i\sigma^2\phi_L^*, \tag{D21}$$

where σ^2 is the second Pauli matrix. Majorana spinors ψ_M can then in the Weyl representation be expressed using the Weyl spinors as

$$\psi_M = \begin{bmatrix} \phi_L \\ -i\sigma^2\phi_L^* \end{bmatrix} \qquad \text{or} \qquad \psi_M = \begin{bmatrix} i\sigma^2\phi_R^* \\ \phi_R \end{bmatrix} \tag{D22}$$

where the two degrees of freedom can be placed in either of the Weyl spinors ϕ_L or ϕ_R. On this form, it is readily confirmed that $\psi_M^c = i\gamma^2\psi_M^* = \psi_M$.

D.5 Transformation Rules of the Clifford Basis

The derivation of the the Dirac equation (D4) and the Dirac Hamiltonian (D8) is based on the transformation properties of the spinors under proper Lorentz transforms. However, the equations governing the behaviour of fermions should also be invariant both under space inversion and time reversal, being symmetries of the underlying Minkowski space. Space inversion and time reversal are both Lorentz transformations, and so will linearly interchange the components of the Dirac spinor according to the Lorentz transformation property of spinors (D5). The general properties of time reversal is investigated in appendix C.

Space inversion corresponds to a Lorentz transformation with ${\Lambda_0}^0 = 1$ and ${\Lambda_k}^k = -1$, acting on Dirac spinors as $\mathcal{P} : \psi(x) \to P\psi(t, -\boldsymbol{x})$. According to the transformation property of the gamma matrices (D7), the space inversion matrix P must commute with γ^0 and anticommute with γ^k. In consequence, the space inversion matrix can be chosen $P = \eta_P\gamma^0$, where η_P is termed the *intrinsic parity* of the fermion described by ψ. Then, as applying space inversion twice must bring back the original spinor, the intrinsic parity $\eta_P = \pm 1$; it can be shown that the positive sign corresponds to fermions and the negative sign to antifermions [45]. In consequence, the space inversion matrix $P = \pm\gamma^0$.

Time reversal corresponds to a Lorentz transformation with ${\Lambda_0}^0 = -1$ and ${\Lambda_k}^k = 1$. However, time reversal is also an antiunitary transformation (C2), and so will act on Dirac spinors as $\mathcal{T} : \psi(x) \to T\psi^*(-t, \boldsymbol{x})$. From the Lorentz transformation property of the gamma matrices (D7), the time reversal matrix T must then satisfy $\gamma^\nu = -T^{-1}(\gamma^\mu)^*{\Lambda_\mu}^\nu T$, where the negative sign comes from the imaginary unit in the Dirac equation (D4). Recalling that γ^0 is hermitian while γ^k are antihermitian (D10), this relation can be written

$$T^{-1}(\gamma^\mu)^T T = -(CT)^{-1}\gamma^\mu CT = \gamma^\mu,$$

where the definition of the charge conjugation matrix (D20) was used. In consequence, the matrix CT anticommutes with all the gamma matrices γ^μ, and so must be a multiple of γ^5, being the only element of the Clifford algebra (D13) having this property. The time reversal matrix thus takes the form $T = \eta_T C^{-1}\gamma^5$, whose exact form will depend on the representation of the gamma matrices due to the charge conjugation matrix C. Hence, time reversal

acts on spinors as $\mathcal{T}\psi(x) = \eta_T C^{-1}\gamma^5\psi^*(-t,\boldsymbol{x})$. Applying the transform twice gives $\mathcal{T}^2\psi = -\psi$ being a general property of fermions, with $|\eta_T| = 1$.

In particular, in the Weyl representation where the charge conjugation matrix takes the form $C = i\gamma^2\gamma^0$ with an inverse $C^{-1} = -C^* = -C$, the time reversal matrix can be expressed $T = -\eta_T C\gamma^5$. Choosing the phase $\eta_T = 1$, the time reversal operator of the Weyl representation takes on the particular form

$$\mathcal{T} = \gamma^1\gamma^3\mathcal{K} = i\Sigma^2\mathcal{K}. \tag{D23}$$

With this convention, the Weyl spinors transform under the rule for fermions (C10) devised in appendix C; in the Weyl representation of the gamma matrices (D3), the time reversal operator acts on Weyl spinors as $\mathcal{T}\phi_{L/R} = i\sigma^2\phi^*_{L/R}$.

From the general transformation properties of the gamma matrices under charge conjugation, space inversion and time reversal, the corresponding transformation properties of all the elements of the Clifford algebra (D13) are readily derived. Notice that even though the transformation properties under the time reversal matrix T are dependent on the representation of the gamma matrices, combining the matrix with the complex conjugation operator $\mathcal{K}$ to give the full operator $\mathcal{T}$ will render representation independent transformation properties of all the Clifford basis elements. The transformation properties under charge conjugation, space inversion and time reversal are summarized in table D.1.

Clifford Basis Elements		Weyl Representation	$\mathcal{P} = \gamma^0$	$\mathcal{T} = \gamma^1\gamma^3\mathcal{K}$	$\mathcal{PT} = i\gamma^2\gamma^5\mathcal{K}$
γ^0	=	$\tau_x \otimes \sigma_0$	$+1$	$+1$	$+1$
$i\boldsymbol{\gamma} = (i\gamma^1, i\gamma^2, i\gamma^3)$	=	$-\tau_y \otimes \boldsymbol{\sigma}$	-1	$+1$	-1
$\gamma^5 = i\gamma^0\gamma^1\gamma^2\gamma^3$	=	$-\tau_z \otimes \sigma_0$	-1	$+1$	-1
$i\gamma^0\gamma^5 = -\gamma^1\gamma^2\gamma^3$	=	$-\tau_y \otimes \sigma_0$	-1	-1	$+1$
$\boldsymbol{\gamma}\gamma^5 = (\gamma^1\gamma^5, \gamma^2\gamma^5, \gamma^3\gamma^5)$	=	$\tau_x \otimes \boldsymbol{\sigma}$	$+1$	-1	-1
$\gamma^0\boldsymbol{\gamma} = (\gamma^0\gamma^1, \gamma^0\gamma^2, \gamma^0\gamma^3)$	=	$-\tau_z \otimes \boldsymbol{\sigma}$	-1	-1	$+1$
$\boldsymbol{\Sigma} = (i\gamma^2\gamma^3, i\gamma^3\gamma^1, i\gamma^1\gamma^2)$	=	$\tau_0 \otimes \boldsymbol{\sigma}$	$+1$	-1	-1

Table D.1: Transformation properties of all products of gamma matrices charge conjugation $\mathcal{C}$, space inversion $\mathcal{P}$, time reversal $\mathcal{T}$ and their combined $\mathcal{PT}$-symmetry. The exact form of the transformation operators are given in the Weyl representation, whereas the transformation properties of all elements are representation independent. The second column gives the Weyl representation of the matrices in terms of two sets of Pauli matrices $\boldsymbol{\sigma}$ and $\boldsymbol{\tau}$ as introduced in chapter 6, where σ_0 and τ_0 are the two-dimensional unit matrix. Imaginary units have been added where needed in order to make all matrices hermitian. Notice that the charge conjugation and time reversal operations are antiunitary.

References

[1] H. Gao et al. "Topological Semimetals from First Principles". In: *Annual Review of Materials Research* 49.1 (2019), pp. 153–183. DOI: 10.1146/annurev-matsci-070218-010049. eprint: https://doi.org/10.1146/annurev-matsci-070218-010049. URL: https://doi.org/10.1146/annurev-matsci-070218-010049.

[2] X. Feng et al. "Two-dimensional topological semimetals". In: (Mar. 2021). arXiv: 2103.13772 [cond-mat.mtrl-sci].

[3] J. Li et al. "Topological semimetals from the perspective of first-principles calculations". In: *Journal of Applied Physics* 128.19 (2020), p. 191101. DOI: 10.1063/5.0025396. eprint: https://doi.org/10.1063/5.0025396. URL: https://doi.org/10.1063/5.0025396.

[4] A. A. Burkov, M. D. Hook, and Leon Balents. "Topological nodal semimetals". In: *Phys. Rev. B* **84** (23 Dec. 2011), p. 235126. DOI: 10.1103/PhysRevB.84.235126. URL: https://link.aps.org/doi/10.1103/PhysRevB.84.235126.

[5] N. P. Armitage, E. J. Mele, and Ashvin Vishwanath. "Weyl and Dirac semimetals in three-dimensional solids". In: *Rev. Mod. Phys.* **90** (1 Jan. 2018), p. 015001. DOI: 10.1103/RevModPhys.90.015001. URL: https://link.aps.org/doi/10.1103/RevModPhys.90.015001.

[6] X. Wan et al. "Topological semimetal and Fermi-arc surface states in the electronic structure of pyrochlore iridates". In: *Phys. Rev. B* 83 (20 May 2011), p. 205101. DOI: 10.1103/PhysRevB.83.205101. URL: https://link.aps.org/doi/10.1103/PhysRevB.83.205101.

[7] J. Rammer and H. Smith. "Quantum field-theoretical methods in transport theory of metals". In: *Rev. Mod. Phys.* **58** (2 Apr. 1986), p. 323. DOI: 10.1103/RevModPhys.58.323. URL: https://link.aps.org/doi/10.1103/RevModPhys.58.323.

[8] G. D. Mahan. *Many-Particle Physics*. New York: (Kluwer Academic/Plenum Publishers, 2000). ISBN: 0306463385.

[9] M. Kargarian, M. Randeria, and N. Trivedi. "Theory of Kerr and Faraday rotations and linear dichroism in Topological Weyl Semimetals". In: *Scientific Reports* **5** (1 Aug. 2015). DOI: 10.1038/srep12683. URL: https://doi.org/10.1038/srep12683.

[10] Y. Fang et al. "Large magneto-optical effects and magnetic anisotropy energy in two-dimensional $Cr_2Ge_2Te_6$". In: *Phys. Rev. B* **98** (12 Sept. 2018), p. 125416. DOI: 10.1103/PhysRevB.98.125416. URL: https://link.aps.org/doi/10.1103/PhysRevB.98.125416.

[11] P. Tang et al. "Dirac fermions in an antiferromagnetic semimetal". In: *Nature Physics* 12.12 (Aug. 2016), pp. 1100–1104. ISSN: 1745-2481. DOI: 10.1038/nphys3839. URL: http://dx.doi.org/10.1038/nphys3839.

[12] J. Linder. *Intermediate Quantum Mechanics*. (bookboon, 2017). ISBN: 0306463385.

[13] J. O. Andersen. *Introduction to Statistical Mechanics*. Bergen: (Fagbokforlaget, 2017). ISBN: 978-82-321-0105-4.

[14] R. P. Feynman, Robert B Leighton, and Matthew Sands. *The Feynman Lectures on Physics Volume III: Quantum Mechanics*. New York: (Basic Books, 2010). ISBN: 978-04-650-2417-9.

[15] N. Young. *An Introduction to Hilbert Space*. Cambridge: (Cambridge Mathematical Textbooks, 2011). ISBN: 9780521337175.

[16] G. Carcassi et al. "Variability as a better characterization of Shannon entropy". Dec. 2019.

[17] R. Kubo. "Statistical-Mechanical Theory of Irreversible Processes. I. General Theory and Simple Applications to Magnetic and Conduction Problems". In: *Journal of the Physical Society of Japan* **12**.6 (Mar. 1957), p. 570. DOI: 10.1143/JPSJ.12.570. eprint: https://doi.org/10.1143/JPSJ.12.570. URL: https://doi.org/10.1143/JPSJ.12.570.

[18] P. Löwdin. "On the Non-Orthogonality Problem Connected with the Use of Atomic Wave Functions in the Theory of Molecules and Crystals". In: *The Journal of Chemical Physics* 18.3 (1950), pp. 365–375. DOI: 10.1063/1.1747632. eprint: https://doi.org/10.1063/1.1747632. URL: https://doi.org/10.1063/1.1747632.

[19] K. S. Novoselov et al. "Electric Field Effect in Atomically Thin Carbon Films". In: *Science* **306**.5696 (Oct. 2004), p. 666. ISSN: 0036-8075. DOI: 10.1126/science.1102896. eprint: https://science.sciencemag.org/content/306/5696/666.full.pdf. URL: https://science.sciencemag.org/content/306/5696/666.

[20] E. Kogan. *Why Dirac points in graphene are where they are?* Bar-Ilan University, Israel, Dec. 2011.

[21] M. V. Berry. "Quantal phase factors accompanying adiabatic changes". In: *Proceedings of the Royal Society of London. A. Mathematical and Physical Sciences* **392**.1802 (Mar. 1984), p. 45. DOI: 10.1098/rspa.1984.0023. eprint: https://royalsocietypublishing.org/doi/pdf/10.1098/rspa.1984.0023. URL: https://royalsocietypublishing.org/doi/abs/10.1098/rspa.1984.0023.

[22] B. Simon. "Holonomy, the Quantum Adiabatic Theorem, and Berry's Phase". In: *Phys. Rev. Lett.* **51** (24 Dec. 1983), p. 2167. DOI: 10.1103/PhysRevLett.51.2167. URL: https://link.aps.org/doi/10.1103/PhysRevLett.51.2167.

[23] A. B. Bernevig. *Topological Insulators and Topological Superconductors*. New Jersey: (Princeton University Press, 2013). ISBN: 069115175X.

[24] D. Vanderbilt. *Berry Phases in Electronic Structure Theory*. Cambridge: (Cambridge University Press, 2018). ISBN: 9781107157651.

[25] G. P. Mikitik and Y. V. Sharlai. "The Berry phase in graphene and graphite multilayers". In: *Low Temperature Physics* **34**.10 (Mar. 2008), p. 794. DOI: 10.1063/1.2981389. eprint: https://doi.org/10.1063/1.2981389. URL: https://doi.org/10.1063/1.2981389.

[26] S. Xu et al. "Discovery of a Weyl fermion semimetal and topological Fermi arcs". In: *Science* **349**.6248 (Aug. 2015), p. 613. ISSN: 0036-8075. DOI: 10.1126/science.aaa9297. eprint: https://science.sciencemag.org/content/349/6248/613.full.pdf. URL: https://science.sciencemag.org/content/349/6248/613.

[27] A. A. Soluyanov et al. "Type-II Weyl semimetals". In: *Nature* **527**.7579 (Nov. 2015), p. 495. ISSN: 1476-4687. DOI: 10.1038/nature15768. URL: http://dx.doi.org/10.1038/nature15768.

[28] S. Xu et al. "Discovery of Lorentz-violating type II Weyl fermions in LaAlGe". In: *Science Advances* **3**.6 (June 2017). DOI: 10.1126/sciadv.1603266. eprint: https://advances.sciencemag.org/content/3/6/e1603266.full.pdf. URL: https://advances.sciencemag.org/content/3/6/e1603266.

[29] S. Guan et al. "Artificial gravity field, astrophysical analogues, and topological phase transitions in strained topological semimetals". In: *npj Quantum Materials* 2.1 (May 2017). ISSN: 2397-4648. DOI: 10.1038/s41535-017-0026-7. URL: http://dx.doi.org/10.1038/s41535-017-0026-7.

[30] A. Ono and S. Ishihara. *Ultrafast reorientation of the Néel vector in antiferromagnetic Dirac semimetals*. 2020. arXiv: 2012.05902 [cond-mat.mes-hall].

[31] L. Šmejkal, T. Jungwirth, and J. Sinova. "Route towards Dirac and Weyl antiferromagnetic spintronics". In: *physica status solidi (RRL) – Rapid Research Letters* 11.4 (2017), p. 1700044. DOI: https://doi.org/10.1002/pssr.201700044. eprint: https://onlinelibrary.wiley.com/doi/pdf/10.1002/pssr.201700044. URL: https://onlinelibrary.wiley.com/doi/abs/10.1002/pssr.201700044.

[32] A. Qaiumzadeh and M. Titov. "Theory of light-induced effective magnetic field in Rashba ferromagnets". In: *Physical Review B* **94**.1 (July 2016). ISSN: 2469-9969. DOI: 10.1103/physrevb.94.014425. URL: http://dx.doi.org/10.1103/PhysRevB.94.014425.

[33] E. A. Galapon. "The Cauchy principal value and the Hadamard finite part integral as values of absolutely convergent integrals". In: *Journal of Mathematical Physics* 57.3 (Mar. 2016), p. 033502. ISSN: 1089-7658. DOI: 10.1063/1.4943300. URL: http://dx.doi.org/10.1063/1.4943300.

[34] N. Nagaosa et al. "Anomalous Hall effect". In: *Rev. Mod. Phys.* 82 (2 May 2010), pp. 1539–1592. DOI: 10.1103/RevModPhys.82.1539. URL: https://link.aps.org/doi/10.1103/RevModPhys.82.1539.

[35] L. I. Magarill, A. V. Chaplik, and M. V. Éntin. "Spin-plasmon oscillations of the two-dimensional electron gas". In: *Journal of Experimental and Theoretical Physics* **92** (Jan. 2001), p. 153. ISSN: 1090-6509. DOI: 10.1134/1.1348471. URL: https://doi.org/10.1134/1.1348471.

[36] K. Uhlířová et al. "The stability and physical properties of the tetragonal phase of bulk CuMnAs antiferromagnet". In: *Journal of Alloys and Compounds* 771 (2019), pp. 680–685. ISSN: 0925-8388. DOI: https://doi.org/10.1016/j.jallcom.2018.08.199. URL: https://www.sciencedirect.com/science/article/pii/S0925838818330809.

[37] L. Šmejkal et al. "Topological antiferromagnetic spintronics: Part of a collection of reviews on antiferromagnetic spintronics". In: (2017). arXiv: 1706.00670 [cond-mat.mes-hall].

[38] L. Šmejkal et al. "Electric Control of Dirac Quasiparticles by Spin-Orbit Torque in an Antiferromagnet". In: *Phys. Rev. Lett.* 118 (10 Mar. 2017), p. 106402. DOI: 10.1103/PhysRevLett.118.106402. URL: https://link.aps.org/doi/10.1103/PhysRevLett.118.106402.

[39] J. Mündelein and H. Schuster. "Darstellung und Kristallstruktur der Verbindungen MnCuX (X = P, As, PxAs1-x) / Preparation and Crystal Structure of Compounds MnCuX (X = P, As, PxAs1-x)". In: *Zeitschrift für Naturforschung B* 47.7 (1992), pp. 925–928. DOI: doi:10.1515/znb-1992-0705. URL: https://doi.org/10.1515/znb-1992-0705.

[40] L. A. Falkovsky and A. A. Varlamov. "Space-time dispersion of graphene conductivity". In: *The European Physical Journal B* 56.4 (Apr. 2007), pp. 281–284. ISSN: 1434-6036. DOI: 10.1140/epjb/e2007-00142-3. URL: http://dx.doi.org/10.1140/epjb/e2007-00142-3.

[41] P. Sharma, A. Principi, and D. L. Maslov. *Optical conductivity of a Dirac-Fermi liquid*. 2021. arXiv: 2106.02616 [cond-mat.str-el].

[42] G. Y. Guo and H. Ebert. "Theoretical investigation of the orientation dependence of the magneto-optical Kerr effect in Co". In: *Phys. Rev. B* 50 (14 Oct. 1994), pp. 10377–10380. DOI: 10.1103/PhysRevB.50.10377. URL: https://link.aps.org/doi/10.1103/PhysRevB.50.10377.

[43] J. Hou and W. Chen. "Hidden antiunitary symmetry behind accidental degeneracy and its protection of degeneracy". In: *Frontiers of Physics* **13**.1, 130301 (July 2018), p. 130301. DOI: 10.1007/s11467-017-0712-8. URL: http://journal.hep.com.cn/fop/EN/abstract/article_20786.shtml.

[44] M. Kachelriess. *Quantum Fields: From the Hubble to the Planck Scale*. New York: Oxford Graduate Texts, 2018. ISBN: 9780198802877.

[45] L. Amitabha and P. B. Pal. *A First Book of Quantum Field Theory*. New Delhi: (Narosa Publishing House, 2005). ISBN: 1842652494.

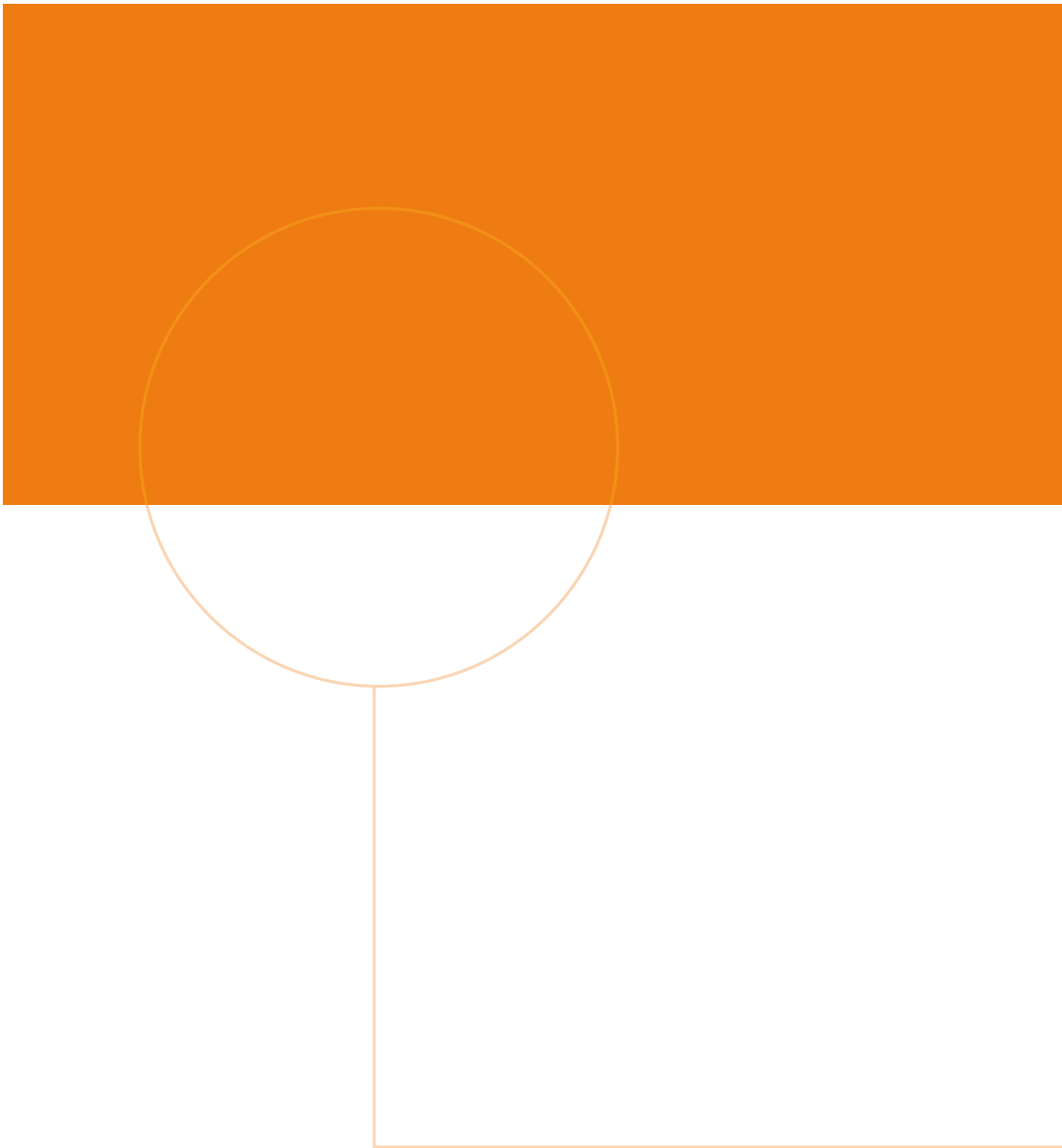

NTNU

Norwegian University of
Science and Technology